

**Department of Structures for Engineering and Architecture**  
**Università degli Studi di Napoli Federico II**

---

---

Ph.D. Thesis

**Flexural Buckling of Steel Cold-Formed Hollow Profiles in the  
Framework of Eurocodes**

A thesis submitted in fulfillment of the  
requirements for the Degree Of  
Doctor of Philosophy in Civil Engineering

by

Arash Poursadrollah

Tutor:

Prof. Eng. R. Landolfo

Co-tutor:

Prof. Eng. M.D'Aneillo

Coordinator:

Prof. Eng. Rosati



**April 2021**

# **Abstract**

The use of cold-formed hollow structural (CFHS) steel has been growing in the past decade due to several advantages such as superior behavior towards lateral-torsional buckling, aesthetic structures, and feasibility of using internal volume to increase load-carrying capacity. The cold-forming process can change drastically the shape of the stress-strain curve and strength parameters of the base material. There are several investigations on buckling tests of hollow section columns; however, studies on cold-formed hollow sections are still lacking. This shortcoming of experimental data becomes more pronounced when the corner behavior of CFHS is under consideration. Only a limited number of corner coupon tests can be found in international literature.

This Ph.D. thesis is developed in line with the progress of the European project INNOvative 3D JOINTS for Robust and Economic Hybrid Tubular Construction (INNO3DJOINTS). The primary objective is to advance, through analytical and experimental research, knowledge on the flexural buckling behavior of CFHS columns. An extensive experimental program ( 21 flexural buckling tests) on SHS and RHS columns has been carried out varying the steel grade (i.e. S275 and S355) and the overall slenderness ratio. This database serves as the basis for the assessment and improvement of the flexural buckling curve for CFHS.

The stress-strain behavior of the sections was investigated by performing tensile coupon tests (81 tests) from both flat and corner areas. special effort was made to obtain the static stress-strain data by pausing the test for 60 seconds during the test. We also employed an innovative method to perform the coupon test on the corner area of CFHS. This procedure will reduce the secondary effect results from methods such as welding a plate or flattening the end grip, and therefore reduce the bias in the results of the corner area.

A comprehensive discussion on the definition of safety and the adopted safety levels in EN1990 and EN1993-1-1 has been presented. The results show some potential criticisms of the application of current rules for plastic design and analysis of such a column and a further investigation is required on the matter. In addition, it is shown that the current material test procedures in BSI and

ATM standards may lead to misevaluate the static strengths of material which is required for the design of structures.

# Acknowledgments:

I would like to thank all the people who contributed in some way to the work described in this thesis. First, I would like to express my special appreciation to my primary supervisor Professor Landolfo who trusted me and gave me the opportunity to do a PhD in his research group and be a part of a big family at the University of Federico II. Without his vision and support, this research would not be possible. I also like to dedicate my greatest gratitude to my second academic advisor Professor D’Aniello “The standing man” who can always bend space-time to spend some time with me against his never-ending busy schedules. He consistently encourages and support me during all these years. Working under his supervision was always an inspiration and honor and I must say, I have learned many things from him both on academic and personal level which will stay with me for the rest of my life.

This thesis relies on results and financial support obtained under European Commission Research Programme of the Research Fund for Coal and Steel (Grant Agreement Number: 749959). This financial support is acknowledged.

I need to mention the bright graduate student Camilla Pellecchia who contributed to the project and more importantly also helped me with my Italian skills.

I would like to thank my home mate, Salvatore Benevento and his beautiful fiancé, Rossella for their delicious Lasagnes.

During the time that I spent in Napoli I had the luxury to meet some really good friends that supported me during difficult times. My special thanks go to my officemate Cristiana who makes the best cakes!

My sincere thanks to my moral advisor Hooman and Hoorah Rahnama for providing me moral support especially during the quarantine time.

Finally, I would like to thank my family for all their support. Especially my sister, it is not possible for me to express my gratitude to you.

Arash Poursadrollah

April, 2021

Disclaimer

The opinions, findings, and conclusions or recommendations expressed in this publication are those of the author and do not necessarily reflect the views of the study sponsor, European Commission Research Programme of the Research Fund for Coal and Steel.

# Table of Contents

<b>Abstract.....</b>	<b>ii</b>
<b>Acknowledgments: .....</b>	<b>iv</b>
<b>Table of Contents .....</b>	<b>vi</b>
<b>List of Figures.....</b>	<b>x</b>
<b>List of Tables .....</b>	<b>xv</b>
<b>Introduction.....</b>	<b>2</b>
1.1    Motivations.....	2
1.2    Objectives.....	2
1.3    Organization and outline .....	3
<b>2    Literature review .....</b>	<b>4</b>
2.1    Historical review of CFHS.....	4
2.2    Hollow sections manufacturing process.....	6
2.3    Characteristics of cold-formed sections .....	11
2.3.1    Stress-strain diagram description.....	11
2.3.2    Residual stress pattern.....	16
2.4    Buckling of an Axially loaded column .....	21
2.4.1    Introduction.....	21
2.4.2    History of column buckling .....	26
2.4.3    Ideal Elastic Column.....	31
2.4.4    Imperfect and Inelastic Column.....	35
2.4.5    Buckling curves method in Eurocode 1993-3-1 .....	38
2.5    Design for stability, why we do what we do!.....	42
2.5.1    How to design for stability?.....	45

<b>3</b>	<b>Probability of failure (Reliability)</b> .....	<b>50</b>
3.1	Introduction .....	50
3.2	Uncertainty .....	50
3.2.1	Different Types of Uncertainty .....	51
3.2.2	Describing Uncertainty .....	53
3.3	Definition of Safety .....	54
3.4	Eurocode 1990.....	56
3.4.1	Introduction.....	56
3.4.2	Reliability in Eurocode 1990 .....	57
<b>4</b>	<b>Experimental Program</b> .....	<b>61</b>
4.1	Introduction .....	61
4.2	Specimens.....	61
4.3	Geometrical imperfections .....	64
4.4	Out-of-straightness measurements .....	66
4.5	Tensile Coupon tests .....	67
4.5.1	Introduction.....	67
4.5.2	Test specimens .....	67
4.5.3	Test set up .....	70
4.5.4	Test procedure.....	72
4.6	Pin-ended column tests.....	75
4.6.1	Introduction.....	75
4.6.2	Test configuration and procedure .....	75
4.7	Results and Discussion.....	78
4.7.1	Geometric imperfection .....	78
4.7.2	Out-of-Straightness .....	81
4.7.3	Material Properties .....	83
4.7.4	Pin-ended column test results .....	91
<b>5</b>	<b>Finite element analysis</b> .....	<b>95</b>

5.1	Introduction .....	95
5.2	Micro Model.....	95
5.2.1	Description of the micro FEM .....	95
5.2.2	Geometry and Boundary conditions .....	96
5.2.3	Finite element mesh .....	97
5.2.4	Material Nonlinearity.....	98
5.2.5	Linear Buckling analysis.....	98
5.2.6	Geometric imperfections.....	99
5.2.7	Residual stress.....	99
5.2.8	Validation of the numerical models.....	100
5.2.9	Parametric Study.....	101
5.2.9.1	Effect of the residual stress.....	101
5.2.9.2	Effect of Geometric Imperfections .....	103
5.3	Macro FEM (OpenSees).....	105
5.3.1	Model Description .....	105
5.3.2	Geometric Imperfections .....	106
5.3.3	Cross-section Fibers.....	107
<b>6</b>	<b>Safety Assessment of EC3-1-1 buckling curve.....</b>	<b>110</b>
6.1	Introduction .....	110
6.2	Background of the ECCS experimental research on column strength.....	110
6.2.1	Interpretation of the results .....	112
6.3	Different levels of safety in Eurocodes .....	113
6.4	Monte Carlo Simulation.....	115
6.5	Finite element reliability analysis of the model .....	120
<b>7</b>	<b>Summary and conclusion.....</b>	<b>124</b>
7.1	Development of Databases for the safety assessment of CFHS.....	124
7.2	Assessment of the flexural buckling curve for CFHS.....	125
<b>8</b>	<b>References.....</b>	<b>127</b>



<b>Appendix A Geometric Measurements and static properties.....</b>	<b>133</b>
A.1 Geometric measurements .....	133
A.2 Tensile coupon test results .....	170
<b>Appendix B Detailed flexural buckling test results and comparison with FE results.....</b>	<b>183</b>

# List of Figures

FIGURE 2-1 LEFT: BRITANNIA BRIDGE (MENAI), MIDDLE: FIRTH OF FORTH BRIDGE (EDINBURGH), RIGHT: ROYAL ALBERT BRIDGE (SALTASH).....	4
FIGURE 2-2 (A) AIR FLUX (B) PAINTING SURFACE FOR HOLLOW SECTIONS AND OPEN SECTIONS .....	5
FIGURE 2-3 HOT ROLLING PROCESS .....	6
FIGURE 2-4. COLD-FORMED A) STRUCTURAL MEMBER B) SHEETING MEMBER .....	7
FIGURE 2-5 DIFFERENT SHAPES OF HOLLOW SECTIONS .....	7
FIGURE 2-6 MANUFACTURING PROCESS OF PRESS-BREAK SECTIONS [3] .....	8
FIGURE 2-7 DIRECT FORMING MANUFACTURING PROCESS [4].....	9
FIGURE 2-8 CONTINUOUS FORMING PROCESS – CIRCLE-TO-RECTANGULAR FORMING [4] .....	9
FIGURE 2-9 LEFT: FLAT ROLLERS USED IN DIRECT FORMING RIGHT: CONCAVE ROLLERS USED IN CONTINUOUS FORMING .....	10
FIGURE 2-10 TYPICAL COLD-FORMED STRESS-STRAIN CURVE ALONG WITH RAMBERG-OSGOOD FORMULA.....	12
FIGURE 2-11 AREA OF ENHANCED MATERIAL PROPERTIES [14] .....	15
FIGURE 2-12 SCHEMATICS ILLUSTRATING TYPICAL RESIDUAL STRESS GRADIENTS INDUCED BY MANUFACTURING PROCESS [18] .....	16
FIGURE 2-13 SCHEMATICS ILLUSTRATING THE SECTIONING METHOD, LEFT: INSTALLATION OF THE STRAIN GAUGES RIGHT: DIVIDING THE SPECIMEN FOR CUTTING.....	17
FIGURE 2-14 DEFORMATION OF THE SPECIMEN AFTER THE RELEASE OF RESIDUAL STRESSES .....	18
FIGURE 2-15 DIFFERENT TYPES OF RESIDUAL STRESSES.....	18
FIGURE 2-16 HOLE-DRILLING METHODS: (A) CONVENTIONAL HOLE-DRILLING METHOD, (B) RING- CORE METHOD .....	19
FIGURE 2-17 HOLE-DRILLING METHODS: (A) CONVENTIONAL HOLE-DRILLING METHOD, (B) RING- CORE METHOD .....	19
FIGURE 2-18 RESIDUAL STRESS MODELS, TOP: PROPOSED MODEL BY [19] BOTTOM: CLASSICAL MODEL .....	20
FIGURE 2-19 RESIDUAL STRESSES MODEL FOR CFS (NORMAL STRENGTH STEEL).....	21

FIGURE 2-20 THE THREE EQUILIBRIUM STATES: (A) STABLE; (B) NEUTRAL; (C) UNSTABLE .....	22
FIGURE 2-21 THE EQUILIBRIUM CONDITION OF A SDOF .....	23
FIGURE 2-22 PE AT THE EQUILIBRIUM POINT .....	24
FIGURE 2-23 PE IN A NONLINEAR SYSTEM .....	25
FIGURE 2-24 STRESS-STRAIN DIAGRAM OF THE COLUMN WITH NONLINEAR MATERIAL .....	29
FIGURE 2-25 LOAD-DEFLECTION DIAGRAM FOR ELASTIC AND INELASTIC BUCKLING .....	30
FIGURE 2-26 CHRONOLOGICAL OVERVIEW OF COLUMN BUCKLING.....	30
FIGURE 2-27 AN IDEAL ELASTIC COLUMN LOADED AXIALLY .....	31
FIGURE 2-28 VERTICAL LOAD VERSUS THE LATERAL DEFLECTION FOR AN IDEAL COLUMN .....	33
FIGURE 2-29 BUCKLING CURVE A) CONSIDERING ONLY STABILITY B) CONSIDERING BOTH STRENGTH AND STABILITY .....	35
FIGURE 2-30 EXPERIMENTAL DATA COMPARED TO EULER AND DESIGN CURVE.....	36
FIGURE 2-31 AXIALLY LOADED COLUMN WITH AN INITIAL BOW IMPERFECTION .....	37
FIGURE 2-32. BUCKLING CURVES FOR FLEXURAL BUCKLING IN EC3-1-1 .....	38
FIGURE 2-33. BIFURCATION POINT.....	42
FIGURE 2-34. AMPLIFICATION VS. BUCKLING .....	43
FIGURE 2-35. REAL COLUMN LOAD PATH.....	43
FIGURE 2-36. RESIDUAL STRESSES IN THE WIDE FLANGE SECTION .....	44
FIGURE 2-37. COLUMN STRENGTH CURVE.....	45
FIGURE 2-38. EFFECTIVE LENGTH APPROACH .....	46
FIGURE 2-39. DESIGNING CANTILEVER COLUMN USING EFFECTIVE LENGTH METHOD .....	47
FIGURE 2-40. DIFFERENT METHODS OF INDUCING OUT-OF-PLUMBNESS .....	48
FIGURE 2-41. DIRECT ANALYSIS METHOD .....	48
FIGURE 2-41. DIRECT ANALYSIS METHOD .....	49
FIGURE 3-1 FUZZY LOGIC TEMPERATURE.....	53
FIGURE 3-2 A) HIGHER ENTROPY B) LOWER ENTROPY .....	54
FIGURE 3-3 A) DEFINITION OF THE PROBABILITY OF FAILURE, DESIGN VALUE AND PROBABILITY OF SURVIVAL .....	56
FIGURE 3-4 LINKS BETWEEN EUROCODES [24] .....	57
FIGURE 3-5 PROBABILITY OF FAILURE FOR A TWO-DIMENSIONS PROBLEM.....	59
FIGURE 3-6 CONTOURS OF JOINT PDF .....	60

FIGURE 4-1 SECTION NOTATION.....	61
FIGURE 4-2 INVESTIGATED CROSS-SECTIONS IN THIS STUDY .....	63
FIGURE 4-3 NUMBER OF SPECIMENS IN TERMS OF LOCAL SLENDERNESS RATIO AND STEEL GRADE	63
FIGURE 4-4 THICKNESS MEASUREMENT LOCATIONS .....	64
FIGURE 4-5 CORNER RADII MEASUREMENTS .....	64
FIGURE 4-6 DIFFERENCE BETWEEN MEASURED AND NOMINAL THICKNESS FOR SPECIMEN S275_200×120×12_B.....	66
FIGURE 4-7 GEOMETRICAL IMPERFECTIONS MEASUREMENT .....	66
FIGURE 4-8 MEASURED IMPERFECTIONS PROFILE FOR SECTION S355_200×100×12.5_A .....	66
FIGURE 4-9 LOCATIONS OF THE TENSILE COUPONS .....	68
FIGURE 4-10 DIMENSION OF FLAT COUPON SPECIMENS.....	68
FIGURE 4-11 A) TYPICAL FLAT COUPON B) TYPICAL TRANSVERSAL COUPON .....	69
FIGURE 4-12 DIMENSION OF CORNER COUPON .....	69
FIGURE 4-13 TEST SET UP FOR FLAT COUPONS IN THIS STUDY .....	70
FIGURE 4-14 DIFFERENT COMPONENTS OF THE CURVED COUPON .....	71
FIGURE 4-15 TEST SET-UP FOR CORNER COUPONS IN THIS STUDY .....	71
FIGURE 4-16 TYPICAL STATIC DROP DURING STRESS RELAXATION .....	72
FIGURE 4-17 STRAIN RATE USED DURING THE TENSILE TEST A) UP TO $F_Y$ B) FROM $F_Y$ TO $F_U$ .....	73
FIGURE 4-18 A TYPICAL DYNAMIC CURVE .....	73
FIGURE 4-19 A) DETERMINATION OF YOUNG'S MODULUS B) OBTAINING A STATIC CURVE FROM A DYNAMIC CURVE.....	74
FIGURE 4-20 LEFT: SCHEMATIC VIEW RIGHT: COLUMN TEST MACHINE .....	76
FIGURE 4-21 HOLLOW SECTIONS PROFILES WITH END PLATES .....	76
FIGURE 4-22 SPECIAL END PLATES.....	77
FIGURE 4-23 TEST CONFIGURATION AND LDTV LAYOUT .....	77
FIGURE 4-24 MEASURED THICKNESS COMPARED TO EN10219 TOLERANCE .....	78
FIGURE 4-25 AVERAGE OF MEASURED CORNER AREA WIDTHS COMPARED TO TOLERANCES SET IN EN 10219.....	79
FIGURE 4-26 EVALUATION OF MEASURED CORNER RADIUS DIMENSIONS AGAINST LIMITATION TO WELDING IN THE COLD-FORMED .....	79
FIGURE 4-27 K-S TEST FOR THE OBSERVED DATA .....	82

FIGURE 4-28 GENERIC REPRESENTATION OF THE STRESS-STRAIN CURVE USING THE 0.2% PROOF STRESS .....	83
FIGURE 4-29 TYPICAL FRACTURE OF A) FLAT B) TRANSVERSAL C) CORNER D) WELD COUPONS ...	83
FIGURE 4-30 SUMMARY OF COUPON TEST RESULTS FOR SECTION S355_200×200×8.....	84
FIGURE 4-31 AVERAGE STRESS REDUCTION WITH (+/- SD) FOR A) FLAT AND CORNER COUPONS B) TRANSVERSAL AND WELD COUPONS C) FLAT COUPONS DIVIDED BY STEEL GRADE D) CORNER COUPONS DIVIDED BY STEEL GRADE .....	85
FIGURE 4-32 DUCTILITY OF TESTED COUPONS FOR THE DIFFERENT CROSS-SECTIONS .....	86
FIGURE 4-33 COMPARISON OF THE STRENGTH PARAMETERS OF THE TEST TO THE VIRGIN MATERIAL .....	88
FIGURE 4-34 EC3-1-1 DUCTILITY REQUIREMENT FOR STEEL A) HARDENING RATIO B) DUCTILITY .	89
FIGURE 4-35 COMPARISON OF THE PROPOSED EQUATION TO THE TESTS DATA .....	91
FIGURE 4-36 LEFT) LOAD VERSUS AXIAL DEFORMATION RIGHT) FAILURE MODE .....	92
FIGURE 4-37 LATERAL DISPLACEMENT EVOLUTION ALONG WITH THE COLUMN HEIGHT .....	92
FIGURE 4-38 NORMALIZED TEST RESULTS WITH DESIGN BUCKLING CURVES .....	93
FIGURE 5-1 COLUMN MODEL BOUNDARY CONDITION .....	96
FIGURE 5-2 BUCKLING LOAD FOR DIFFERENT MESH SIZE .....	97
FIGURE 5-3 FINITE ELEMENT MESH OF THE MODEL .....	97
FIGURE 5-4 GLOBAL AND LOCAL EIGNEMODES .....	98
FIGURE 5-5 APPLIED RESIDUAL STRESSES IN THE NUMERICAL MODEL.....	99
FIGURE 5-6 OBSERVED FAILURE MODE IN THE NUMERICAL MODEL AND EXPERIMENTAL TEST ....	100
FIGURE 5-7 LOAD AXIAL DEFORMATION FOR SPECIMEN S275_100×100×8 .....	100
FIGURE 5-8 EFFECT OF RESIDUAL STRESS FOR DIFFERENT SECTION AND DIFFERENT LOCAL SLENDERNESS RATION .....	102
FIGURE 5-9 EFFECT OF RESIDUAL STRESSES.....	103
FIGURE 5-10 EFFECT OF RESIDUAL STRESS FOR DIFFERENT SECTION AND DIFFERENT LOCAL SLENDERNESS RATION .....	104
FIGURE 5-11 EFFECT OF RESIDUAL STRESSES.....	104
FIGURE 5-12 DISTRIBUTED PLASTICITY MODEL .....	105
FIGURE 5-13 CURVATURE DISTRIBUTION OF THE COLUMN.....	106
FIGURE 5-14 INITIAL OUT-OF-STRAIGHTNESS .....	107

FIGURE 5-15 MATERIAL CALIBRATION FOR STEEL 02 MATERIAL A) FLAT B) CORNER .....	107
FIGURE 5-16 FIBER-BASED CROSS-SECTION OF THE COLUMN.....	108
FIGURE 5-17 LOAD-AXIAL DEFORMATION OF THE TEST RESULT AND OPENSEES MODEL.....	109
FIGURE 6-1 EXPERIMENTAL TESTS RESULTS AND THE FITTED BUCKLING CURVE, ERROR BARS SHOW MEAN MINUS TWO STD [44] .....	113
FIGURE 6-2 SEPARATION OF LOAD AND RESISTANCE SIDE OF THE PROBLEM .....	114
FIGURE 6-3 DIFFERENT LEVEL OF SAFETY IN EUROCODE SERIES.....	115
FIGURE 6-4: GENERATED RANDOM NUMBERS FOR THE UNCERTAIN PARAMETERS (S 275).....	116
FIGURE 6-5 GENERATED CORRELATED RANDOM VARIABLES .....	117
FIGURE 6-6 MCS FOR TWO DIFFERENT SLENDERNESS RATIO AND THEIR CORRELATION .....	117
FIGURE 6-7 Q-Q PLOT FOR THE BUCKLING LOAD VERSUS THEORETICAL LOGNORMAL QUANTILES B) LILLIEFORS GOODNESS-OF-FIT TEST .....	118
FIGURE 6-8 RESULTS OF MC SIMULATION FOR S355 .....	119
FIGURE 6-9 EC CURVE WITH THE PROPOSED $\Lambda$ AND $\Lambda_0$ .....	120
FIGURE 6-10. SCHEMATIC PRESENTATION OF FORM METHOD FOR A BIVARIATE PROBLEM.....	121
FIGURE 6-11 RANKING OF RANDOM VARIABLES BASED ON THEIR IMPACT ON THE RELIABILITY INDEX (I.E., $\beta$ ) FOR A) $\lambda=1.8$ B) $\lambda=0.55$ .....	123

# List of Tables

TABLE 2-1 RECOMMENDED REPRESENTATIVE VALUES FOR STRAIN HARDENING EXPONENTS N AND M [7].....	13
TABLE 2-2. BUCKLING CURVE SELECTION FOR A CROSS-SECTION WITH STEEL QUALITY S235, S275, S355 AND S420 .....	39
TABLE 2-3 IMPERFECTION FACTORS FOR BUCKLING CURVES. ....	40
TABLE 3-1 DEFINITION OF CONSEQUENCES CLASSES (TABLE B1 EN1990).....	58
TABLE 3-2 CONSEQUENCES AND RELIABILITY CLASSES, AND VALUES FOR THE RELIABILITY INDEX .....	58
TABLE 4-1 SHS SPECIMEN MEASUREMENTS .....	62
TABLE 4-2 RHS SPECIMEN MEASUREMENTS .....	62
TABLE 4-3 NOMINAL AND MEASURED DIMENSIONS OF SPECIMENS .....	65
TABLE 4-4 COLUMN OUT-OF-STRAIGHTNESS MEASUREMENTS.....	81
TABLE 4-5 CDF VALUES FOR THE MAXIMUM IMPERFECTION .....	82
TABLE 4-6 TENSILE COUPON TEST RESULTS FOR YIELD STRESS.....	87
TABLE 4-7 TENSILE COUPON TEST RESULTS FOR ULTIMATE STRESS .....	87
TABLE 4-8 CHARACTERISTIC VALUE OF THE HARDENING RATIO AND DUCTILITY.....	89
TABLE 4-9 STATISTICAL VALUES FOR THE INPUT PARAMETERS OF R-O AND STEEL02 MATERIAL .	90
TABLE 4-10 COMPARISON BETWEEN TEST RESULTS AND DIFFERENT BUCKLING CURVES.....	94
TABLE 6-1 COMPARISON OF LOADING TECHNIQUES FOR VARIOUS TESTING METHODS .....	111
TABLE 6-2 SUMMARY OF THE RANDOM VARIABLES.....	115
TABLE 6-3 $\lambda_0$ AND A VALUES OBTAINED FROM OPTIMIZATION FOR FLEXURAL BUCKLING OF COLD-FORMED SECTIONS .....	120
TABLE 6-4 RESULTS OF FORM ANALYSIS FOR $\lambda = 0.55$ AND 1.8.....	122





# **Introduction**

## **1.1 Motivations**

The use of cold-formed hollow structural (CFHS) steel has been growing in the past decade due to several advantages such as superior behavior towards lateral-torsional buckling, aesthetic structures, and feasibility of using internal volume to increase load-carrying capacity. The behavior of CFHC is different from their hot-rolled counterparts in several aspects, such as the residual stress pattern and the stress-strain response of the section. However, only a limited number of experimental tests are available in international literature dealing with CFHS members manufactured with recent technology. This lack of knowledge is more pronounced for the response of the corner area of CFHS. This is mainly due to the difficulty of conducting a stress-strain test on a curved geometry of coupons extracted from the corner area.

Furthermore, the objective of designing a structure based on the Eurocodes is to have a consistent level of safety within different structures. This point is particularly important since it allows us to use our resources efficiently and economically. However, it will be shown that different Eurocodes adopts different level of safety.

## **1.2 Objectives**

The majority of previous investigations on buckling behavior of steel tubular members have involved hot-formed and built-up sections. Comparatively, little work has been done to establish a database for cold-formed hollow sections. It is well known that cold-forming causes strain hardening of the steel material. Therefore, its mechanical features are changed. The main goal of this research is to investigate the different characteristics of the cold-formed profiles and provide recommendations if necessary. The enhancement of strength parameters is measured through an extensive coupon stress-strain test, together with investigating the sensitivity of these parameters to the strain rate effect.

A detailed and step-by-step assessment of the current buckling curve is presented. The ultimate goal is to develop an improved buckling curve for designing of flexural buckling of cold-formed sections.

### **1.3 Organization and outline**

In order to pursue the objectives described earlier, this thesis has been organized into the following chapters.

A literature review of the historical background and the main experimental studies on CFHS is presented in chapter two. The same chapter also discusses the main characteristics of CFHS compared to its counterpart hot rolled sections.

Chapter three discusses thoroughly the definition of the safety and accepted risk in the framework of Eurocodes. The objective is to provide a clear and unambiguous definition of the concept of structural safety for chapter six. It also discusses the principles and provisions of EN1990 regarding the level of safety as the heading document in the Eurocode series.

Chapter four focuses on the experimental program regarding CFHS. 21 flexural buckling tests and 81 tensile stress-strain coupon tests have been conducted. Preliminary measurements were also performed and described in this chapter. It consists of measurements of the geometrical dimensions and imperfections such as out-of-straightness of the columns. Furthermore, the results provided in this chapter will serve as a database for the probabilistic assessment in chapter fourth.

Chapter five presents finite element models and numerical simulations of the tested specimens. Two models have been developed and calibrated, whose description is given in this chapter. One of them can be employed in evaluating the member in detail (Micro model), while the other one can predict the maximum buckling load with acceptable accuracy (Macro model), which can be employed in time-consuming analysis types such as probabilistic analyses.

Chapter six addresses the basic idea for the European statistical approach to the column strength problem and highlights the different levels of safety adopted from the intended level (discussed in chapter three) through a historical review on the development of the current flexural buckling curve. It also presents a probabilistic approach to solve the issue and propose a new buckling curve for Eurocode's next generation with uniform safety.

## 2 Literature review

### 2.1 Historical review of CFHS

In the past 30 years, a marked development has been seen in the fabrication and use of structural steelwork, with a general tendency towards utilizing thinner-walled members as primary load-bearing components. Material cost considerations have motivated these developments and the recognition that thin-walled members are generally more efficient in overall stability performance. The use of hollow steel sections started at the beginning of the 19th century in the construction of bridges, as shown in Figure 2-1. The first rectangular hollow sections were used in the construction of the Britannia Bridge in Menai (1850).



Figure 2-1 Left: Britannia Bridge (Menai), Middle: Firth of Forth Bridge (Edinburgh), Right: Royal Albert Bridge (Saltash)

An important turning point in the history of hollow sections was Alexander Graham Bell (1907) 's attempt to build a light resistance plane wing from a hollow section spatial truss.

Industrial-scale production of hollow sections started in the 60s in England. Square, Rectangular and circular shapes were standardized (SHS, RHS, and CFHS, respectively).

In the 1950s, issues related to manufacturing, end cutting, and welding of hollow sections were solved, enabling the spread use of this type of structure. The main obstacle became the lack of knowledge of its structural behavior as well as their connections resistance [1]. In the middle of this scenario, in 1962, the hollow sections producers created the International Committee for the Study and Development of Tubular Structures (CIDECT) to join the resources available in industries, universities, and other international organizations. The main focus is on structural design, structural behavior, connection

resistance, fatigue, corrosion resistance, manufacturing, and maintenance of hollow sections. Some of the main advantages of the hollow sections are highlighted here [1]:

- The tubular shape is attractive from the architectural point of view
- Hollow sections, especially the circular ones, have the most effective resistance to torsion moment because the material is uniformly distributed around the polar axis. The torsional constant for tubular sections is between 200 up to 300 times greater than for open sections.
- Tubular sections have an impressive advantage for structures exposed to air and water currents. The drag coefficients are much lower than those of open sections with sharp edges (Figure 2-2 (a)) [1].
- Compared to open sections, they have a smaller superficial area, leading to lower painting and fire-protecting costs and reducing the need for maintenance services (Figure 2-2(b)).

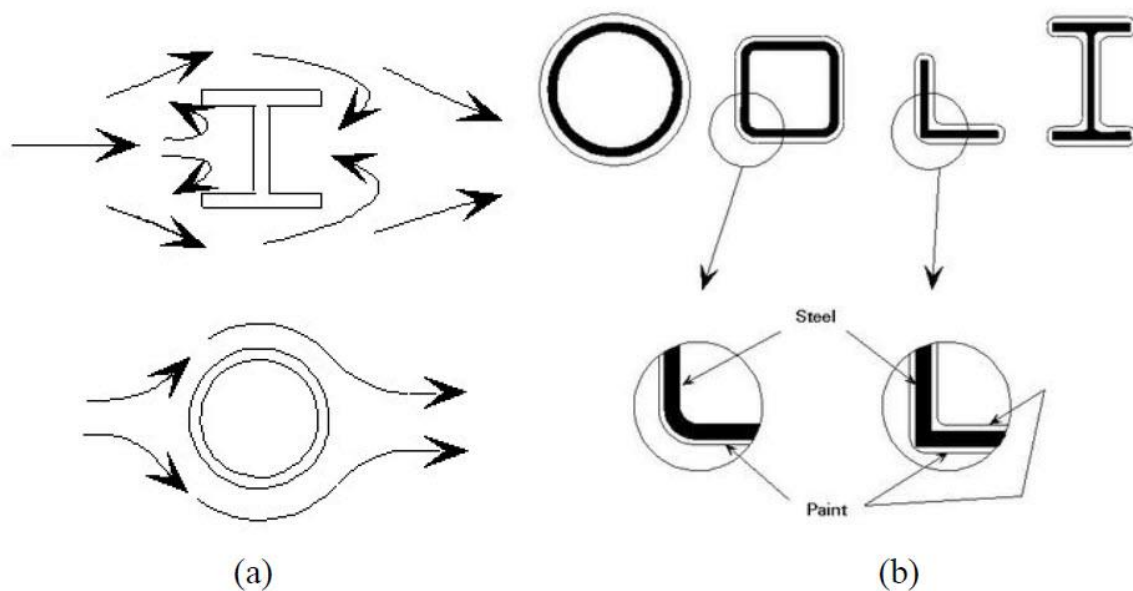


Figure 2-2 (a) Air flux (b) painting surface for hollow sections and open sections

- The inner space of a hollow section can be used to combine the structural resistance to a second function such as (i) filled with concrete to enhance compression strength or to protect against fire; (ii) incorporate a heat and ventilation system in the tubular columns
- Square and rectangular hollow section's connections are simpler.

On the other hand, they have some disadvantages, such as the difficulty of inspection due to their closed form.

The development of thin-walled technology has not, however, been without problems. The instability probably represents the most common cause of structural failure, and the introduction of thin-walled structural members has added the possibility of both local instability and the interaction with overall instability. Not surprisingly, the refinement of thin-walled structural theory and commensurate testing has grown into a major research area from its beginnings almost a century ago.

## 2.2 Hollow sections manufacturing process

In general, "rolling" is a process that uses a pair of rolls to form materials. There are two rolling techniques, hot-rolling and cold roll-forming based on the temperature of the metal being used. If the temperature is above the crystallization temperature of the metal, the process is called hot-rolling; otherwise, it is called cold-rolling. In hot-rolling, hot-molten steel is passed several times through pairs of rolls to achieve the desired profile. Most structural steel components such as I-Shape, L-Shape, and so forth, are hot-rolled, as shown in Figure 2-3.

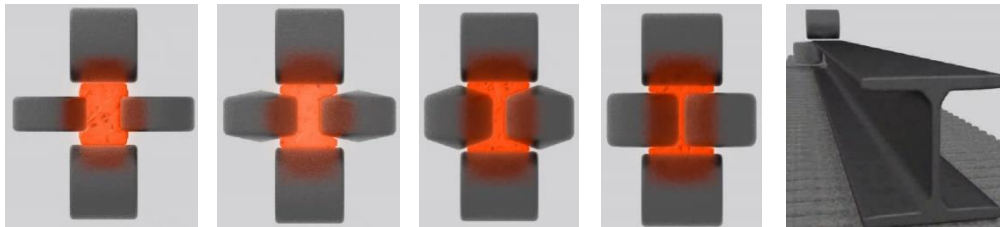


Figure 2-3 Hot rolling process

Contrary to the hot-roll process, Cold-rolling is a process that passes metal through rollers at temperatures below its crystallization temperature. This increases the material strength and improves the surface finish. Cold roll-forming uses thin sheets of steel to form into various shape sections such as floor and roof panels or C or Z shapes. These shapes are called cold-formed shapes. Nowadays, cold-formed structural member products can be classified into two main typologies:

- Structural members.
- Sheeting.

Typical sections belonging to the first typology of cold-formed products are shown in Figure 2-4 (a). They are structural members used as columns and beams. The second category of cold-formed

sections is plane load-bearing members. This typology (see Figure 2-4(b)) is generally used when a space-covering function under moderate distributed loading is needed [2] (e.g., roof decks, floor decks, wall panels).

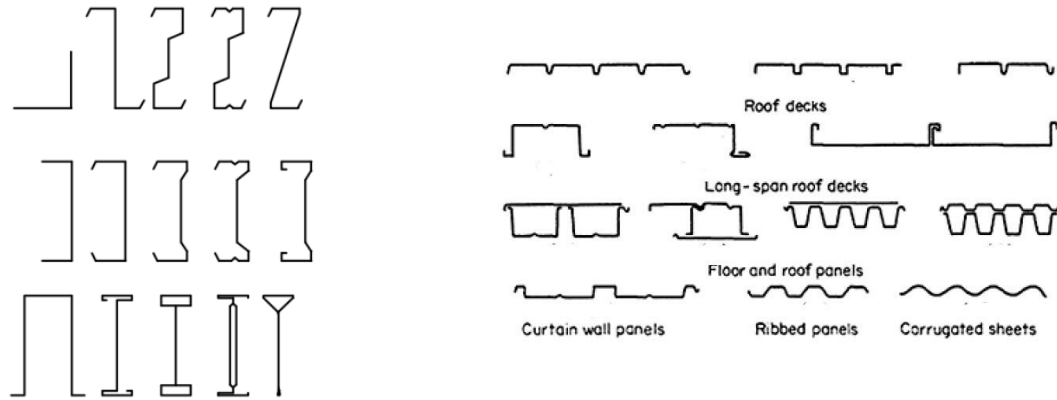


Figure 2-4. Cold-formed a) structural member b) Sheeting member

Hollow section is a type of the first category, with a hollow tubular cross-section, as shown in Figure 2-5.



Figure 2-5 Different shapes of hollow sections

Cold-formed sections can be generally obtained through two manufacturing methods: by rolling or by press-breaking [2].

Press-breaking is a process of cold-forming of sections from a flat sheet. Longitudinal fold is applied along the sheet by a tool pressing the material into a die. This process is used to create open sections such as angles and channels. The manufacturing process is shown in Figure 2-6.

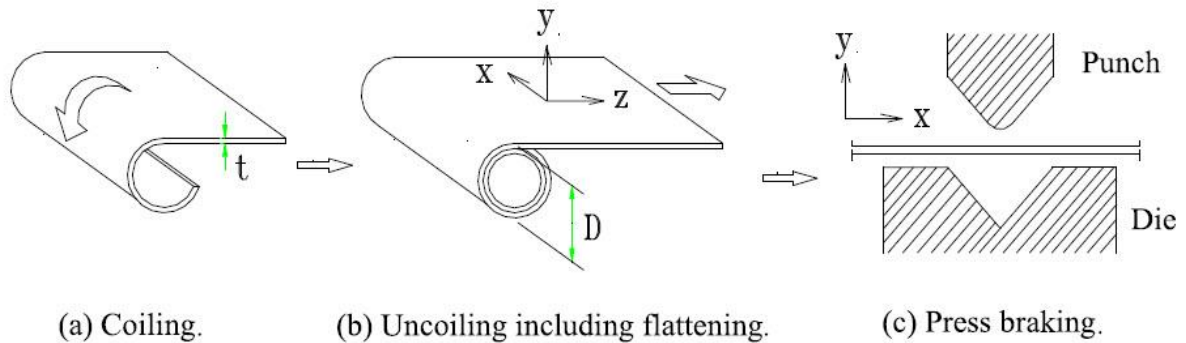


Figure 2-6 Manufacturing process of press-break sections [3]

The rolling process is commonly employed to produce cold-formed hollow sections. Cold rolling allows producing of large volumes of identical structural sections with low fabrication tolerances. Internationally, there are two standard manufacturing methods for cold-formed hollow sections: direct forming and continuous forming. For both methods, the coil strip is progressively cold-bent into the desired shape by passage through a series of pressure rollers, during which the rollers induce a controlled amount of cold-bending (depending on the sizes of the used rollers) to the coil strip. Thus, the mechanical properties are theoretically consistent in the longitudinal direction of the RHS product. However, some gradual variations in the longitudinal direction will occur for both methods. The feature of the final product in cold-formed structures are highly affected by the manufacturing type. The direct-forming process is illustrated in Figure 2-7, and it includes the following step

1. roll-forming a coil strip directly into an open section with the desired rectangular shape
2. joining the edges of the open section by welding to form a closed rectangular shape

The strip edges are heated by either high frequency (HF) induction or electric resistance welding and then forged together by weld rolls to create a continuous longitudinal weld without the addition of filler metal. The most common welding process is electric resistance welding, where the edges of the strip are heated normally by a high-frequency electrical current. The external weld is usually cleaned off mechanically to improve the external appearance of the tube.

Before the forming process is applied, the flat steel may have already experienced the coiling, uncoiling, and flattening process. In this case, the cold-working is concentrated at the four corners, whereas the flat faces (not containing the weld) of the final product have similar properties to the feed material.

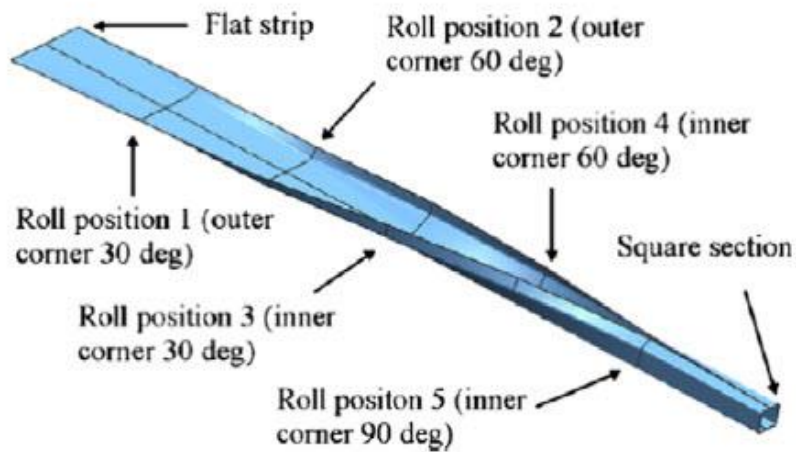


Figure 2-7 Direct forming manufacturing process [4]

The continuous-forming process is illustrated in Figure 2-8 and includes:

1. roll-forming a coil strip first into a circular open tube
2. joining the edges of the open tube by welding to form a closed circular shape
3. flattening the circular tube walls to form the desired rectangular shape

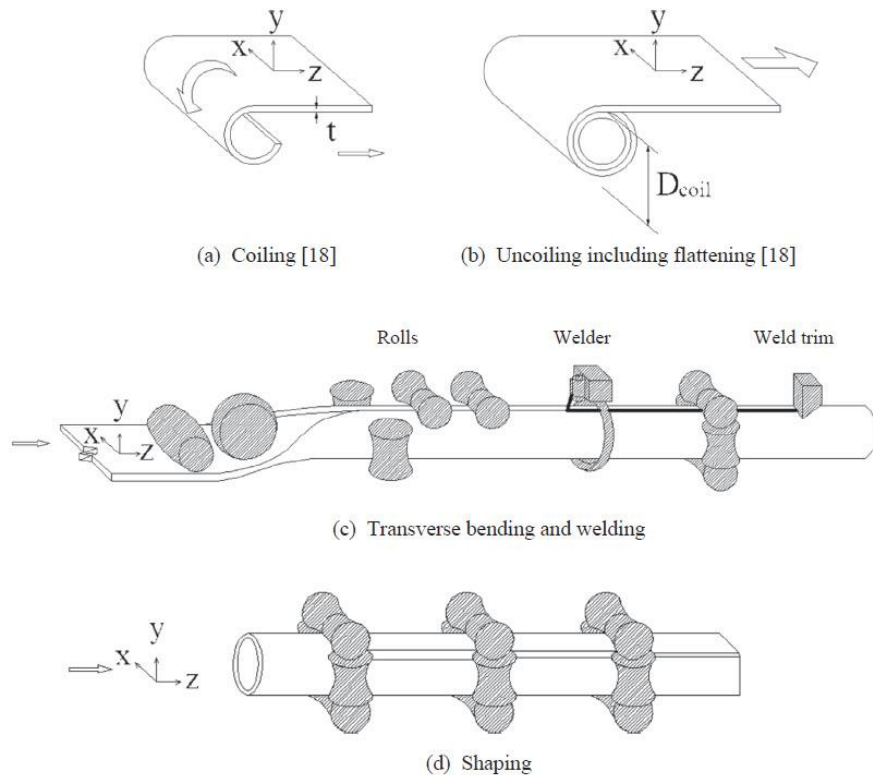


Figure 2-8 Continuous forming process – circle-to-rectangular forming [4]



The continuous-forming process is used more frequently compared to the direct-forming process. As described above, the difference is during the continuous-forming method; a welded circular tube is first formed from a steel strip and then shaped into a desired cross-sectional shape. In the current study, only the continuous-forming method is investigated.

Figure 2-9 shows the flat and concave rollers used in the direct-forming and continuous forming process, respectively.

Although the appearance of the sections can be similar, the mechanical behaviors of CFS produced by different cold-forming methods can be substantially different. For direct-formed CFS, the cold-working is concentrated at the four corners, and thus the flat faces (not containing the weld) of the final CFS product have similar properties to the coil material. For continuous-formed CFS, the entire cross-section contains high degrees of cold-working. Thus, the final RHS product has a higher yield and ultimate strengths and lower ductility compared to the coil material.



Figure 2-9 left: Flat rollers used in direct forming Right: Concave rollers used in continuous forming  
The main disadvantages of cold-forming are:

- The mechanical properties of cold-formed hollow sections are inhomogeneous around the perimeter due to the difference in strain hardening during cold forming
- The tensile plastic elongation of a cold-formed hollow section is lower and depends on the location in the sections.
- There may be microcracks in the corners of cold-formed hollow sections, which will reduce the safety of the structure and fatigue properties. Therefore, allowance of welding on cold-formed corner region is limited in design rules.

- Cold forming reduces the impact toughness of cold-formed hollow sections, which restricts their use at low temperatures.

## 2.3 Characteristics of cold-formed sections

### 2.3.1 Stress-strain diagram description

Cold-formed steels are generally characterized by a rounded stress-strain response with no sharply defined yield point. The Ramberg-Osgood (R-O) model was initially proposed for stainless steel stress-strain behavior [5]. However, it is commonly used to simulate any rounded stress-strain response. In its original form, the equation for the strain is:

$$\varepsilon = \frac{\sigma}{E_0} + K \left( \frac{\sigma}{E_0} \right)^n \quad 2-1)$$

where,  $E_0$  is the young's modulus, and  $K$  and  $n$  are constants depend on the material being considered. The expression was modified one year later by Hill [6] in the following equation:

$$\varepsilon = \frac{\sigma}{E_0} + c \left( \frac{\sigma}{R_p} \right)^n \quad 2-2)$$

Where  $R_p$  denotes proof strength, and  $c$  is the corresponding plastic strain. Thus, the formula is given by (for generally adopted 0.2% proof strength):

$$\varepsilon = \frac{\sigma}{E_0} + 0.002 \left( \frac{\sigma}{\sigma_{0.2}} \right)^n \quad 2-3)$$

The first term on the right side,  $\frac{\sigma}{E_0}$  is equal to the elastic part of the strain, while the second term accounts for the plastic part. The R-O model implies that plastic strain is present even for very low levels of stress. Nevertheless, for low applied stresses and the commonly used values of the material constants, the plastic strain remains negligible compared to the elastic strain. On the other hand, for stress levels higher than  $\sigma_{0.2}$  plastic strain becomes progressively larger than elastic strain. The schematic representation of the model is shown in Figure 2-10.

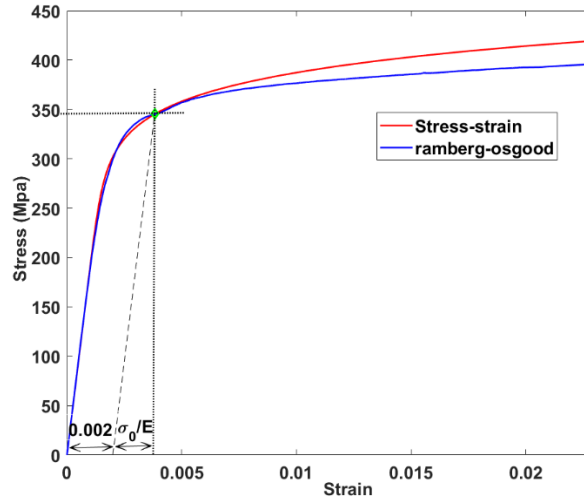


Figure 2-10 Typical cold-formed stress-strain curve along with Ramberg-Osgood formula

The strain corresponding to the yield point is the sum of the elastic and plastic components. It can be seen that Eq. 2-3) is incapable of representing different regions of the stress-strain curve with a single value of  $n$ . This observation led to several developments and extensions to the R-O model. Gardner and Yun [7] provides a comprehensive review of the many models proposed in the past, including some recommendations to improve the models. According to Gardner, adoption of a two-stage Ramberg-Osgood model originally developed for stainless steel [8], but with the revised predictive expressions, gives more accurate and precise results. The two-stage stress-strain relationship is given by:

$$\varepsilon = \begin{cases} \frac{f}{E} + 0.002 \left( \frac{f}{f_y} \right)^n & \text{for } f \leq f_y \\ \frac{f - f_y}{E_{0.2}} + \left( \varepsilon_u - \varepsilon_{0.2} - \frac{f_u - f_y}{E_{0.2}} \right) + \varepsilon_{0.2} & \text{for } f_y < f < f_u \end{cases} \quad (2-4)$$

The recommended values and predictive expressions for the key input parameters into Eq. (2-4) are as follows:

The first strain hardening exponent  $n$  may be determined from either Eq. (2-5) or (2-6).

$$n = \frac{\ln(20)}{\ln\left(\frac{f_y}{\sigma_{0.01}}\right)} \quad (2-5)$$

$$n = \frac{\ln(4)}{\ln\left(\frac{f_y}{\sigma_{0.05}}\right)} \quad (2-6)$$

The latter has been shown by Rasmussen and Hancock [9] and Arrayago et al. [10] to yield more consistent  $n$  values in comparison to curves fitted to stainless steel stress-strain data by regression analysis. When the measured  $\sigma_{0.05}$  proof stress is available the above Eq. can be employed to compute the strain hardening parameters, or otherwise taken from Table 2-1.

Table 2-1 Recommended representative values for strain hardening exponents  $n$  and  $m$  [7]

	<b>n</b>	<b>m</b>
Flat Coupons	7.6	3.8
Corner coupons	7	4.2

The tangent modulus of the stress-strain curve at the yield strength (0.2% proof stress)  $E_{0.2}$  is defined as:

$$E_{0.2} = \frac{E}{1 + 0.002n \frac{E}{f_y}} \quad (2-7)$$

The strain  $\epsilon_u$  corresponding to the ultimate tensile strength  $f_u$  may be obtained from:

$$\epsilon_u = 0.6 \left( 1 - \frac{f_y}{f_u} \right) \quad (2-8)$$

The ultimate tensile strength  $f_u$ , if unknown, may be determined using the following predictive expression:

$$\frac{f_u}{f_y} = 1 + \left( \frac{130}{f_y} \right)^{1.4} \quad (2-9)$$

The second strain hardening exponent  $m$  may be determined either from Eq. (2-10) or Eq. (2-11), the latter of which requires knowledge of the measured 1% proof stress  $\sigma_{1.0}$ :

$$m = 1 + 3.3 \frac{f_u}{f_y} \quad (2-10)$$

$$m = \frac{\ln \left( 0.008 + \frac{\sigma_1 - f_y}{E} - \frac{\sigma_1 - f_y}{E_{0.2}} \right) - \ln \left( \epsilon_u - \epsilon_{0.2} - \frac{f_u - f_y}{E_{0.2}} \right)}{\ln(\sigma_1 - f_y) - \ln(f_u - f_y)} \quad (2-11)$$

It is well known that cold-forming causes strain hardening of the steel material. Hence its yield and ultimate strengths increase while its ductility decreases. Early investigations on the corner properties of cold-formed steel shapes [11] have shown that, for steel shapes cold-bent from the same virgin steel, values of yield strength are larger for smaller inside radius-to-thickness ratios since they correspond to larger degrees of cold-forming [12]. Based on these investigations, equations have been developed and adopted by AISI S100-07, using the material properties of the virgin steel and the bending radius as input, for estimation of the average yield strength of the cold-formed section [13, 14]. Similar investigations have been conducted on cold-formed RHS [13]. These studies revealed that, depending on the cross-sectional geometry, the mechanical behaviors of the flat face and the corner are sometimes substantially diverse due to the different degrees of cold-forming.

The first generally accepted model for the enhanced yield strength of carbon steel was established by Karen in 1967 [15]. The model provides a relation between the enhanced yield strength and the inner radius of a corner to the thickness ratio together with the original yield strength. It is suggested that since corner areas represent 5% - 30% [15] of a cross-sectional area, the influence of the enhanced strength should be involved in structural design.

$$f_{yc} = \frac{B_c}{(r_i/t)^m} f_{yv} \quad (2-12)$$

Where:

$$B_c = 3.69 \cdot \frac{f_{uv}}{f_{yv}} - 0.819 \left( \frac{f_{uv}}{f_{yv}} \right)^2 - 1.79 \quad (2-13)$$

$$m = 0.192 \frac{f_{uv}}{f_{yv}} - 0.068 \quad (2-14)$$

$f_{yc}$  - yield strength of corner material,

$f_{yv}$  - yield strength of the virgin material,

$f_{yu}$  - ultimate tensile strength of the virgin material,

$r_i$  - inner bend radius,

$t$  - sheet thickness,

Karren proved that the region of the increased strength continues after the corner area by one or two wall thickness and the range depends on the method of cold-forming. The corner area means

the region of the pure geometric corner extended by a part of the section wall. This area represents enhanced material properties as it is displayed in Figure 2-11.

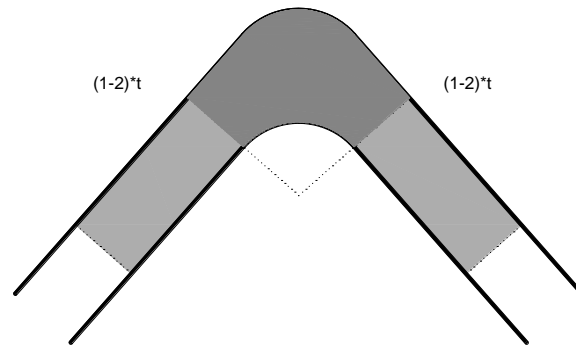


Figure 2-11 Area of enhanced material properties [14]

Karen and Winter suggested the relationship for the gross sectional tensile yield strength  $f_{ya}$  for all cold formed sections as [16].

$$f_{ya} = C \times f_{yc} + (1 - c) \times f_{yf} \quad (2-15)$$

Where:

$C$  is the ratio of corner area to the gross sectional area,

$f_{yc}$  is the average tensile yield strength of corners cited above

$f_{yf}$  is the average tensile yield strength of flat parts, conservatively yield strength of the virgin material.

Compared to Karren and Winter recent European design standard EN 1993-1-3 [17] set the following formula for the yield strength of a cold-formed section made of carbon steel as:

$$f_{ya} = f_{yb} + \frac{knt^2}{A_g} (f_u - f_{yb}) \quad \text{but} \quad f_{ya} \leq \frac{f_u + f_{yb}}{2} \quad (2-16)$$

Where:

$f_{yb}$  is the nominal yield strength of the virgin material,

$f_u$  is the nominal ultimate tensile strength,

$A_g$  is the cross-sectional area,

$t$  is the sheet thickness before cold forming,

$n$  is the number of  $90^\circ$  bends (bends with angles less than  $90^\circ$ , should be counted as a fraction of  $n$ ),

$k$  is the coefficient depending on the type of forming (7 for cold rolling and 5 for other methods)

Abdel-Rahman and Sivakumaran also concluded that the strength enhancement exists in areas adjacent to the corners though these are not significant as in the curved corner area. They proposed to use an average enhanced yield strength in the area of corner extending to a distance of  $\pi r_i/2$ .

### 2.3.2 Residual stress pattern

Residual stresses are the stresses in the interior of a body existing even without the action of external loadings and they are self-balanced. Almost all manufacturing processes create residual stresses. Further, stresses can also develop during the service life of the manufactured component. Because residual stresses are non-zero but have zero force resultant, they must be non-uniform, sometimes quite substantially so, with large stress gradients. Figure 2-12 [18] shows an example of typical stress gradients found in manufactured components. It shows welding residual stresses and indicates a stress gradient of  $\sim 200$  MPa/mm adjacent and parallel to the weld.

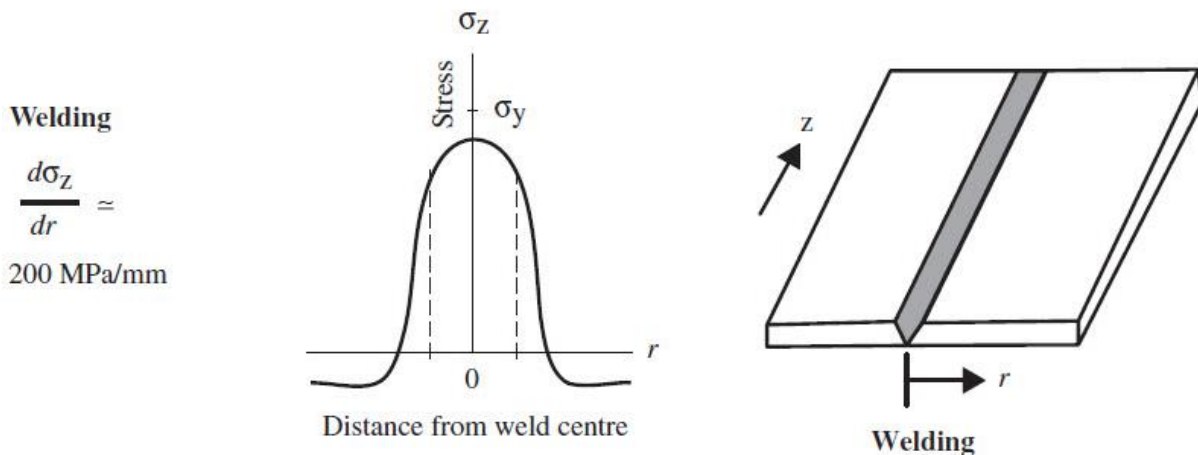


Figure 2-12 Schematics illustrating typical residual stress gradients induced by manufacturing process [18]

These stresses may be beneficial or not to the structures, depending on their magnitude, sign, and distribution. Any perturbation as material removal, thermal or mechanical loads alters the residual stresses state and causes the redistribution so that stresses meet equilibrium again. Residual stresses superpose the stresses caused by operation loadings. The techniques of residual stress measuring are classified into three types, according to the damage caused to the based material: destructive, semi-destructive, and non-destructive. The sectioning technique is one of the most

common (destructive method) techniques to evaluate residual stresses. A brief overview of a range of relaxation methods for measuring residual stresses is summarized as follows [18]:

The splitting method mimics the deformations seen in material cracking due to excessive residual stresses. A deep cut is sawn into a specimen and the opening or closing of the adjacent material indicates the sign and the approximate size of the residual stresses present. This method is commonly used as a quick comparative test for quality control during material production.

The sectioning method combines several other methods to evaluate residual stresses within a given specimen. It typically involves attachment of strain gages, or sometimes the use of diffraction measurements and sequentially cutting out parts of the specimen. The strain relaxations measured as the various parts are cut out provide a valuable source of data from which both the size and location of the original residual stresses can be determined. The method is demonstrated in Figure 2-13.

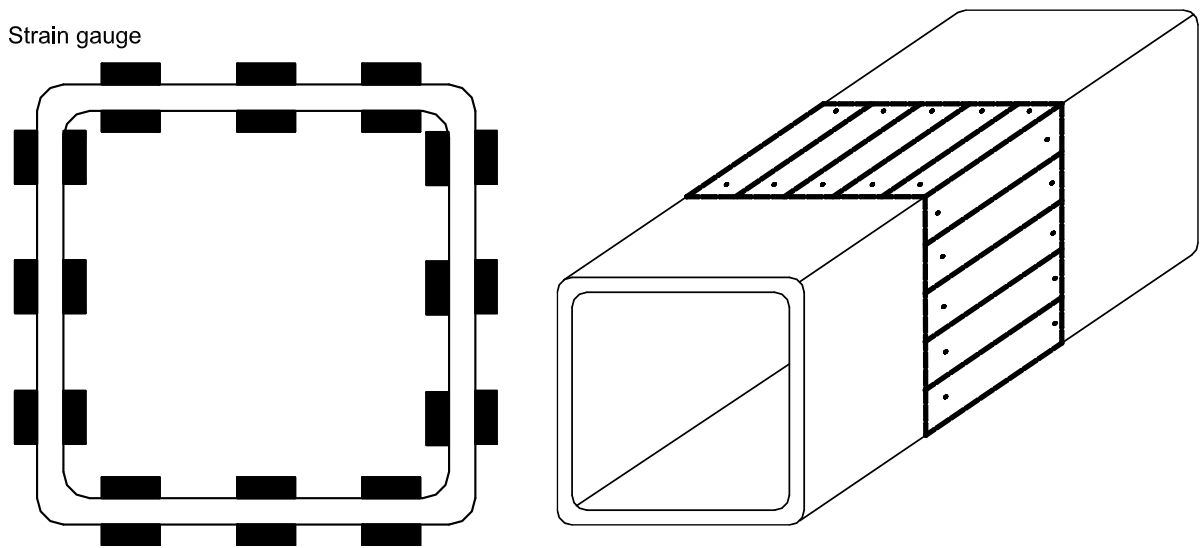


Figure 2-13 Schematics illustrating the sectioning method, left: Installation of the strain gauges Right: Dividing the specimen for cutting

After cutting each section, the remaining material will deform as shown in Figure 2-14. This deformation can be recorded through the pre-installed strain gauges at the top and bottom of the specimen.



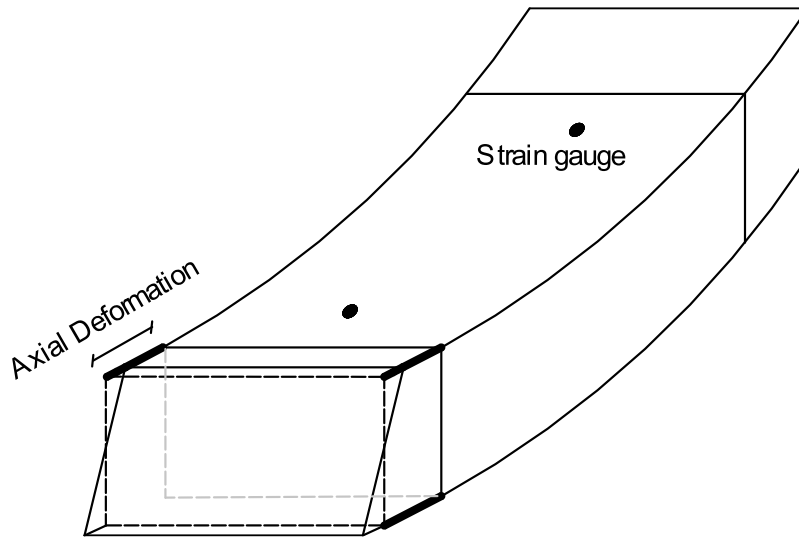


Figure 2-14 Deformation of the specimen after the release of residual stresses

There are three types of residual stress, membrane, bending, and through thickness. The sum of the top and bottom reading from strain gauges are zero. This means that there is not any axial elongation, while, there is bending in the section due to different signs of the readings. These types of residual stresses are illustrated Figure 2-15.

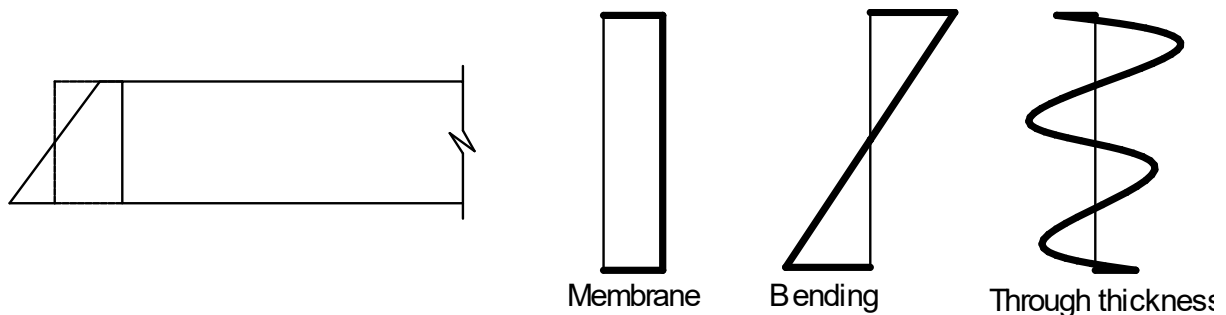


Figure 2-15 Different types of residual stresses

The layer removal method involves observing the deformation caused by the removal of a sequence of layers of material. The method is suited to flat plate and cylindrical specimens where the residual stresses vary with depth from the surface but are uniform parallel to the surface. The method involves measuring deformations on one surface, for example using strain gauges, as parallel layers of material are removed from the opposite surface.

The hole-drilling method is probably the most widely used relaxation method for measuring residual stresses. It involves drilling a small hole in the surface of the specimen and measuring the deformations of the surrounding surface, traditionally using strain gages, and more recently using

full-field optical techniques. Figure 2-16 illustrates the process. The hole-drilling method is popular because it can give reliable and rapid results with many specimen types.

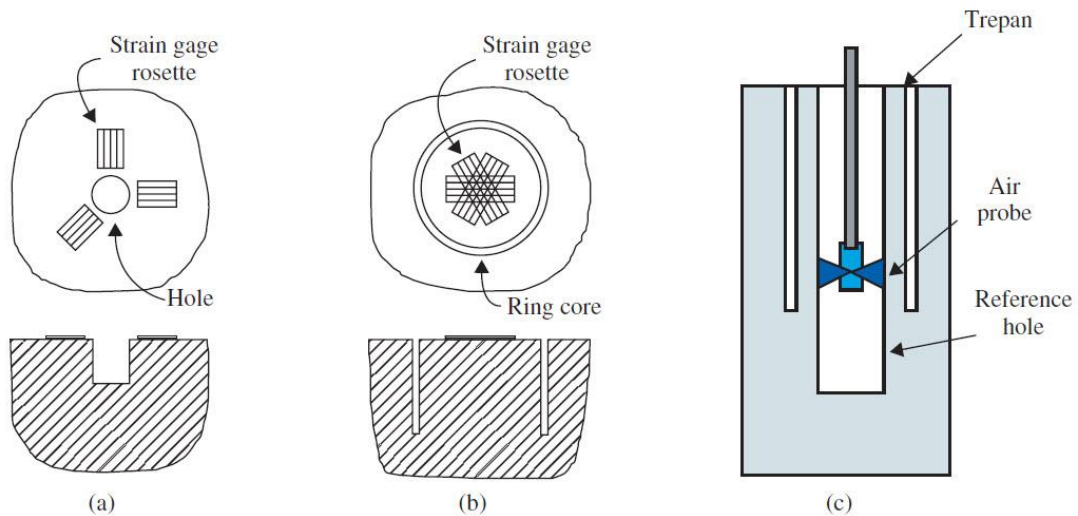


Figure 2-16 Hole-drilling methods: (a) conventional hole-drilling method, (b) ring-core method and (c) deep-hole method.

The slitting method, illustrated in Figure 2-17, is also conceptually similar to the hole-drilling method, but using a long slit rather than a hole. Alternative names are the crack compliance method, the sawcut method, or the slotting method. Strain gages are attached on the front or back surfaces, or both, and the relieved strains are measured as the slit is incrementally increased in depth using a thin saw, milling cutter, or wire EDM.

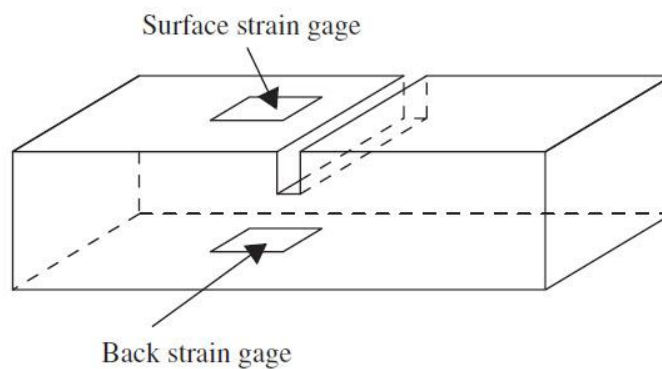


Figure 2-17 Hole-drilling methods: (a) conventional hole-drilling method, (b) ring-core method and (c) deep-hole method.

Previous experimental measurements of residual stresses in steel hollow profiles showed a predominant flexural distribution through the wall thickness instead of the classical constant distribution. Landolfo and Mazzolani [19] were among the pioneers of investigating residual stresses in cold-formed hollow sections. They performed a series of experimental tests on cold-formed hollow sections using the “sectioning method” and proposed a numerical model for the residual stresses patterns. The residual stresses pattern is different compared to its hot-rolled counterpart. The classical model of longitudinal residual stresses is shown, together with the proposed model by Mazzolani.

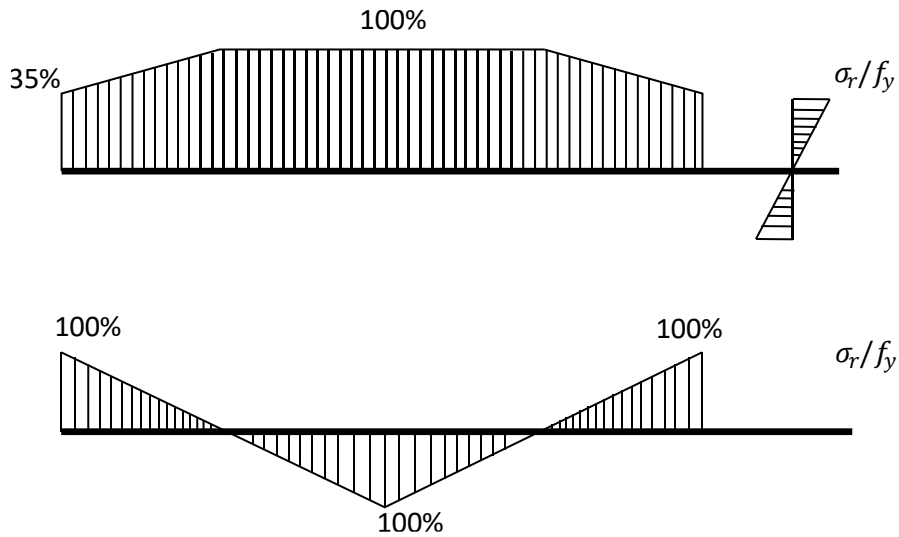


Figure 2-18 Residual stress models, Top: proposed model by [19] bottom: Classical model

Somodi and Kövesdi [20] investigate the residual stress distribution in HSS cold-formed hollow section members. They measured longitudinal residual stresses using the sectioning technique. Based on the test results, the shape and the intensity of the measured residual stresses are determined and evaluated. The development of the residual stress model can be found in [20]. The bending residual stress is the dominant type in CFS, and it can be computed for the flat part by the following equation (for normal strength steel):

$$\sigma_{rb,flat} = \pm(0.8f_y - 67Mpa) \quad (2-17)$$

The general shape of the residual stress model for CFS is illustrated in Figure 2-19.

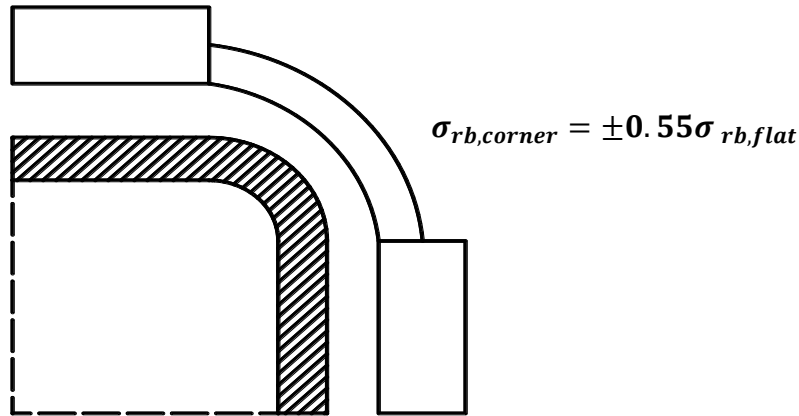


Figure 2-19 residual stresses model for CFS (normal strength steel)

## 2.4 Buckling of an Axially loaded column

### 2.4.1 Introduction

A physical phenomenon of a reasonably straight, slender member (or body) bending laterally (usually abruptly) from its longitudinal position due to compression is referred to as buckling. There are two kinds of buckling: (1) bifurcation-type buckling; and (2) deflection-amplification-type buckling [11].

Most, if not all, buckling phenomena in the real-life situation are the deflection amplification type. A bifurcation-type buckling is a purely conceptual one that occurs in a perfectly straight (geometry) homogeneous (material) member subjected to a compressive loading of which passes through the centroidal axis of the member. It is ridiculously improbable to observe a bifurcation-type buckling in nature and real columns. Structural members resisting tension, shear, torsion, or even short stocky columns fail when the stress in the member reaches a certain limiting strength of the material. Therefore, once the limiting strength of a material is known, it is a relatively simple matter to determine the load-carrying capacity of the member. Buckling, both the bifurcation and the deflection-amplification type, does not take place as a result of the resisting stress reaching a limiting strength of the material. The stress at which buckling occurs depends on a variety of factors ranging from the dimensions of the member to the boundary conditions to the properties of the material of the member. Determining the buckling stress is a fairly complex undertaking. If buckling does not take place because certain strength of the material is exceeded, then, why, one

may ask, does a compression member buckle? A clear conceptual definition of the phenomena is given by Salvadori and Heller (1963) [11].

*“A slender column shortens when compressed by a weight applied to its top, and, in so doing, lowers the weight’s position. The tendency of all weights to lower their position is a basic law of nature. It is another basic law of nature that, whenever there is a choice between different paths, **a physical phenomenon will follow the easiest path**. Confronted with the choice of bending out or shortening, the column finds it easier to shorten for relatively small loads and to bend out for relatively large loads. In other words, when the load reaches its buckling value **the column finds it easier to lower the load by bending than by shortening.**”*

The concept of the stability of various forms of equilibrium of a compressed bar is frequently explained by considering the equilibrium of a ball in various positions as shown in Figure 2-20.

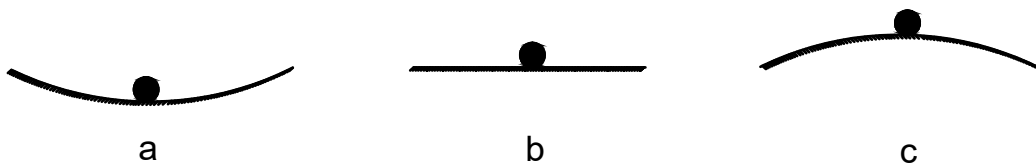


Figure 2-20 The three equilibrium states: (a) stable; (b) neutral; (c) unstable

Although the ball is in equilibrium in each position shown, a close examination reveals that there are important differences among the three cases. If the ball in part (a) is displaced slightly from its original position of equilibrium, it will return to that position upon the removal of the disturbing force. A body that behaves in this manner is said to be in a state of stable equilibrium. In part (a), any slight displacement of the ball from its position of equilibrium will raise the center of gravity. A certain amount of work is required to produce such a displacement and after the removal of the force, the member finds it easier to find its way to its original position. The ball in part (c), if it is disturbed slightly from its position of equilibrium, does not return but continues to move down from the original equilibrium position. The equilibrium of the ball in part (c) is called an unstable equilibrium. In part (c), any slight displacement from the position of equilibrium will lower the

center of gravity of the ball and consequently will decrease the potential energy of the ball. Thus, in the case of stable equilibrium, the energy of the system is a minimum (local), and in the case of unstable equilibrium it is a maximum, thus, based on nature's it tries to find a solution with less energy (local). The ball in part (b), after being displaced slightly, neither returns to its original equilibrium position nor continues to move away upon removal of the disturbing force. This type of equilibrium is called a neutral equilibrium.

This also can be explained through the energy of a single degree of freedom (SDOF). Consider a SDOF consisting a mass and a stiffness as shown Figure 2-24. At equilibrium the force in the spring is equal the weight of the system.

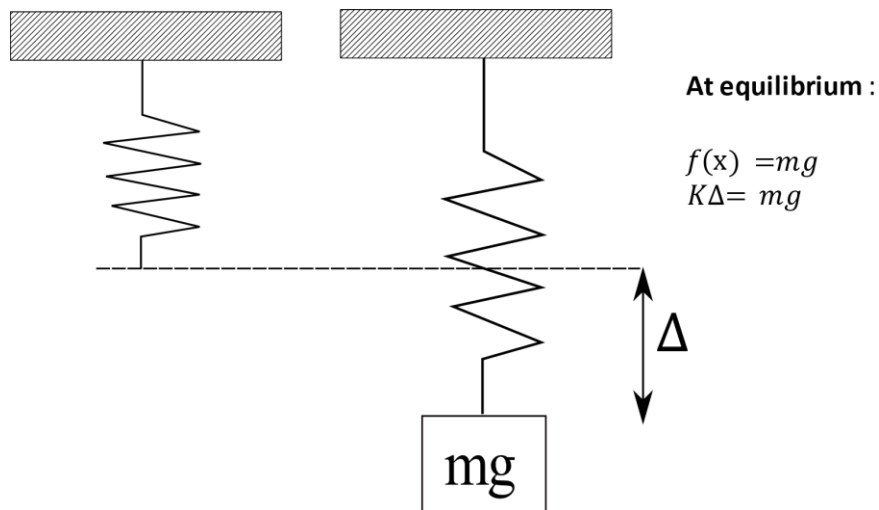


Figure 2-21 The equilibrium condition of a SDOF

The strain (i.e., potential) energy stored in the spring is the integration of the force in the spring integrated over the extension of the spring as stated in Eq. (2-18).

$$\bar{U} = \int_0^x f(x)dx = \int_0^x kxdx = 1/2kx^2 \quad (2-18)$$

The potential energy of the system is defined as the energy stored in the spring minus the work done by the external load when the mass is moved by the distance x. So, the potential energy at any distance can be computed from Eq. (2-22).

$$PE = \bar{U} - mgx = 1/2kx^2 - mgx \quad (2-19)$$

This is the energy that a system has and as explained previously, systems in nature tends to find their minimum state of energy. Therefore, when we take the derivative of the Eq. (2-22) with respect to extension  $x$ , we get the equilibrium equation (see Figure 2-24). If the system stays at the final state of  $\Delta$  (i.e., an equilibrium point) and we substitute  $\Delta$  in the equation for the change of rate in potential energy, we will reach Eq. (2-20).

$$\frac{dPE}{dx} = kx - mg \xrightarrow{\Delta} k\Delta = mg \tag{2-20}$$

This implies that at  $\Delta$  the rate of change of potential energy of the system is equal to zero. This means the potential energy is either **maximum** or **minimum** at  $\Delta$ . One can answer this dilemma by taking the second derivative of the Eq (2-20). Calculating the second derivative results in constant  $K$ . If  $K$  is positive the potential energy is minimum at equilibrium as shown in (2-25).

$$\begin{array}{ccc} \frac{dPE}{dx} = kx - mg & \xrightarrow{\text{At equilibrium point}} & \left. \frac{dPE}{dx} \right|_{\Delta} \quad kx - mg = 0 \\ \frac{d^2 PE}{dx^2} = k & \xrightarrow{\hspace{1.5cm}} & k > 0 \end{array} \quad \left. \vphantom{\begin{array}{ccc} \frac{dPE}{dx} = kx - mg \\ \frac{d^2 PE}{dx^2} = k \end{array}} \right\} \text{PE is minimum at equilibrium}$$

Figure 2-22 PE at the equilibrium point

Therefore if the relation between the force and displacement follows a more general nonlinear curve, one can find the state of equilibrium by looking at the slope of the curve. As shown in Eq. (2-26)The potential energy is minimum when the slope of the force-displacement curve is positive which is the case in the first part of the curve. However, in the second part of the curve, the slope is negative meaning that the potential energy is at its maximum (the same as the case c in Figure 2-20).

This means any perturbation in equilibrium in the second part of the curve, cannot be maintained. If we assumed that the equilibrium is achieved at a point in the descending branch and for any reason, the spring is perturb, the force in the spring will decrease and the outside force will overcome the force in the spring and the spring will keep extending.

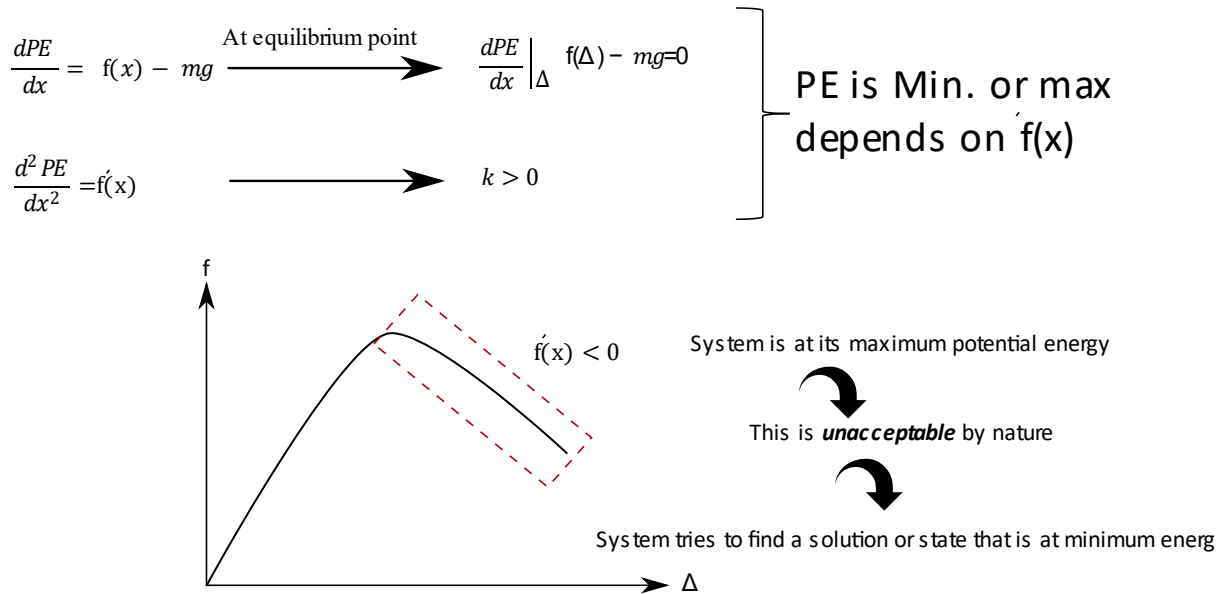


Figure 2-23 PE in a nonlinear system

If the equilibrium is neutral, there is no change in energy during a displacement in the conservative force system. The response of the column is very similar to that of the ball. The straight configuration of the column is stable at small loads, but it is unstable at large loads. It is assumed that a state of neutral equilibrium exists at the transition from stable to unstable equilibrium in the column. Then the load at which the straight configuration of the column ceases to be stable is the load at which neutral equilibrium is possible. This load is usually referred to as the critical load. To determine the critical load, eigenvalue, of a column, one must find the load under which the member can be in equilibrium, both in the straight and in a slightly bent configuration. How slightly? The magnitude of the slightly bent configuration is indeterminate. It is conceptual. This is why the free body of a column must be drawn in a slightly bent configuration. The method that bases this slightly bent configuration for evaluating the critical loads is called the method of neutral equilibrium (neighboring equilibrium, or adjacent equilibrium). At critical loads, the primary equilibrium path (stable equilibrium, vertical) reaches a bifurcation point and branches into neutral equilibrium paths (horizontal). This type of behavior is called the buckling of bifurcation type.

Very slender columns fail by buckling when the material is still linear-elastic (elastic buckling), and the classic Euler formula is applicable in the determination of the critical buckling load. In contrast, very stocky columns fail by yielding and crushing of the material, and hence their strength



depends solely on the ultimate compressive strength of the material; no consideration of buckling or stability is necessary. Between these extremes, for columns with intermediate slenderness, buckling occurs after the material has become plastic but before it crushes, which is known as inelastic buckling. In this case, the simple elastic buckling solution is no longer valid, and the inelastic behavior of the material must be taken into account.

## 2.4.2 History of column buckling

The story of the column buckling formula has had continuity over a 239-year period and starts with Robert Hooke. In 1678 Robert Hooke provides a necessary preliminary concept to the development of the elastic buckling theory when he stated that the displacement of any springy body was in proportion to the load causing the displacement [11]. Hooke confirms that this relationship, now known as Hooke's law, could be applied to all springy bodies such as metal, wood, stone, hair, horns, silk, bones, glass, etc., His findings were made on the basis of many experiments. The second necessary ingredient to develop the buckling formula was due to Jacob Bernoulli who studied the deflection and curvature in a cantilever beam. He asserted, in 1705, on the basis of Hooke's Law, that the curvature at any point in a bent rod was in proportion to the resisting moment developed in the rod at that point.

Leonard Euler (1707-1783) studied under Jacob Bernoulli's brother John (1667-1748). Euler adopted Jacob's assumption regarding the moment-curvature relationship and in the Appendix to his 1744 book on variational calculus he presented the column formula that still bears his name [11].

Euler derived his formula on the assumption that what he termed the "stiffness moment" at any point in the column was equal to  $E\kappa^2/\rho$ , where  $E\kappa^2$  (i.e., known as EI today) was a constant to be determined by means of experiment and  $\rho$  was the radius of curvature of the bent member. He had only imperfect ideas of the relationship between the actual shape of the cross-section and his " $E\kappa^2$ " and he stated in his later 1759 treatise [77] on columns:

*"it would seem that the stiffness moment is proportional to the square of the thickness, or even to its cube. To begin with, I should indicate that this (stiffness) moment is **not limited to elastic bodies** . . . It concerns in essence a force (moment) by means of which any body resists a change in curvature, and*

*it is totally immaterial whether such a body after flexure is endowed with a force to reestablish its original shape or not."*

His physical insight into the problem of elastic and inelastic buckling and his mathematical genius was so far ahead of his time that his solution did not find any application in structural engineering for more than a century. Euler's doubt illustrates the fact that the concept of moment of inertia of the cross-section was not known at the time, nor had the stress distribution and location of the neutral axis of a bent beam been established. By stiffness moment Euler was referring to what is now termed EI in the elastic range.

Although Euler was the father of the elastic buckling theory, he himself did not limit his formula and thus showed an understanding of inelastic buckling behavior that was superior to that of some later investigators. Progress beyond Euler's early statements concerning inelastic behavior remained dormant for many years, stymied initially by a lack of knowledge as to relationships between stress, strain, curvature, and bending moment in the inelastic range. Engesser (1889)[11] had suggested that column strength in the range beyond proportional limit might be obtained simply by the substitution of  $E_t$  (tangent-modulus the slope of the stress-strain diagram) in place of E in the Euler formula. Note that the tangent modulus decreases as the stress increases beyond the proportional limit. According to the tangent-modulus theory of inelastic buckling, the column remains straight until the inelastic critical load is reached. When the stress is below the proportional limit, the tangent modulus is the same as the ordinary elastic modulus E. we usually obtain the tangent-modulus load by an iterative procedure. We begin by estimating the value of  $P_t$ . This trial value, call it  $P_1$ , should be slightly larger than  $\sigma_{pl}A$ , which is the axial load when the stress just reaches the proportional limit. Knowing  $P_1$ , we can calculate the corresponding axial stress  $P_1/A$  and determine the tangent modulus  $E_t$  from the stress-strain diagram. Next, we use the Euler buckling formula with  $E_t$  to obtain a second estimate of  $P_t$ . Let us call this value  $P_2$ . If  $P_2$  is very close to  $P_1$ , we may accept the load  $P_2$  as the tangent-modulus load. However, it is more likely that additional cycles of iteration will be required until we reach a load that is in close agreement with the preceding trial load. This value is the tangent-modulus load.

The tangent-modulus theory is distinguished by its simplicity and ease of use. However, it is conceptually deficient because it does not account for the complete behavior of the column. To explain the difficulty, we will consider again a straight column with nonlinear material. When this column first departs from the straight position, bending stresses are added to the existing

compressive stresses  $P/A$ . These additional stresses are compressive on the concave side of the column and tension on the convex side. Therefore, the compressive stresses in the column become larger on the concave side and smaller on the other side. On the concave side of the column (where the compressive stress is increased), the material follows the tangent modulus  $E_t$ . However, on the convex side (where the compressive stress is decreased), the material follows the unloading line AB on the stress-strain diagram shown in Figure 2-24. This line is parallel to the initial linear part of the diagram, and therefore its slope is equal to the elastic modulus  $E$ . Thus, at the onset of bending, the column behaves as if it were made of two different materials, a material of modulus  $E_t$  on the concave side and a material of modulus  $E$  on the convex side. In 1889, Considère performed 32 column tests and suggested that if buckling occurred above the proportional limit the elastic modulus should be replaced in the Euler formula by an  $E_{\text{eff}}$ . He stated that the effective modulus should be somewhere between the elastic and tangent modulus. Engesser subsequently modified his views upon column strength and showed how to calculate the reduced modulus for any cross-section. Thus, the reduced-modulus theory is also known as the Considère-Engesser theory. The reduced-modulus theory is difficult to use in practice because  $E_r$  depends upon the shape of the cross-section as well as the stress-strain curve and must be evaluated for each particular column. Moreover, this theory also has a conceptual defect. In order for the reduced modulus  $E_r$  to apply, the material on the convex side of the column must be undergoing a reduction in stress. However, such a reduction in stress cannot occur until bending actually takes place. Therefore, the axial load  $P$ , applied to an ideal straight column, can never actually reach the reduced-modulus load  $P_r$ . To reach that load would require that bending already exist, which is a contradiction.

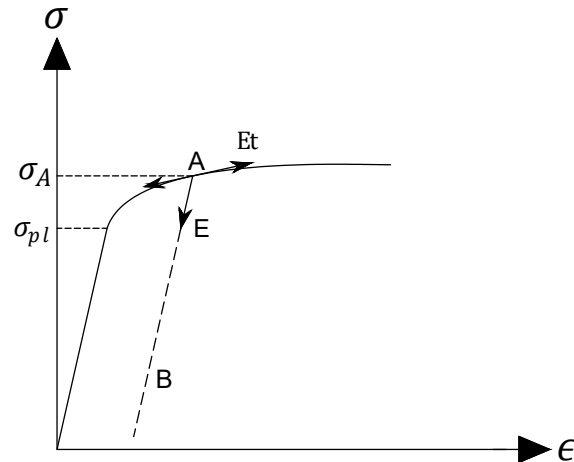


Figure 2-24 Stress-strain diagram of the column with nonlinear material

Neither the tangent-modulus theory nor the reduced-modulus theory is entirely rational in explaining the phenomenon of inelastic buckling. Nevertheless, an understanding of both theories is necessary in order to develop a more complete and logically consistent theory. Such a theory was developed by F. R. Shanley in 1946 [11]. The Shanley theory overcomes the difficulties with both the tangent modulus and reduced-modulus theories by recognizing that it is not possible for a column to buckle inelastically in a manner that is analogous to Euler buckling. In Euler buckling, a critical load is reached at which the column is in neutral equilibrium, represented by a horizontal line on the load-deflection diagram (Figure 2-25). As already explained, neither the tangent-modulus load  $P_t$  nor the reduced-modulus load  $P_r$  can represent this type of behavior. In both cases, we are led to a contradiction if we try to associate the load with a condition of neutral equilibrium. In other words, the underlying assumption that a deflected shape suddenly becomes possible with no change in load is not correct. When the load reaches the tangent modulus load (which is less than the reduced-modulus load), bending can begin only if the load continues to increase. Under these conditions, bending occurs simultaneously with an increase in load, resulting in a decrease in strain on the convex side of the column. Thus, the effective modulus of the material throughout the cross-section **becomes greater than  $E_t$ , and therefore an increase in load is possible**. However, the effective modulus is not as great as  $E_r$ , because  $E_r$  is based upon full strain reversal on the convex side of the column. In other words,  $E_r$  is based upon the amount of strain reversal that exists if the column bends without a change in the axial force, whereas the presence of an increasing axial force means that the reduction in strain is not as great. Thus, instead of neutral

equilibrium, where the relationship between load and deflection is undefined, we now have a definite relationship between each value of the load and the corresponding deflection. This behavior is shown by the curve labeled “Shanley theory” in Figure 2-25.

Note that buckling begins at the tangent-modulus load; then the load increases but does not reach the reduced-modulus load until the deflection becomes infinitely large (theoretically). However, other effects become important as the deflection increases, and in reality, the curve eventually goes downward, as shown by the dashed line.  $v$

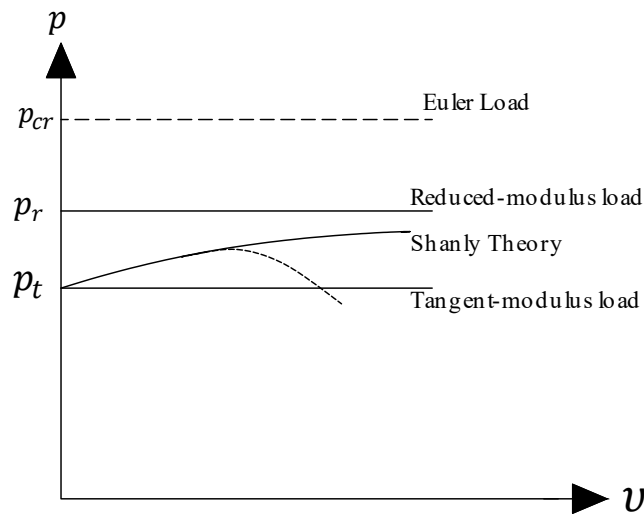


Figure 2-25 load-deflection diagram for elastic and inelastic buckling

It is important to keep in mind that although these theories are essential for understanding the problem, nowadays we use the finite element method with the right input to model column buckling. A chronological overview of the column buckling is shown in Figure 2-26

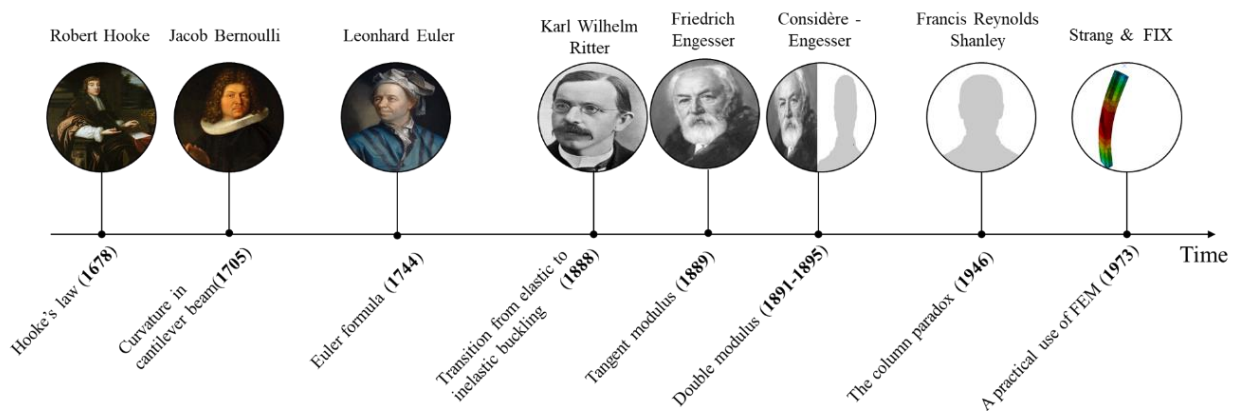


Figure 2-26 Chronological overview of column buckling

### 2.4.3 Ideal Elastic Column

To determine the critical load, eigenvalue, of a column, one must find the load under which the member can be in equilibrium, both in the straight and in a slightly bent configuration. How slightly? The magnitude of the slightly bent configuration is indeterminate. This is why the free body of a column must be drawn in a slightly bent configuration as shown in Figure 2-27.

The simplest example for column buckling is a perfectly straight elastic column, with frictionless pins at its ends, a symmetrical cross-section, and an axial load applied exactly along the column axis.

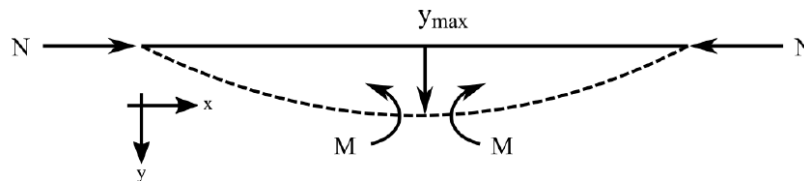


Figure 2-27 An ideal elastic column loaded axially

The deflection follows the first buckling mode, a half-sine wave, for a pinned-pinned column in this derivation. Under the considered assumptions, the column remains perfectly elastic until the critical buckling load. At that point, the external bending moment at an arbitrary point of the column can be expressed as:

$$M_{ext}(x) = N_{cr} \cdot y(x) \quad (2-21)$$

Since the deformation of the member is small, the curvature can be approximated by the second derivative of the deflection. The corresponding bending moment is expressed

$$M_{in}(x) = -EI \frac{d^2y}{dx^2} \quad (2-22)$$

In order to have equilibrium, the external and internal moment should be equal, which leads to the following equations:

$$-EI \frac{d^2y}{dx^2} = N_{cr} \cdot y(x) \quad (2-23)$$

$$\frac{d^2y}{dx^2} + \frac{N_{cr}}{EI} y(x) = 0 \quad (2-24)$$

Which also can be written as:

$$y'' + \omega^2 y(x) = 0 \text{ with } \omega^2 = \frac{N_{cr}}{EI} \quad (2-25)$$

The way to solve the differential equation follows the general solution in equation (2-26). The first and second derivatives of the general solution are as in equation (2-27) and (2-28).

$$y(x) = A \cdot \sin(\omega x) + B \cdot \cos(\omega x) \quad (2-26)$$

$$y'(x) = A\omega \cdot \cos(\omega x) - B\omega \cdot \sin(\omega x) \quad (2-27)$$

$$y''(x) = -A\omega^2 \cdot \sin(\omega x) - B\omega^2 \cdot \cos(\omega x) \quad (2-28)$$

Considering the boundary condition for the above differential equation, the constants A and B can be derived as follows:

$$y(0) = 0 \rightarrow A \cdot \sin(0) + B \cdot \cos(0) \rightarrow B = 0 \quad (2-29)$$

$$y(L) = 0 \rightarrow A \cdot \sin(\omega L) = 0 \quad (2-30)$$

Equation (2-30) can be satisfied in two ways. The first solution is  $A=0$ , which is the trivial solution meaning that the amplitude of the deformed shape is zero and therefore the column remains straight. In addition, we note that when A equals zero, Eq. (2-30) is satisfied for any value of the quantity  $\omega L$ . Consequently from Eq. (2-25) the axial load P may also have any value. This solution of the differential equation (known in mathematics as the trivial solution) is represented by the vertical axis of the load-deflection diagram in Figure 2-28. It gives the behavior of an ideal column that is in equilibrium (either stable or unstable) in the straight position (no deflection) under the action of the compressive load P.

The additional solution is when the second term equals to zero, which leads to the following equation:

$$\sin(\omega L) = 0 \rightarrow \omega L = 0, \pi, 2\pi, \dots \quad (2-31)$$

However, since  $\omega L = 0$  means that  $P=0$ (see Eq. (2-25)). Therefore, using equation (2-25) the considered solutions are:

$$N_{cr} = \frac{\pi^2 EI}{L^2}, \frac{4\pi^2 EI}{L^2}, \dots \quad (2-32)$$

where n is any integer or reflector of buckling mode. It is evident that the lowest value of the critical buckling load is when  $n=1$ .

The eigenvalues  $N_{cr}$  called critical loads, the values of load  $P$  for which a nonzero deflection of the perfect column is possible. The deflection shapes at critical load, representing the eigenmodes are given by

$$y = A \sin \frac{n\pi x}{L} \quad (2-33)$$

Note that  $A$  is undetermined, including its sign; that is, the column magnitude of the buckling mode shape cannot be determined. Also, it can be seen that the buckling load is independent of the deflection (i.e.,  $y$ ). A curve of the applied load versus the deflection at a point in a structure such as that shown in Figure 2-28 is called the equilibrium path. Points along the primary (initial) path (vertical) represent configurations of the column in the compressed but straight shape; those along the secondary path (horizontal) represent bent configurations. Eq (2-32) determines a periodic bifurcation point, for each value of  $n$ . Based on Eq (2-33), the secondary path extends indefinitely in the horizontal direction.

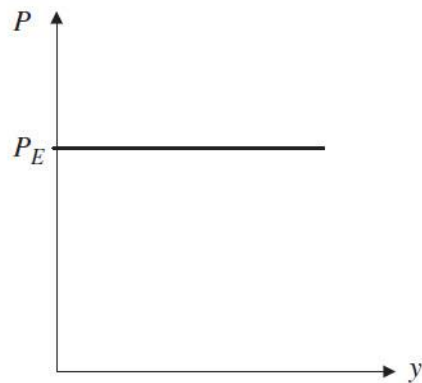


Figure 2-28 Vertical load versus the lateral deflection for an ideal column

Only when  $P$  has one of the values given by Eq. (2-32) it is theoretically possible for the column to have a bent shape (given by Eq. (2-33)). For all other values of  $P$ , the column is in equilibrium only if it remains straight. It is important to note that provided the structure remains exactly vertical it can be in equilibrium even it is unstable (i.e., the system is at its maximum local energy such as shown in Figure 2-20(b) which is in contrast with the law's nature in which objects choose a minimum energy solution). However, in this situation, even a minute disturbance, such as a breath of wind or even the impact of a single molecule, can cause the column to buckle laterally. Therefore, the values of  $P$  given by Eq. (2-32) are the critical loads for this column. It is interesting



to note that the critical load of the column is proportional to the flexural rigidity  $EI$  and inversely proportional to the square of the length. Of particular interest is the fact that the strength of the material itself, as represented by a quantity such as the proportional limit or the yield stress, does not appear in the equation for the critical load. Therefore, increasing a strength property does not raise the critical load of a slender column. It can only be raised by increasing the flexural rigidity, reducing the length, or providing additional lateral support.

Using the radius of gyration, the critical buckling load is expressed in terms of a load as in Eqs. (2-34) or as stress in (2-35). Notice that the term for the length,  $L$ , was replaced by the critical buckling length  $L_{cr}$ .

$$N_{cr} = \frac{\pi^2 EI}{L_{cr}^2} \quad (2-34)$$

$$\sigma_{cr} = \frac{\pi^2 E}{\left(\frac{L_{cr}}{i}\right)^2} \quad (2-35)$$

The new parameter that arose,  $L_{cr}/i$  indicates the slenderness  $\lambda$  of the column. A rewriting of the previous equation using the slenderness parameter results in the expression as follows:

$$\sigma_{cr} = \frac{\pi^2 E}{\lambda^2} \quad (2-36)$$

In order to include the strength of the material together with the stability, the critical buckling stress from equation (2-35) can be assumed equal to the yield stress to find the corresponding  $\lambda$ .

$$\sigma_{cr} = \frac{\pi^2 E}{\lambda_1^2} = f_y \rightarrow \lambda_1 = \pi \sqrt{\frac{E}{f_y}} \quad (2-37)$$

Figure 2-29(a) shows the elastic buckling curve considering only the stability as the criteria, while Figure 2-29(b) shows the elastic buckling curve considering both stability and strength of the material.

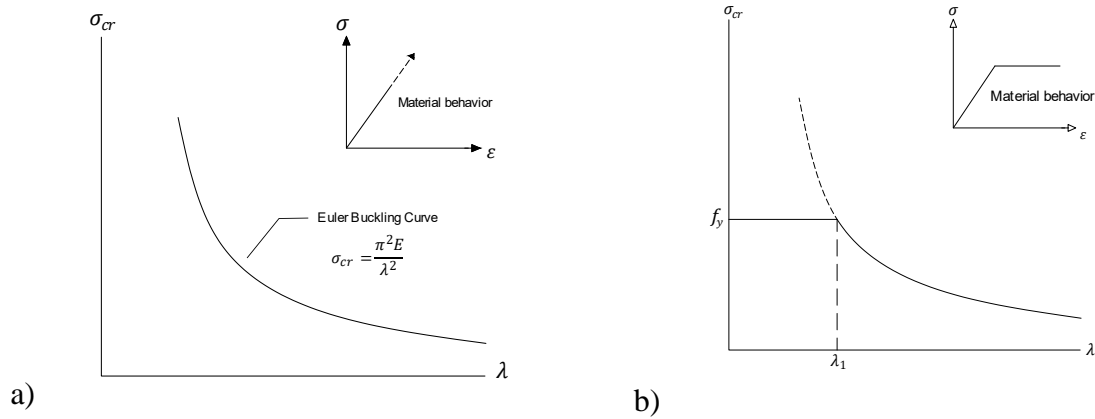


Figure 2-29 Buckling curve a) considering only stability b) considering both strength and stability

The relation can be further developed by normalizing the parameters and introducing two new parameters; the relative slenderness ratio  $\bar{\lambda}$  and the reduction factor with regard to buckling  $\chi$ .

$$\bar{\lambda} = \frac{\lambda}{\lambda_1} \quad (2-38)$$

$$\chi = \frac{\sigma_{max}}{f_y} \quad (2-39)$$

#### 2.4.4 Imperfect and Inelastic Column

The equations for critical loads were derived for ideal columns, with the following assumptions: (1) columns for which the loads are precisely applied (2) the construction is perfect (3) and the material follows Hooke's law. As a consequence, we found that the magnitudes of the small deflections at buckling were undefined (i.e., In mathematical terminology, we solved a linear eigenvalue problem. The critical load is an eigenvalue and the corresponding buckled mode shape is an eigenfunction.). The theory for ideal columns is limited to small deflections because we used the second derivative  $y''$  for the curvature. A more exact analysis, based upon the exact expression for curvature shows that there is no indeterminacy in the magnitudes of the deflections at buckling. Instead, for an ideal, linearly elastic column, the load-deflection diagram goes upward rather than being constant. Thus, after a linearly elastic column begins to buckle, an increasing load is required to cause an increase in the deflections.

When experimental data from buckling tests are compared to the theoretical Euler buckling curve as in Figure 2-30 it can be seen that depending on relative slenderness, the load-carrying capacity differs. The design curve is lower than the Euler curve, and the difference is larger for columns with intermediate slenderness ratio. The reason for this behavior is the initial imperfections of the column. Members with low relative slenderness are not affected by this as much since the load-carrying capacity is governed by yielding and not by buckling. The load-carrying capacity for members with very high slenderness is governed by elastic buckling, where the stresses are much lower than the yield stress. Hence, the effect of the initial imperfections is not as decisive. The initial imperfections can be divided into two categories: *geometrical* and *material imperfections* [21].

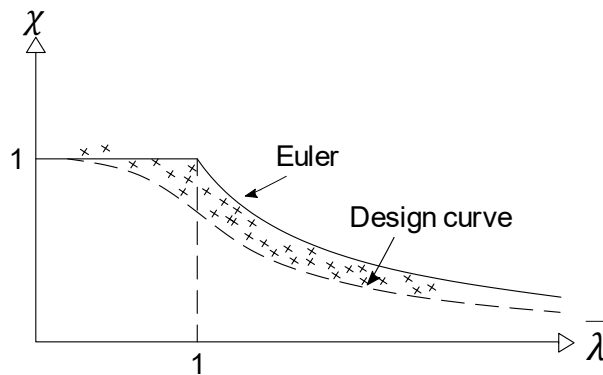


Figure 2-30 Experimental data compared to Euler and design curve

When steel members are subjected to both axial compression and strong axis bending, the structural response is highly complex and depends on many factors, such as for example, initial geometric imperfections, which can vary in both amplitude and shape. The effect of geometrical imperfections can be visualized by considering a pinned-pinned, axially loaded column with an initial bow imperfection  $e_0$  shaped as a half-sine wave as in Figure 2-31.

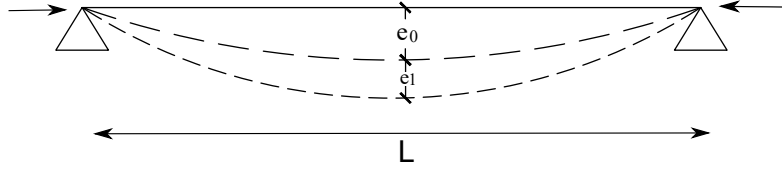


Figure 2-31 Axially loaded column with an initial bow imperfection

Assuming a sinusoidal deflection, the initial geometrical imperfection can be expressed as:

$$e_0 = a \cdot \sin\left(\frac{\pi x}{l}\right) \quad (2-40)$$

Due to the initial bow imperfection, a first-order bending moment,  $M$ , arises which is expressed as:

$$M_l = N \cdot (e_0 + e_1) \quad (2-41)$$

This bending moment will cause an additional lateral deformation. Thus, an even larger deflection and bending moment. This iterative process can be written in the form of a differential equation:

$$EI \frac{d^2 e}{dx^2} + N(e_0 + e_1) = 0 \quad (2-42)$$

By inserting equation (2-49) into the differential equation and divide by  $EI$ , the following expression arises:

$$\frac{d^2 e}{dx^2} + \frac{N}{EI} \left( a \cdot \sin\left(\frac{\pi x}{l}\right) + e_1 \right) = 0 \quad (2-43)$$

The general solution of the differential equation is:

$$e_1 = A \cdot \sin(\omega x) + B \cdot \cos(\omega x) + \frac{\frac{Na}{EI}}{\frac{\pi^2}{l^2} \frac{N}{EI}} \sin\left(\frac{\pi x}{l}\right) \quad (2-44)$$

Where:

$$\omega = \sqrt{\frac{N}{EI}} \quad (2-45)$$

By inserting the boundary condition into the general solution, the additional deformation at the midpoint becomes:

$$e_1 \left( x = \frac{L}{2} \right) = \frac{N/N_{cr}}{1 - N/N_{cr}} \cdot e_0 \quad (2-46)$$

The total deformation is obtained by adding the value of the initial imperfection (Eq. (2-49) at  $x=L/2$ ) at midspan to the additional deformation, which results in the following equation:

$$e_{max} = a + \frac{N/N_{cr}}{1 - N/N_{cr}} \cdot e_0 \quad (2-47)$$

This can be inserted in equation (2-41) to get the maximum bending moment  $M_{max}$ .

$$M_{II} = \frac{1}{1 - N/N_{cr}} \cdot M_I = \frac{N}{1 - N/N_{cr}} e_0 \quad (2-48)$$

Material imperfections, which also is referred to as residual stresses, is a phenomenon arising from when the steel is exposed to heating or cooling or the manufacturing process. According to Ziemian (2010), the residual stresses are self-balancing as well as dependent on the material properties, cross-section geometry and manufacturing method. This causes a wide spectrum of residual stresses, which in turn causes a variation in the stress pattern.

### 2.4.5 Buckling curves method in Eurocode 1993-3-1

In EN-1993-1-1 [17] (EC3-1-1), one of the design methods used to determine the buckling resistance of a column is based on the five buckling curves which are shown in Figure 2-32.

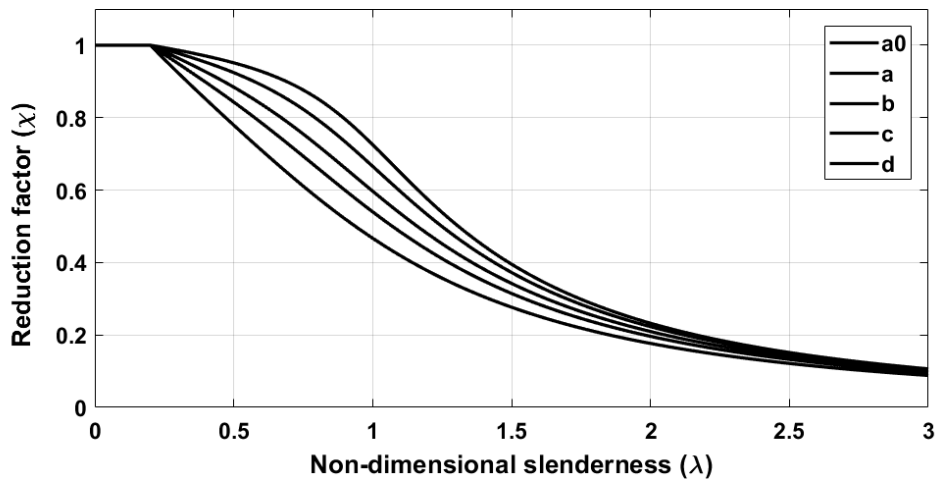


Figure 2-32. Buckling curves for flexural buckling in EC3-1-1

The compressed member should be verified against buckling failure by calculating the ratio between the design value of the compression force,  $N_{ed}$  and the design buckling resistance,  $N_{b,Rd}$ , according to Eq.

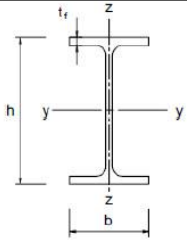
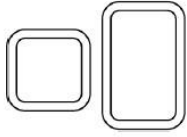
$$\frac{N_{Ed}}{N_{b,Rd}} \leq 1.0 \quad (2-49)$$

For cross-section class 1 to 3, the buckling resistance is calculated as in Eq. (2-50) cross-section class 4 is not treated in this study.

$$N_{b,Rd} \leq \frac{\chi A f_y}{\gamma_{M1}} \quad (2-50)$$

The reduction factor can be calculated analytically but also directly from the buckling curves. The correct buckling curve is selected by following Table 2-2, which is a simplified version of the one in EC3-1-1 [22].

Table 2-2. Buckling curve selection for a cross-section with steel quality S235, S275, S355 and S420

	Cross section	Limits	Buckling about axis	Buckling curve	
Rolled section		$h/b > 1.2$	$t_f \leq 40 \text{ mm}$	y-y z-z	a b
			$40 \text{ mm} < t_f \leq 100 \text{ mm}$	y-y z-z	b c
		$h/b \leq 1.2$	$t_f \leq 100 \text{ mm}$	y-y z-z	b c
			$t_f > 100 \text{ mm}$	y-y z-z	d d
Hollow section		hot finished	any	a	
		cold formed	any	c	

The analytical way of calculating the buckling reduction factor is based on the Ayrton-Perry formula which was derived in 1978 by Rondal and Maquoi [23]. They propose a formulation based on the Ayrton-Perry formula and calibrate the model to best fit the tabulated data of buckling curves.

This was described with the differential equation in Eq.(2-51), where N is the axial compression load, e the lateral displacement, and  $e_0$  represents the initial imperfection, as shown in Figure 2-31.

$$EI \frac{d^2 e(x)}{dx^2} + N (e(x) + e_0(x)) = 0 \quad (2-51)$$

by assuming a sinusoidal imperfection, the total translation, e, becomes:

$$e = \frac{1}{1 - \frac{N}{N_{cr}}} \cdot e_0 \quad (2-52)$$

The load-carrying capacity corresponds to the onset of yielding at the most compressed fiber. In the current scenario, the midspan cross-section is the most critical one. In this section, both axial force and bending moment due to initial imperfection are present. Eq. (2-53) express the yield criterion in this section.

$$\frac{N}{A} + \frac{N \cdot e}{w_{el}} = f_y \quad (2-53)$$

By inserting Eq. (2-52) into Eq. (2-53), the following expression arises:

$$\chi + \frac{\chi}{(1 - \chi \bar{\lambda}^2)} \frac{e_0 A}{w_{el}} = 1 \quad (2-54)$$

Alternatively, written in the form of the Ayrton-Perry formula as in Eq. (2-55), according to da Silva et al. [24].

$$(1 - \chi)(1 - \chi \bar{\lambda}^2) = \frac{e_0 A}{w_{el}} \cdot \chi = \eta \chi \quad (2-55)$$

The factor  $\eta$  correlates to expression(2-56), with  $\alpha$  representing the imperfection factor.

$$(1 - \chi)(1 - \chi \bar{\lambda}^2) = \frac{e_0 A}{w_{el}} \cdot \chi = \eta \chi \quad (2-56)$$

The imperfection factor is determined by the following table, which is found in EC3-1-1.

Table 2-3 Imperfection factors for buckling curves.

<b>Buckling curve</b>	<b>a0</b>	<b>a</b>	<b>b</b>	<b>c</b>	<b>d</b>
Imperfection factor, $\alpha$	0.13	0.21	0.34	0.49	0.76

Further, the Ayrton-Perry equation can be written in a quadratic form:

$$(1 - \chi)(1 - \chi \bar{\lambda}^2) = \eta \chi = \alpha \chi (\bar{\lambda} - 0.2) \quad (2-57)$$

The minimum solution for the buckling reduction factor,  $\chi$ , in the quadratic equation is:

$$\chi = \frac{\phi - \sqrt{\phi^2 - \bar{\lambda}^2}}{\bar{\lambda}^2} \quad (2-58)$$

The factor  $\phi$  is determined by:

$$\phi = 0.5[1 + \alpha(\bar{\lambda} - 0.2) + \bar{\lambda}^2] \quad (2-59)$$

Further, Eq. (2-59) is multiplied with the following expression:

$$\phi + \sqrt{\phi^2 - \bar{\lambda}^2} \quad (2-60)$$

Resulting in that, the final form of the critical buckling factor becomes as in Eq. (2-61), which is the formula used in EN-1993-1-1 (2005) [17].

$$\chi = \frac{1}{\phi + \sqrt{\phi^2 - \bar{\lambda}^2}} \quad (2-61)$$



## 2.5 Design for stability, why we do what we do!

Too often, structural engineers have been designing for stability like a black box in the sense that they follow equations and get the answers. Now that we have understood the mathematical perspectives of a column buckling load, it's beneficial to look from the global point of view, the procedure that we follow for designing against stability. The goal of this section is to provide an easy and conceptual basis for the stability design. Consider an ideal column as discussed previously. It is apparent if we apply any compressive load, there is no lateral displacement until we reach critical load,  $P_{cr}$ , (i.e., bifurcation point). At this point the column can continue its load-deformation path in two ways as shown in Figure 2-33, it can either have a sudden, uncontrolled lateral displacement (i.e., Buckling) or continue bearing the load and remains straight. Considering the law of nature, the column is much easier to move laterally rather than remaining straight at bifurcation point. Theoretically, it can continue bearing the load and avoid any lateral deflection, however, even a breath of wind can activate the buckling mode after the bifurcation point.

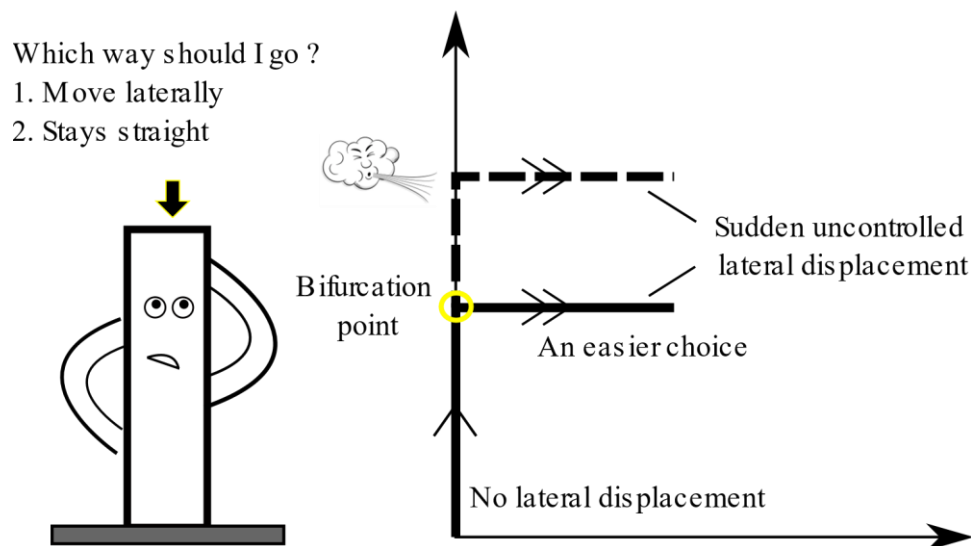


Figure 2-33. Bifurcation point

Oppose to buckling we have amplification. The straight bar discussed earlier does not have any lateral displacement as shown in Figure 2-34 (a). However, if we apply a lateral load, there is some lateral deflection and if we combined the two, it can be seen that the response is different compared to having only a lateral load even that the compressive force itself does not induce any lateral deflection in the assumed bar.

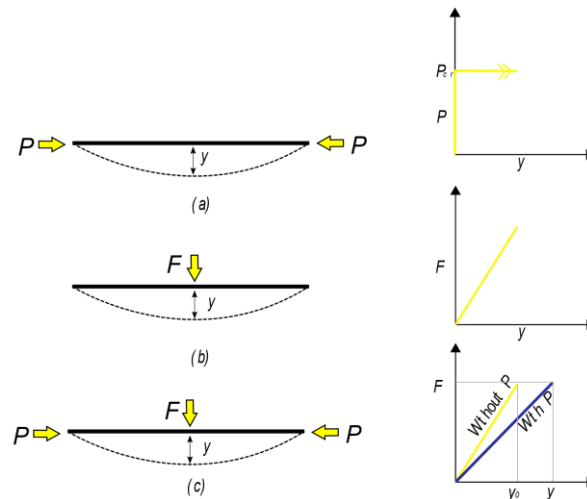


Figure 2-34. Amplification Vs. Buckling

In Figure 2-34 (c),  $y_0$  may be the result of lateral load as shown above or an initial imperfection. We can have a structure with an initial out-of-plumbness of  $y_0$  and by applying a vertical load on it,  $y_0$  will increase to  $y$ . The point is we always have a  $y_0$  in the real world which leads to amplification rather than buckling (see Figure 2-35). Every real member or structure has some initial imperfection; even if it is very small; or it has initial lateral load or both. This means failure of a member loaded in pure compression always involves lateral displacement and a significant amount of flexure. The failure mode of such member is neither crushing in compression ( $AF_y$ ), nor buckling ( $\pi^2EI/l^2$ ), but by compression and flexure.

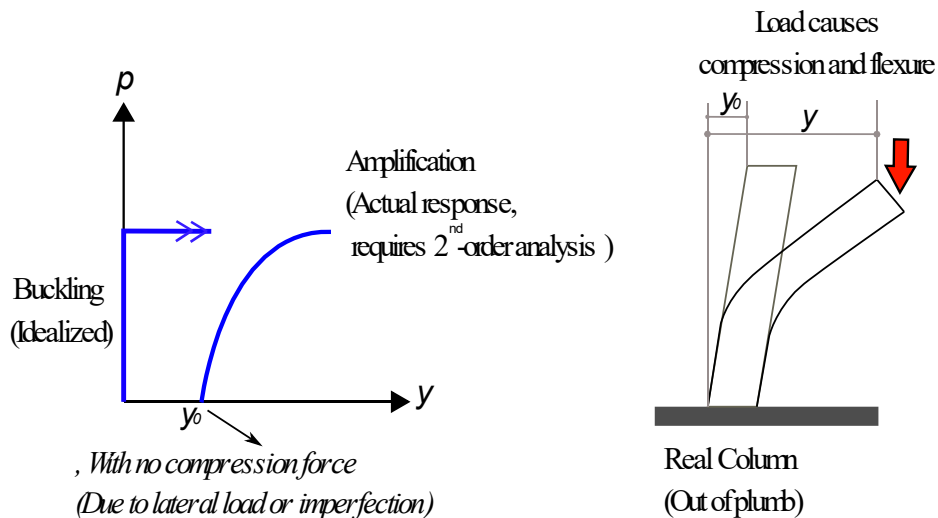


Figure 2-35. Real column load path

To capture the actual response, requires a 2<sup>nd</sup>-order analysis, since, the relationship between the applied load and displacement is not linear. The linear analysis show; regardless of the compressive forces; the displacement is just  $y_0$ . It is important to note that  $y_0$  must be modeled either by initial imperfection or initial lateral load. because if one neglects modeling  $y_0$ , then it does not matter what type of analysis to run. Therefore, the correct prediction of response requires both 2<sup>nd</sup>-order analysis and correct  $y_0$ . In addition to  $y_0$ , the analyst must consider the effect of inelasticity (residual stress). This is due to residual stresses. As discussed earlier, a part of the section will start yielding when stress due to axial and flexure is less than yield stress (e.g., let's say  $0.7F_y$ ) meaning the stiffness of the section decreases (i.e.,  $E$  is not anymore, the initial modulus). Subsequently, a decrease in stiffness means more second-order effects. Figure 2-36 shows a common column cross-section and its typical residual stress pattern. It can be seen that at the tips of the flange the residual stresses are negative which has a detrimental effect when applying the axial load. The final state of the section can be seen the Figure 2-36 (e). The  $E$  in the red part of the section is not  $E_0$  anymore.

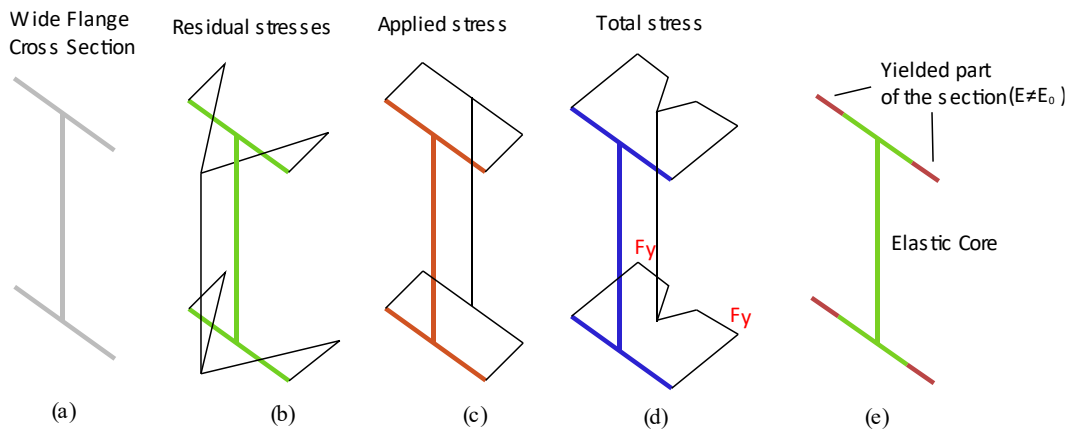


Figure 2-36. Residual stresses in the wide flange section

This has physical significance when we are trying to reinforce an existing column in a structure to increase its capacity. A common way to strengthen a column is to weld some plates to flange tips to box the column which improves the weak axis of the original W section substantially and has a smaller effect on what used to be the strong direction. Now the section might have equals moments of inertia in both directions. However, if that reinforcement was to apply additional load to the system (e.g., increase of floor loads), the stresses in the interior original W section may be high enough to exceed the yield point and if that occurs (i.e., the original core may yield) which will

leave just the two new plates to resist any stability. Now the controlling buckling capacity may be what used to be the strong axis since the section only has these plates, remaining to handle instability. Any yielded portion of a steel column contributes nothing to the stability strength of that member even though the entire cross-section supports the load.

In summary, the compression strength of a perfect single member is the lesser of its buckling load or yield strength which has been shown graphically in Figure 2-37 which is composed of an upper line controlling the yield strength then following a parabolic curve that controls buckling strength. For a real member with a reasonable amount of imperfection and residual stress, the curve is downgraded to the adjusted blue curve. So, the column buckling curve in every code represents the strength of a column with imperfections and a normal level of residual stresses. It is important to note that this curve represents a failure not by pure compression, but by both compression and flexion, even though the applied load is compressive. In other words, this is the kind of failure that is represented by each point on this strength curve.

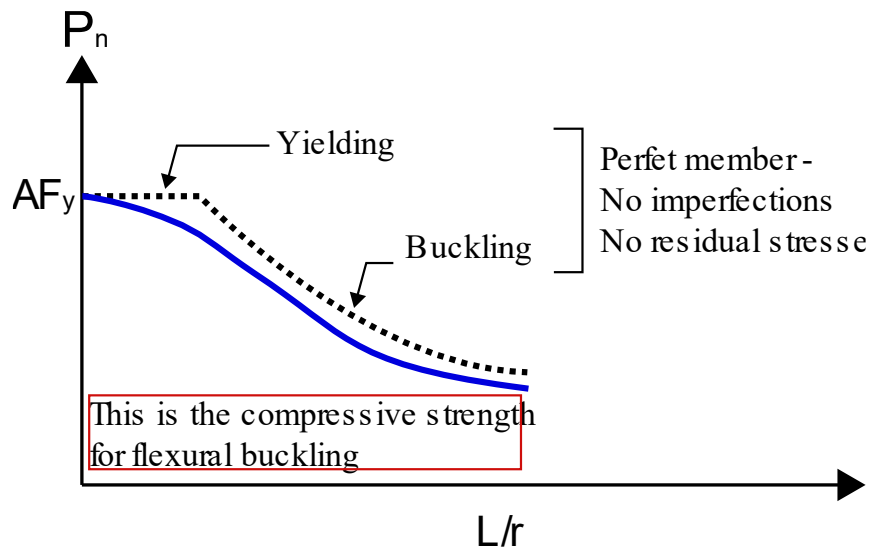


Figure 2-37. Column strength curve

### 2.5.1 How to design for stability?

There are two main approaches as describes below.

- The effective length method (ELM)

The steps to design a member based on effective length method is as follows:

1. Finding forces and moment in all members from a 2<sup>nd</sup>-order analysis (either direct 2<sup>nd</sup>-order analysis or 1<sup>st</sup>-order analysis adjusted by  $B_1$  and  $B_2$ ) neglecting imperfections and inelasticity (i.e., residual stresses).
2. Check the member capacity using column curve (i.e., strength equation) that includes effects of imperfections and inelasticity.

This has been demonstrated in Figure 2-38. It can be seen that on the left side of the figure corresponding to demand on the member is being underestimated by neglecting imperfections (both inelasticity and out-of-plumbness). While the capacity on the right side of the plot is considering these effects. In this method, in order to compensate for neglecting those effects on the demand side, a K factor is used on the capacity side of the equation.

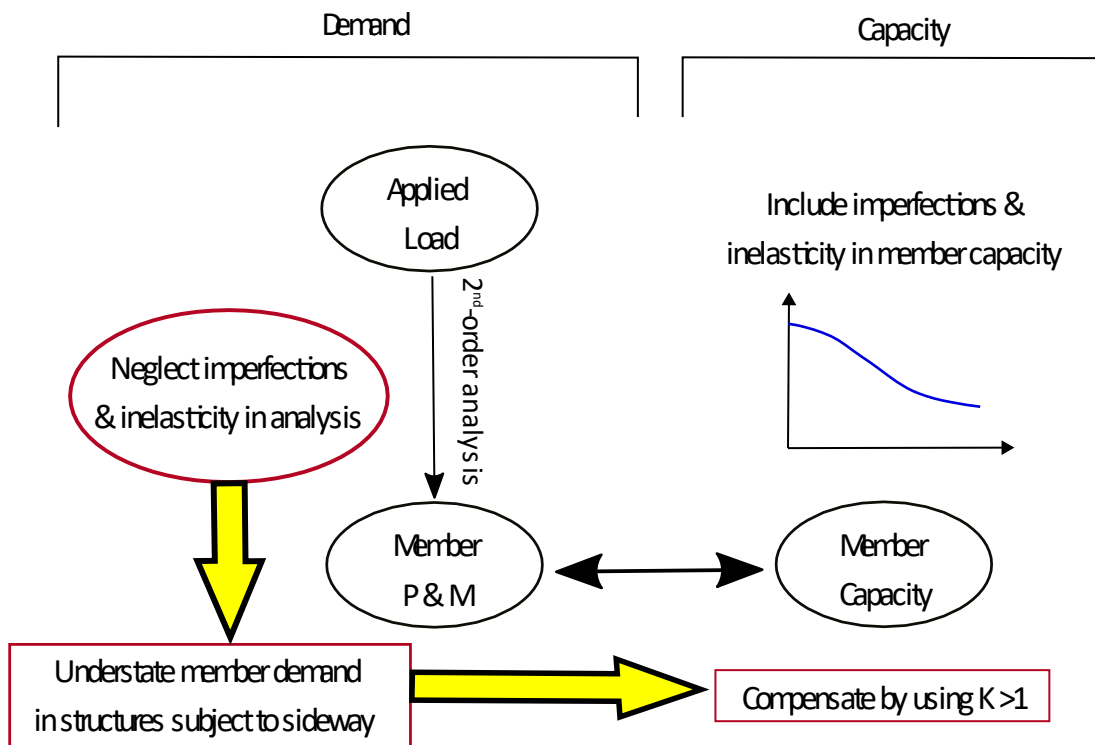


Figure 2-38. Effective length approach

The purpose of this K factor is explained in more detail using an example. Let's consider designing a cantilever column under a compressive force  $P$  neglecting the imperfections. The steps discussed previously regarding the traditional method has been shown graphically in Figure 2-39 . It should be noted that the column strength curve in Figure 2-39(b) does not represent a straight member. All coordinates of that curve represent the strength of a member that is slightly out-of-straight. Therefore, the coordinate of a point corresponding to  $\text{Length}=2 \times L$  represents a member shown in

Figure 2-39(c) and this imaginary member is actually the same as a cantilever column with some actual out-of-plumbness. Usually, the amount of out-of-straightness in those column strength curves is  $L/1000$ , which in this example results in  $2L/1000$ . This is in line with the code's recommendation of having a maximum column out-of-plumpness of  $L/500$

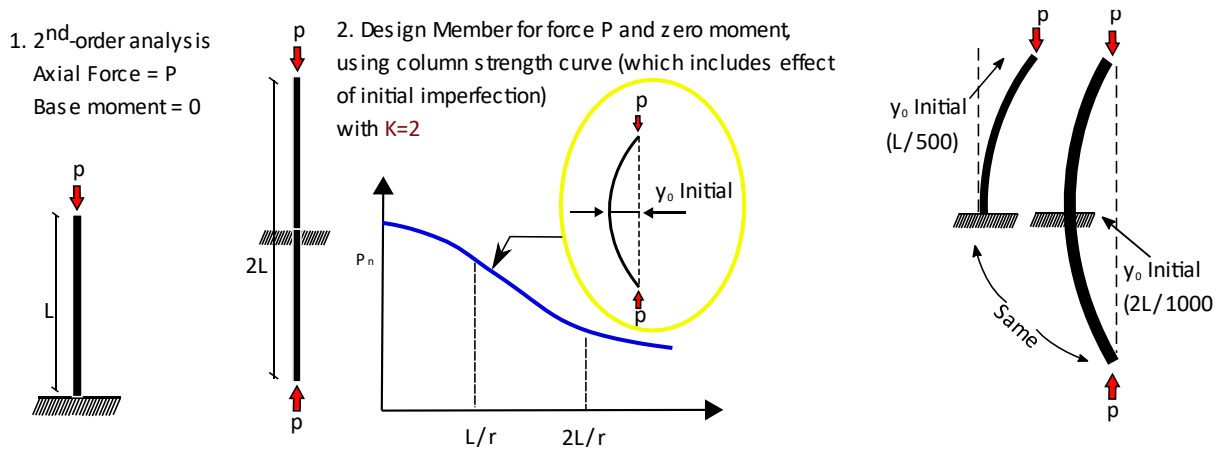


Figure 2-39. Designing cantilever column using effective length method

They are some obvious issues with this methodology. The first problem is that this process gives a zero-base moment for the column. This is not the case in reality which we know that the failure is going to be mostly a flexural failure with a significant amount of moment at the base. Therefore, although it gives you a correct column size, it under-designed beams and connections. Another issue with this methodology is that one must calculate the K factor which is not always straightforward. There are some alignment charts to compute the K-factor, however, few real word buildings meet the conditions for applicability of the alignment chart.

- The direct analysis method (DM).

In this approach, we consider inelasticity and imperfections explicitly and we use K equals to one. This method is demonstrated in Figure 2-41. The geometric imperfection can be applied either by applying the notional load or alternatively by directly modeling the imperfection via modifying the initial geometry of the model. Notional load is a lateral load applied at each story as a fraction of the vertical load 's of the story ( $Y_i$ ) which usually 0.002 of the applied gravity loads. This  $0.002Y_i$  is equivalent to an initial out-of-plumbness of  $1/500$  (see Figure 2-40).

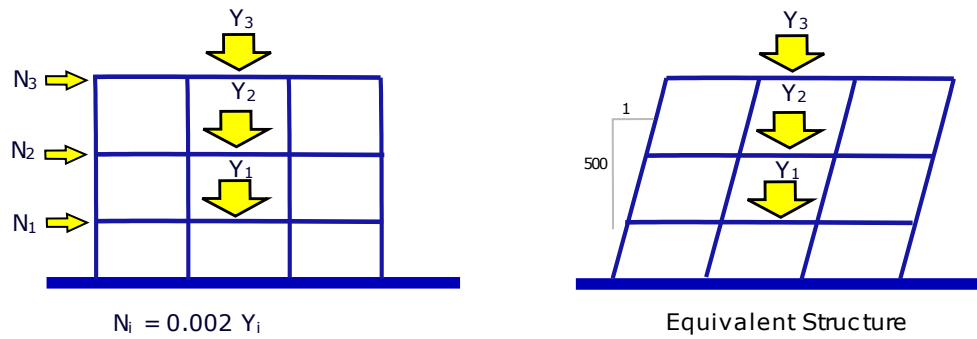


Figure 2-40. Different methods of inducing out-of-plumbness

The notional load induces the equivalent initial out-of-plumbness to the frame and it is easier to apply compared to modifying the initial coordinates of the nodes in the model.

Residual stresses are incorporated in the model by reducing the flexural and axial stiffness in the analysis. In other words, instead of using the nominal stiffnesses, we use the following stiffnesses:

$$EI^* = 0.8\tau_b EI \tag{2-62}$$

$$EA^* = 0.8EA$$

$\tau_b$ , is one when the axial force on the member is less than the half of yield and otherwise is a number less than one.

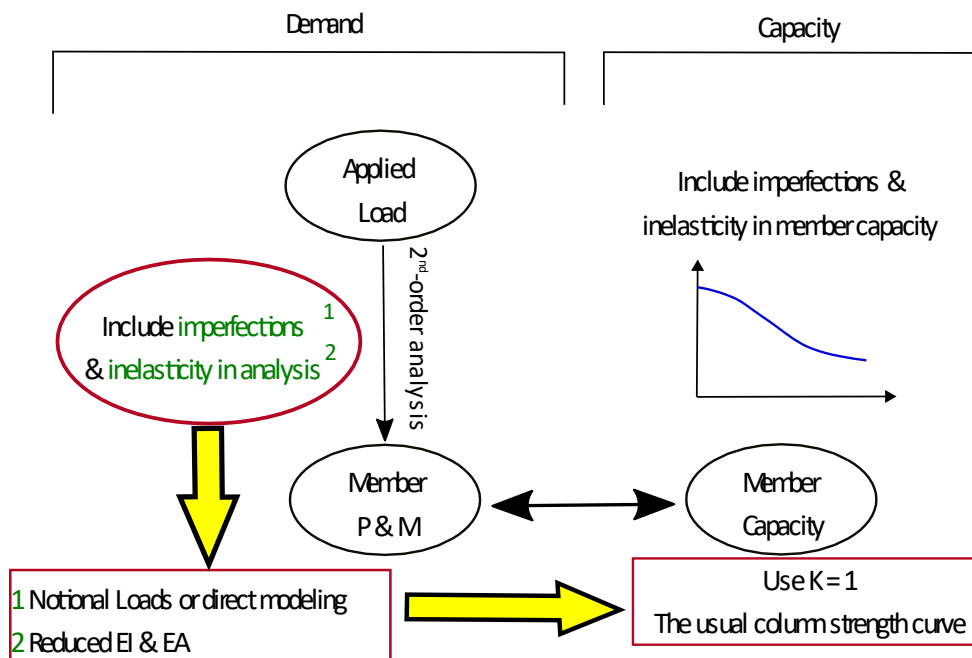


Figure 2-41. Direct analysis method

We can compare two approaches through a very simple problem. a single cantilever column with the fix base and an axial load applied at the top is shown in

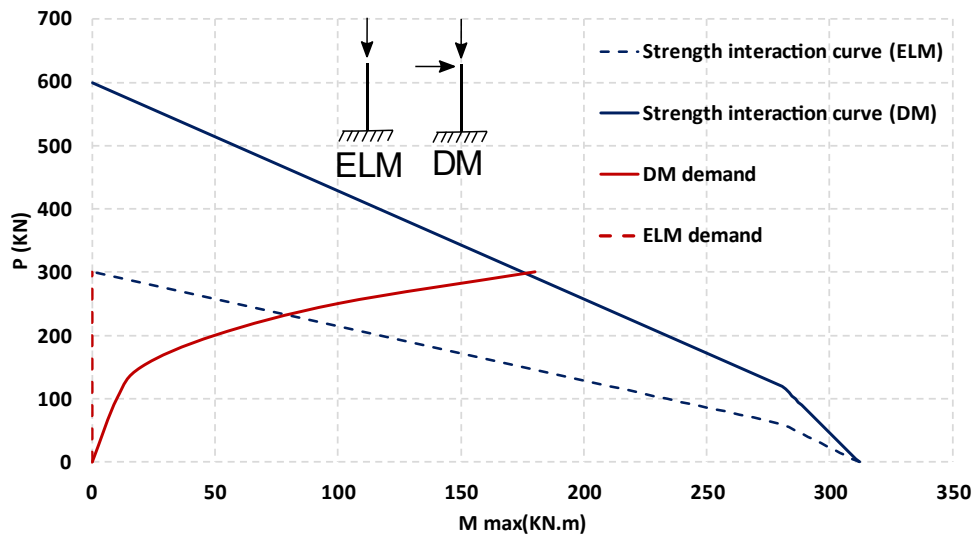


Figure 2-42. Direct analysis method

For the ELM we are just applying an axial load at the top while for the DM in addition to the axial load  $P$  we applied a notional lateral load of  $0.002P$  and reduce the column flexural stiffness. Now we compare the two methods by tracing our axial load and moment as we increase the load.

As we increase the axial load, there is no moment in the column until we reach the 300 kN strength capacity. The blue lines (both dashed and continuous) represent the column strength interaction curve for the two methods (i.e, using a K factor of two and one for ELM and DM respectively). The solid red line represents the demand on the column using DM method in which we reduce the flexural stiffness and applied a notional lateral load. It can be observed that as we increase the load, we now have a moment in our column. in this particular example, it can be seen that column axial capacity is almost the same in both methods while ELM miscalculates the moment in the column. for this example, it can be argued that the column based should be designed for what base moment. The ELM the moments necessary to stabilized the frame at the strength limit state will be underestimated.



## 3 Probability of failure (Reliability)

### 3.1 Introduction

This chapter describes the basic requirements for understanding the safety framework employed in the Eurocode series and provides supporting material that will be extremely helpful for the assessment of buckling curves in chapter 6. The problem of safety is a multi-disciplinary problem that incorporates different branches of science. The uncertainties present in many aspects of this problem also require that the assessment be made in terms of probabilities, adding a further layer of complexity. The aim of the present chapter is to provide a fundamental understanding of safety. For the purpose of coherency, this chapter is separated from chapter 2. This structure will allow the readers to better understand and follow the discussion.

### 3.2 Uncertainty

Certainty or determinism is the philosophical view that all events are determined entirely by previously existing causes. In the history of science, Laplace's demon [25] was the first published articulation of causal or scientific determinism.

*“We may regard the present state of the universe as the effect of its past and the cause of its future. An intellect which at a certain moment would know all forces that set nature in motion, and all positions of all items of which nature is composed, if this intellect were also vast enough to submit these data to analysis, it would embrace in a single formula the movements of the greatest bodies of the universe and those of the tiniest atom; for such an intellect nothing would be uncertain, and the future just like the past would be present before its eyes.”*

*Pierre Simon Laplace, A Philosophical Essay on Probabilities [25]*

This intellect is often referred to as Laplace's demon. In engineering words, he is claiming that if we could have developed a very detailed and perfectly ideal FEM of the universe, and have the capability to run in, considering the current state of the universe as its initial state,

we can predict the future with certainty. Thus, it would be possible to assess the exact number of floods and earthquakes together with their time occurrences.

Uncertainty refers to a situation involving imperfect or unknown knowledge. In other words, the lack of certainty is a state of limited knowledge where it is impossible to precisely describe the existing state, a future outcome, or more than one possible outcome. Generally, this uncertainty is intertwined with our world. For instance, in quantum mechanics, the uncertainty principle (i.e., Heisenberg's uncertainty principle [26]) states, that the more precisely the position of some particle is determined, the less precisely its momentum can be predicted from initial conditions, and vice versa, which can be expressed as:

$$\sigma_x \sigma_v \geq \hbar/2 \quad (3-1)$$

where  $\hbar$  is a constant,  $\sigma_x$  and  $\sigma_v$  are the standard deviation (std) of the position and velocity of a particle. In other words, since the right-hand side of the inequality is a constant, if one tries to measure the position of a particle with a higher degree of accuracy, it results in measuring the velocity of the particle with less accuracy (higher Std) regardless of the utility or technology that they have used for measuring.

### **3.2.1 Different Types of Uncertainty**

Classification of uncertainty can be made in a variety of ways considering different viewpoints. While many sources of uncertainty may exist, they are generally categorized as either aleatory or epistemic. An anecdote (reported by E.T. Bell) tells that the famous philosopher and mathematician Bertrand Russell in a lecture held in 1929, stated “*Probability is the most important concept in modern science, especially as nobody has the slightest notion of what it means*”. We experience a similar situation regarding the characterization of uncertainty into two types: aleatory and epistemic.

While there can be many sources of uncertainty, it is convenient to categorize the character of uncertainties as either aleatory or epistemic in the context of modeling. The word aleatory derives from the Latin ‘*alea*’, which means the rolling of dice [27]. Therefore, an aleatoric uncertainty is one that is assumed to be the inherent randomness of a phenomenon. Interestingly, the word is also used in the context of music, film, and other arts, where a randomness or improvisation in the performance is implied. The word epistemic derives from the Greek ‘*ἐπιστήμη*’ (episteme), which

means knowledge. Thus, an epistemic uncertainty is one that is presumed as being caused by lack of knowledge (or data). The reason that it is convenient to have this distinction within an engineering analysis model is that the lack of knowledge part of the uncertainty can be represented in the model by introducing auxiliary non-physical variables.

Most problems of engineering interest involve both types of uncertainties. Some have suggested that a clear distinction between the two types can be made. However, in the modeling phase, it is often difficult to determine whether a particular uncertainty should be put in the aleatory category or the epistemic category. Consider a basic random variable  $X$  describing a material property constant, such as the compressive strength of concrete. Should the uncertainty in  $X$  be categorized as aleatory or epistemic? The answer depends on the circumstances. If the desired strength is that of the concrete in an existing building, then the uncertainty should be categorized as epistemic if specimens taken from the building can be tested. On the other hand, the uncertainty in the strength of concrete in a future building should be categorized as aleatory, if there will be no attempts to make more detailed modeling related to, for example, the control of the concrete production. Until the building has been realized, no amount of testing will reduce the variability inherent in the strength of concrete of the future building. The character of the aleatory uncertainty “transforms” into epistemic uncertainty as the building is realized.

One can divide uncertainties based on their sources. For instance, *Statistical uncertainty*, which is the uncertainty in the estimation of the parameters of the considered distribution; or *modeling uncertainty*, rooted in imperfect mathematical idealization of reality that we are investigating. The latter can be considered as aleatory or epistemic uncertainty. In one model, an addressed uncertainty may be aleatory, in another model, it may be epistemic [27]. So, the characterization of uncertainty becomes a pragmatic choice dependent on the purpose of the application. In order to avoid this ambiguity, uncertainties are characterized as epistemic, if the modeler sees a possibility to reduce them by gathering more data or by refining models. Uncertainties are categorized as aleatory if the modeler does not foresee the possibility of reducing them. From a pragmatic standpoint, it is useful to thus categorize the uncertainties within a model, since it then becomes clear as to which uncertainties have the potential of being reduced.

### 3.2.2 Describing Uncertainty

Uncertainty can be described in several ways, as follows:

- Probability

Probability is a number between 0 and 1, where, roughly speaking, 0 indicates non-occurrence of the event, and 1 indicates certainty. The higher the probability of an event, the more likely it is that the event will occur. For example, the probability of occurring an earthquake with  $M \geq 7$ .

- Fuzzy logic

An alternative approach is offered by possibility theory [28] based on the representation of uncertain parameters by fuzzy numbers. In fuzzy mathematics, fuzzy logic is a form of many-valued logic in which a truth value (a number between 0 and 1) is assigned to an event. It is employed to handle the concept of partial truth, where the truth value may range between completely true and completely false. By contrast, in Boolean logic, the truth values of variables may only be the integer values 0 or 1. For example, in Figure 3-1, at the left-hand side of the plot, the truth value of cold is one. However, as we go further to the right, we arrive at a transition range that different people might answer differently to whether it is hot or warm?

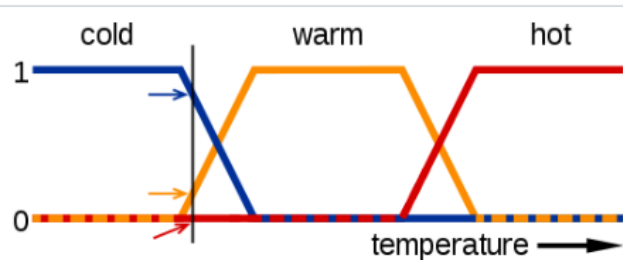


Figure 3-1 Fuzzy logic temperature

It can be seen that the truth value of cold is decreasing, while the truth value of warm is increasing until it reaches a range that everyone unanimously agrees on being warm. The same inference can be made on the second transition from warm to cold. A basic application of this concept is the temperature measurement for anti-lock brakes in mechanical systems.

- Entropy

Entropy is often roughly used as a measure of the unpredictability of a phenomenon. For example, Figure 3-2 (b) can be assembled again with fewer questions compared to Figure 3-2 (a). The number of black dots is the same in both figures.

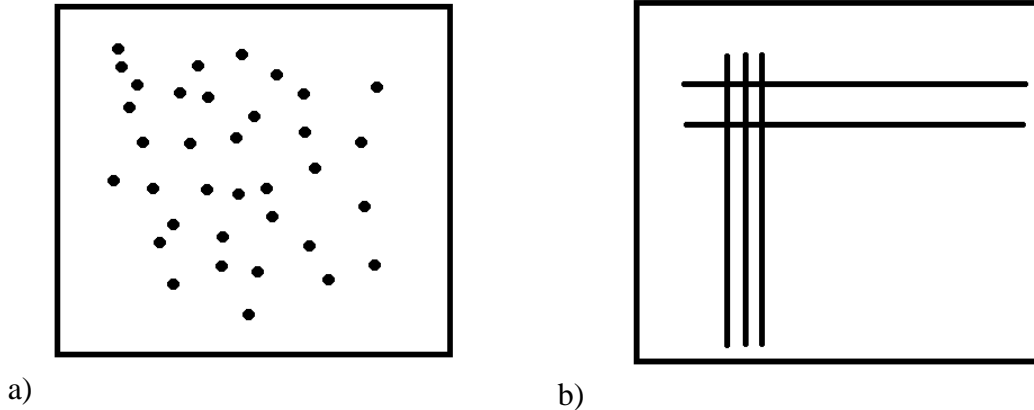


Figure 3-2 a) higher entropy b) lower entropy

### **3.3 Definition of Safety**

In the previous section, the definition of uncertainty was established. Further, we have seen different types of uncertainty and the methods to describe them mathematically. In general, repeated measurements of the same physical phenomena results in multiple outcomes. Among these multiple outcomes, some outcomes are more frequent than others. The occurrence of multiple outcomes without any pattern is described by terms such as uncertainty, randomness, and stochasticity. For instance, if several "identical" specimens of a steel bar were loaded until failure in a laboratory, each specimen would fail at different values of the load. we define these various results by a random variable. In other words, a random variable contains all the possible or observed outcomes of the parameter under consideration. In general, the response variable could be functionally related to more than one random variable. For instance, one can consider the buckling load is a function of random variables  $f_y$  and  $t_w$ . Since the response is a function of other random variables, it will also be random, whether the exact functional relationship between them is known or not. Suppose that the response variable is denoted by  $R$  (e.g., the yield stress of the steel or the buckling load of a column). A probability density function (PDF) is a plot that shows the frequency of each possible value taken by the response variable and the area under the curve between any two values gives the probability of random variable falling within those ranges.

Therefore, when designing any component, it is necessary to select one of these outcomes (i.e., design value) among all possible outcomes of the response variable that we have observed. Usually, if the parameter under consideration is a resistance parameter, we choose a particular rare outcome from the lower tail of the distribution, meaning the probability that the actual resistance is less than the design value is limited to a certain probability. It must be borne in mind that theoretically, the two tails of the PDF extend to infinity, making it unrealistic to design a system with zero probability of failure. In simple words, although observing some results can be highly improbable, it is possible. Thus, we must agree on an acceptable probability of failure (an acceptable risk) for our system during its lifetime. In order to define this mathematically, we use the first moment and second of the probability distribution (denoted by  $\mu$  and  $\sigma$  respectively), since, they are simple and straightforward to compute. The design value of any parameters is defined by Eq.(3-2). It specifies the design value of a random variable "R" as an outcome that stays "K" standard deviation ( $\sigma$ ) from the mean ( $\mu$ ).

$$R_d = \mu_R - K \times \sigma_R \quad (3-2)$$

By specifying the value of K, we can control the probability of failure ( $R \leq R_d$ ) for our system. Figure 3-3 shows these definitions schematically. It is possible to standardize any random variables and transform their distribution to a target distribution. The probability of failure indicated in Figure 3-3 can also be expressed as an index commonly denoted by the symbol  $\beta$ , which can be related to the probability of failure ( $p_f$ ) using the following equation:

$$p_f = \Phi(-\beta) \quad (3-3)$$

where  $\Phi$  is the standardized cumulative distribution function of the. Thus, there is a unique mapping with  $\beta$  and the probability of failure (i.e., the blue area Figure 3-3). By specifying a value for  $\beta$ , equivalently we are limiting the probability of having resistance less than  $R_d$  to the probability of failure defined by Eq.(3-3).

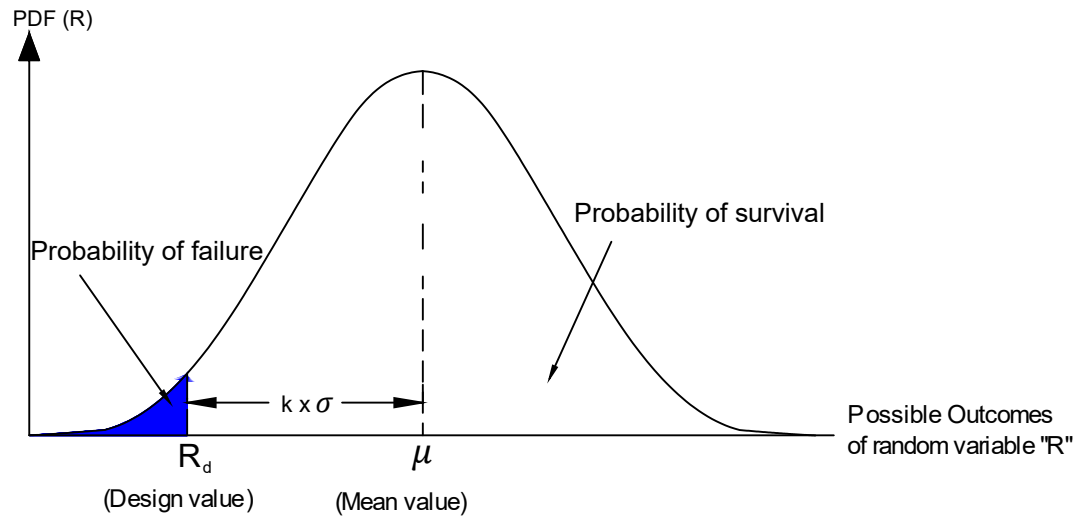


Figure 3-3 a) Definition of the probability of failure, design value and probability of survival

## 3.4 Eurocode 1990

### 3.4.1 Introduction

The European Union has spent several decades (since 1975) developing and unifying the rules for the design of structures. This work has culminated in a set of European standards called the Eurocodes. The flowchart in Figure 3-4 illustrates the relationship between the Eurocodes [24]. Initially, the Eurocodes were presented as Pre-Standards (ENVs), and between 2002 and 2007 were converted into European Standards (ENs). This was followed by the development and publication of the National Annexes in each CEN country and the translation of the Eurocodes into the various national languages.

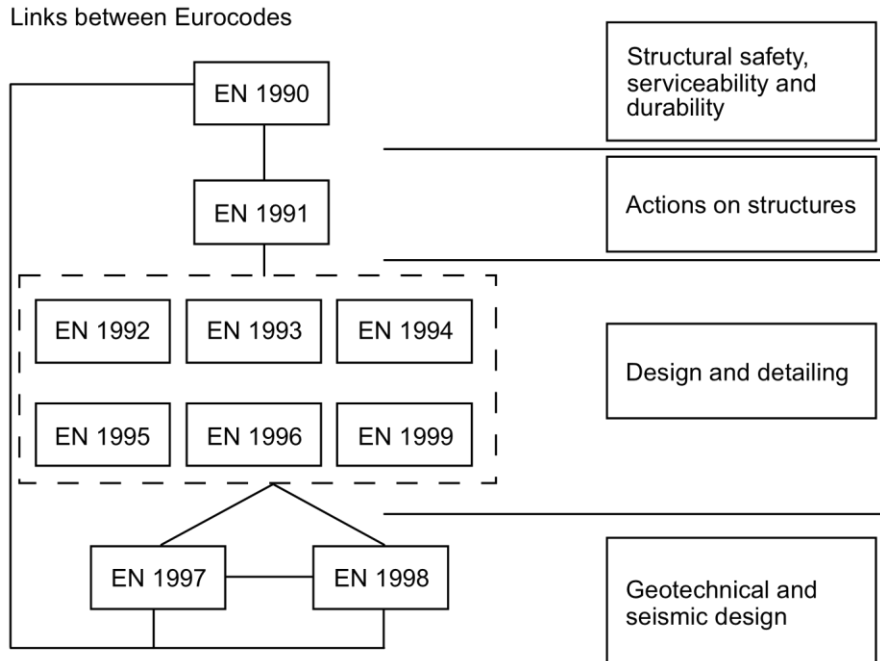


Figure 3-4 Links between Eurocodes [24]

EN 1990, Eurocode: Basis of Structural Design, is the head document in the Eurocode suite, and it establishes for all the structural Eurocodes the principles and requirements for safety, serviceability and durability of structures; it further describes the basis of design and verification and provides guidelines for related aspects of structural reliability. The clauses in EN 1990 are set out as either *Principles* or *Application* rules. The principles are identified by the letter P and are general statements and definitions that cannot be replaced by any other alternatives.

### 3.4.2 Reliability in Eurocode 1990

The basic requirement in clause 2.1(1)P stipulates that “A structure shall be designed and executed in such a way that it will, during its intended life, with appropriate degrees of reliability and in an economical way

- sustain all actions and influences likely to occur during execution and use, and
- meet the specified serviceability requirements for a structure or a structural element.

EN 1990, classifies structures according to consequence classes (CC) as given in Table 3-1 that are directly linked to reliability classes (RC) with associate minimum values for the reliability index  $\beta$  (I.e., the blue area in Figure 3-3).



Table 3-1 Definition of consequences classes (Table B1 EN1990)

Consequences Class	Description	Examples of buildings and civil engineerin2 works
CC3	high consequence for loss of human life, or economic, social or environmental consequences very great.	Grandstands) public buildings where consequences of failure are high (e.g. a Concert hall.)
CC2	medium consequence for loss of human life, economic, social or environmental consequences considerable.	Residential and office buildings, public buildings where consequences of failure are medium (e.g. an office building)
CCI	low consequences for loss of human life, and economic, social or environmental consequences small or negligible.	Agricultural buildings where people do not normally enter (e.g. storage buildings), greenhouses

Table 3-2 Consequences and reliability classes, and values for the reliability index

Consequences class	Reliability class	Values for $\beta$			
		Ultimate limit states		Serviceability	
		1-year reference period	50-year reference period	1 year reference period	50 year reference period
CC3	RC3	5.2	4.3		
CC2	RC2	4.7	3.8	2.9	1.5
CCI	RC1	4.2	3.3		

According to the above table, for CC2, corresponding to medium consequences, the corresponding reliability class RC2 is characterized by a minimum reliability index of 3.8 for a 50 years reference period.

The limit state defined previously as  $R \leq R_d$ , can be generally expressed through a limit state function (L.S.F)  $g(\mathbf{x})$ , that defines the event of failure. Where  $\mathbf{x}$  is vector of random variables in the problem. The failure must be defined so that  $g(\mathbf{x}) = 0$  separates the failure domain (i.e.,  $\Omega \equiv g(\mathbf{x}) < 0$ ) and safety domain ( $g(\mathbf{x}) > 0$ ) (e.g.,  $g=R- R_d$ ). Thus, the probability of failure can be obtained in the same manner as in the previous section. However, instead of using a pdf, a joint pdf of random variables is used in its general form. Let us consider that  $\mathbf{x}$  is a vector of random variables and  $\varphi(\mathbf{x})$  is the joint probability density function of all random variables. In other words,  $\varphi(\mathbf{x})$  contains the likelihood of all the possible combination outcomes of  $\mathbf{x}$  and the area under the joint pdf gives the probability that each of the random variables  $x_1, x_2, \dots$  falls in any particular range. Therefore, the  $p_f$  can be computed as:

$$p_f = \text{prob}(g \leq 0) = \int_{g \leq 0} \varphi(\mathbf{x}) d\mathbf{x} \quad (3-4)$$

The above equation indicates a multi-space dimension (the same size of vector  $\mathbf{x}$ ). Since we are bounded to three-dimension space, the above integral is illustrated by considering two random variables as shown in Figure 3-5. The figure shows the joint pdf  $f(\mathbf{x})$  and its contours which are projections of the surface of  $f(\mathbf{x})$  on  $X_1 - X_2$  plane. It is also possible to use the vertical axis to show the L.S.F  $g$ , since it is also a function of random variables ( $X_1 - X_2$ ). The L.S.F will intersect with  $X_1 - X_2$  plane at some points, which is an indication of  $g(\mathbf{x}) = 0$ .

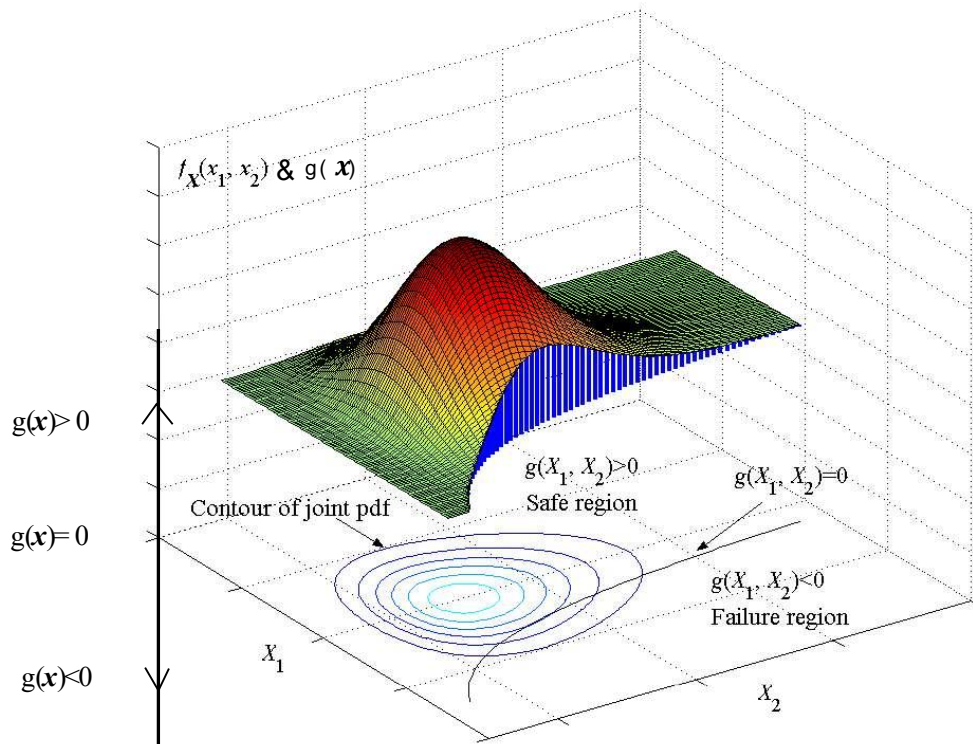


Figure 3-5 Probability of failure for a two-dimensions problem

In our two-dimensional problem, we have a L.S.F surface (hyper-surface for the higher than 2-D problems). Therefore, given the definition of L.S.F earlier, the failure region is specified and the probability of failure is the area of the joint pdf over the failure region.

Imagine that the surface of the integrand  $f(\mathbf{x})$  forms a “hill”. If the hill were cut by a knife that has a blade-shaped with the curve  $g(\mathbf{x}) = 0$ , the hill would be divided into two parts. If the part on the side of  $g(\mathbf{x}) < 0$  were removed, the part left would be on the side of  $g(\mathbf{x}) > 0$  as shown in Figure 3-5. The volume left is the probability integration in Eq. (3-4), which represents the reliability. In

other words, the reliability is the volume underneath  $f(\mathbf{x})$  on the side of safe region  $g(\mathbf{x}) > 0$ . Obviously, the probability of failure will be the volume underneath  $f(\mathbf{x})$  on the side of failure region  $g(\mathbf{x}) < 0$ , the removed part. To show the integration region more clearly, the contours of integrand  $f(\mathbf{x})$  and the integration boundary  $g(\mathbf{x}) = 0$  are plotted again in the random variable space (X-space) in Figure 3-6. The reliability index corresponding to this area (probability of failure) can be computed using Eq.(3-3).

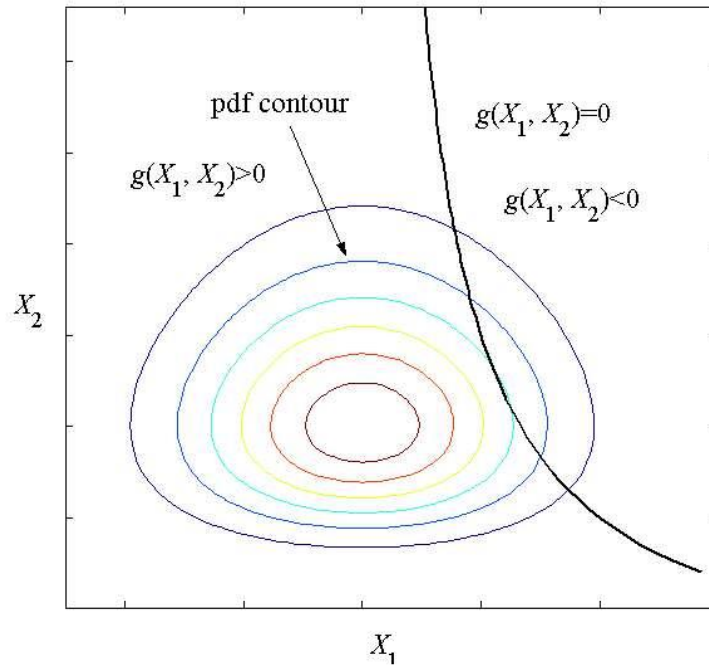


Figure 3-6 Contours of joint pdf

# 4 Experimental Program

## 4.1 Introduction

This chapter describes a set of experiments executed at the Department of structures for engineering and architecture of the University of Federico II. The investigations involve tensile stress-strain tests and buckling tests. In total, 21 buckling tests are performed on both RHS and SHS with two different steel grades. Prior to testing the specimens, each section was subject to careful geometrical measurements. For each specimen, the external widths of all four sides, the thicknesses at 18 different locations, and the outside corner radii of all four corners of the section were measured. A comprehensive statistical assessment of the data is presented, which will be used later in chapter four for probabilistic evaluation of the flexural buckling curve. The columns are fabricated by the cold-forming continuous method.

## 4.2 Specimens

In this study, continuous-formed square hollow section specimens with different  $B_{nom}/t_{nom}$  ratios are selected since the  $B_{nom}/t_{nom}$  ratio is a good indicator of the overall amount of cold-forming contained in the cross-section. All specimens were fabricated by the continuous-forming method with friction stir welding. The nominal size and the basic properties of SHS and RHS are listed in Table 4-1 and Table 4-2, respectively. The prefix 'S' with its following number represents the steel grade of the profile. The letter shown in the specimen label after the section dimension represents a different length for the same profile. All symbols in the tables below correspond with those in Figure 4-1.

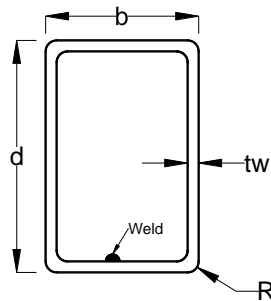


Figure 4-1 Section notation

It is important to note that the effective length is considered from the top pin's center to the bottom pin. In total, 21 specimens are investigated by using two different steel grades (S275, S355). All specimens fulfill the requirements of the cross-section class one; thus, no local buckling will occur during the testing. In order to have a good dispersion of results, specimens are selected in a way to have a global non-dimensional slenderness ratio  $\bar{\lambda}$  between 0.1 and 2.

Table 4-1 SHS specimen measurements

Name	B (mm)	D (mm)	t <sub>nom</sub> (mm)	b/t <sub>w</sub>	d/t <sub>w</sub>	L (mm)	L <sub>eff</sub>	A (mm <sup>2</sup> )	I (mm <sup>4</sup> )	$\bar{\lambda}$
S275_60X6_A	60	60	6	10.00	10.00	850	1020	1200	21.6	0.54
S275_60X6_B	60	60	6	10.00	10.00	1750	1920	1200	21.6	1.02
S275_50X6_A	50	50	6	8.33	8.33	2150	2320	963	17.5	1.53
S275_50X6_B	50	50	6	8.33	8.33	2900	2600	963	17.5	1.71
S355_50X6_C	50	50	6	8.33	8.33	1850	2020	963	17.5	1.51
S355_50X6_D	50	50	6	8.33	8.33	2550	2720	963	17.5	2.03
S275_100X8_A	100	100	8	12.50	12.50	500	640	2720	36.7	0.2
S275_100X8_B	100	100	8	12.50	12.50	1190	1310	2720	36.7	0.41
S355_100X8_C	100	100	8	12.50	12.50	1250	1420	2720	36.7	0.51
S355_100X8_D	100	100	8	12.50	12.50	2650	2820	2720	36.7	1.01
S355_200X8_A	200	200	8	25.00	25.00	950	1220	5920	77.6	0.21
S355_200X8_B	200	200	8	25.00	25.00	2750	3020	5920	77.6	0.51

Table 4-2 RHS specimen measurements

Name	B (mm)	D (mm)	t <sub>nom</sub> (mm)	b/t <sub>w</sub>	d/t <sub>w</sub>	L (mm)	L <sub>eff</sub> (mm)	A (mm <sup>2</sup> )	I (mm <sup>4</sup> )	$\bar{\lambda}$
S275_60X40X6_A	60	40	6	10.00	6.67	1100	1270	963	14.3	1.02
S275_60X40X6_C	60	40	6	10.00	6.67	2350	2520	963	14.3	2.03
S275_60X40X6_D	60	40	6	10.00	6.67	1750	1920	963	14.3	1.55
S355_70X50X6_A	50	70	6	8.33	11.67	1300	1470	1200	18.4	1.05
S355_70X50X6_B	50	70	6	8.33	11.67	1200	1470	1200	18.4	1.05
S355_70X50X6_C	50	70	6	8.33	11.67	850	1020	1200	18.4	0.73
S355_70X50X6_D	50	70	6	8.33	11.67	2570	2740	1200	18.4	1.95
S355_70X50X6_E	50	70	6	8.33	11.67	2000	2170	1200	18.4	1.54
S355_220X140X8_A	140	220	8	17.50	27.50	2000	2250	5280	56.5	0.52
S355_220X140X8_B	140	220	8	17.50	27.50	700	950	5280	56.5	0.22
S355_200X100X12.5_A	100	200	12.5	8.00	16.00	2700	2950	6200	37.9	1.02
S355_200X100X12.5_B	100	200	12.5	8.00	16.00	1200	1450	6200	37.9	0.5
S275_200X120X12_B	200	120	12	16.67	10.00	80	330	6490	38.2	0.1
S275_200X120X12_A	200	120	12	16.67	10.00	200	450	6490	38.2	0.14

Note that since all specimens were designed to buckle among the minor axis, the gyration radius in the above tables is about the weak axis for the RHS. The test specimens are shown in Figure 4-2. It should be noted that the columns in common practice are generally bigger than the ones considered in this study. In the experimental program, the capacity of the testing machine and the available budget play an important role. However, the results and findings can be generalized.

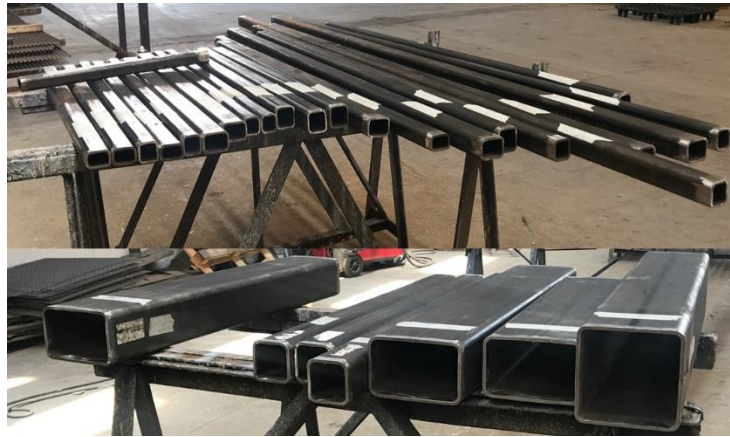


Figure 4-2 Investigated cross-sections in this study

Figure 4-3 shows graphically the number of selected specimens respective to the local non-dimensional parameter  $(H+T)/(2T)$ .

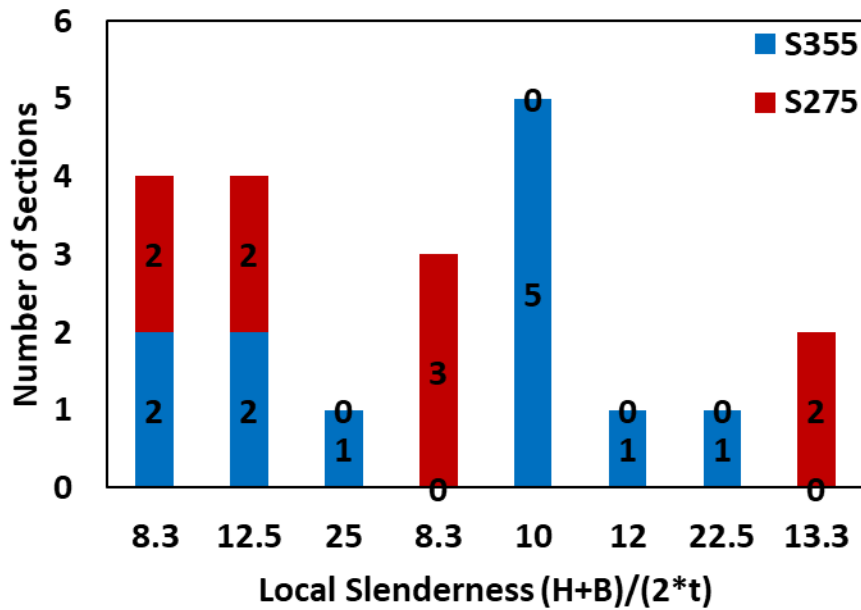


Figure 4-3 Number of specimens in terms of local slenderness ratio and steel grade

### 4.3 Geometrical imperfections

Prior to testing the specimens, each section was subject to careful geometrical measurements. For each specimen, the external widths of all four sides and the thicknesses at 18 different locations were measured. Figure 4-4 shows an example of measuring the thickness along with the location of those measurements around the section. It should be noted that the thickness was measured at both ends of each specimen.

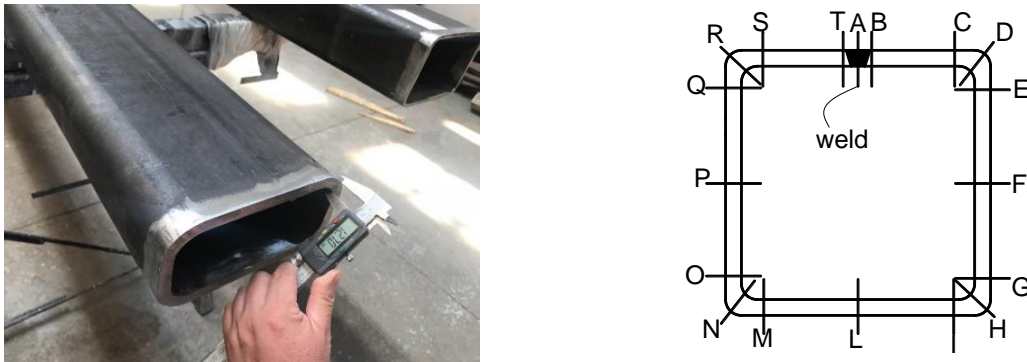


Figure 4-4 Thickness measurement locations

The outside corner radii of all four corners of the section were also measured at three different sections, at both ends and in the middle. Figure 4-5 shows the three sections used for measuring the corner radii. Each section has four corners, and at each corner, two widths were recorded, as shown in Figure 4-5. The thickness, corner radii and widths of all measured locations of the specimens are listed in Appendix A.1.

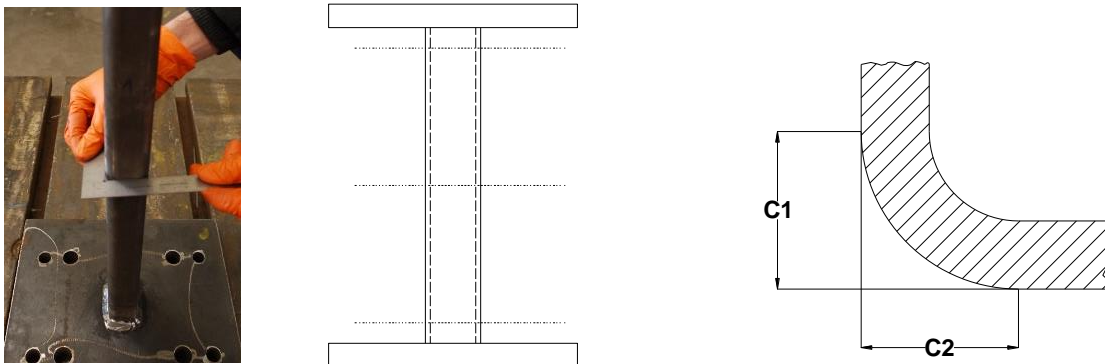


Figure 4-5 Corner radii measurements

The average of measured width and thickness ( $B_{avg}$  and  $t_{avg}$ ) are compared to the nominal values ( $B_{nom}$  and  $t_{nom}$ ) in Table 4-3. The measured outside corner radii of all specimens are normalized to their corresponding  $t_{avg}$ . Note that due to the time window of the experimental activity and height of some specimens, measuring the corner radius or the widths of few specimens was not feasible.

Table 4-3 Nominal and measured dimensions of specimens

ID	$B_{nom}$ (mm)	$t_{nom}$ (m)	$B_{avg}/B_{nom}$	$t_{avg}$ (mm)	$t_{avg}/t_{nom}$	$r_{o,avg}/t_{avg}$
S275_50×6_A	50	6	1.0037	5.71	0.951	1.869
S355_50×6_C	50	6	1.0027	5.75	0.958	1.957
S355_50×6_D	50	6	0.9993	5.73	0.955	2.037
S275_100×8_A	100	8	1.0006	7.98	0.998	2.302
S275_100×8_B	100	8	1.0018	8.13	1.016	0.000
S355_100×8_D	100	8	0.9997	7.90	0.988	2.347
S275_60×40×6_A	60-40	6	1.0030	6.28	1.046	1.653
S275_60×40×6_B	60-40	6	1.0038	6.29	1.048	1.644
S275_60×40×6_C	60-40	6	1.0058	6.26	1.043	1.644
S275_60×40×6_D	60-40	6	1.0033	6.29	1.048	1.617
S355_70×50×6_A	70-50	6	1.0028	5.72	0.953	1.851
S355_70×50×6_B	70-50	6	1.0036	5.76	0.960	1.910
S355_70×50×6_C	70-50	6	1.0035	5.63	0.939	1.871

Typical measurements of the thickness around the section are shown in Figure 4-6 for section S275\_200×120×12\_B, together with the allowable tolerance. It can be seen that despite the variation around the section, all values are within the allowable range.

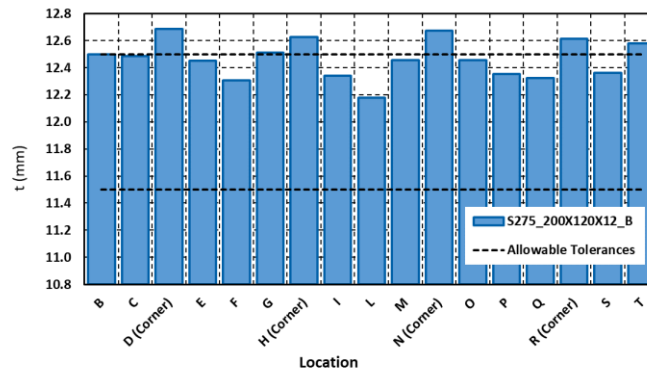




Figure 4-6 Difference between measured and nominal thickness for specimen S275\_200×120×12\_B

#### 4.4 Out-of-straightness measurements

Out-of-straightness measurements were taken using a KONI-007M optical level and micro-staff with a net accuracy of 0.005 mm. The laser target plate was placed at five different points along the columns' height to capture the specimens' out\_of\_straightness as shown in Figure 4-7.

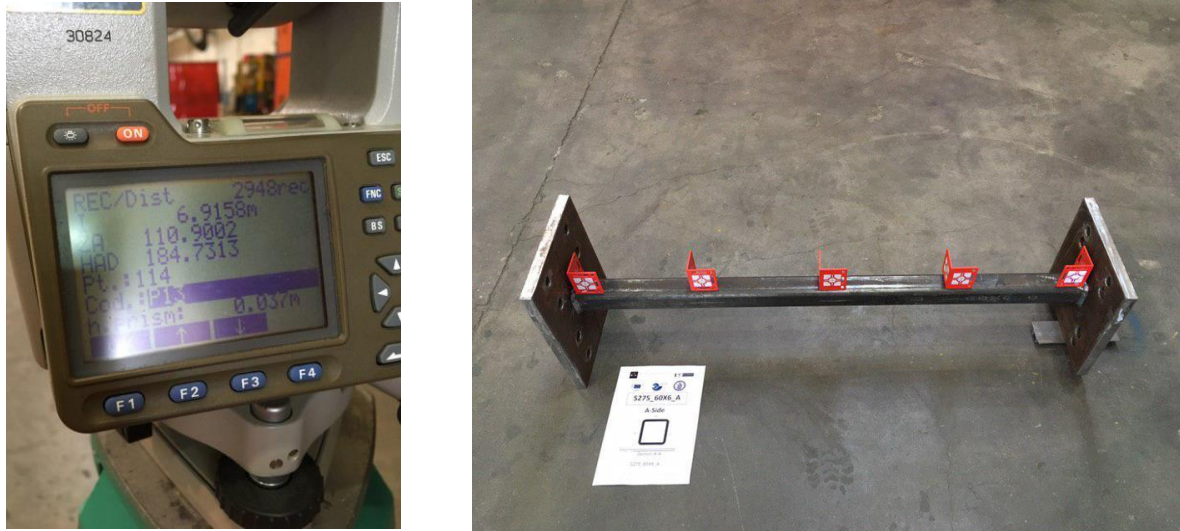


Figure 4-7 Geometrical imperfections measurement

Figure 4-8 shows the measured out\_of\_straightness schematically for section S355\_200×100×12.5\_A.

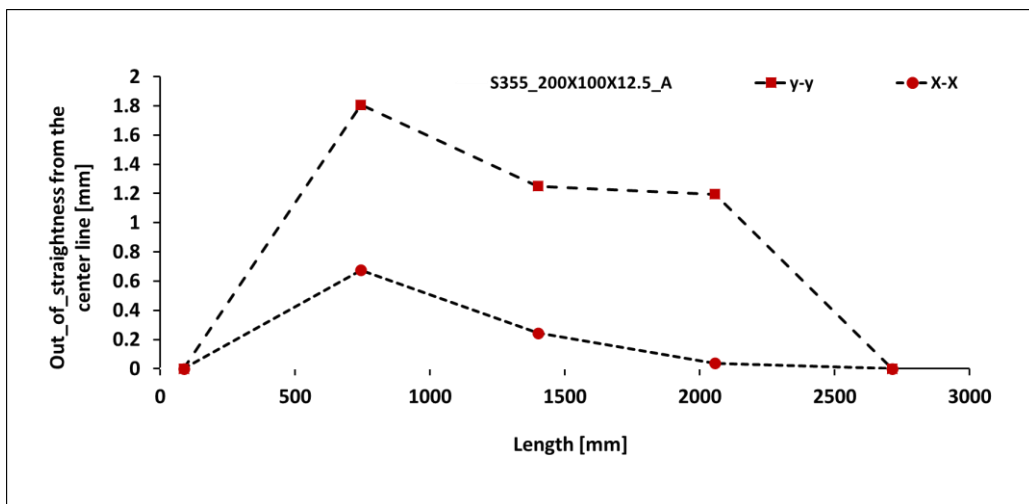


Figure 4-8 Measured imperfections profile for section S355\_200×100×12.5\_A

## **4.5 Tensile Coupon tests**

### **4.5.1 Introduction**

The variation in cold work performed around the section during the cold-forming process produces a gradient in the yield stress, with the highly worked corners exhibiting significantly higher yield stress than the virgin material. While the beneficial effects of this increase in the yield stress, over that of the virgin material are considerable, ductility is reduced due to the cold work, leading to corner regions that may have limited capacity to undergo plastic deformations without fracture. Also, previous investigations [29, 30, 31] have found that stress increases with loading rate for various metallic materials. Thus, the determination of yield strength and ultimate strength is sensitive to the loading rate during testing. In this study, this effect is considered in the experimental activity and static curve is obtained from the dynamic curve. Another issue with cold-formed hollow sections is the curved corner of the section. This region, due to cold-forming, has higher yield and ultimate strength. This is a well-known phenomenon; however, it is difficult to measure the cross-sectional area or apply uniform tensile stress to coupon specimen during testing because of the shipment's curved geometry. In this study, an innovative way of testing the curved coupon is proposed to reduce the bias in the results.

### **4.5.2 Test specimens**

Tests were performed both for the direction of rolling and direction transverse to the sheet's fabrication rolling (see Figure 4-9). A total of 83 Tensile coupon tests were carried out. Thirty-five tests form the flat part, 30 tests from the corners area; also, 18 tests are done in the transversal direction of the plate containing the weld (see Figure 4-9). It should be noted that for some sections such as 50×50, extracting a transversal coupon is impractical.

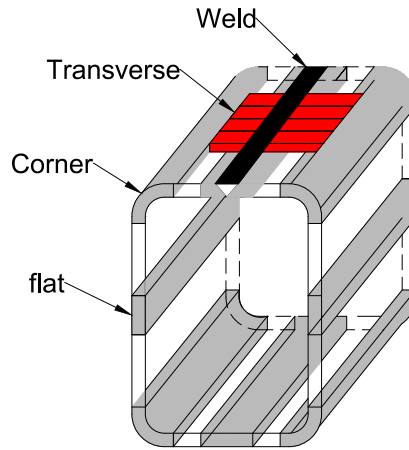


Figure 4-9 Locations of the tensile coupons

Depending on the section's geometry and the coupon's location, four types of coupon's geometry are considered, as shown in Figure 4-10.

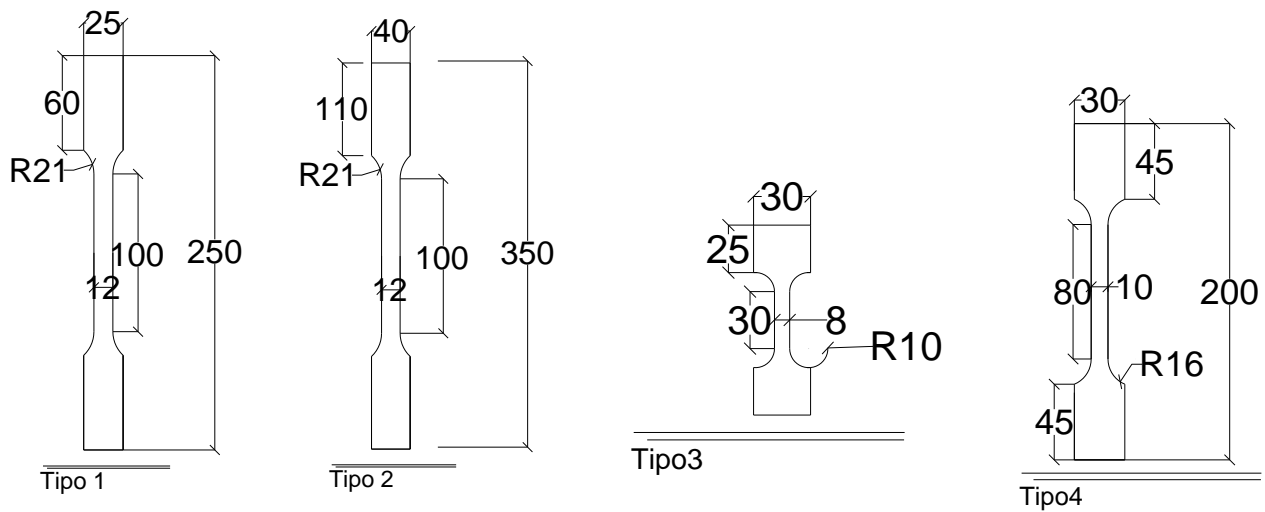


Figure 4-10 Dimension of flat coupon specimens

Type 1 and 2 are for the longitudinal test, while type 3 and 4 are for the transversal tests. The coupon's test dimensions conform to the British Standard BS EN ISO 6892-1 [32]. The dimension of each specimen was measured prior to testing. For the flat coupon specimens, the Vernier digital caliper was used to measure the thickness ( $t$ ) and width ( $B$ ) of the rectangular cross-section at five different cross-sections. Figure 4-11 shows typical flat and transversal coupons.

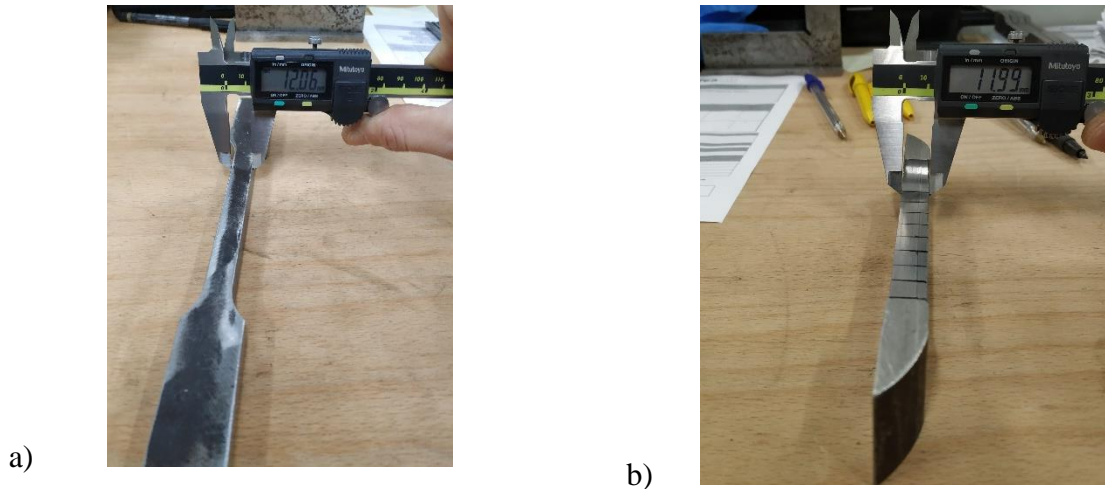


Figure 4-11 a) typical Flat coupon b) typical transversal coupon

The dimensions of the corner coupons are shown in Figure 4-12

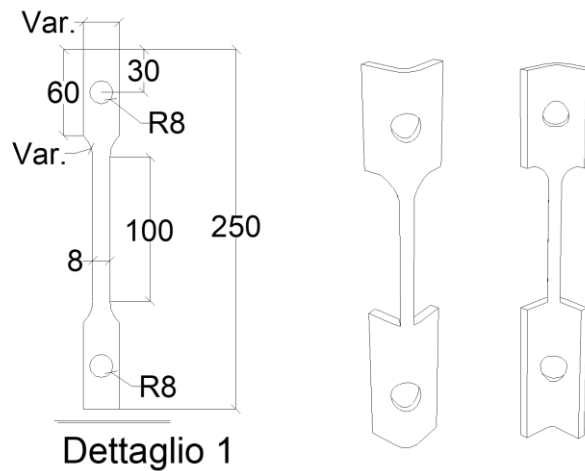


Figure 4-12 Dimension of corner coupon

Measuring the area of the unsymmetrical cross-section of the curved coupons is not a straightforward procedure. In this study, the area was computed by the weights and density method. In the weight and density method, the cross-sectional area equals to the mass of the specimen divided by the length and then also divided by the density of the material. Also, it should be noted, in weld coupons, the area of seem welding is not taken into consideration in the area of the coupon if there is any extra part due to welding.

### 4.5.3 Test set up

Schenck 250 kN hydraulic testing machine, driven by displacement control, was utilized to perform tensile coupon tests. Tensile loading was applied to the flat coupons by gripping both ends with a pair of flat surface clams. MTS extensometer of 100 mm gauge length is used to monitor the longitudinal strain of the test specimens. Figure 4-13 shows the test configuration for a typical flat coupon.

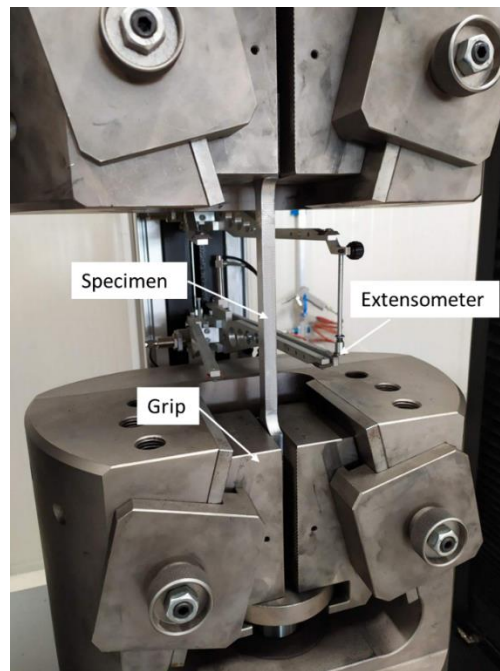


Figure 4-13 Test set up for flat coupons in this study

The curved coupons cannot be gripped by flat surface clamps due to their curved surface. Different methods have been proposed to overcome this issue, however, all of them introduced secondary effects to the test specimen. For example, the method of flattening the curved surface at the two ends of the coupons introduces eccentricity and caused additional bending, especially for curved coupons with a small radius. To remedy this issue, two holes were drilled at a distance of 30 mm from both ends of the coupons (see Figure 4-14). The tensile force was applied by two pins through the holes, which is in line with the centroid of the cross-section in order to avoid bending stress in the coupons. In addition, two mechanical connectors were manufactured, for transferring the load from the grip to the pin. Different component of the curved coupon test is shown in Figure 4-14.

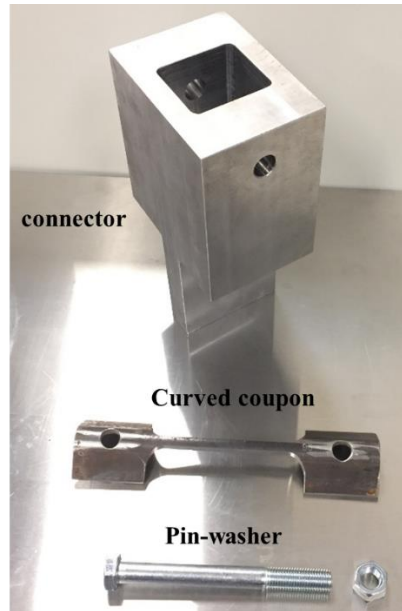


Figure 4-14 Different components of the curved coupon

It should be noted that the curved coupon has been cut by water jet to minimize the secondary effect due to cutting. Also, to ensure that the deformation will occur in the gauge length, the section's resistance with the hole has been checked. Figure 4-15 shows the configuration of the test for the curved coupon.

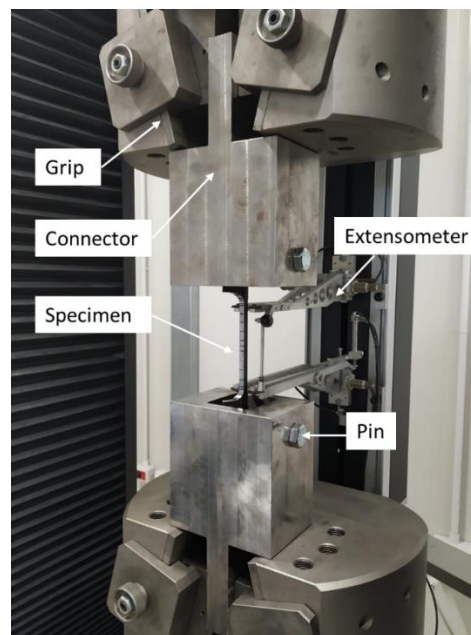


Figure 4-15 Test set-up for corner coupons in this study

#### 4.5.4 Test procedure

It is well-known that the design parameters such as yield and ultimate strength are sensitive to the loading rate of the tensile coupon test. Previous studies indicate that stress increases with the loading rate for various metallic materials. Therefore, if the test is held at critical locations, it can be observed that stress reduces gradually during the holding period. This phenomenon is called "stress relaxation". Figure 4-16 shows a typical stress relaxation of the coupon test.

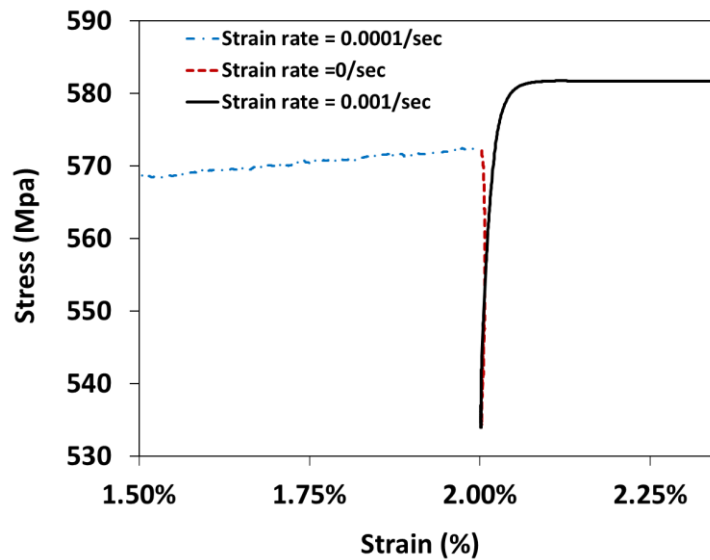


Figure 4-16 Typical static drop during stress relaxation

To evaluate the effect of loading rate on  $f_y$  and  $f_u$ , the test was held for 60 seconds at two fixed loading points to obtain the static drop. The 1<sup>st</sup> static drop was obtained at 0.4% strain rate intending to capture the effect of loading rate on the yield stress, while the second stop is at 2% strain rate intending to be near the ultimate stress. It is worthwhile noting that considering the large number of tests, it was neither practical to stop the test more than 60 s nor stop the test manually for each test at different points.

Commonly, standards give a lower and upper bound for the strain rate control method and separate the test into two ranges before and after yielding. The provision of American Specification (ASTM) [33] and European Code (BSI) [34] is investigated in this paper. As shown in Figure 4-17, two loading rates are considered in this study, which complies with the lower bound of both standards.

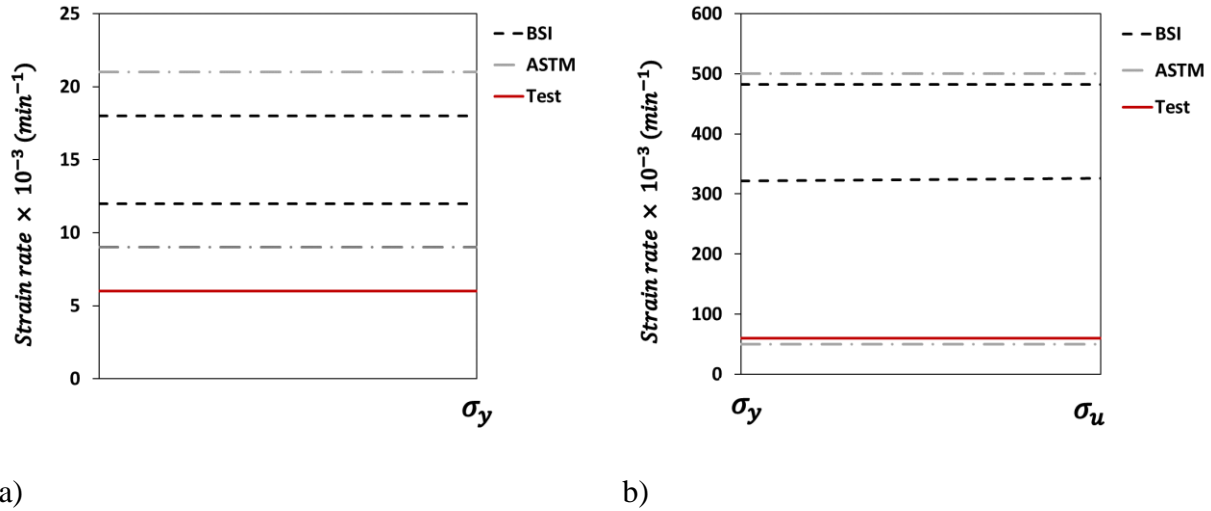


Figure 4-17 Strain rate used during the tensile test a) up to  $f_y$  b) from  $f_y$  to  $f_u$

A typical stress-strain curve obtained based on the discussed procedure is plotted in Figure 4-19.

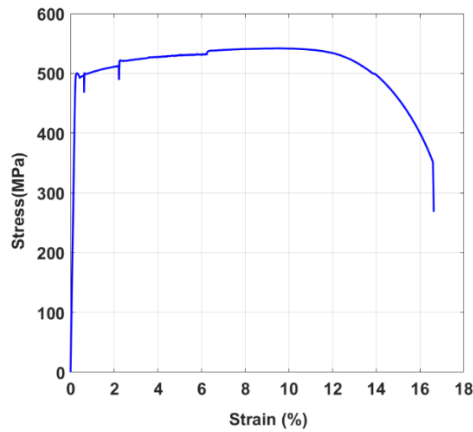


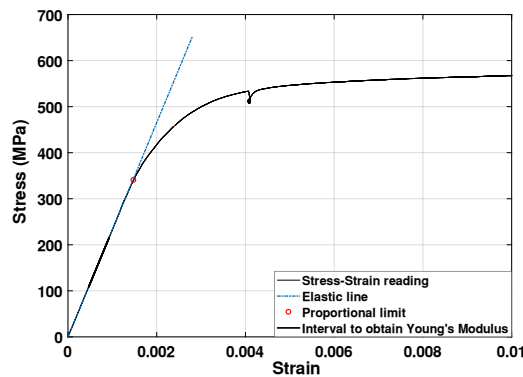
Figure 4-18 A typical dynamic curve

In summary, the procedure for obtaining static material properties include the following steps:

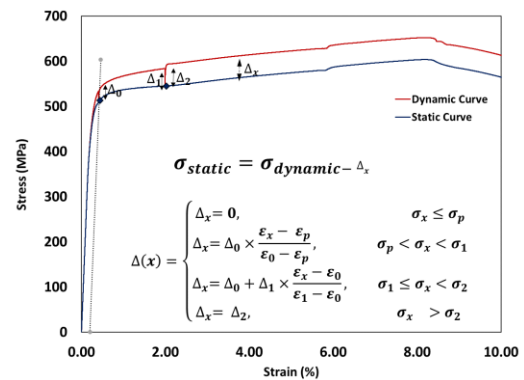
1. A moving average filter is applied to smooth out short-term fluctuation. Then, the true stress-strain curve is calculated from the engineering stress-strain curve. The dimension of the cross-section for flat coupons was measured using the Vernier digital caliper. However, due to the corner coupon's curvature, the area of corner coupons was computed by the weight and density method.



2. The material yield strength is determined by the 0.2% strain offset method. An initial young's modulus ( $E$ ) is assumed based on Eurocode 1993-part 1 (EC3-1-1) [17] recommendation to compute the 0.2% proof stress. Based on the recommendation of [35], a stress interval of 20-45% of the 0.2% proof stress is considered to evaluate the young's modulus (see Figure 4-19). Afterward, the new yield stress is computed based on the new Young's modulus.
3. The proportional limit is determined at the separation of a straight line with the slope of the elastic portion of the curve and the stress-strain curve, as shown in Figure 4-19.
4. The static stress-strain curve is obtained by dividing the original curve into three segments, as shown schematically in Figure 4-19. The first part is from origin up to the proportional limit ( $\sigma_p$ ). The second part is obtained by reducing the stress proportionally from  $\sigma_p$  up to the yield point. The third part is derived from the first drop point to the second drop point, and the stress is reduced in proportion with the corresponding strain. The last part of the curve is plotted, reducing the stress constantly by the same amount of static drop at the second point.



a)



b)

Figure 4-19 a) Determination of Young's modulus b) obtaining a static curve from a dynamic curve

## **4.6 Pin-ended column tests**

### **4.6.1 Introduction**

The full-scale testing of columns provides essential information, both on the maximum strength and the load-deformation characteristics of the particular section tested. Results can be used to establish column curves for design purposes and to provide calibration of analytical models to be used subsequently for parametric studies. A total of 21 global flexural buckling tests are carried out at the University of Federico II, Department of Structures for Engineering and Architecture. The experimental tests include both RHS and SHS for steel grades 275 and 355. All test specimens fulfill the requirements of the cross-section class 1. Thus, no local buckling occurred before global buckling in the test.

### **4.6.2 Test configuration and procedure**

All pin-ended column tests were performed with the ITALSIGMA machine, which could accommodate columns up to 3000 mm and a maximum of 3000 KN capacity. The pin-ended column machine is shown in the picture and schematically in Figure 4-20.

All columns were tested between pinned bearings. The column length specified in Table 4-1 and Table 4-3 ( $L_{eff}$ ) used in all column strength calculations is the distance between pinned bearing centers. Consequently, it is equal to the specimen length plus two end plates and the pin's radius at each end. The ends of the tested columns were milled flat and welded to the ended plates designed for the maximum possible force. For each specimen, the bolts and end plated were designed individually. Figure 4-20 shows the constructed profiles for the buckling test.

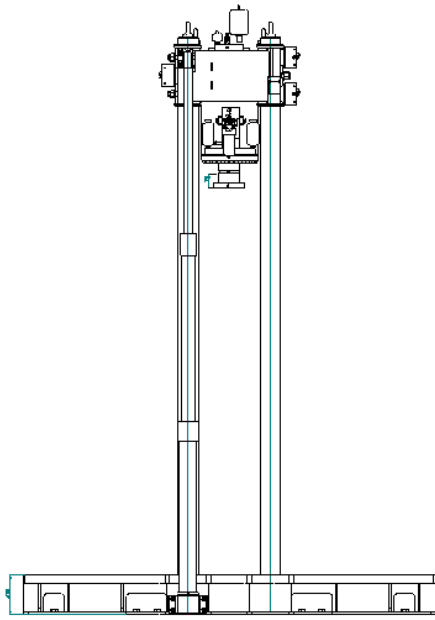


Figure 4-20 left: Schematic view Right: Column test machine



Figure 4-21 Hollow sections profiles with end plates

Instrumentation for each column test consists of five linear voltage displacement transducers (LDTV), two on the bottom plate and three along with the column height at the middle, 25%, and 75% of the height. The load and specimen axial deformation were recorded by the machine operational system continuously. The test procedure is designed to apply the axial load at a rate of 0.3 mm /min until failure, using a boundary condition with pinned ends ( $k=1$ ). In order to simulate simple support at both ends, special plates with slots in which cylinders will be inserted are fabricated. Figure 4-22 shows the special plate with slots. This configuration provides hinge support conditions in one direction and fixed support conditions in the perpendicular direction, so the flexural buckling always occurs to the hinge direction. Figure 4-23 shows the column assembly in the hydraulic press during the tests, with the LDTVs positioned at different points.



Figure 4-22 Special end plates

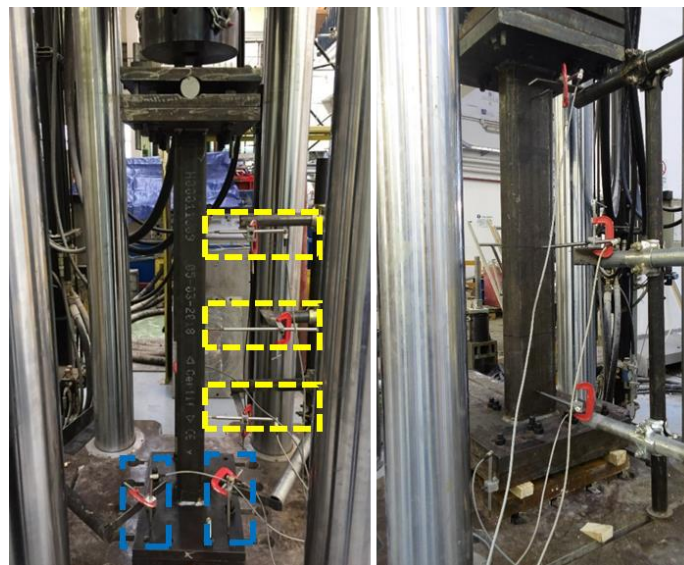


Figure 4-23 Test configuration and LDTV layout

## 4.7 Results and Discussion

### 4.7.1 Geometric imperfection

The dimensions of all cross-sections were measured according to EN-10219-2 [36]. The external corner radius is calculated as the average of the corner width (see Figure 4-5).

Figure 4-24 shows the normalized thickness measurements compare to tolerances of EN102019 [36]. The error bars show the maximum and minimum values within these measurements.

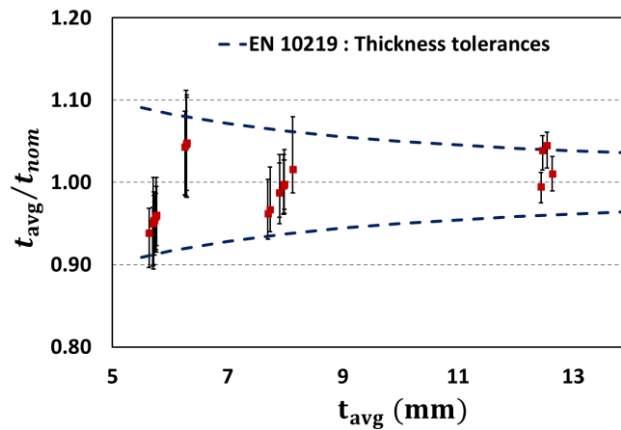


Figure 4-24 Measured thickness compared to EN10219 tolerance

The judgment of the corner radius is more challenging compare to thickness. In practice, the widths of the corner area are measured instead of the corner radius itself. Figure 2 24 shows the normalized measurements by the average thickness along with the allowable tolerance. It is obvious that there is a large scatter in the widths. The error bars show one standard deviation above and below the mean value. The deviation of widths within a single section can be significant. However, in terms of average, nearly all the sections satisfy the limit sets by the EN10219.

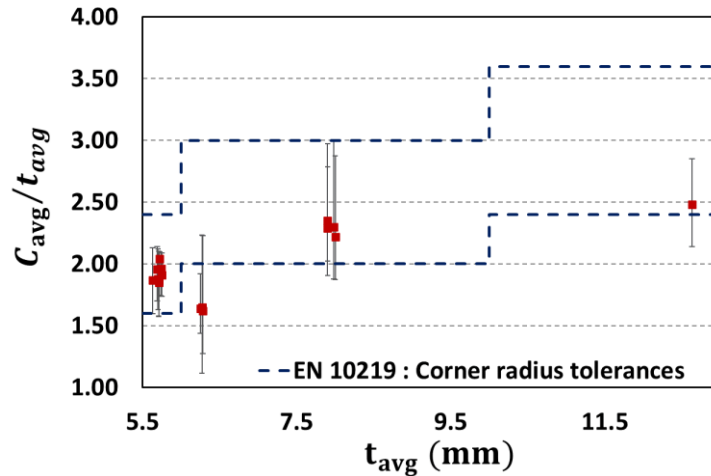


Figure 4-25 Average of measured corner area widths compared to tolerances set in EN 10219

In Eurocode 3-part 8 [37] clause 4.14, sets criteria for the welding in the cold-formed zones or adjacent to them. According to this clause, welding may be carried out within a length  $5t$  either side of a cold-formed zone provided that one of the following conditions is met [37]:

- the cold-formed zones are normalized after cold-forming but before welding;
- the  $r/t$ -ratio satisfies the relevant value obtained from Table 4.2 in [37].

the second condition is compared against the external measured corner radius to the section's average thickness in Figure 2 25. It is observed that the criteria are fulfilled for the investigated section. However, according to the same clause these criteria can be ignored if the thickness of the section is less than 12.5 and is Al-killed with a quality J2H.

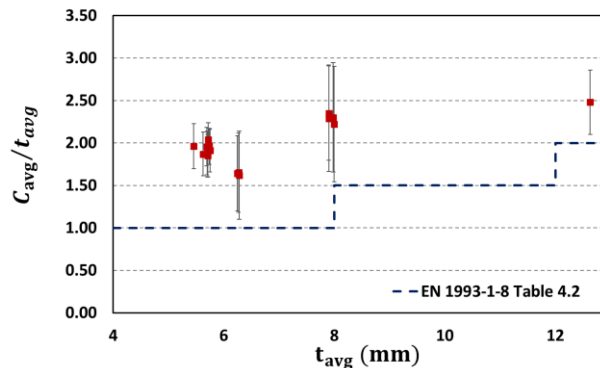


Figure 4-26 Evaluation of measured corner radius dimensions against limitation to welding in the cold-formed

The following conclusion can be drawn from the measurements of geometrical dimensions:

- The overall dimensions of the sections fulfilled tolerance in the product standard EN10219.
- The average values of the thickness are well within the requirement of the standard.
- On average most of the sections satisfy the criteria for the corner. However, the variation in the corner radius is more pronounced compared to the thickness.

### 4.7.2 Out-of-Straightness

As discussed above, the longitudinal imperfection is measured. The maximum magnitude of the out-of-straightness for each section in each direction is given in Table 3-4 where  $L^*$  is the specimen length, and  $x$  is in the direction of the longer dimension if it is a rectangular section.

Table 4-4 Column out-of-straightness measurements

SECTION	Specimen Length $L^*$ (mm)	Max. out of straightness $\Delta_0$ (mm)		$\Delta_0/L^*$	
		X axis	Y axis	X axis	Y axis
		S355_200×100×12.5_A	2700	0.674	1.8067
S355_220×140×8_A	2000	0.446	0.957	1/4477	1/2087
S275_60×6_A	1200	0.303	0.512	1/3959	1/2343
S355_200×8_B	2750	0.700	1.265	1/3928	1/2174
S275_60×6	1200	0.16	0.158	1/7454	1/7573
S275_50×6	1200	0.0922	0.100	1/13012	1/11989
S355_50×6	1200	0.0844	0.0324	1/14208	1/37027
S275_100×8	1200	0.130	0.0485	1/9211	1/24710
S355_100×8	1200	0.111	0.0410	1/10750	1/29241
S355_200×8	1200	0.255	0.0853	1/4698	1/14064
S275_60×40×6	1200	0.0783	0.129	1/15323	1/9275
S355_70×50×6	1200	0.0829	0.151	1/14465	1/7949
S355_200×100×12.5	1200	0.0552	0.191	1/21735	1/6275
S355_220×140×8	1200	0.0980	0.357	1/12233	1/3361
S355_200×120×12	1200	0.205	0.143	1/5852	1/8373

A lognormal distribution is fitted to the data. This has been justified by conducting a Kolmogorov-Smirnov goodness-of-fit test. The K-S test compares the observed cumulative frequency and the CDF of an assumed theoretical distribution. Here, a 5% significance level is considered to accept or reject the proposed distribution. The math is omitted here, but the test is illustrated in Figure 4-27.



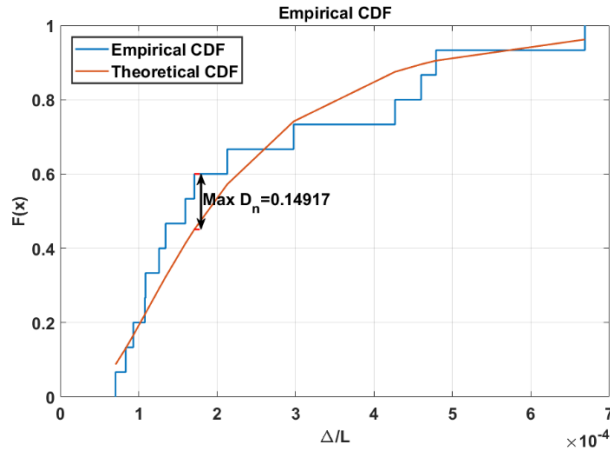


Figure 4-27 K-S test for the observed data

The imperfection magnitude corresponds to the different probability of non-exceedance is listed in Table 4-5. The cumulative distribution function (CDF) values are written as  $P(\Delta < (1/\alpha) \times L)$  and indicates the probability of having an imperfection,  $\Delta$ , less than a specific value  $L/\alpha$ . Table 4-5 indicates that the commonly adopted amplitude of geometric imperfection (i.e.,  $L/1000$ ) in the literature corresponds to the 99% CDF probability.

Table 4-5 CDF values for the maximum imperfection

Probability	$\alpha$
0.25	8694
0.5	5355
0.75	3299
0.95	1643
0.99	1007

### 4.7.3 Material Properties

The tensile stress-strain behavior and ductility around the cross-sections of the investigated RHS and SHS specimens were obtained through tensile coupon tests. The key test results from the tensile coupon test are presented and discussed in this section. The yield stresses are determined by the 0.2% stress offset method, which is the stress at which 0.2% of plastic deformation occurs. Figure 4-28 shows the generic representation of 0.2% proof stress.

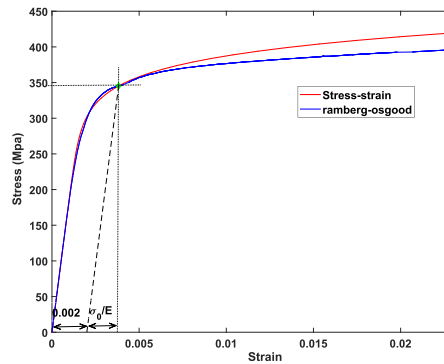


Figure 4-28 Generic representation of the stress-strain curve using the 0.2% proof stress

Figure 4-29 shows a typical fracture of the flat, curve, weld and transversal coupons.

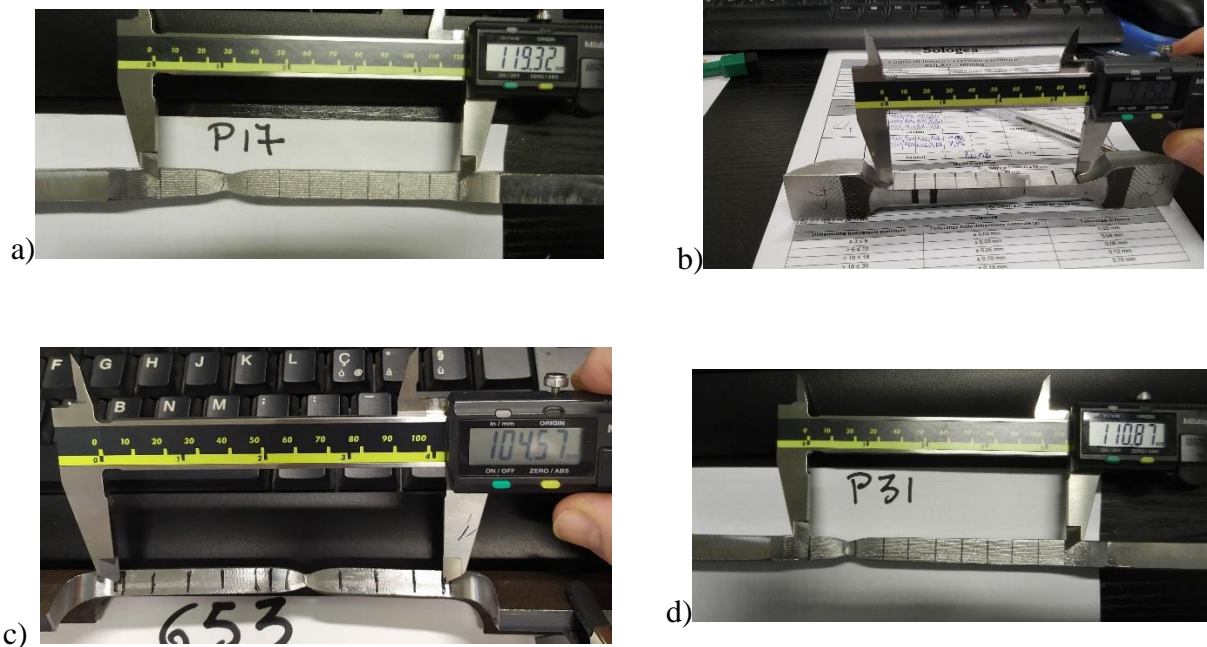


Figure 4-29 typical fracture of a) Flat b) Transversal c) Corner d) Weld coupons

Comparisons of typical flat and corner tensile coupon test results from specimen S355\_200×200×8 is shown in Figure 4-30. The tensile stress-strain curves of all coupons can be found in Appendix B.

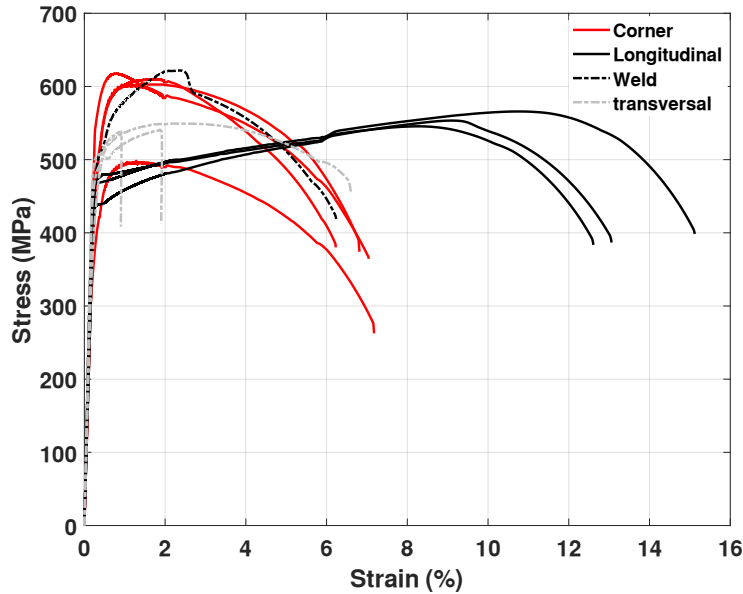


Figure 4-30 Summary of coupon test results for section S355\_200×200×8

To investigate the effect of strain rate on the strength parameters of material, the database is classified into different groups. In all plots in Figure 4-31, the vertical axis is the reduction in stress during the stress relaxation (i.e., 60 sec) in percent. In the first row of Figure 4-31 results are divided based on the extracted coupons' location, while in the second row, the results are separated based on the steel grade of the specimens. The following observation can be made from Figure 4-31.

- The second drop is slightly more than the first one for flat and corner coupons.
- The static drop for the transversal and weld coupons is not sensitive to the location of the stop on the stress-strain curve.
- Reduction in yield stress (i.e., first drop) due to strain rate effect decreases as the steel grade increase, whereas the opposite is true for the second drop (Figure 4-31 (c and d)). The same pattern can be observed for corner coupons too.
- The current BSI and ASTM standards systematically overestimate the material strength parameters such as  $\sigma_y$  and  $\sigma_u$  by 5% and 5.68%, respectively, on average. The maximum difference is 7.7% and 9.1% for flat and corner coupons. It is important to remember that the strain rate

considered in this study was below the recommended lower bound of the investigated standards (see Fig. 8). This error is expected to be more pronounced when the upper bound of the recommended range is used.

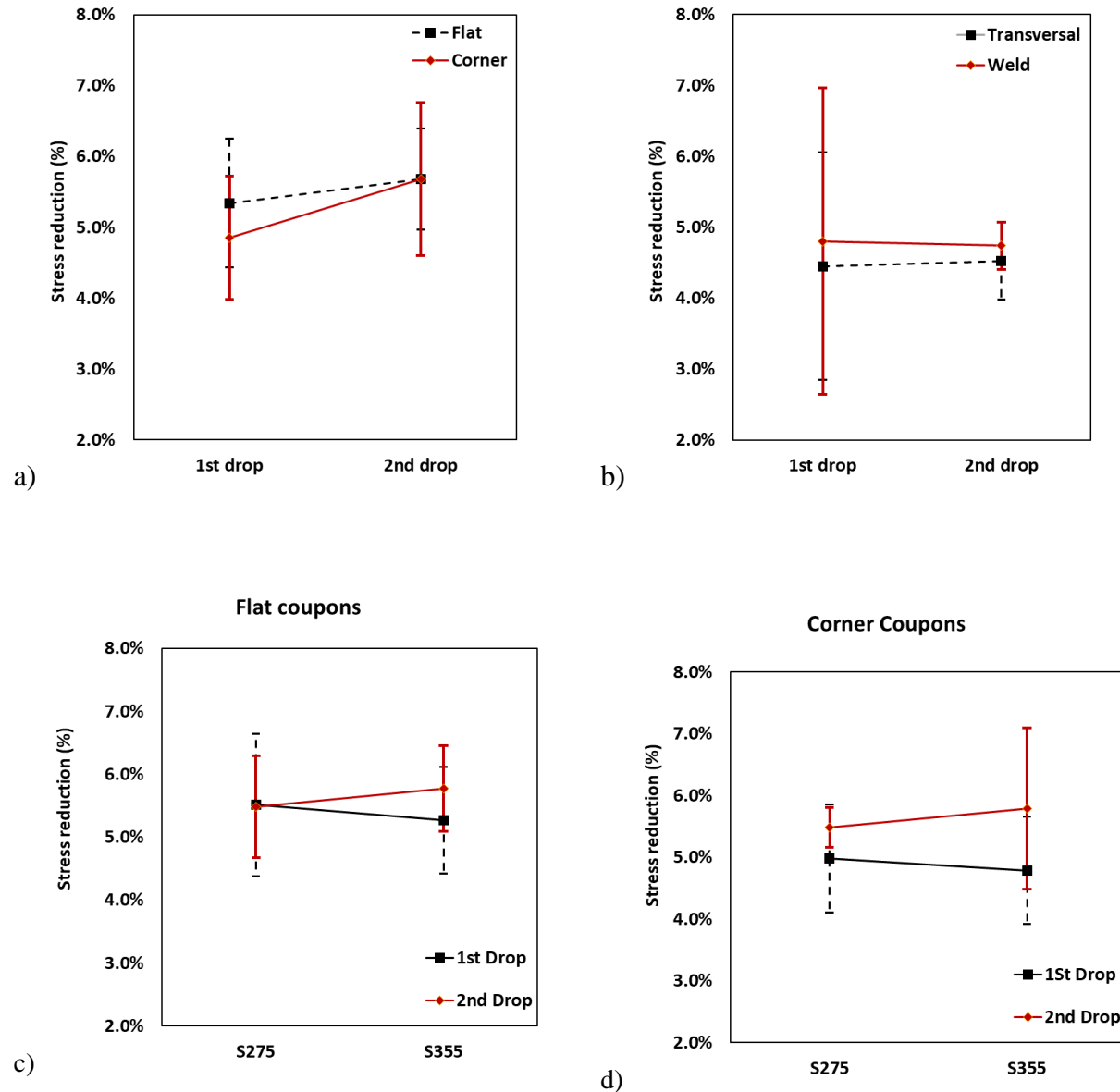


Figure 4-31 Average stress reduction with (+/- SD) for a) flat and corner coupons b) transversal and weld coupons c) flat coupons divided by steel grade d) corner coupons divided by steel grade

Ductility is defined as the deformation at ultimate stress over the deformation at yield stress. The average ductility of the different coupons type is shown in Figure 4-32. It should be noted that in some cases, it was impractical to extract a transversal coupon due to the dimension of the section.

Also, in a few tests, a premature failure occurred in the griped length, causing spurious reduced ductility, which was excluded from the results.

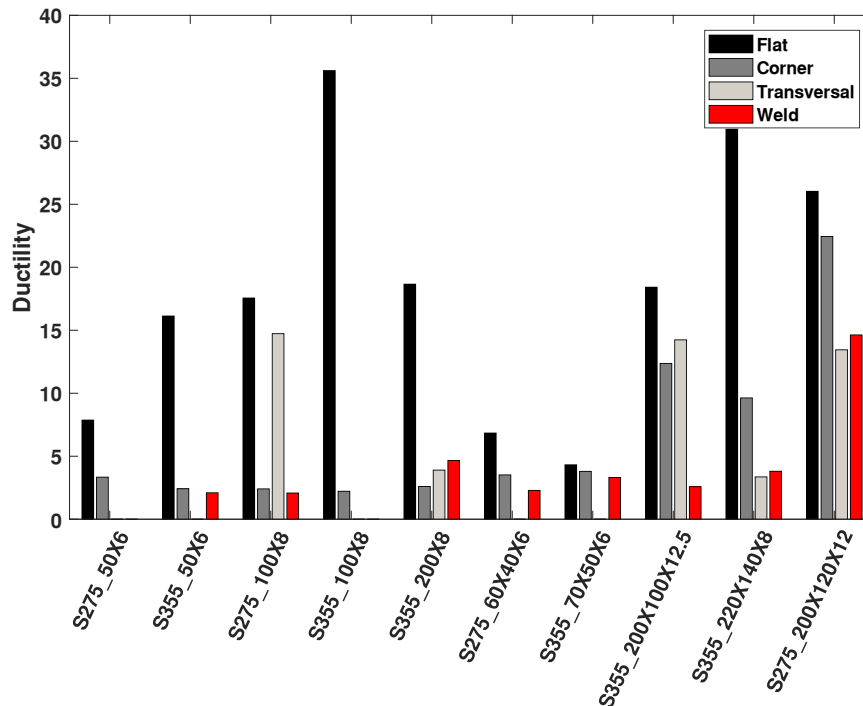


Figure 4-32 Ductility of tested coupons for the different cross-sections

The following observation can be made:

- In all cases, the flat coupon shows more ductility than the corner coupons. On average, the ductility in flat coupons is 4.8 times the corner coupons. This is mainly because that the degree of cold-forming in corners are more significant than the flat part
- In room temperature, the stress-strain curve of the longitudinal weld has similar ductility (also shape, see Figure 4-30) to those of the corner coupons.

It is also interesting to note that visual inspection of the transversal coupons reveals that the zone containing the weld is not the weakest position. In all cases, for transversal coupons, fractures are initiated from the non-welded part.

The key test results from the tensile coupon tests are summarized and compared to the nominal values in Table 4-6 and Table 4-7. The material yield strength is taken as the 0.2% proof stress method.

Table 4-6 Tensile coupon test results for yield stress

Section ID	Flat			Corner	
	$f_{y,nom}$	$f_{y,avg}$	$(f_{y,avg}-f_{y,nom})/f_{y,nom}$	$f_{y,avg}$	$(f_{y,avg}-f_{y,nom})/f_{y,nom}$
	[MPa]	[MPa]	(%)	[MPa]	(%)
S275_50×6	275	471.0	71%	471.3	71%
S355_50×6	355	481.9	35%	524.7	48%
S275_100×8	275	454.1	65%	505.0	84%
S355_100×8	355	453.4	28%	542.2	53%
S355_200×8	355	463.8	31%	536.1	51%
S275_60×40×6	275	470.6	71%	510.6	86%
S355_70×50×6	355	429.7	21%	477.5	34%
S355_200×100×12.5	355	535	51%	523.0	47%
S355_220×140×8	355	445.6	26%	521.9	47%
S275_200×120×12	275	363.2	32%	400.3	46%

Table 4-7 Tensile coupon test results for Ultimate stress

Section ID	Flat			Corner	
	$f_{u,nom}$	$f_{u,avg}$	$(f_{u,avg}-f_{u,nom})/f_{u,nom}$	$f_{u,avg}$	$(f_{u,avg}-f_{u,nom})/f_{u,nom}$
	[MPa]	[MPa]	(%)	[MPa]	(%)
S275_50×6	430	503.7	17%	492	14%
S355_50×6	510	525.2	3%	565.2	11%
S275_100×8	430	509.3	18%	553.4	29%
S355_100×8	510	532.0	4%	554.8	9%
S355_200×8	510	554.9	9%	582.5	14%
S275_60×40×6	430	501.2	17%	542.6	26%
S355_70×50×6	510	518.5	2%	557.5	9%
S355_200×100×12.5	510	601.6	18%	616.1	21%
S355_220×140×8	510	598.1	17%	597.7	17%
S275_200×120×12	430	485.5	13%	503.1	17%

Where the subscript of “avg” stands for the average of the strength parameter measured from the coupon tests. The virgin (before cold-forming) material strength parameters were available from company certificates. Based on this information, all coupons' strength parameters are compared to the corresponding virgin parameters in Figure 4-33. This figure shows the increase in yield and ultimate strength as a function of local slenderness ratio and the measured yield stress from the tests.

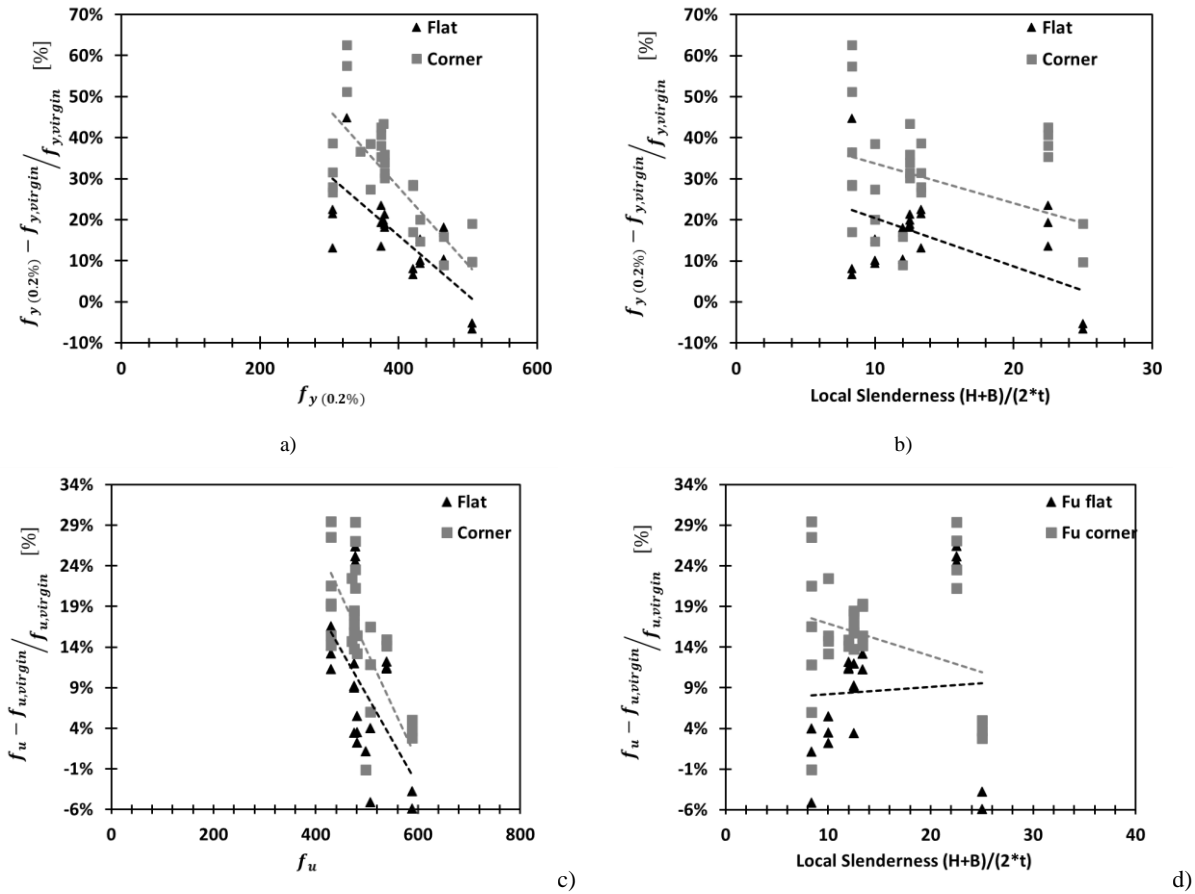


Figure 4-33 Comparison of the strength parameters of the test to the virgin material

The following observation can be made:

- The increase in yield strength reduces as the local slenderness ratio increases.
- There is no evident relationship between the local slenderness ratio and the ultimate strength enhancement.
- The effect of cold-forming for both flat and corner coupons is fading away by increasing the yield stress.

EC3-1-3 gives supplementary rules for cold-formed members; however, in the scope of this standard, it states that this part does not apply to rectangular hollow sections for which reference should be made to EC3-1-1. In EC3-1-1, clause 3.2.2, gives the ductility requirements for steel material. The minimum ductility required by this standard is expressed in terms of the following limits:

- $f_u/f_y > 1.1$ ;
- elongation at failure not less than 15%.
- $\epsilon_u \geq 15 \times \epsilon_y$

Figure 4-34 shows the first and third criteria using a box plot. On each box, the central mark (i.e., red line) indicates the median, and the bottom and top edges of the box indicate the 25th and 75th percentiles, respectively. The whiskers extend to the most extreme data points not considered outliers, and the outliers are plotted individually using the '+' symbol.

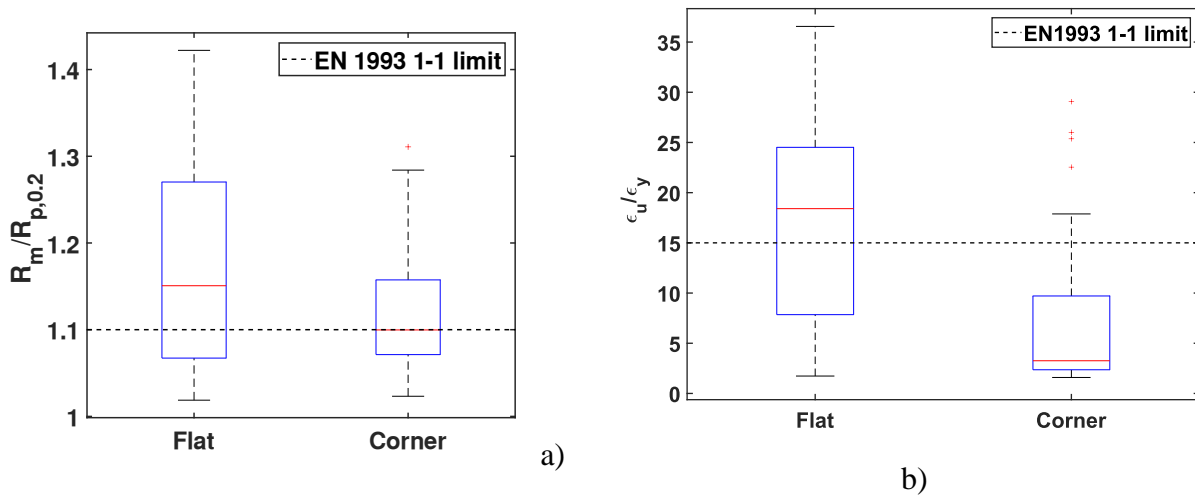


Figure 4-34 EC3-1-1 ductility requirement for steel a) hardening ratio b) ductility

Table 4-8 Characteristic value of the hardening ratio and ductility

Criteria	flat	corner
$\epsilon_u \geq 15 \epsilon_y$	6.19	1.27
$f_u/f_y > 1.1$	0.98	1.011

It should be noted that the elongation at failure criteria in EC3- 1-1 is given on a gauge length of  $5.65\sqrt{A_0}$ . The gauge length of the coupons tested in this study is fixed at 100 mm. There are some conversion factors for converting different gauge lengths to other gauge lengths at room temperature. However, these factors do not apply to cold-reduced steels.

The following observation can be made from Table 4-8:

- On average, flat coupons and corner coupons satisfy the hardening criteria based on the EC recommendation.



- For the ductility criteria, the corner coupon does not fulfill the limit on average, while the flat coupons meet the limit.
- The cold-formed process changes the stress-strain curve dramatically. Based on characteristic value, none of the requirements for the ductility of steel is fulfilled.

Therefore, based on these observations a plastic analysis of the CFHS column may be questionable and further investigation of the matter is advisable. As discussed in the first chapter, the R-O model is extensively used for numerical modeling of rounded stress-strain material behavior. It is shown that a two-stage R-O model can accurately describe cold-formed stress-strain response using equation (2-4).

The key statistical assessment of the two hardening exponents (i.e., n and m) are provided in Table 4-9. Although most researchers utilize the R-O model for numerical modeling, the Giuffrè-Menegotto-Pinto steel material known as Steel02 in OpenSees is used in chapter four for safety assessment. This material model is also capable of simulating a rounded stress-strain response. Thus, the statistical values for the input parameters of this model are also presented in Table 4-9

Table 4-9 Statistical values for the input parameters of R-O and Steel02 material

	R-O				Steel 02			
	Flat		Corner		Flat		Corner	
	n	m	n	m	R <sub>0</sub>	b	R <sub>0</sub>	b
Mean	13.92	2.41	7.07	5.38	3.2	0.0042	3	0.0081
CoV.	27%	52%	25%	40%	21%	43%	16%	79%

The relation between  $f_u/f_y$  ratio with yield strength is shown in Figure 4-35. The figure clearly shows an inverse relationship between  $f_u/f_y$  ratio and the yield strength as other researchers have reported. Using regression analysis, a new expression is proposed for predicting the ultimate strength based on yield strength (equation (4-3)).

$$f_u/f_y = 0.83 + 203.8/f_y \quad (4-1)$$

$$f_u/f_y = 1 + (130/f_y)^{1.4} \quad (4-2)$$

$$f_u/f_y = 27.85 \times \left(1/f_y\right)^{0.515} \quad (4-3)$$

For comparison purposes, the empirical relationship proposed by Fukumoto [38] and Gardner [7], as given by equations (4-1) and (4-2), respectively, are also plotted in Fig. 13. Equation (4-1) is overestimating the ratio consistently for cold-formed steels. Equation (4-2) improves the prediction for cold-formed steel; however, it overestimates  $f_u/f_y$  ratio as the yield strength increases. It should be noted that the proposed equation is only applicable for steel grades of S275 and S355, while the applicability of equation (4-2) is for steel 340 N/mm<sup>2</sup> to 1200 N/mm<sup>2</sup>.

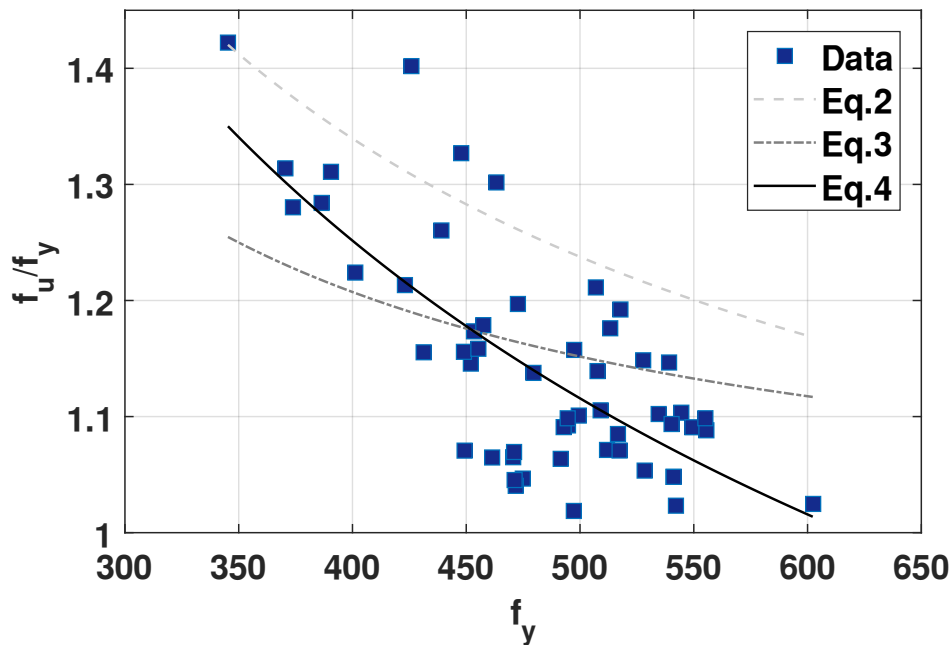


Figure 4-35 Comparison of the proposed equation to the tests data

#### 4.7.4 Pin-ended column test results

Most of the specimens failed in overall flexural buckling about the minor axis of their cross-sections. The relationship between the axial load and the axial deformation of section S355\_70×50×6\_A is shown in Figure 4-36 as an example. It also shows the failure mode of the test specimens.

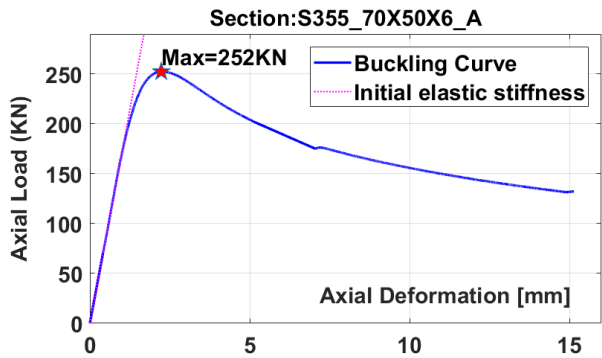


Figure 4-36 left) Load versus axial deformation Right) Failure mode

In order to evaluate the actual boundary conditions that occurred in the tests, the results obtained with the displacement transducers are presented and discussed. Figure 2 37 illustrates the results of the lateral displacements of three selected points along with the column height for various applied load magnitudes. These results were acquired with the aid of three displacement transducers positioned at three points along with the column height, as discussed in the previous section. Figure 4-37 illustrates these curves for the specimen S355\_100×8\_D

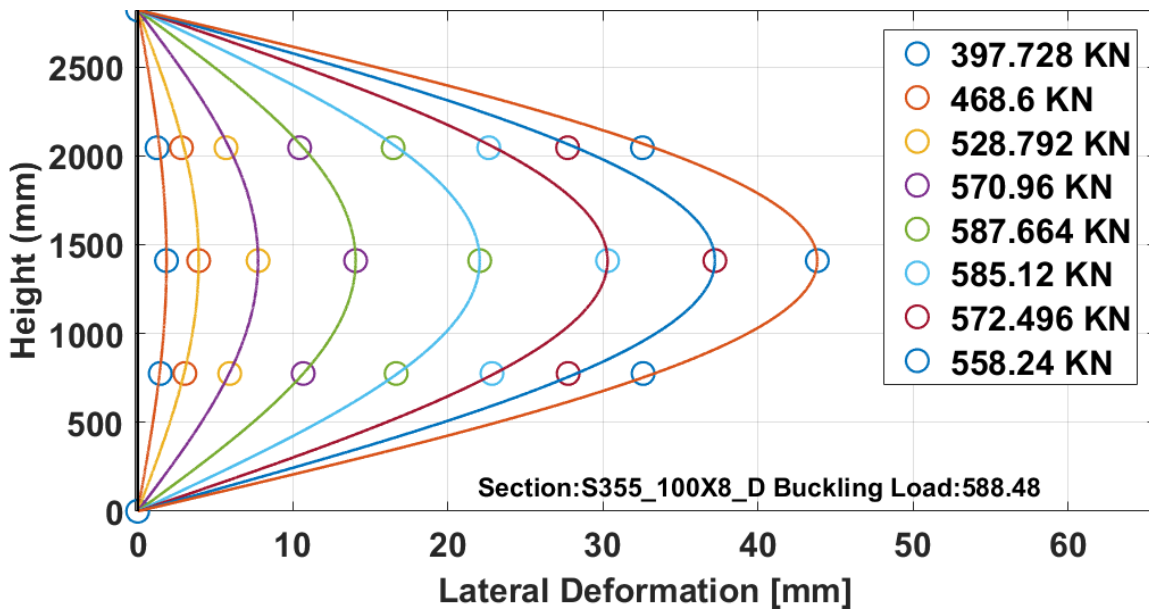


Figure 4-37 Lateral displacement evolution along with the column height

It is observed that before the ultimate load is reached, the curve exhibits a similar behavior associated with a column configuration with hinged support.

From the measured maximum load, the buckling reduction factor is determined by the following equation:

$$\chi_{test} = \frac{P_{test}}{(f_{y,nom} A_{nom})} \quad (4-4)$$

The calculated reduction factor is plotted in **Error! Reference source not found.** along with European buckling curves.

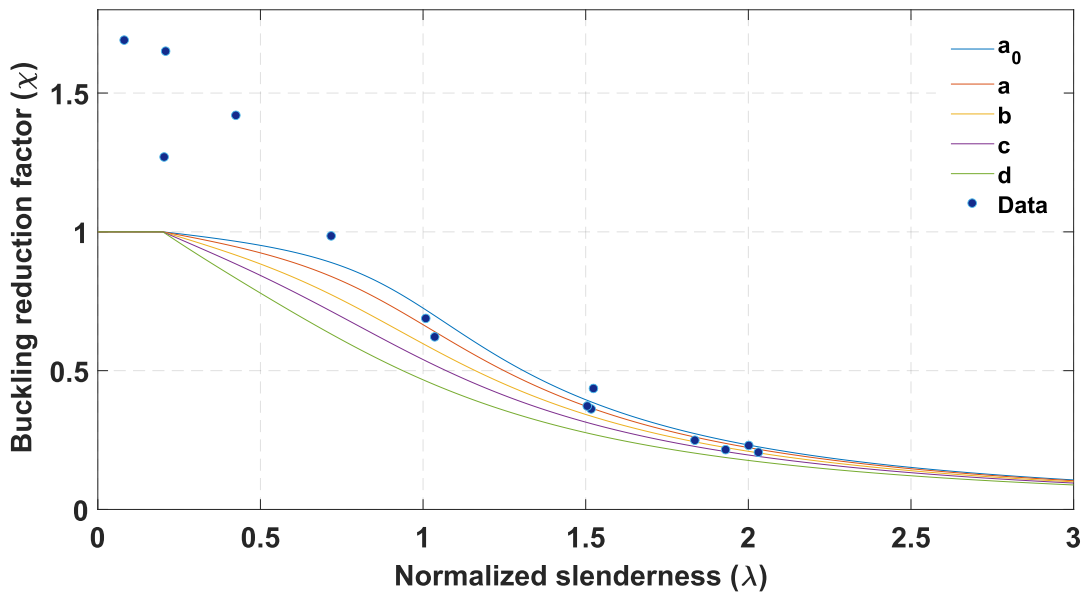


Figure 4-38 Normalized test results with design buckling curves

Figure 4-38 shows that for stocky columns range, a higher buckling curve can be used than curve c. In order to evaluate the results in more detail,

Table 4-10 summarizes the comparison of the reduction factor from test results with different design buckling curves. Furthermore, the buckling curve formula in American code [39] is also presented in the form of a reduction factor by the following equation:

$$\begin{aligned} \chi &= 0.658 \lambda_n^2, \quad \lambda_n \leq 1.5 \\ \chi &= \frac{0.877}{\lambda_n^2}, \quad \lambda_n > 1.5 \end{aligned} \quad (4-5)$$

Table 4-10 Comparison between test results and different buckling curves

Section ID	Test Result $\chi$	European Code			American Code
		Curve a	Curve b	Curve c	$\chi/\chi_{b,AISC}$
		$\chi/\chi_{a,EC}$	$\chi/\chi_{b,EC}$	$\chi/\chi_{c,EC}$	
S275_60×40×6_A	0.699	1.08	1.20	1.33	1.08
S275_60×40×6_C	0.233	1.08	1.14	1.22	1.10
S275_60×40×6_D	0.443	1.25	1.36	1.48	1.21
S275_50×6_A	0.366	1.01	1.10	1.20	0.97
S275_100×8_B	1.434	1.51	1.56	1.61	1.54
S355_100×8_D	0.609	0.92	1.03	1.14	0.93
S355_70×50×6_A	0.592	0.93	1.04	1.15	0.94
S355_70×50×6_B	0.627	0.99	1.10	1.22	0.99
S355_70×50×6_C	0.999	1.20	1.30	1.41	1.25
S355_200×100×12.5_B	1.224	1.32	1.38	1.45	1.36
S355_220×140×8_B	1.215	1.22	1.22	1.23	1.24
S355_70×50×6_D	0.217	0.93	0.99	1.06	0.94
S355_70×50×6_E	0.286	0.81	0.87	0.95	0.78
S355_50×6_C	0.374	1.02	1.11	1.20	0.97
S355_50×6_D	0.205	0.95	1.01	1.08	0.97
S355_100×8_C	1.064	1.15	1.21	1.27	1.18
Mean		1.09	1.16	1.25	1.09
SD		0.18	0.17	0.17	0.19

The following observation can be made from

Table 4-10:

- All of the test results are higher than the corresponding column buckling curve (curve c) for cold-formed sections.
- On average, curve c underestimates the buckling load by 25%
- The American code yields a more realistic prediction of the buckling load on average. However, in a few cases, the buckling resistance falls below the buckling curve.

These results give an overview of the performance of the current buckling curve and indicates an underestimation of the flexural buckling resistance in general.

# 5 Finite element analysis

## 5.1 Introduction

This chapter presents the development of two finite element model (FE) based on the experimental data. The first part of the chapter discusses a Micro FEM. Numerical simulation performed using the commercial software ABAQUS [40]. This software provides almost all types of FE analysis. The model's development is presented in this chapter, and the results are validated with the measured responses from the laboratory tests. Three key features are considered in the model: geometrical imperfection, residual stress, and the material's mechanical behavior. This model is used to run a parametric study of different variables on the buckling curve in detail. While a second model (macro-model) is also developed and verified in OpenSees [41] for running numerous numerical simulations. It is worth mentioning while software such as Abaqus are very powerful and can model a phenomenon in detail, they require considerable computational time compared to a macro model.

Advancement of knowledge and substantial developments in computational technology have made more realistic 3D model possible. Although capturing an accurate response of the experimental test is intended, the model's computational cost is also important.

## 5.2 Micro Model

### 5.2.1 Description of the micro FEM

The procedure of the FE-analyses of this report was divided into two types of analyses depending on requested output data: a buckling analysis and a second order post-buckling analysis. The differences between them are specified in the step manager in which the designer can request which analysis Abaqus will perform and what data outputs should be generated. Within each of the two models, there are two stages: the initial and the analysis specific. The support and load conditions are applied in the latter. The first analysis type is called Linear perturbation, Buckle and was used for the buckling analysis. This analysis includes a linear perturbation procedure and may also be referred to as an eigenvalue buckling analysis, which will be used to estimate the critical

buckling load (bifurcation load). Secondly, for the second-order buckling analysis (or post-buckling analysis), an analysis type called dynamic implicit is used. This analysis type is suitable to obtain the limit load for structures that experience unstable collapse. It is possible to include geometrical and material non-linear collapse.

### 5.2.2 Geometry and Boundary conditions

The geometry of the column is identical to the test specimens described in the previous section. The boundary conditions specified are very similar to the actual boundary conditions of the experimental test, as shown in Figure 5-1.

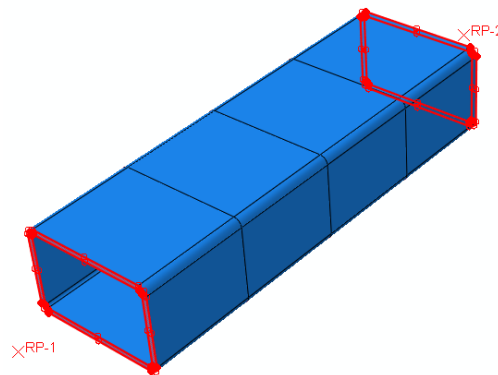


Figure 5-1 Column model boundary condition

Two reference points were defined at the centroids of the cross-sections for the definition of the support conditions. A rigid connection is used between two reference points and two end sections of the column. Pin boundary conditions are imposed on both ends of the specimen to simulate the pinned connections. The rotation of the hinges is permitted only around the weak axis. As shown above, to simulate the test situation, the hinge rotation center is considered farther from the specimen's end. Thus, the critical length of the specimen is always longer than the geometrical length. All three translational displacements of one end of the column are always fixed, while the other end can move along the longitudinal axis to trigger the compression force. The load is applied through displacement control to the column's centerline, which corresponds to the loading situation used in the laboratory test.

### 5.2.3 Finite element mesh

The column is modeled entirely using eight-node reduced integration solid elements (i.e., C3D8R). For selecting the mesh size and scheme, a convergence study based on linear buckling analysis was conducted with different mesh size for uniform and a two-mesh scheme. As can be seen from Figure 5-2 the results are converging by using a finer mesh; however, the computational time increases exponentially with uniform mesh. On the other hand, the two-mesh scheme was computationally efficient while providing good response.

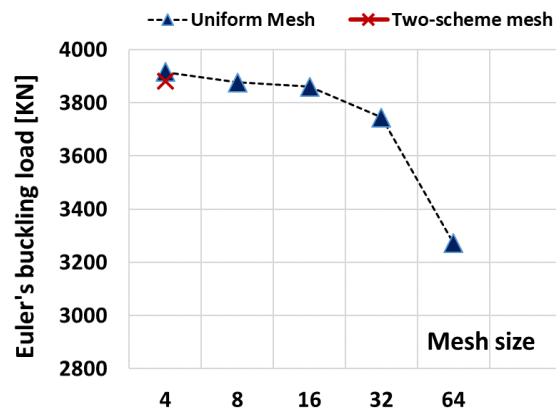


Figure 5-2 Buckling load for different mesh size

The selected mesh scheme helps to increase the computational efficiency of the model. since most of the deformation is concentrated to the middle part of the specimen, a denser mesh is considered in this part as shown in Figure 5-3.

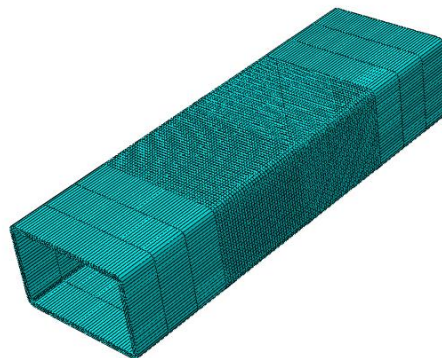


Figure 5-3 Finite element mesh of the model



## 5.2.4 Material Nonlinearity

The material behavior is adopted from the comprehensive coupon tests that have been described previously. For each part of the cross-section, the average of the available results is used. The plastic part of the true stress-strain curve was defined in Abaqus.

## 5.2.5 Linear Buckling analysis

The linear buckling analysis requires solving an Eigen-value problem defined by the column geometric matrices and elastic stiffness. ABAQUS [40] obtains the solution through the sub-space iteration method. In this work, the linear buckling analysis was performed to obtain the mode shapes and the corresponding Eigen-values. The analysis was done by selecting the linear perturbation buckle step in ABAQUS and selecting the number of modes. The displacements of the modes were saved in a node file by modifying the Keywords of the model. The global buckling mode shape, which has the most significant influence on the buckling load and a local mode shape, is shown in Figure 5-4 for specimen S355\_220X140X8. The three modes correspond to minor axis flexural buckling.

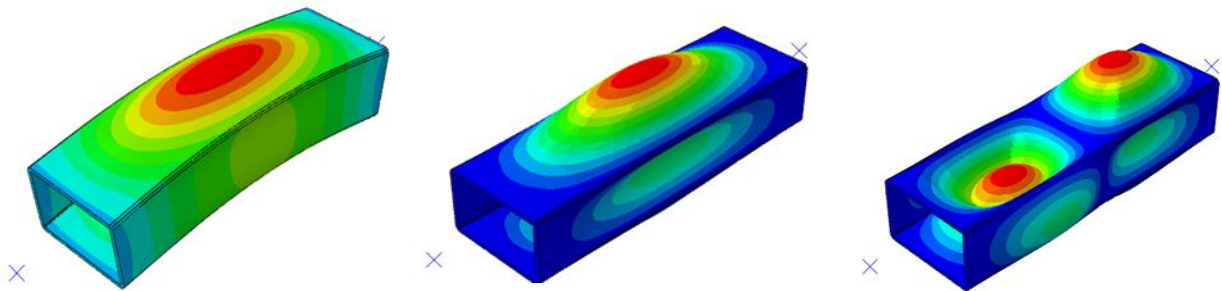


Figure 5-4 Global and local eignemodes

It should be noted that the post-buckling response of a structure with many closely spaced eigenvalues may be highly sensitive to the mesh size and scheme that is imposed on the model. In such cases, a slight change to the mesh can cause significant changes in post-buckling behavior. In the current study, the first eigenvalue is significantly lower than the second mode, so we can safely assume that the first eigenmode will dominate.

### 5.2.6 Geometric imperfections

The initial bow imperfection can be incorporated in the model by defining a linear combination of buckling mode shapes by editing the Keyword of the model [42]. These mode shapes are from the preliminary linear buckling analysis that was discussed previously. The amplitudes of the eigenshapes are scaled to the imperfection magnitudes to be applied in the numerical simulations ( $L/1000$  for global,  $0.7 \times b/1000$  for local imperfections). Previous research results showed that a numerical simulation using global imperfection with an amplitude of  $L/1000$  give appropriate results to the Monte Carlo based column buckling curve development. Therefore, it is used in the current simulations. Because in the parametric study, the global buckling phenomenon is studied, always the global imperfection is considered as the leading imperfection. The local imperfection is considered as the accompanying imperfection, so its magnitude is multiplied by 0.7, according to EN1993-1-5 [22]. However, it should be mentioned that the local imperfection has a minor effect on the calculated flexural buckling resistance

### 5.2.7 Residual stress

The residual stress distribution on cold-formed steel sections significantly depends on the manufacturing process. Considering this, a residual stress model proposed by Somodi [20] is chosen, which has a test-based source. The model has been discussed in section 2.3.4. Figure 5-5 shows the applied residual stresses to the numerical model at the initial state of the analysis.

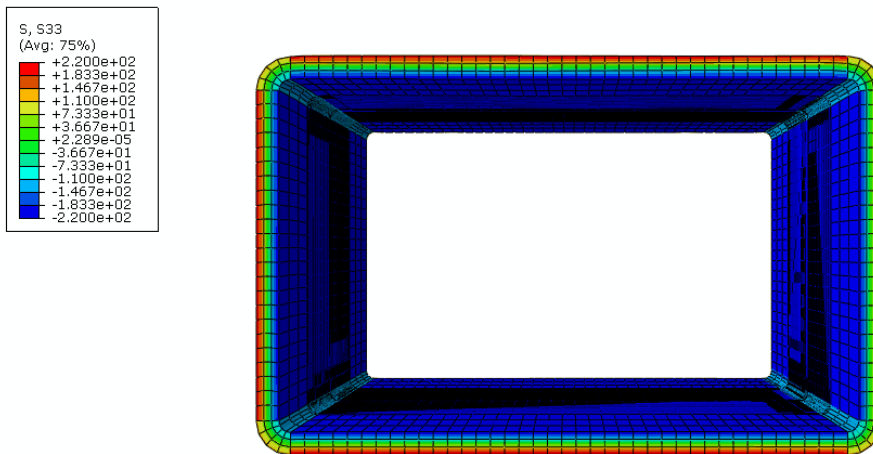


Figure 5-5 applied residual stresses in the numerical model

### 5.2.8 Validation of the numerical models

The numerical model is verified based on the test results. Thus, the applied numerical model should work with high accuracy for different steel grades with different material properties. Two typical failure modes, global and local buckling (the latter occurs after yielding), are presented in Figure 5-6.

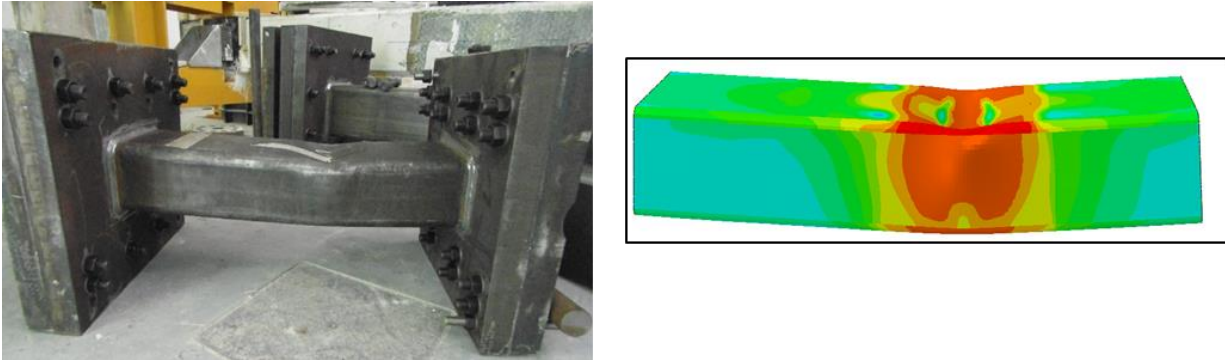


Figure 5-6 Observed failure mode in the numerical model and experimental test

The measured and computed load-axial deformation diagrams are also compared, for one specimen. It can be seen in Figure 5-7. The load-deformation curves show a good agreement between the measured and calculated test results. All the test and numerical simulations buckling curve and deformed shape can be found in appendix B.

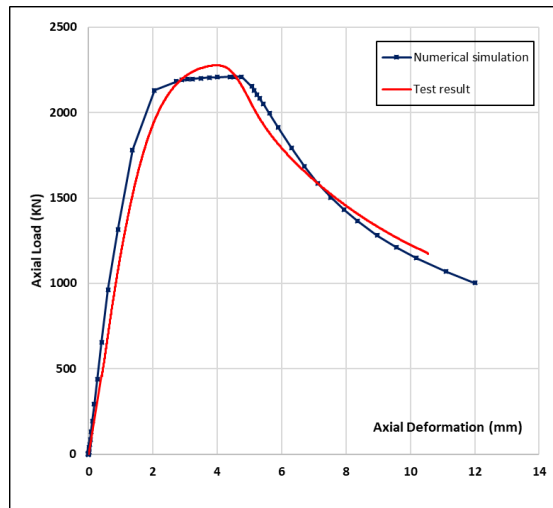


Figure 5-7 Load axial deformation for specimen S275\_100x100x8

## 5.2.9 Parametric Study

In this section, attempts are made to evaluate the effects of different imperfections on the overall buckling behavior of cold-formed steel columns. In total, four different cross-sections, including two rectangular and two squares (220×140×8, 70×50×, 200×8, 100×8) with two different local slenderness ratios, were employed for the parametric study. Also, two steel grades (S 275, S 355) were involved in the parametric analyses.

### 5.2.9.1 Effect of the residual stress

To investigate the effect of the residual stress, four different sections were selected. Two rectangular and two square sections. Each of the square or rectangular sections are representative of different local slenderness ratio. Furthermore, in each case, two different steel grades have been investigated. To understand the effect of residual stress separately, all other imperfections are kept as constant such as geometric imperfection or material behavior. The backbone of the investigation is the comparison of the buckling resistance based on the corresponding buckling curves in the global slenderness range of 0.2–2.0. The numerically determined buckling curves with and without the residual stress model are presented and compared for S275 and S355 material grades, as shown in Figure 5-8. Figure 5-9 shows the results for only rectangular sections, making it easier to interpret. The same interpretation can be seen in square sections. The following observation can be made from the plots:

- The variation of the  $\chi$  factor for all cases, including different steel grades, follows the same pattern. The detrimental effect of the residual stress begins at global slenderness ratio  $\sim 0.4$ . This adverse effect increases drastically until it reaches a pivot point. The corresponding  $\bar{\lambda}$ , for this pivot point is  $\sim 0.85$  and the maximum reduction in buckling strength of the column is 14% and 11% for steel grade S355 and S275, respectively.
- After the pivot point, the effect of the residual stress starts to diminish gradually, as  $\bar{\lambda}$  increases until it approaches an asymptotic value.
- Increasing the steel grade from S275 to S 355 amplifies residual stress on overall buckling strength. However, this amplification is significant for the intermediate slenderness ratio (0.7  $\sim$  1.5). As the global slenderness ratio increases, the effect of different steel grades

becomes insignificant. The result indicates that at most, using S355 decreases the buckling strength of the column by 3% more compare to S275.

- As the local slenderness ratio increases, the buckling resistance of the section is more affected by the residual stress effect.

For very stocky columns, the tension component of the bending residual stress has advantageous effects, since, in order to reach the plastic capacity of the section, first the compression force should overcome this component.

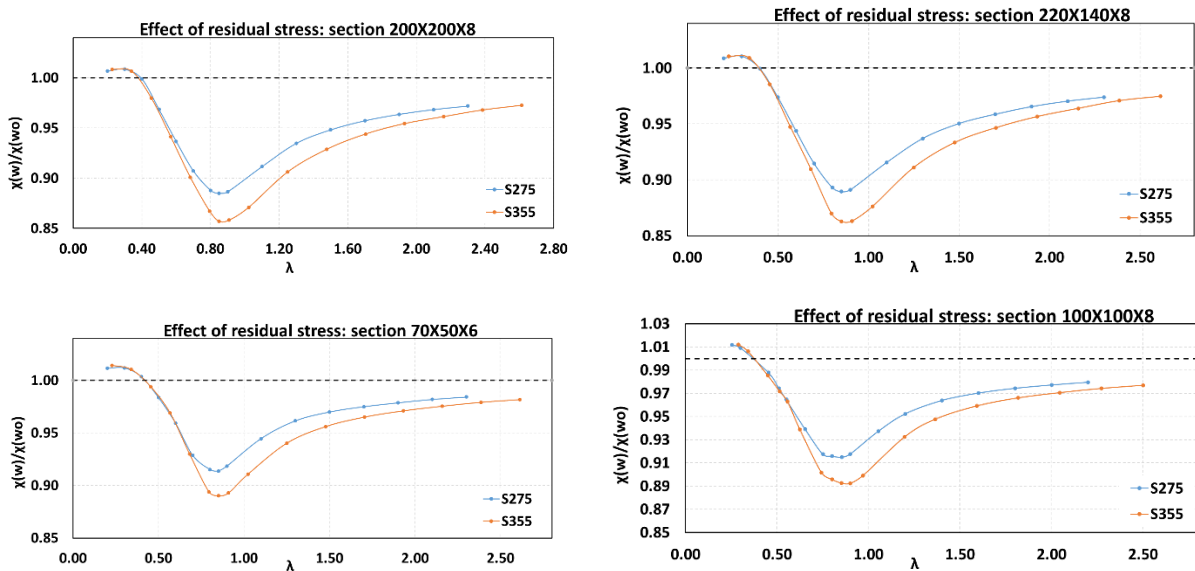


Figure 5-8 Effect of residual stress for different section and different local slenderness ration

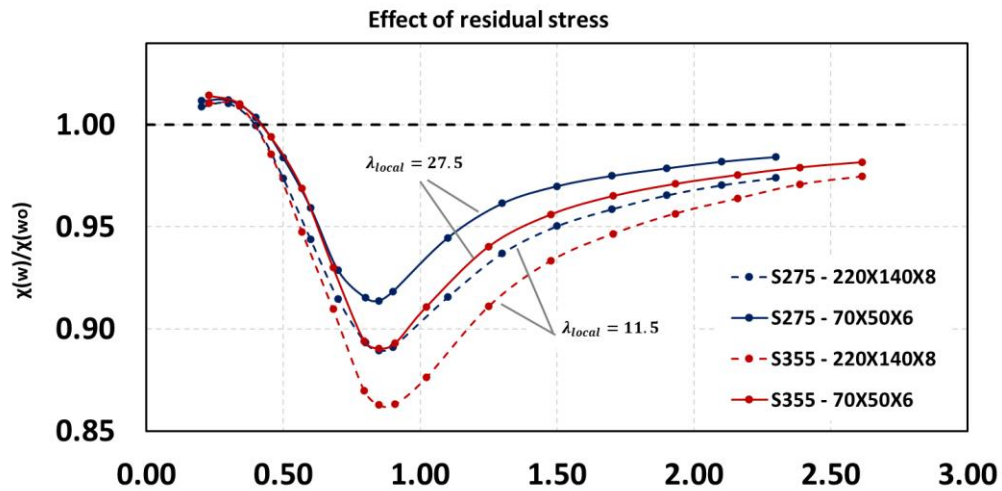


Figure 5-9 Effect of residual stresses

### 5.2.9.2 Effect of Geometric Imperfections

The effect of geometric imperfection is investigated using a hollow section column with cross-sections size of 70×50×6 and 220×140×8, representing different width-to-thickness ratios for two steel grades. Figure 5-10 shows the result for each section individually.

To make the results more readable, the results are presented in Figure 5-11 in one graph. The vertical axis is showing the variation in the reduction factor by increasing the geometric imperfection's amplitude. The main conclusions are as follows:

- For columns with a high slenderness ratio ( $1.5 < \bar{\lambda}$ ) the buckling resistance of the section is not sensitive to the amplitude of the geometric imperfections.
- The effect is relatively less severe for steel grade S355 compared with S275.
- The effect of the geometric imperfection is highest when the global slenderness ratio is about 0.7. In this case, changing the amplitude from 1/1000 to 1/500, reduces the buckling resistance by ~9%.

By increasing the local slenderness ratio, the effect of selecting a higher amplitude as geometrical imperfection is less severe

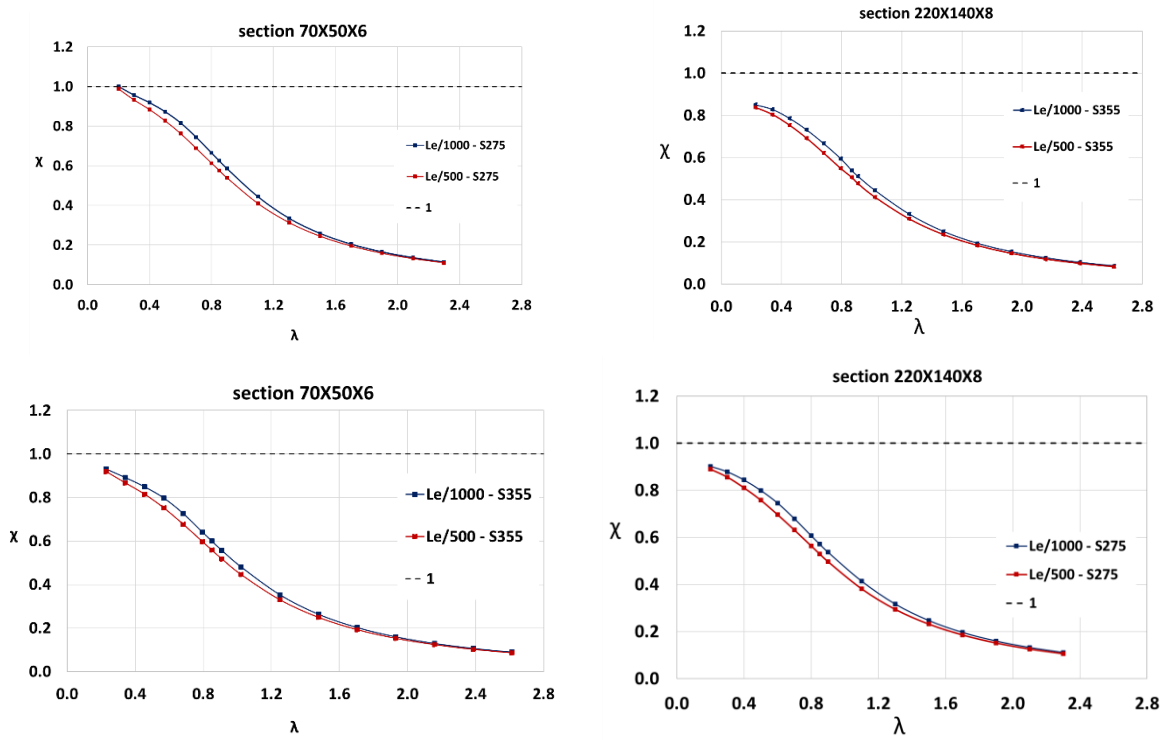


Figure 5-10 Effect of residual stress for different section and different local slenderness ration

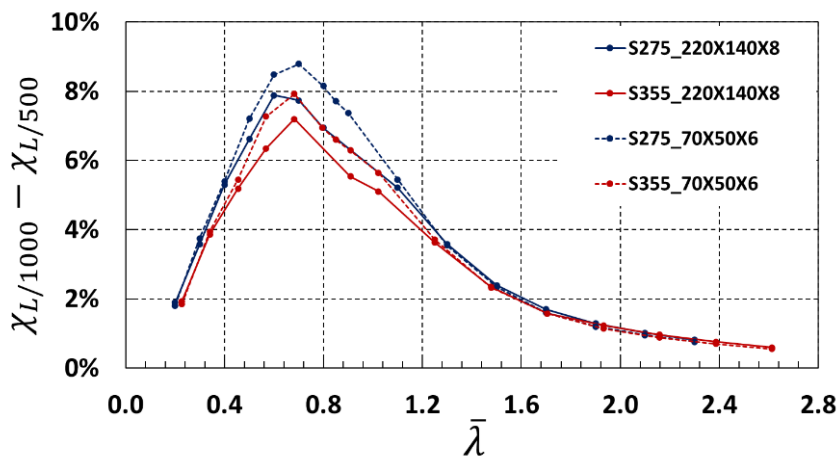


Figure 5-11 Effect of residual stresses

### 5.3 Macro FEM (OpenSees)

The model developed in the previous section is not a suitable choice for a full probabilistic analysis due to several reasons. Firstly, in a FEM that works at the micro-level, it is not practical to run numerous simulations (e.g., 3000) at each slenderness ratio due to the computational time. It is also not quite straightforward or depending on the parameter impossible, to consider some basic parameters as an uncertain variable. For instance, software such as Abaqus can handle yield stress as a random variable. However, in a 3D model, considering the thickness or the corner radius as a random variable is almost impossible. On the contrary, when we are modeling at macro level with software such as OpenSees, it is possible and straightforward to consider any parameters as a random variable.

#### 5.3.1 Model Description

There are two main approaches for modeling nonlinear behavior I) Concentrated plasticity II) Distributed Plasticity. The proposed model in OpenSees is a fiber-based (i.e., distributed plasticity) cross-section model. Contrary to concentrated plasticity models (elastic element with rotational springs at element ends) force-based element (FBE) and displacement-based element (DBE) permit the spread of plasticity along the element (distributed plasticity models). Distributed plasticity models allow yielding to occur at any location along the element (see Figure 5-12), which is especially important in the presence of distributed element loads (girders with high gravity loads).

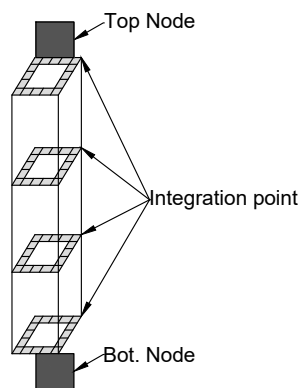


Figure 5-12 Distributed plasticity model



The column is made of displacement-based beam-column elements. This type of element is based on the displacement formulation and considers the spread of plasticity along the element.

The displacement-based approach follows standard finite element procedures where we interpolate section deformations from an approximate displacement field then use the principle of virtual displacements (PVD) to form the element equilibrium relationship. To approximate nonlinear element response, constant axial deformation and linear curvature distribution are enforced along the element length. In other words, in this type of element, the input is the nodal displacement and the output is the nodal force which is in line with the global solution of the system. As a result, displacement-based elements have fewer convergence problems and are more stable. A Major limitation of the classical displacement approach is the assumption of cubic interpolation functions, which result in a linear curvature distribution along the element. This assumption leads to satisfactory results under linear or nearly linear response. To overcome this shortcoming, a mesh refinement of the column is necessary (see Figure 5-13) to capture a more realistic curvature along the height of the column.

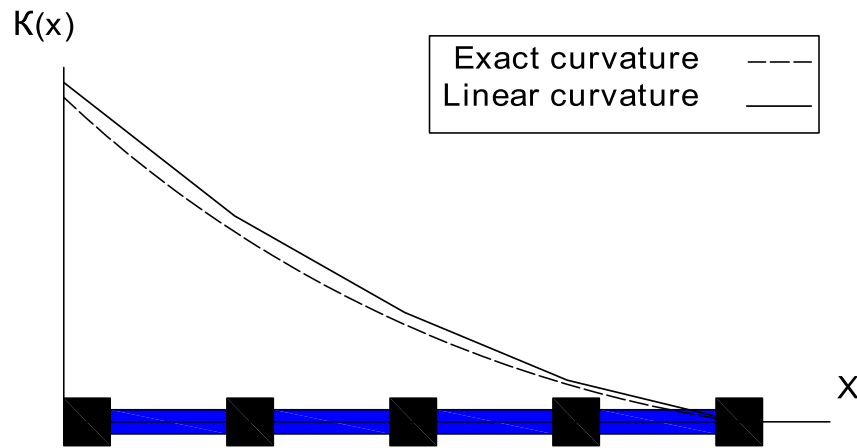


Figure 5-13 Curvature distribution of the column

### 5.3.2 Geometric Imperfections

The global imperfection is modeled as a half-sin wave shape with a maximum value at column mid-height. This has been applied by shifting the nodes' location from their initial position in a plane of buckling proportional to the node at the middle height of the column (see Figure 5-14). The amplitude of the geometrical imperfection was fixed at  $L/1000$ . It should be noted that the

number of elements in the column is a function of the height of the column and its capability to give accurate results. This number is different for each column, but on average 15 elements are selected for the model.

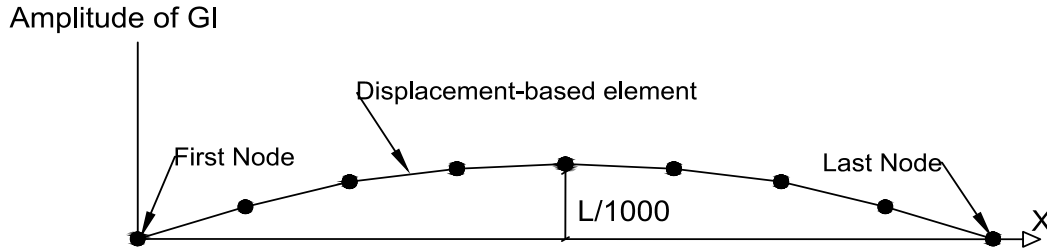


Figure 5-14 Initial out-of-straightness

### 5.3.3 Cross-section Fibers

The Steel02 material available in OpenSees was used to model the material behavior. The steel02 material is a modified version of the well-known Giuffre–Menegotto–Pinto model [43]. The steel02 properties used in the model were based on the tensile coupon test presented in chapter three. Figure 5-15 shows that steel02 material is capable of simulating both flat and corner areas stress-strain behavior

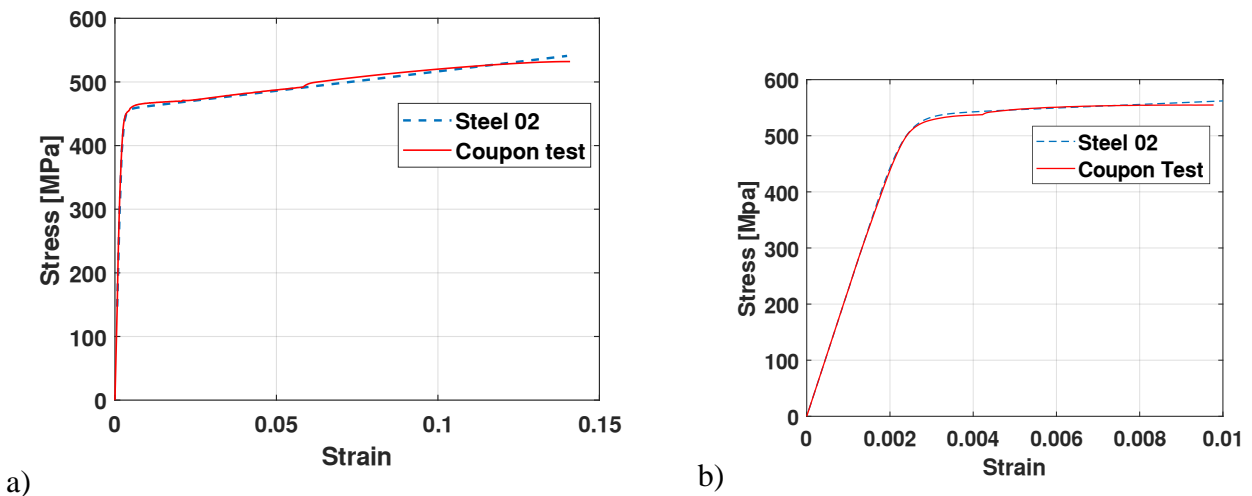


Figure 5-15 Material Calibration for Steel 02 material a) Flat b) Corner

The cross-section is divided in a way to have three parent fiber along the thickness to implement the residual stress pattern described in the introduction. Furthermore, this parent fiber will be subdivided into smaller fiber to increase the accuracy of the results.

The external zone has tension (positive) residual stress, while the internal zone has compression (negative) residual stress due to cold-forming, and the middle zone is free of residual stress. This pattern will result in a local bending moment, which is the dominant type of residual stress in cold-formed sections. The general overview of the cross-section without showing the children fiber (smaller segment) is illustrated in Figure 5-16. The figure is color-coded. The black area indicates the corner area, which has a different stress-strain behavior compared to the flat part. The strength enhancement of the corner area compared to the flat part is extended after the corner area to the flat part. The grey area represents the transition area between the corner and the flat parts. Also, residual stresses are different for the inner and outer fibers, as highlighted in the zoom circle.

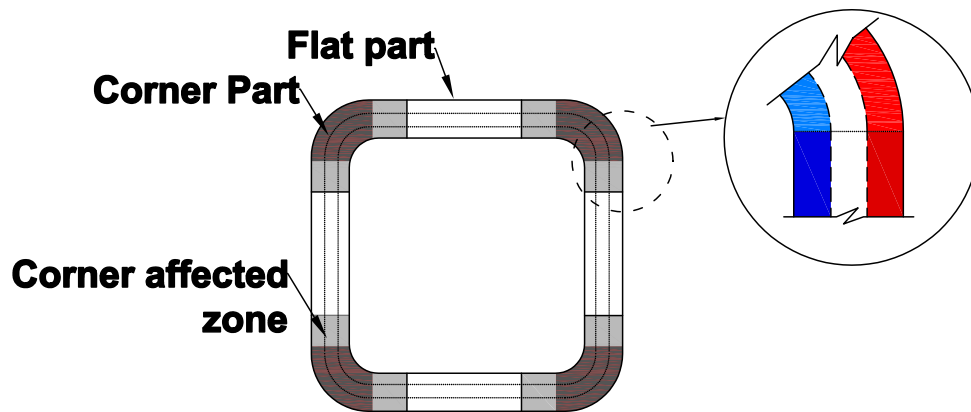


Figure 5-16 Fiber-based cross-section of the column

The model is verified by comparing the simulated load-axial deformation with the experimental test results for different slenderness ratio as shown in Figure 5-17.

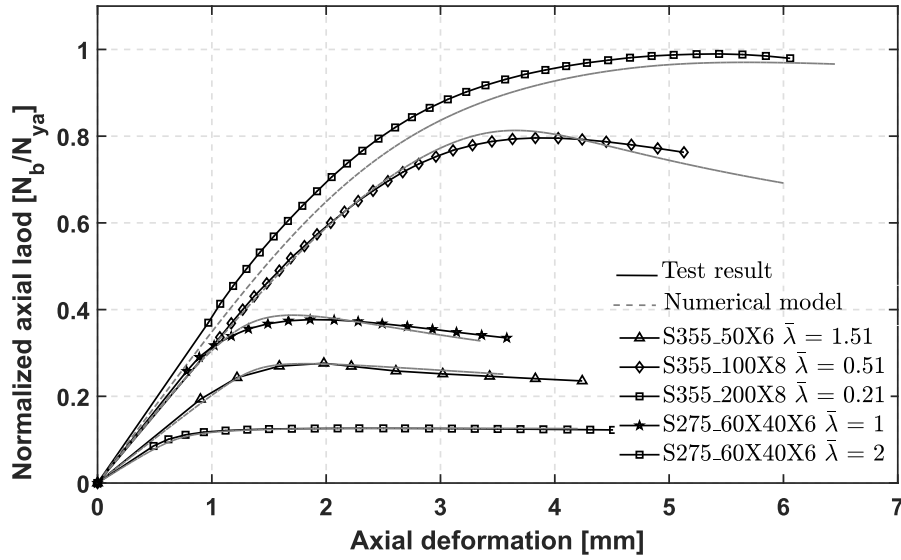


Figure 5-17 Load-Axial deformation of the test result and OpenSees model

The vertical axis is normalized by the actual yield strength computed as:

$$N_{ya} = f_{y,flat} \times A_{flat} + f_{y,corner} \times A_{corner} \quad (5-1)$$

where,  $f_{y,flat}$ , and  $f_{y,corner}$  are the average yield stress of the flat and corner area respectively.

# **6 Safety Assessment of EC3-1-1 buckling curve**

## **6.1 Introduction**

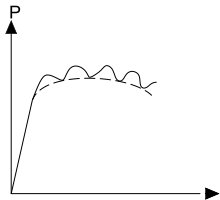
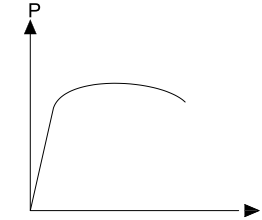
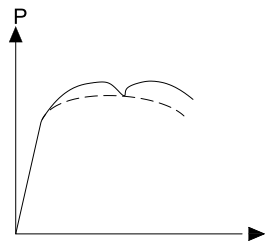
This chapter is devoted to evaluating the safety of the buckling curve method in EC3-1-1. A detailed discussion on the definition of the word safety is established in chapter two which serves as prerequisite for the current chapter. First, a discussion on the background of the current buckling curve in EC3-1-1 is presented. By comparing the basis of the buckling curve with the provisions of Eurocode 1990, it is demonstrated that different levels of safety are adopted in the Eurocode series. Then an improved buckling curve that has a uniform safety and corresponds to the intended level of safety is proposed.

## **6.2 Background of the ECCS experimental research on column strength**

The mission of the European Convention for Constructional Steelwork (ECCS) is amongst others to promote the use of steelwork in construction through the development of standards and promotion material. There are different technical committees within ECCS, one of these technical committees is the “Technical Committee (TC8)”. TC8 is active in the field of stability of steel structures. TC8 was first established in 1958 to regulate common European rules for the stability of structural members and components in steel and to suppress the considerable differences existing at that time in the national codes of the member countries. Logically the first objective of this committee was to deal with the basic problem of axially loaded, hinged compression members. At that time, the theory of bifurcation was the state of the art for computing the buckling load of an axially loaded column. As discussed extensively in chapter two, this theory is based on the assumption of a perfectly straight member of homogeneous material, without any residual stresses due to the fabrication process, and of a perfectly centered axial load. Due to these fatal errors of bifurcation theory, different national codes adopted more or less arbitrarily determined safety factors.

The TC8 decided to carry out an extensive research program concerning compression members. As it was felt that it would be difficult, as well as unnecessary for practical purposes, to separate in the experimental research the influences of the various parameters, such as residual stresses, or inhomogeneity of material or geometrical imperfections, it was decided to consider the behavior of rolled sections in the "as delivered" condition, in this way it was possible to deliver an envelope of the influence of all the parameters involved. Furthermore, they performed tests in a way to have for each slenderness ratio and type of section several parallel tests large enough to allow the determination of the collapse load with a given probability.

Table 6-1 Comparison of loading techniques for various testing methods

Method	Typical column curve	Loading	Testing Time	Accuracy of static curve	Remarks
FL1		Static	4-6 hours	0.5-1% for hydraulic testing machine	-Time consuming -Dynamic curve not available except $P_{ul}$
EC1		Dynamic	15-20 min	Static curve not available	-Static curve not available
EC2		Semi-Dynamic	30-40 min	0.5-1 %	-Only the ultimate static point available

The experimental campaign is conducted in testing laboratories of seven European countries (Belgium, France, Germany, Italy, Netherlands, United Kingdom, Yugoslavia) on a uniform basis and with a strictly applied and controlled testing procedure. The European program has included 1067 main buckling tests on various types of members (I, H, T, round, and square hollow sections) and the corresponding stub and tension tests. Thanks to the interest shown by the column research council (CRC) for this research, a complementary program has been carried out at Lehigh

University. The test pieces were collected in various European countries along with the same rules as for the main program. The proposed method may be considered a compromise between static and dynamic testing methods. The main features of the proposed method are shown in the Table 6-1.

These additional tests have completed the information needed for establishing the ECCS column curves.

### **6.2.1 Interpretation of the results**

The interpretation of the test results has been made employing a statistical analysis to obtain a consistent degree of safety for all types of stress. It was decided to determine the stress corresponding to the mean value of test results minus twice the standard deviation (M-2SD) for each slenderness ratio.

After the wide and comprehensive experimental research on compression members initiated by D. Sfantesco within the ECCS, several investigators have contributed to a more complete and more detailed theoretical analysis of the stochastic aspect of these problems. A substantial complement to the ECCS experimental research was brought by Strating and Vos [44] by simulating on the computer the ECCS curve using a Monte Carlo method, thus providing the possibility to derive theoretically the distribution function of buckling stresses in the right format. The distribution of the data over the global slenderness ratio is mostly affected by the test results obtained from section IPE160 since most of the flexural buckling test was conducted on this section [44]. Figure 6-1 shows the result of experimental tests together with the fitted buckling curve.

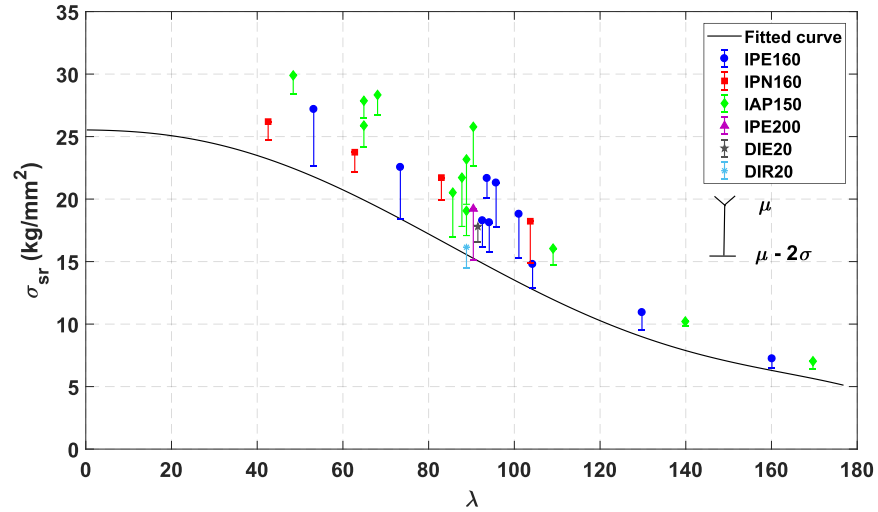


Figure 6-1 Experimental tests results and the fitted buckling curve, error bars show mean minus two Std [44]

It is important to note that the first set of draft standards of Eurocodes were published around 1984. These standards were titled “Common Unified Rules” and were prepared both as general set of rules (the current EN 1990 “Basis of Design” the heading documents of Eurocode series) and for the specific materials, such as reinforced concrete, steel, timber (the current EN 1992, EN 1993, EN 1995 etc.).

### 6.3 Different levels of safety in Eurocodes

EN 1993-1 [17] is the first of six parts of EN 1993 Design of Steel Structures. It gives generic design rules intended to be used with the other parts, EN 1993-2 to EN 1993-9. As discussed in chapter 3, a structure designed by Eurocode series should obtain a minimum reliability intended by Eurocode 1990. In clause 2.1.1 (p) EC3-1-1, it states “The design of steel structures shall be in accordance with the general rules given in EN 1990”. The minimum reliability index for most of the structures (CC2) is 3.8 as discussed earlier (see Table 3-2). Furthermore, EN 1990 allows us to separate the load and resistance side of a problem using the so-called FORM sensitivity factors  $\alpha_R$  and  $\alpha_E$ . This will reduce the size of the problem. This separation is demonstrated in



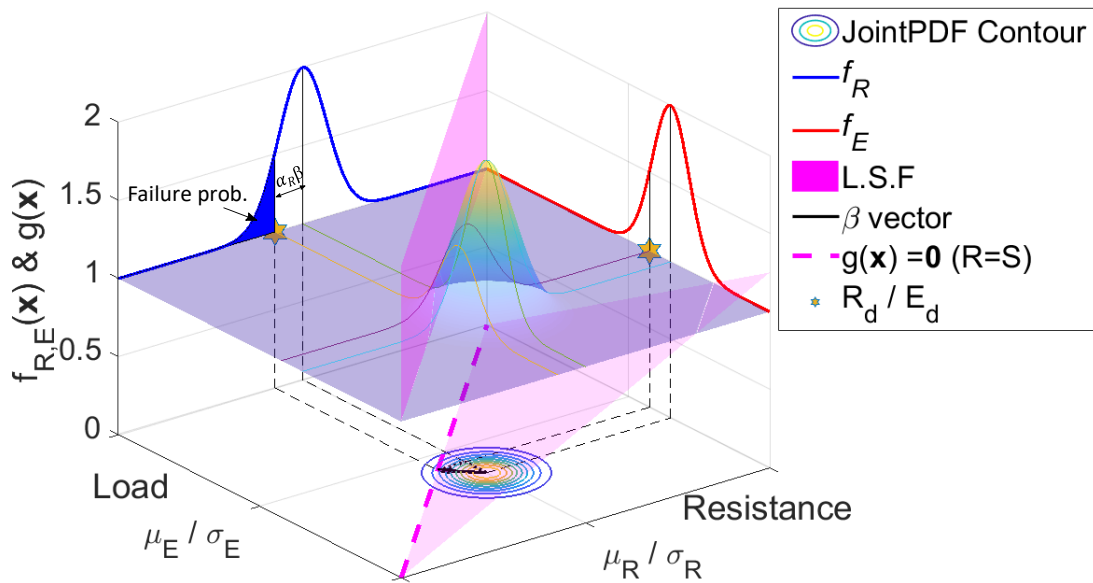


Figure 6-2 Separation of load and resistance side of the problem

This simplification results in a reliability index of 3 ( $3.8 \times 0.8$ ), indicating a probability of failure of 0.11% using Eq.(3-3). In other words, if we have two random variables in our problem and only consider the resistance side of the problem, the volume (The removed area) in Figure 3-5 should be maximum 0.11%.

As explained in previous section according to the E.C.C.S. [45] criteria, the acceptable probability of failure is 2.3%. In other words, we are acknowledging there is a 2.3% probability that the actual buckling resistance of the compression member can be less than the considered resistance. The corresponding  $\beta$  can be computed using the inverse function of the formula given in Eq.(3-3), which leads to  $\beta = 2$ . It is evident that the level of safety within the European buckling curve method in EC3-1-1 is different (lower) than the required level of safety by EN1990 as the heading document. In other words, if we assume a standard normal distribution for the resistance variable (i.e.,  $\mu = 0$ ,  $\sigma = 1$ ), the different safety level adopted in the Eurocode series can be demonstrated by Figure 6-3.

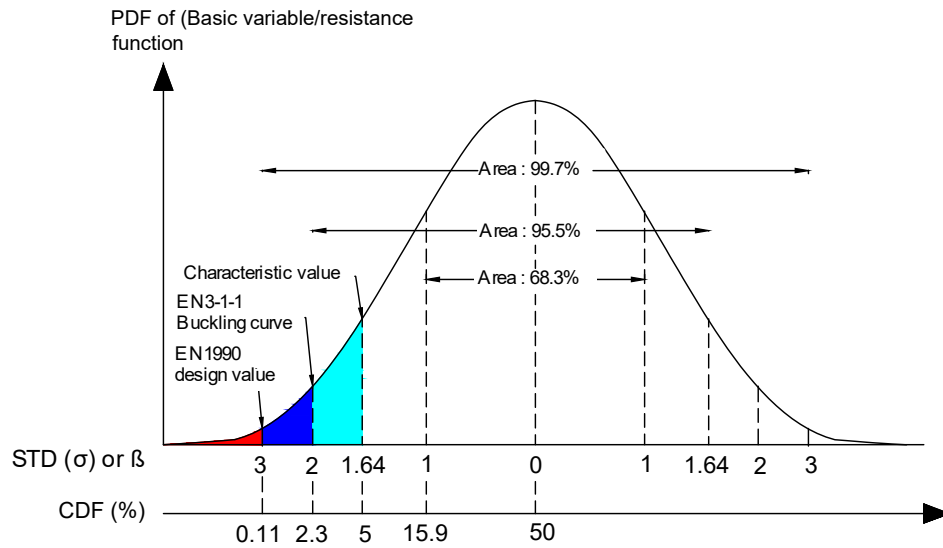


Figure 6-3 Different level of safety in Eurocode series

## 6.4 Monte Carlo Simulation

Once validate the accuracy of the developed FEM, the deterministic model is transformed into a probabilistic model. The uncertainties in the model are described by random variables. The list of random variables considered in this study is presented in Table 6-2.

Table 6-2 Summary of the random variables

Symbols	Description	Characteristics (mean, Std)
$f_{y, flat}$	Yield stress (Flat)	Ln (439,30.7) MPa
$f_{y, corner}$	Yield stress (Corner)	Ln (474,33.18) MPa
$t_w$	Thickness of the section	Ln (8,0.33) mm
$r_{corner}$	Corner radius of the cold-formed section	Ln (18.08,1.62) mm
$E_{flat}$	Young's Modulus (Flat)	Ln (210000, 10500) MPa
$E_{corner}$	Young's Modulus (Corner)	Ln (200000, 1000) MPa
GI	Geometric Imperfection	LN (L/1000,L/10000)
$\alpha$	Affected zone after corner (fraction of $t_w$ )	Exp (1,0.05)
$R_{0,flat}$	Steel 02 Model parameter	Ln (3.2, 0.64)

$b_{flat}$	Steel 02 Model parameter	Ln ( 0.004, 0.0018)
$R_{0,corner}$	Steel 02 Model parameter	Ln (3,0.47)
$b_{corner}$	Steel 02 Model parameter	Ln (0.0089, 0.008)

Except for  $\alpha$ , the rest of the random variables are assumed to be distributed lognormally. The mean and standard deviation are obtained from the extensive experimental program discussed previously. Random variable  $\alpha$  indicates the corner affected zone in cold-formed sections (i.e., the grey area in Figure 5-16). In this study, the uncertainty in  $\alpha$  is modeled with an exponential distribution that defines the affected zone as a multiplier of thickness. The correlations among random variables are also included in this study as follows:  $f_{y, flat}$  and  $f_{y, corner}$  (0.75),  $r_{corner}$  and  $t_w$  (0.95) and  $E_{flat}$  and  $E_{corner}$  (0.9). The probability density function (PDF) of the generated random variables for Steel grade 275 is illustrated in Figure 6-4.

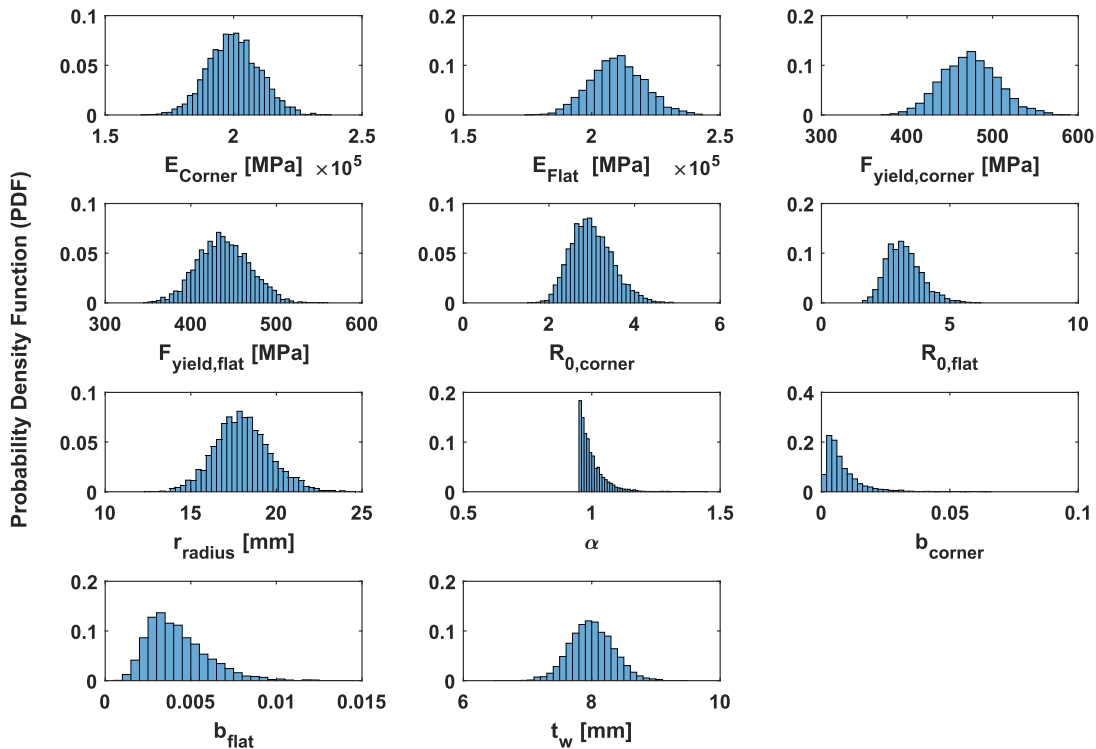


Figure 6-4: Generated random numbers for the uncertain parameters (S 275)

Figure 6-5 shows the correlation between the generated data.

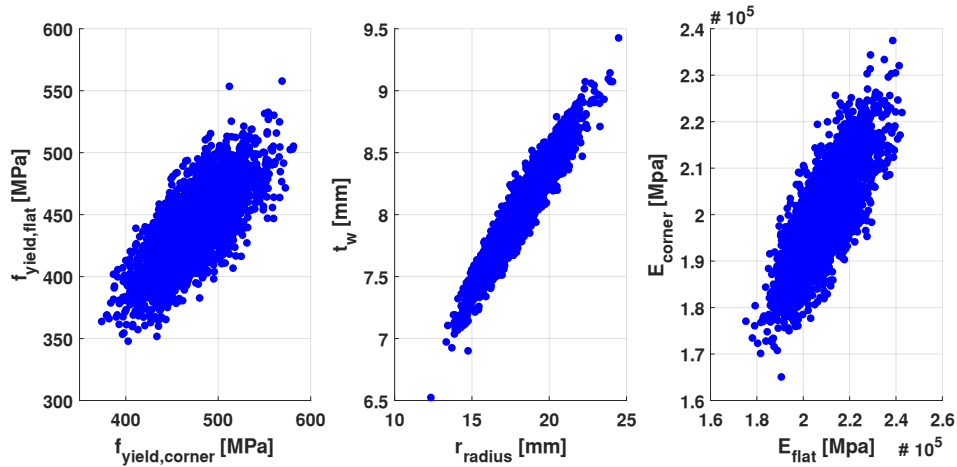


Figure 6-5 Generated correlated random variables

A series of MCS (3000 samples per  $\bar{\lambda}$ ) are executed from  $\bar{\lambda} = 0.2$  to  $\bar{\lambda} = 2$  with a step of 0.2 for both steel grades S275 and S355. In order to avoid any dependency between the results, the random numbers are generated separately for each analysis (i.e., different seed). A typical result of the MCS is presented in Figure 6-6. It shows the scatter plot for computed buckling load at two  $\bar{\lambda}$ , along with their histograms.

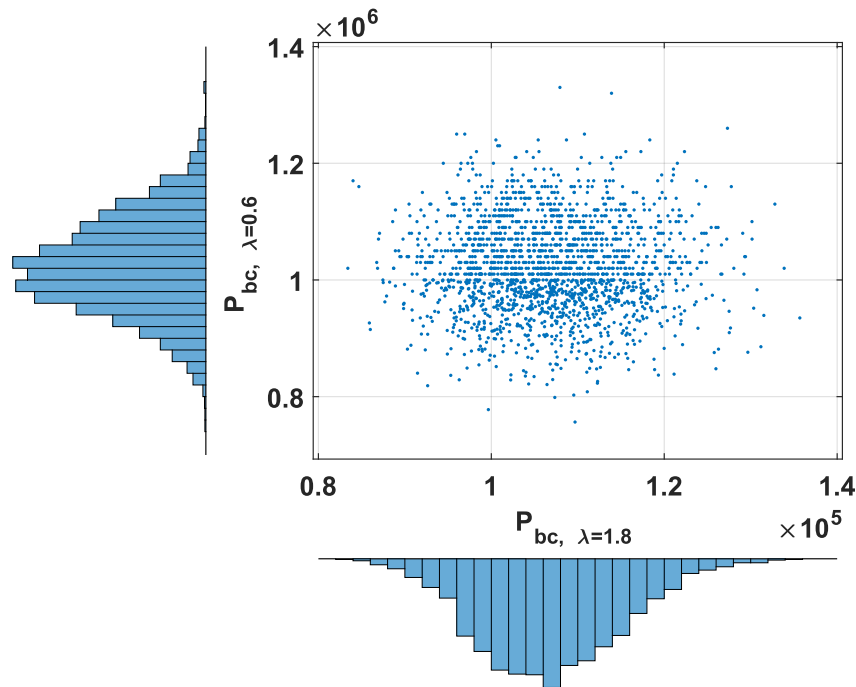


Figure 6-6 MCS for two different slenderness ratio and their correlation

A theoretical probability distribution model is often used to describe the scatter in the data, with lognormal being a typical choice for a resistance function. By visual assessment of the quantile-quantile (Q-Q) plot of the data, it can be observed that data are distributed lognormally. However, in order to check the validity of the assumption mathematically, a Lilliefors goodness-of-fit [46] test is employed. This test is more suitable than the Kolmogorov-Smirnov test [47] when the parameters of the null distribution are unknown and must be estimated. The test fails to reject the assumption at the 5% significance level. The theoretical and empirical CDF of the buckling load is plotted in Figure 6-7.

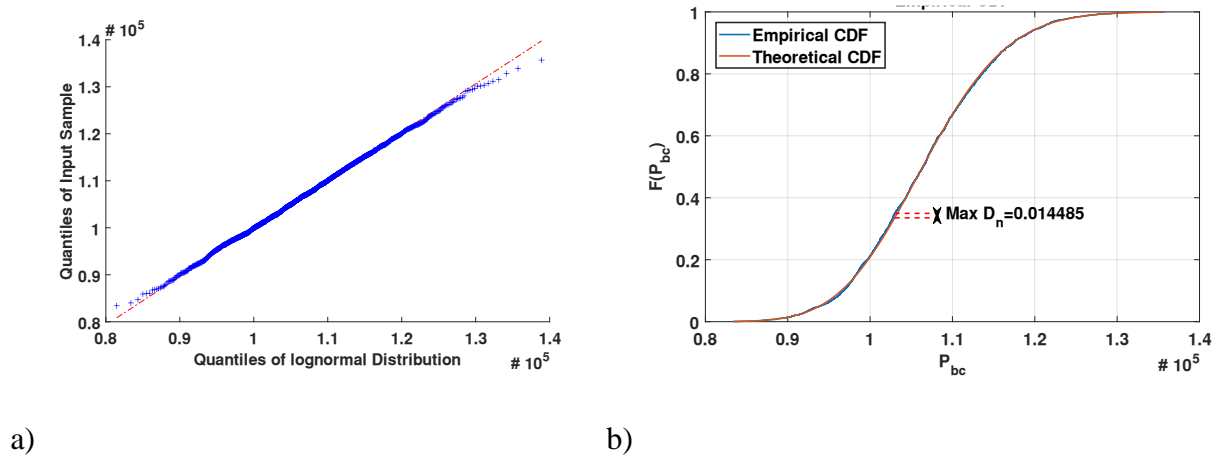


Figure 6-7 a) Q-Q plot for the buckling load versus theoretical lognormal quantiles b) Lilliefors goodness-of-fit test

Based on the results of Monte Carlo simulations, the buckling reduction factors ( $\chi$ ) are calculated using the following Eq.

$$\chi = \frac{P_{bl}}{A_{nom} \cdot f_{y,nom}} \quad (6-1)$$

Where  $A_{nom}$  is the nominal area and  $f_{y,nom}$  is the nominal yield strength of the cross-section. As noted previously, in order to obtain the safety level intended by EN 1990, (see Figure 6-3) a reduction factor corresponding to the CDF (probability of non-exceedance) of 0.11% should be adopted as the design value. Figure 6-8 shows the distribution of  $\chi$  factor for each  $\bar{\lambda}$  along with the design values. It can be observed that the distribution becomes wider as it goes to the stocky range.

This behavior can be explained by recognizing that uncertainties have less impact on the slender columns. In other words, the parameters that are important for nonlinear buckling are both more uncertain and have a greater effect on buckling load as compared to the parameters that control the buckling load at the elastic level.

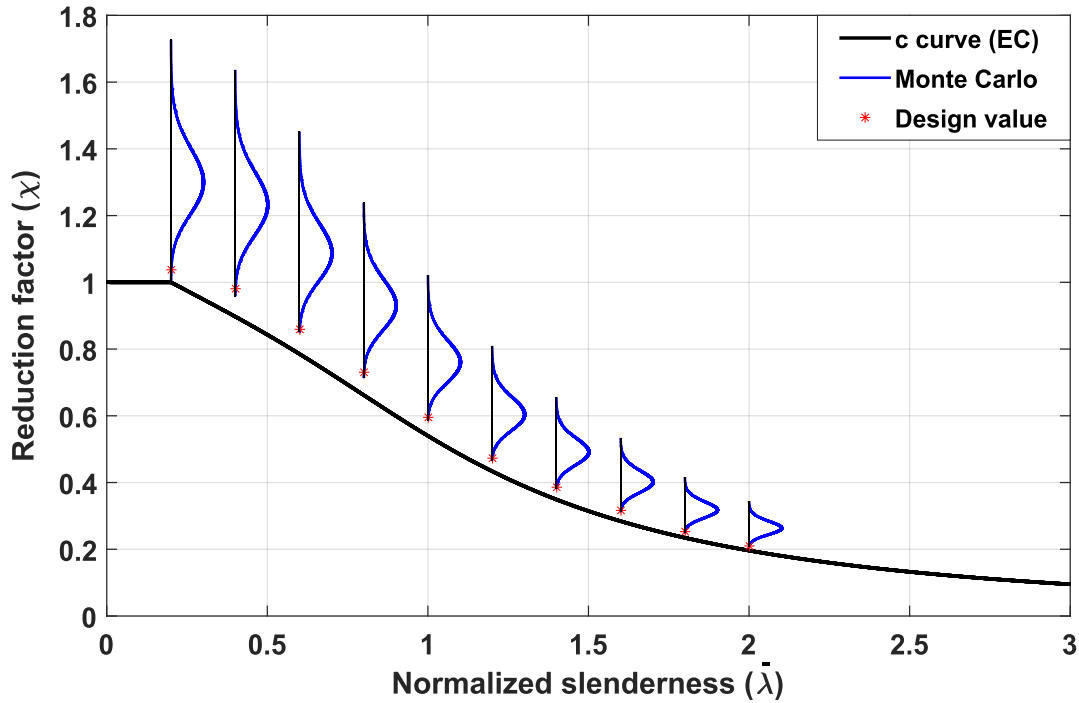


Figure 6-8 Results of MC simulation for S355

The European stability design rules for steel columns are classically based on Ayrton- Perry formulations that was discussed previously. These curves rely on the calibration of imperfection factors ( $\alpha$ ) and a constant parameter  $\lambda_0$ ; that defines the plateau part of the curve; in order to estimate the maximum resistance. In order to find the new values for the parameters  $\alpha$  and  $\lambda_0$ , the problem can be formulated as an optimization problem with the following objective function:

$$\Theta_{\bar{\lambda}_i} = \chi_{MC,d(\bar{\lambda}_i)} - \chi_{EC(\bar{\lambda}_i)} \quad (6-2)$$

$$\{\hat{\alpha}, \hat{\lambda}_0\} = \underset{\bar{\lambda}_i=0.2}{\operatorname{argmin}} \left\{ \sum_{\bar{\lambda}_i=0.2}^2 (\Theta_{\bar{\lambda}_i}) \mid \Theta_{\bar{\lambda}_i} \geq 0 \right\} \quad (6-3)$$

Where  $\chi_{MC,d(\bar{\lambda}_i)}$  is the design value of the reduction factor at a global slenderness ratio  $i$ ; obtained from Monte Carlo simulation; and  $\chi_{EC(\bar{\lambda}_i)}$  is the EC buckling curve at the same global slenderness ratio  $i$ . The results of the optimization are displayed Table 6-3.

Table 6-3  $\lambda_0$  and  $\alpha$  values obtained from optimization for flexural buckling of cold-formed sections

	S275	S355
$\hat{\alpha}$	0.27	0.32
$\hat{\lambda}_0$	0.42	0.42

Figure 6-9 shows the updated buckling curve corresponding to a reliability index of 3 for both steel grades.

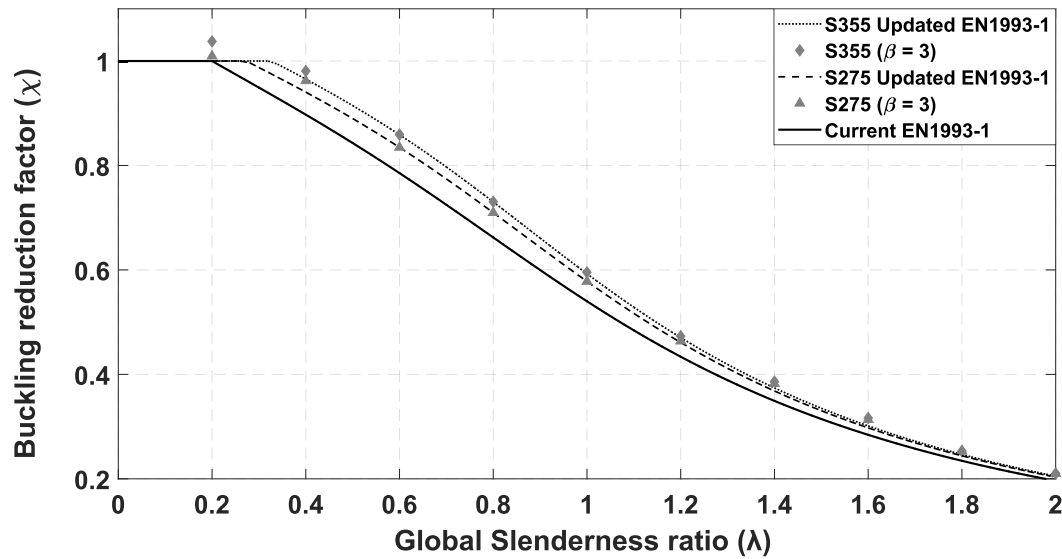


Figure 6-9 EC curve with the proposed  $\alpha$  and  $\lambda_0$

## 6.5 Finite element reliability analysis of the model

As described previously, the level of safety in the current buckling curve method of EC3-1-1 is different from the considered safety in EN 1990. Another issue that has to be addressed, is having a non-uniform level of safety across  $\bar{\lambda}$  as can be seen from Figure 6-8. To further address this issue, a first-order reliability method (FORM) is employed to assess the safety of the current buckling curve. As mentioned earlier, the probability of failure for a single random variable problem is the area under the PDF over the failure limit as shown in Figure 3-3. In case of having a vector of random variables, the probability of failure or equivalently the reliability index of a system is given by an n-fold integral as follows:

$$P_f = \int \dots \int_{\Omega} f(\mathbf{x}) d\mathbf{x} \quad (6-4)$$

Where  $f(\mathbf{x})$  is the joint probability distribution function for random variables, which are collected in the vector  $\mathbf{x}$ , and  $\Omega$  is the failure domain. Different probabilistic methods (eg., MCS, FORM, and SORM) try to solve this integral using different approaches. In the FORM method, an approximation of the probability integral is obtained by linearization of the L.S.F denoted by  $g(\mathbf{x})$  using a Taylor series expansion in the standard normal space at an optimal point. Figure 6-10 shows the FORM method schematically for a vector of two random variables. For further information on FORM and its by-products, refer to textbooks, such as Der Kiureghian [48] and Ditlevsen and Madsen [49]

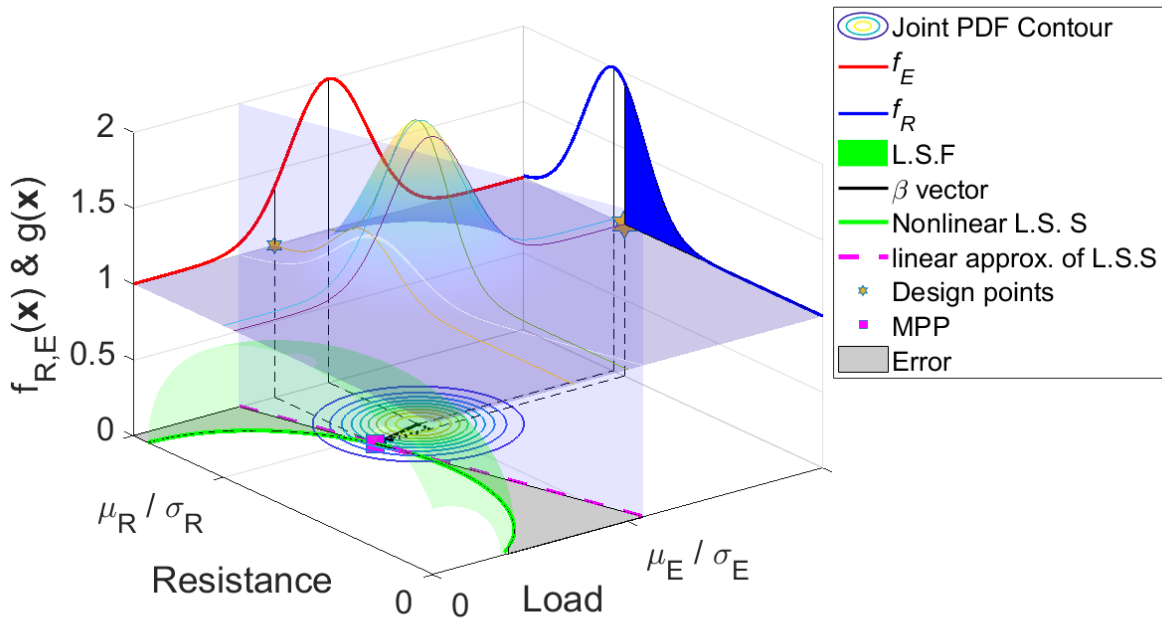


Figure 6-10. Schematic presentation of FORM method for a bivariate problem

Two main components of this method are random variables and L.S.F, in which random variables describe the uncertainty and a L.S.F that defines the event of failure. The failure must be defined so that  $g(\mathbf{x}) = 0$  separates the failure domain (i.e.,  $\Omega \equiv g(\mathbf{x}) < 0$ ) and safety domain ( $g(\mathbf{x}) > 0$ ) [48]. To this end, the L.S.F,  $g$ , is defined as:

$$g(\mathbf{x}) = \chi_{model(\bar{\lambda})}(\mathbf{x}) - \chi_{EN(\bar{\lambda})} \quad (6-5)$$



where  $\mathbf{x}$  is a vector of random variables. The first term is the output of the OpenSees model described in the previous section, while the second term is the reduction factor computed based on EC3-1-1 buckling curve method at the same  $\bar{\lambda}$ . Therefore, failure is defined when the L.S.F is negative. FORM analysis is then carried out for  $\bar{\lambda} = 1.8$  and  $0.55$  representing an elastic and nonlinear buckling, respectively. As discussed above, FORM analysis gives the first approximation of the failure probability, and the accuracy of this approximation depends on the nonlinearity of the L.S.F. Therefore, the results of FORM method are also compared to a MCS using the importance sampling variance reduction technique as a benchmark method. The analyses are conducted with Rt ( [50] [51] ), a computer program for multi-model reliability analysis. The results are listed in Table 6-4.

Table 6-4 Results of FORM analysis for  $\bar{\lambda} = 0.55$  and  $1.8$

$\bar{\lambda}$	$\beta$ index from FORM	Corresponding probability of failure	$\beta$ index from MCS (Importance Sampling)	Corresponding probability of failure	$\beta$ index required by EN 1990
1.8	3.12	0.089%	3.018	0.127%	3.04
0.55	3.58	0.017%	3.48	0.025%	3.04

Comparing the FORM method with the benchmark method shows that FORM method provides an acceptable approximation of the probability of failure and the nonlinearity in the L.S.F is not significant. Furthermore, it can be seen that two cold-formed columns designed based on the current buckling curve in EC3-1-1 lead to different levels of safety. This indicates that different coordinates of the buckling curve correspond to the different level of safety. An important by-product of the FORM analysis is parameter importance measures to rank the variables according to their relative importance [48]. It should be noted that this ranking is computed considering the correlation between random variables. Figure 6-11 shows the impact of each random variable on the failure defined by Eq.(6-5).

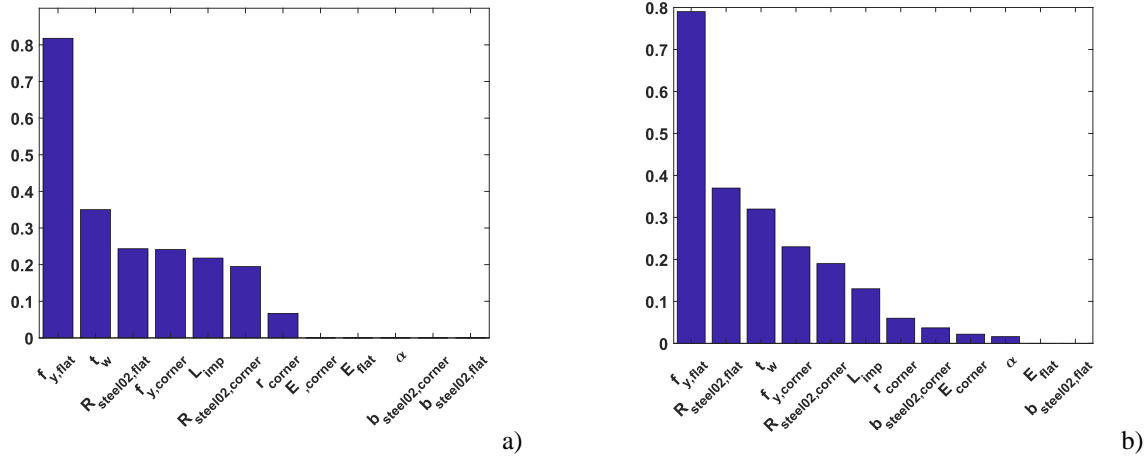


Figure 6-11 Ranking of random variables based on their impact on the reliability index (i.e.,  $\beta$ ) for a)  $\bar{\lambda}=1.8$  b)  $\bar{\lambda}=0.55$

Figure 6-11 shows that the random variable  $f_{y,flat}$  has the most influence on the probability of failure at both  $\bar{\lambda}$ . This is rather an expected result based on engineering judgments; however, it is interesting to see other ranks in this list. Remarkably, it is found that random variable  $R_{steel02,flat}$  is in second place followed by the thickness of the section for  $\bar{\lambda} = 0.55$ .  $R_{steel02,flat}$  is a parameter of the material model that controls the shape of the transition curve in the material model which indicates the importance of material behavior in the stocky range. One might note that the effect of some random variables is zero, meaning that they are not activated in the reliability analysis or had no influence on the probability of failure that has been defined by the corresponding L.S.F. This will help to reduce the size of the problem by replacing a constant value (e.g., the average of random variable) instead of considering them as a random variable. These results help us to efficiently utilize and assign our resources based on the importance of each parameter. For instance, it would be wiser to spend the budget on more coupon tests for determining the yield stress rather than doing tests to find the length of the affected zone.

## 7 Summary and conclusion

The primary objective of this research is to characterize and investigate the flexural behavior of cold-formed rectangular and square hollows sections. An extensive experimental program including 21 flexural buckling tests and 82 compressive coupon tests was carried out. The results of the experimental program provide a solid basis for the comprehensive numerical simulations and assessment of the flexural buckling of CFHS. The major results of this research are summarized in the following sections.

### 7.1 Development of Databases for the safety assessment of CFHS

In order to provide supporting information for modeling of SHS and RHS flexural buckling behavior, a series of coupon tests have been carried out from the different positions of the cross-sections, namely, from corners, from four flat sides, and from perpendicular to the weld line. An innovative procedure for testing the corner coupons of SHS and RHS has been implemented for the first time at the Università degli Studi di Napoli Federico II. In addition, to investigate the effect of strain rate on the strength parameters of the material, the straining is paused during the loading process at two points to allow the relaxation of the stress-strain curve. The extensive coupon tests discussed in chapter 4, has resulted in the following:

- The second drop is slightly more than the first one for flat and corner coupons. The static drop for the transversal and weld coupons is not sensitive to the location of the stop on the stress-strain curve.
- Reduction in yield stress (i.e., first drop) due to strain rate effect decreases as the steel grade increase, whereas the opposite is true for the second drop (Figure 4-31 (c and d)). The same pattern can be observed for corner coupons too.
- The current BSI and ASTM standards systematically overestimate the material strength parameters such as  $\sigma_y$  and  $\sigma_u$  by 5% and 5.68%, respectively, on average. The maximum difference is 7.7% and 9.1% for flat and corner coupons. It is important to remember that the strain rate considered in this study was below the recommended lower bound of the

investigated standards (see Fig. 8). This error is expected to be more pronounced when the upper bound of the recommended range is used.

- In all cases, the flat coupon shows more ductility than the corner coupons. On average, the ductility in flat coupons is 4.8 times the corner coupons. This is mainly because that the degree of cold-forming in corners are more significant than the flat part. In room temperature, the stress-strain curve of the longitudinal weld has similar ductility (also shape, see Figure 4 30.) to those of the corner coupons.
- En1993-1-1 requires three criteria for the structural steel. Based on the results, On average, flat coupons and corner coupons satisfy the hardening criteria based on the EC3-1-1 recommendation. For the ductility criteria, the corner coupon does not fulfill the limit on average, while the flat coupons meet the limit. The cold-formed process changes the stress-strain curve dramatically. Based on characteristic value, none of the requirements for the ductility of steel is fulfilled. Therefore, based on these observations a plastic analysis of the CFHS column may be questionable and further investigation of the matter is advisable.

## **7.2 Assessment of the flexural buckling curve for CFHS**

The information collected in the experimental program is used to evaluate the current flexural buckling curve method of EN1993-1-1 for CFHS. In order to assess the current buckling curves for cold-formed hollow profiles a comprehensive and a step-by-step discussion has been presented starting from the definition safety. Then a chronological review of the current buckling curve is discussed to highlight the inconsistency of the safety through different levels of Eurocode series. An extensive MCS has been performed to propose a new buckling curve that is consistent with the level of safety presented in EN1990. Then a classical reliability method (FORM) is employed to further investigate the level of safety within the current buckling curve. The following conclusion is drawn from this study:

- By reviewing the historical background of the current flexural buckling curve in EN1993-1-1 and comparing it with the principles and specifications stipulated in EN1990 as the head documents of the Eurocode series, it has been shown that the level of safety in these documents are different.

- Improved buckling curves that neither overestimate nor underestimate the flexural buckling strength of cold-formed sections have been proposed through a comprehensive Monte Carlo simulation.
- Using a first order reliability method, it was shown that different coordinates of the current buckling curve correspond to different levels of safety. Therefore, two columns with various  $\bar{\lambda}$  designed based on this curve, has different safety in their designs. This is in contrast with the concept of uniform safety.

## 8 References

- [1] R. V. Pillar, "INFLUENCE OF RESIDUAL STRESSES ON THE STRENGTH," COPPE , RIO DE JANEIRO, 2015.
- [2] R. L. a. F. M. A. Ghersi, *Metalic Cold-Formed Thin-walled Members*, London: spon press, 2002.
- [3] J. T. b. K. C. W.M. Quacha, "Effect of the manufacturing process on the behaviour of press-braked thin-walled steel columns," *Engineering structures*, vol. 32, pp. 3501-3515, 2010.
- [4] G. Z. Y. M. Y. G. X. L. S.H. Li, "Residual stresses in roll-formed square hollow sections," *Thin-Walled Struct*, vol. 47, pp. 505-513, 2009.
- [5] W. Ramberg and W. R. Osgood, "Description of stress–strain curves by three parameters," National Advisory Committee For Aeronautics, Washington DC, 1943.
- [6] H.N. Hill, "Determination of stress-strain relations from the offset yield strength values," National Advisory Committe for Aeronautics, Washington, D.C, 1944.
- [7] X. Y. Leroy Gardner, "Description of stress-strain curves for cold-formed steels," *Construction and Building Materials*, vol. 128, pp. 527-538, 2018.
- [8] E. R. E. Mirambell, "On the calculation of deflections in structural stainless steel beams," *J. Constr. Steel Res*, vol. 54, no. 1, pp. 109-133, 2000.
- [9] G. H. KJR Rasmussen, "Design of cold-formed stainless steel tubular members. II: Beams," *Journal of Structural Engineering*, vol. 119, no. 8, pp. 2368-2386, 1993.

- [10] I. Arrayago and L. Gardner, "Gardner, Description of stress-strain curves for stainless steel alloys," *Materials & Design*, vol. 87, pp. 540-552, 2015.
- [11] B. S. W. G. Chajes A, "Effects of cold-straining on structural sheet steels," *J Struct Div Proc Am Soc Civ Eng*, vol. 89, no. 2, pp. 1-32, 1963.
- [12] K. K. Corner, "properties of cold-formed steel shapes," *J Struct Div Proc Am Soc*, vol. 93, no. 1, pp. 401-32, 1967.
- [13] B. P. Davison TA, "Column behaviour of cold-formed hollow structural steel," *Can J Civ Eng*, vol. 10, no. 1, pp. 125-41, 1983.
- [14] H. S. H. G. Key PW, "Column behaviour of cold-formed hollow sections," *J Struct Eng*, vol. 114, no. 2, pp. 390-407, 1988.
- [15] K. W. Karren, "Corner Properties of cold-formed steel shapes," in *ASCE Proceedings*, 1967.
- [16] K. W. a. G. W. Karren, "Effect of cold-forming on light-gage steel members," in *ASCE Proceedings*, 1967.
- [17] E.-1.-1.-1. (2005)., Eurocode 3: Design of steel structures - part 1-1: General rules and rules for buildings, European Committee for Standardisation.
- [18] G. S. Schajer, Practical residual stress measurement methods, Vancouver: Wiley, 2013.
- [19] R. Landolfo and F. Mazzolani, "The influence of the variation through the thickness of residual stresses in tubular columns," *Journal of Constructional Steel Research*, no. 19, pp. 49-57, 1991.
- [20] B. K. B. Somodi, "Residual stress measurements on cold-formed HSS hollow," *J. Constr. Steel Res*, vol. 128, pp. 706-720, 2017.
- [21] A. HENRIKSSON, "Initial bow imperfection for flexural buckling of steel members," CHALMERS UNIVERSITY OF TECHNOLOGY, Gothenburg,, 2017.
- [22] E.-1.-5. E. 3, "Design of Steel Structures - Part 1.5 Plated Structures," 2005.

- [23] J. Rondal and M. René J., "Mise en équation des nouvelles courbes européennes de," *Constr. Métallique*, vol. 1, p. 17–30., 1978.
- [24] L. S. d. Silva, R. Simões and H. Gervasio, Design of steel structures: Eurocode 3, part 1-1, general rules and rules for buildings, ECCS-European Convention for Constructional Steelwork, 2010.
- [25] L. Pierre Simon, "A Philosophical Essay on Probabilities, translated into English from the original French 6th ed.," Dover Publications, New York, 1951.
- [26] W. Heisenberg, "Über den anschaulichen Inhalt der quantentheoretischen Kinematik und Mechanik," *Zeitschrift für Physik (in German)*, vol. 43 , no. (3–4), p. 172–198, 1927.
- [27] A. Der Kiureghian and O. Ditlevsen, "Aleatory or epistemic? Does it matter?," *Structural Safety*, vol. 31, pp. 105-112, 2009.
- [28] L. Biacino and G. Gerla , "Fuzzy logic, continuity and effectiveness," *Archive for Mathematical Logic*, vol. 41, pp. 643-667, 2002.
- [29] M. A. Hoge KG, "The temperature and strain rate dependence of the flow," *Journal of Materials Science*, vol. 12, no. 8, p. 1666–72, 1977.
- [30] K. E., "Relaxation behavior and modeling," *International Journal of Plasticity*, vol. 17, no. 10, p. 1419–36, 2001.
- [31] W. S. Y. W. Pan CL, "Strain rate and aging effect on the mechanical properties of," *Thin-Walled Struct*, vol. 39, p. 429–44, 2001.
- [32] B. M. m. –. T. t. –. P. 1. M. o. t. a. a. temperature., Brucel: CEN, 2009.
- [33] *ASTM. Standard test methods for tension testing of metallic materials*, West Conshohocken: American Society for Testing and Materials, 2013.
- [34] *BSI. Metallic materials – Tensile testing – Part 1: Method of test at ambient temperature.*, Brussels: CEN, 2009..



- [35] Y. Huang and B. Young, "The art of coupon tests," *Journal of Constructional Steel Research*, vol. 96, pp. 159-175, 2014.
- [36] CEN, *Cold formed welded structural hollow sections of non-alloy and fine grain structural steel Part 2: Tolerances, dimensions and sectional properties*, Brussels: CEN, 1997.
- [37] CEN, *Eurocode 3: Design of steel structures Part 1-8: Design of joints*, Brussels: CEN, 2010.
- [38] Y. Fukumoto, "New constructional steels and structural stability," *Eng. Struct.*, vol. 18, no. 10, pp. 786-791, 1996.
- [39] "AISC Specification for structural steel buildings".
- [40] D. Systemes, *Abaqus*, Simulia, 2014.
- [41] F. McKenna, *Object-oriented finite element programming: frameworks for analysis, algorithms and parallel computing*, California: Department of Civil Engineering, University of California, 1997..
- [42] D. C. o. N. S. B. P. Dinis, "FEM-based analysis of the local," *Computers and Structures*, vol. 85, pp. 1461-1474, 2007.
- [43] P. P. Menegotto M, "Method of analysis for cyclically loaded reinforced concrete plane frames including changes in geometry and non-elastic behavior of elements under combined normal force and bending," in *resistance and ultimate deformability of structures acted on by well defined repeated loads*, 1973..
- [44] j. Strating and H. Vos, "Computer simulation of the ECCS buckling curve using a Monte-Carlo method," in *Proc. of the international colloquium on column strength.*, 1973.
- [45] "ECCS European recommendations for steel construction".
- [46] H. W. Lilliefors, "On the Kolmogorov-Smirnov test for the exponential distribution with mean unknown," *Journal of the American Statistical Association*, vol. 64, p. 387–389, 1969.

- [47] F. J. J. Massey, "The Kolmogorov-Smirnov Test for Goodness of Fit.," *Journal of the American Statistical Association*, vol. 46, no. 253, pp. 68-78, 1951.
- [48] A. D. Kiureghian, "First- and second-order reliability methods," in *Engineering design reliability handbook*, CRC Press, 2005.
- [49] O. D. Ditlevsen, *Structural Reliability Methods*, 2007.
- [50] H. Nasrazadani and M. Mahsuli, "Probabilistic Framework for Evaluating Community Resilience: Integration of Risk Models and Agent-Based Simulation," *Journal of Structural Engineering*, vol. 146, no. 11, 2020.
- [51] M. Mahsuli and T. Haukaas, "Computer Program for Multimodel Reliability and Optimization Analysis," *Journal of Computing in Civil Engineering*, vol. 27, no. 1, 2013.
- [52] M. & Å. B. Al-Emrani, in *Steel structures course literature*, Chalmers University of, 2013.
- [53] M. Sun, "Mechanical Behaviour of Cold-Formed Hollow Structural Section Material," Toronto, 2014.
- [54] J. T.-C. Jönsson, "European column buckling curves and finite element modelling including," *Journal of Constructional Steel Research*, vol. 128, pp. 136-151, 2017.
- [55] "UNI EN 10219 Standards".
- [56] J. P. J. Z. X.-L. V. D. V. G. WARDENIER, "Hollow Sections in Structural Applications," in *CIDECT*, Geneva, Switzerland, 2010.
- [57] R. S. A. d. I. K. e. T. SILVA, "entre perfis estruturais tubulares circulares," in *Dissertação de Mestrado em Engenharia Civil*, Rio de Janeiro, 2012.
- [58] CEN , EN 1990 Eurocode - Basis of structural design, 2002.
- [59] Wikimedia Foundation, "Wikipedia," 31 05 2020. [Online]. Available: [https://en.wikipedia.org/wiki/Uncertainty\\_principle](https://en.wikipedia.org/wiki/Uncertainty_principle).
- [60] OpenSees, "Open System for Earthquake Engineering Simulation," Pacific Earthquake (PEER), 2007. [Online]. Available: <http://opensees.berkeley.edu>.



# Appendix A Geometric Measurements and static properties

## A.1 Geometric measurements

Several experimental measurements and tests were done throughout this report. Their measurements and results are presented below.

For all the specimens the following legend is used to report in the table. It should also be mentioned that for few specimens, measurements such as width or corner radius are not reported. This is mainly because of the time window in the laboratory in which we forced to do the buckling test before measuring those data.

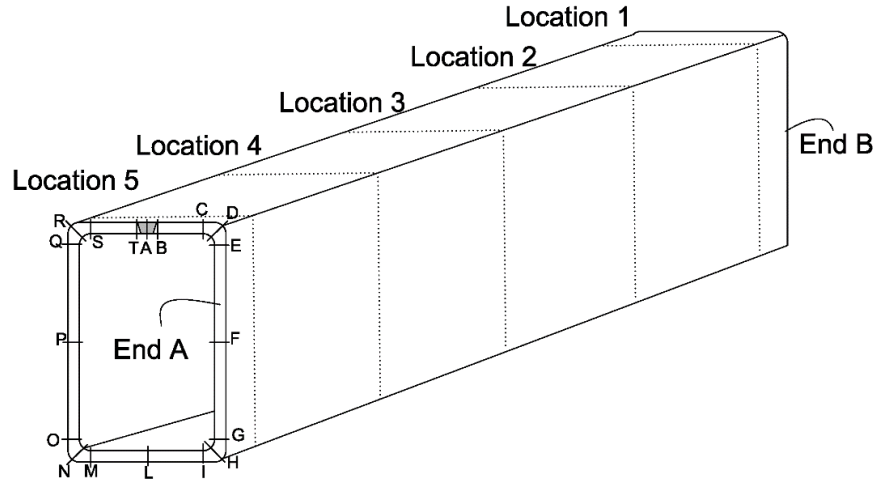


Figure A. 1 The location of measured data for all specimens

Table A. 1 Measured thickness, corner radius, and width for specimen S275\_50X50X6\_A

Thickness (mm)			Corner radius (mm)						Avg.	
Location	End A	End B	Location (mm)	50		1075		2100		
				R1	R2	R1	R2	R1	R2	
B	5.84	5.7	Corner 1 (D)	12	11	12	10	11	10	11.00
C	5.84	5.68	Corner 2 (H)	11	11	11	10	11	9	10.50
D (Corner)	6.03	6.04	Corner 3 (N)	10	11	10	10	10	10	10.17
E	5.77	5.76	Corner 4 (R)	11	11	11	11	10	12	11.00
F	5.57	5.49	Average:	<b>10.67</b>						
G	5.77	5.64	<hr/>							
H (Corner)	6.02	5.75	<b>width</b>							
I	5.77	5.52	Location (mm)	50	537	1075	1613	2100		
L	5.38	5.36	face 1	50.23	50.09	50.16	50.25	50.25	50.20	
M	5.51	5.48	face 2	50.1	50.14	50.33	50.31	50.15	50.21	
N (Corner)	5.71	5.82	face 3	50.07	50.16	50.04	50.04	50.21	50.10	
O	5.64	5.73	face 4	50.2	50.2	50.18	50.17	50.38	50.23	
P	5.51	5.55	<hr/>							
Q	5.7	5.72								
R (Corner)	5.8	5.8								
S	5.65	5.99								
T	5.56	5.99								
Average	<b>5.71</b>		<hr/>							

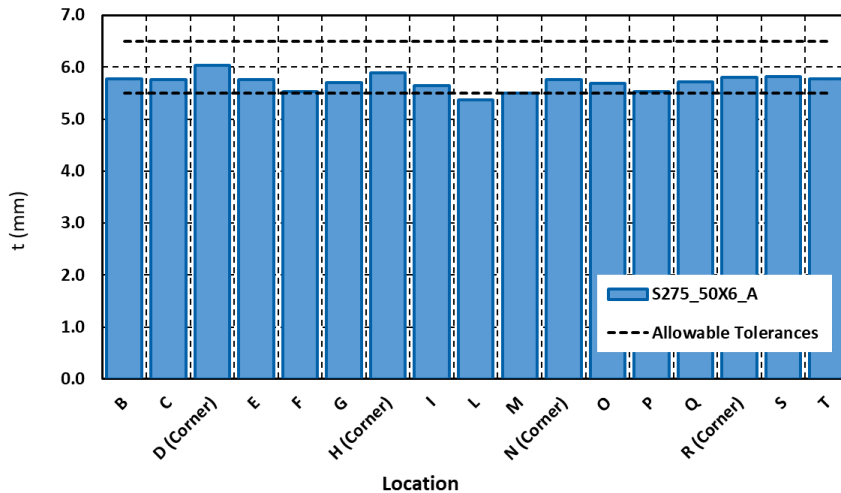


Figure A. 2 Difference between measured and nominal thickness for Specimen S275\_50X6\_A.

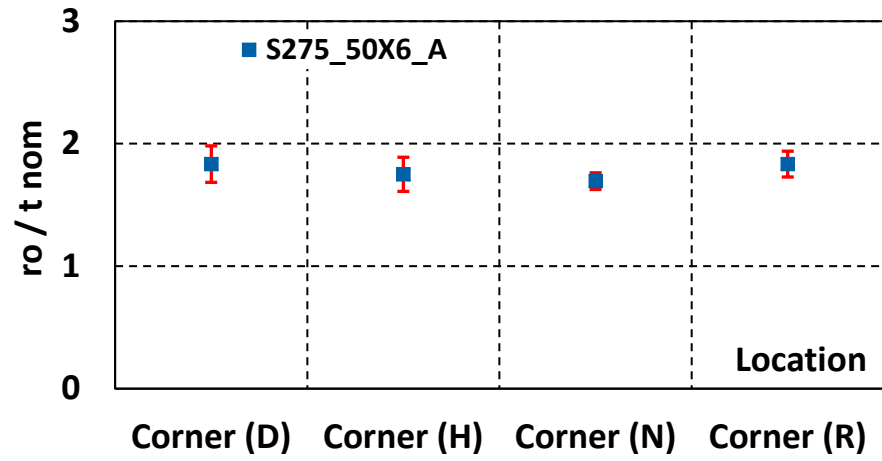


Figure A. 3 Normalized corner radii

Table A. 2 Measured thickness, corner radius, and width for specimen S275\_50X50X6\_B

Thickness (mm)			Corner radius (mm)						Avg.
Location	End A	End B	0		0				
			Location (mm)	R1	R2	R1	R2	R1	R2
B	5.84	5.55							
C	5.84	5.67	Corner 1	0	0	0	0	0	0
D (Corner)	5.8	5.77	Corner 2	0	0	0	0	0	0
E	5.72	5.78	Corner 3	0	0	0	0	0	0
F	5.62	5.5	Corner 4	0	0	0	0	0	0
G	5.86	5.75	Average:	<b>0.00</b>					
			<b>width</b>						
H (Corner)	5.87	5.77	Location (mm)	0	0	0	0	0	
I	5.66	5.66							
L	5.39	5.39	face 1	0	0	0	0	0	0.00
M	5.44	5.52	face 2	0	0	0	0	0	0.00
N (Corner)	5.72	5.81	face 3	0	0	0	0	0	0.00
O	5.67	5.9	face 4	0	0	0	0	0	0.00
P	5.57	5.55							
Q	5.76	5.72							
R (Corner)	5.8	5.85							
S	5.62	5.89							
T	5.61	5.89							
Average	<b>5.70</b>								

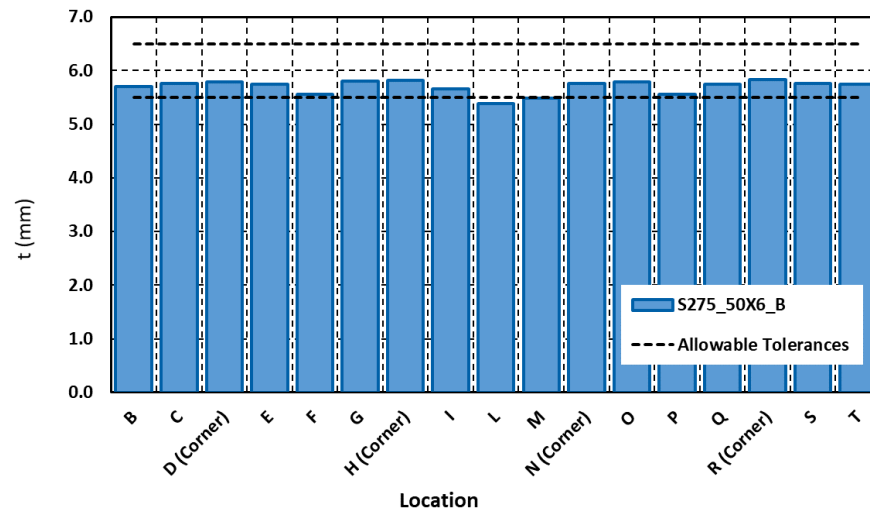


Figure A. 4 Difference between measured and nominal thickness for Specimen S275\_50X6\_B



Table A. 3 Measured thickness, corner radius and width for specimen S355\_50X50X6\_C

Thickness (mm)			Corner radius (mm)						Avg.	
Location	End A	End B	Location (mm)	50		925		1800		
				R1	R2	R1	R2	R1	R2	
B	5.72	5.8	Corner 1	11	12	12	12	11	11	11.50
C	5.72	5.81	Corner 2	12	10	12	11	12	11	11.33
D (Corner)	5.68	5.82	Corner 3	11	11	11	11	11	11	11.00
E	5.85	5.9	Corner 4	11	10	11	12	11	12	11.17
F	5.69	5.57	Average:	<b>11.25</b>						
G	5.83	5.79	<hr/>							
H (Corner)	5.77	5.71	<b>width</b>							
I	5.57	5.73	Location (mm)	50	460	925	1390	1800		
L	5.54	5.55	face 1	49.99	50.03	50.28	49.97	50.08	50.07	
M	5.6	5.43	face 2	50.14	50.73	50.34	50.18	50.06	50.29	
N (Corner)	5.75	5.74	face 3	49.9	50.3	49.9	50.38	50.01	50.10	
O	5.81	5.83	face 4	50.02	50.09	50.05	50.24	50.04	50.09	
P	5.6	5.71	<hr/>							
Q	5.88	5.76								
R (Corner)	5.95	5.8								
S	5.98	5.87								
T	5.83	5.87								
Average	<b>5.75</b>		<hr/>							

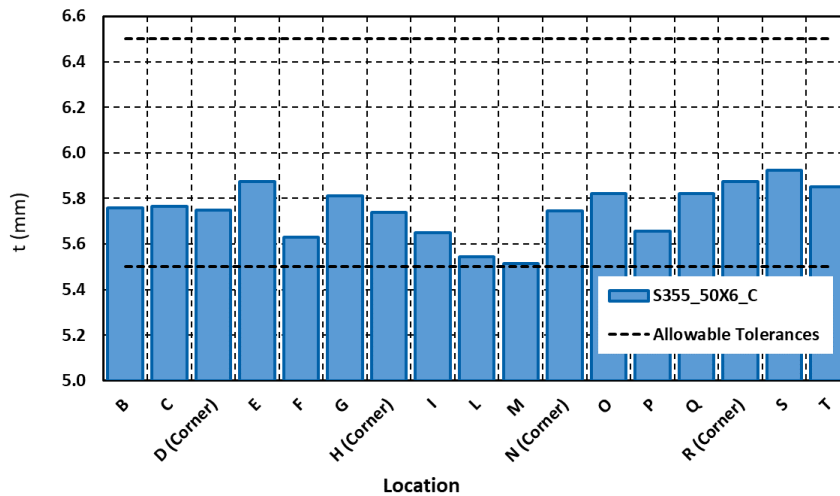


Figure A. 5 Difference between measured and nominal thickness for Specimen S355\_50X6\_C

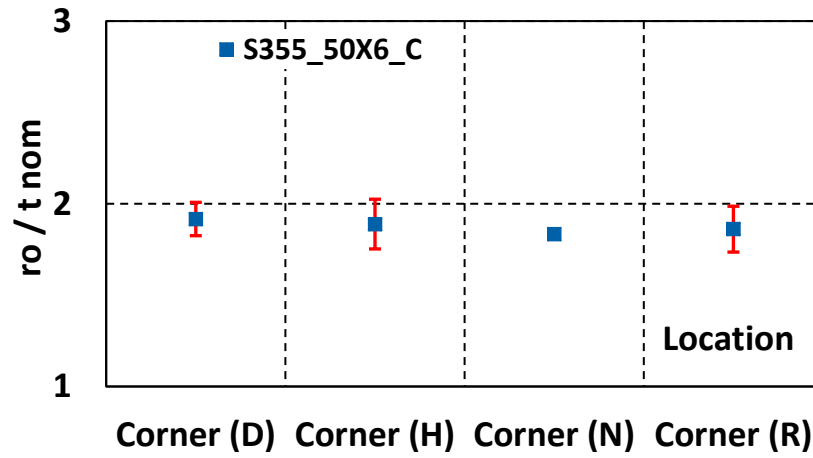


Figure A. 6 Normalized corner radii for specimen S355\_50X6\_C

Table A. 4 Measured thickness, corner radius and width for specimen S355\_50X50X6\_D

Thickness (mm)			Corner radius (mm)						Avg.	
Location	End A	End B	Location (mm)	50		1275		2500		
				R1	R2	R1	R2	R1	R2	
B	5.81	5.79	Corner 1	12	12	12	12	12	12	12.00
C	5.81	5.91	Corner 2	12	12	11	10	12	11	11.33
D (Corner)	5.68	5.78	Corner 3	11	12	12	12	11	12	11.67
E	5.82	5.9	Corner 4	12	11	12	12	12	11	11.67
F	5.65	5.53	Average:	<b>11.67</b>						
G	5.77	5.76	<hr/>							
H (Corner)	5.7	5.78	<b>width</b>							
I	5.64	5.73	Location (mm)	50	660	1275	1890	2500		
L	5.5	5.52	face 1	50.11	49.73	49.95	49.93	50.51		50.05
M	5.57	5.44	face 2	50.04	49.86	50.01	49.98	50.01		49.98
N (Corner)	5.82	5.69	face 3	50.04	49.8	49.86	49.81	49.88		49.88
O	5.81	5.8	face 4	49.92	49.8	50.07	49.98	50.03		49.96
P	5.52	5.7	<hr/>							
Q	5.82	5.8								
R (Corner)	5.82	5.76								
S	5.79	5.75								
T	5.81	5.75								
Average	<b>5.73</b>		<hr/>							

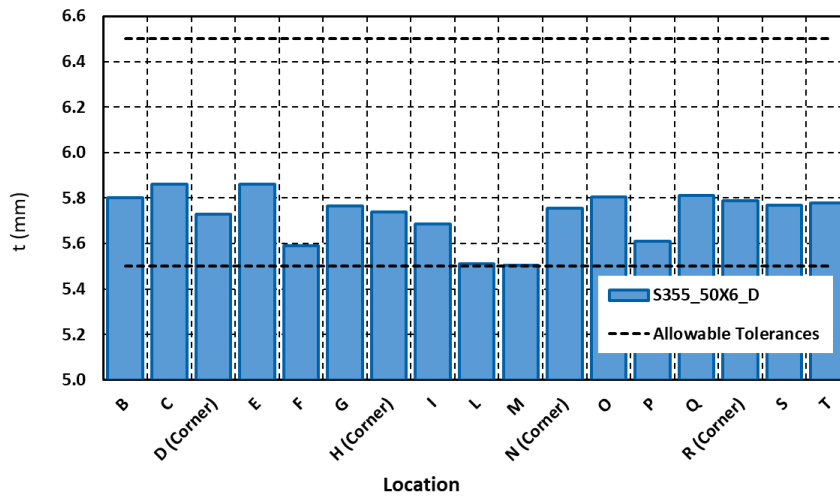


Figure A. 7 Difference between measured and nominal thickness for Specimen S355\_50X6\_D

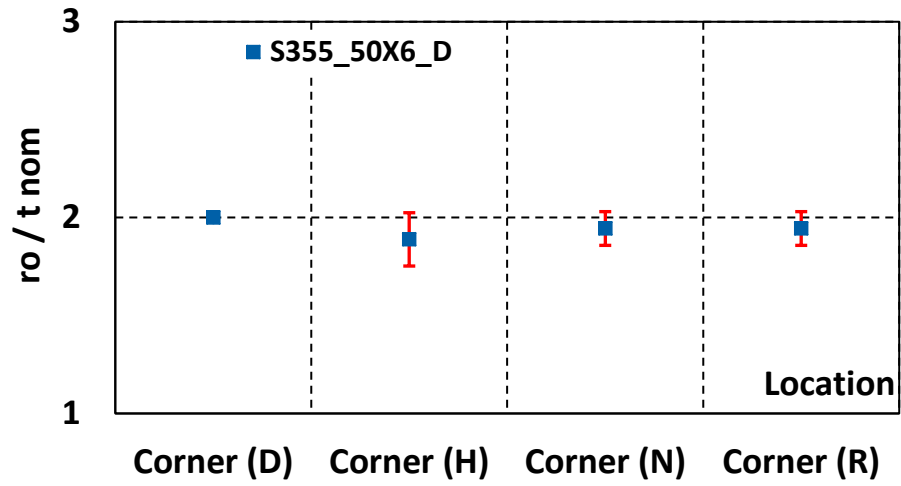


Figure A. 8 Normalized corner radii for specimen S355\_50X6\_D

Table A. 5 Measured thickness, corner radius and width for specimen S275\_100X8\_A

Thickness (mm)			Corner radius (mm)						Avg.	
Location	End A	End B	Location (mm)	50		250		450		
				R1	R2	R1	R2	R1	R2	
B	7.92	7.92	Corner 1	18	19	18	18	18	18	18.17
C	7.79	7.87	Corner 2	17	16	17	15	18	16	16.50
D (Corner)	8.27	8.06	Corner 3	15	15	16	19	17	18	16.67
E	8.08	7.91	Corner 4	22	23	21	22	21	24	22.17
F	8.12	8.1	Average:	<b>18.38</b>						
G	7.87	7.9								
H (Corner)	8.2	8.34	<b>width</b>							
I	7.78	7.83	Location (mm)	50	0	250	0	450		
L	7.69	7.79	face 1	100.12	0	99.92	0	100.4	60.09	
M	7.74	7.96	face 2	99.97	0	100.06	0	99.93	59.99	
N (Corner)	8.22	8.43	face 3	100.2	0	99.97	0	100.01	60.04	
O	7.89	8.01	face 4	100.2	0	99.83	0	100.15	60.04	
P	7.74	7.95								
Q	7.84	8.05								
R (Corner)	8.12	8.44								
S	7.76	8.03								
T	7.78	8.01								
Average	<b>7.98</b>									

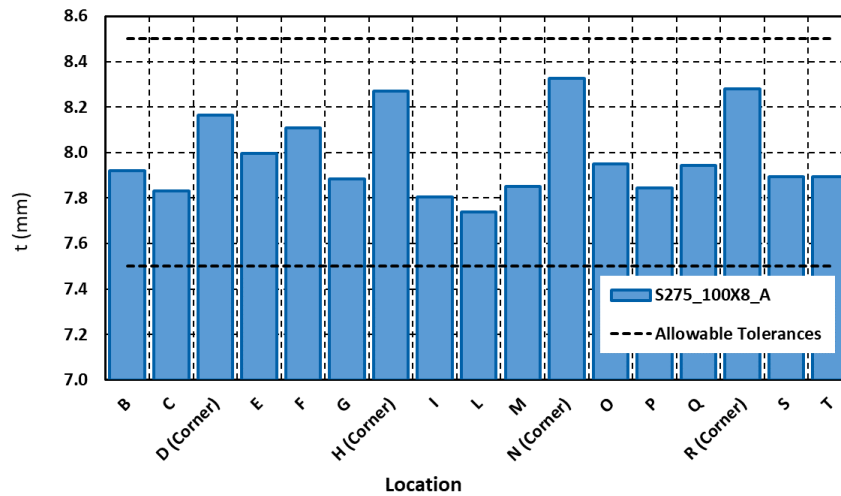


Figure A. 9 Difference between measured and nominal thickness for Specimen S275\_100X8\_A

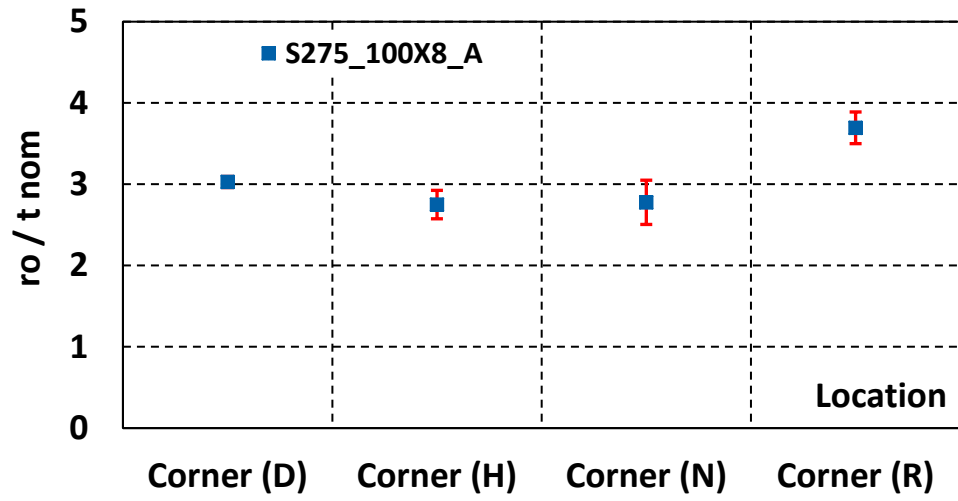


Figure A. 10 Normalized corner radii for specimen S275\_100X8\_A

Table A. 6 5 Measured thickness, corner radius and width for specimen S275\_100X8\_B

Thickness (mm)			Corner radius (mm)						Avg.	
Location	End	End	Location (mm):	50	595		1140			
	A	B								
B	8	8.1		R1	R2	R1	R2	R1	R2	
C	8.01	8.01	Corner 1	19	15	19	15	17	16	16.83
D (Corner)	8.65	8.27	Corner 2	15	17	16	17	15	16	16.00
E	8.19	8.2	Corner 3	17	17	18	18	16	17	17.17
F	7.86	7.96	Corner 4	23	22	22	23	23	21	22.33
G	8.25	8.1	<b>Average:</b>	<b><u>18.08</u></b>						
H (Corner)	8.27	8.29	<b>width</b>							
I	8.11	8.06	Location (mm):	50	270	595	920	1140		
L	7.96	8.13	face 1	99.92	100.72	99.92	99.94	100.16	100.13	
M	8.1	8.18	face 2	100.16	100.79	100.24	100.45	100.43	100.41	
N (Corner)	8.31	8.42	face 3	99.98	100.03	100.07	99.92	100.08	100.02	
O	8.12	8.37	face 4	99.96	100.01	100.01	100.41	100.32	100.14	
P	7.96	7.91								
Q	8.17	8.04								
R (Corner)	8.37	8.27								
S	7.82	8.14								
T	8.01	7.79								
<b>Average</b>	<b><u>8.13</u></b>									

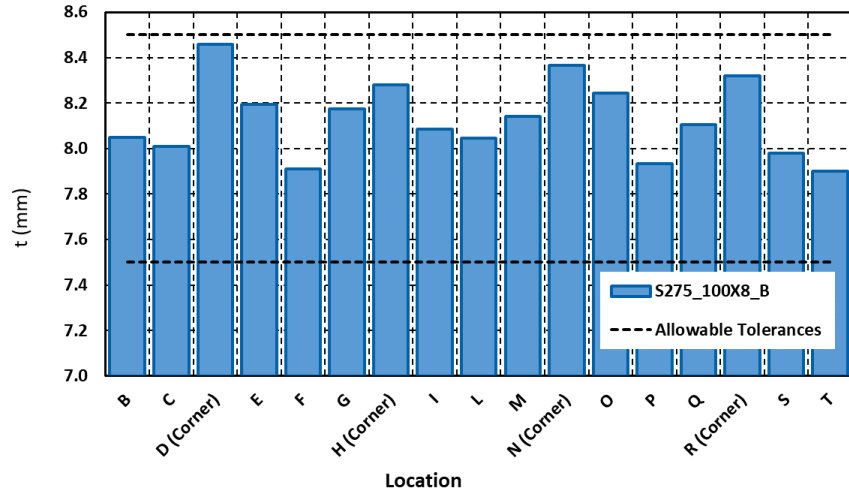


Figure A. 11 9 Difference between measured and nominal thickness for Specimen S275\_100X8\_B

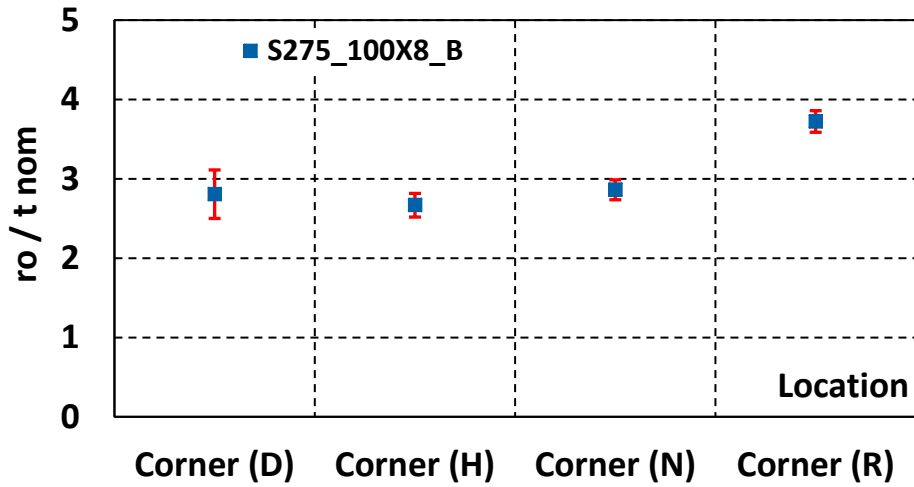


Figure A. 12 Normalized corner radii for specimen S275\_100X8\_B



Table A. 7 Measured thickness, corner radius and width for specimen S355\_100X8\_C

Thickness (mm)			Corner radius (mm)				Avg.		
Location	End A	End B	Location (mm)	R1	R2	0	0		
B	7.82	7.72				R 1	R 2		
C	7.82	7.68	Corner 1	0	0	0	0	0.00	
D (Corner)	8.18	7.8	Corner 2	0	0	0	0	0.00	
E	8.27	7.65	Corner 3	0	0	0	0	0.00	
F	8.08	7.68	Corner 4	0	0	0	0	0.00	
G	8.12	7.86	Average:	<b>0.00</b>					
H (Corner)	8.26	7.88	<b>width</b>						
I	8.15	7.16	Location (mm)	0	0	0	0	0	
L	7.75	7.46	face 1	0	0	0	0	0.00	
M	8.16	7.83	face 2	0	0	0	0	0.00	
N (Corner)	8.48	8.06	face 3	0	0	0	0	0.00	
O	8.06	7.78	face 4	0	0	0	0	0.00	
P	7.99	7.62							
Q	8.04	7.87							
R (Corner)	8.15	8.04							
S	7.96	7.57							
T	7.86	7.78							
Average	<b>7.90</b>								

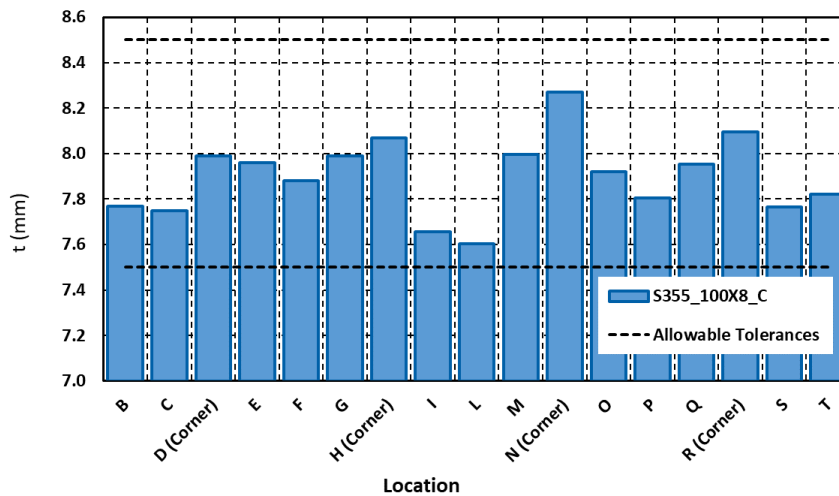


Figure A. 13 Difference between measured and nominal thickness for Specimen S355\_100X8\_C

Table A. 8 Measured thickness, corner radius and width for specimen S355\_100X8\_D

Thickness (mm)			Corner radius (mm)						Avg.	
Location	End A	End B	Location	50		1325		2600		
			(mm)	R1	R2	R1	R2	R1	R2	
B	7.77	7.74	Corner 1	20	21	16	19	22	22	20.00
C	7.79	7.83	Corner 2	19	18	21	22	19	21	20.00
D (Corner)	8.14	8.16	Corner 3	16	17	17	18	16	18	17.00
E	7.91	7.93	Corner 4	16	19	16	16	16	20	17.17
F	7.75	7.78	Average:	<b>18.54</b>						
G	7.85	7.92								
H (Corner)	8.15	8.22	<b>width</b>							
I	7.8	7.81	Location (mm)	50	690	1325	1960	2600		
L	7.65	7.67	face 1	99.75	99.72	100.0 8	99.75	100.2	99.89	
M	7.8	7.89	face 2	99.82	100.0 2	99.77	100.0 3	99.88	99.90	
N (Corner)	8.17	8.16	face 3	99.99	100.0 7	100.0 6	100.3 5	99.93	100.08	
O	7.82	7.92	face 4	100.0 7	99.91	100.1 3	99.99	100	100.02	
P	7.72	7.76								
Q	7.87	7.97								
R (Corner)	8.16	8.22								
S	7.86	7.89								
T	7.69	7.83								
Average	<b>7.90</b>									

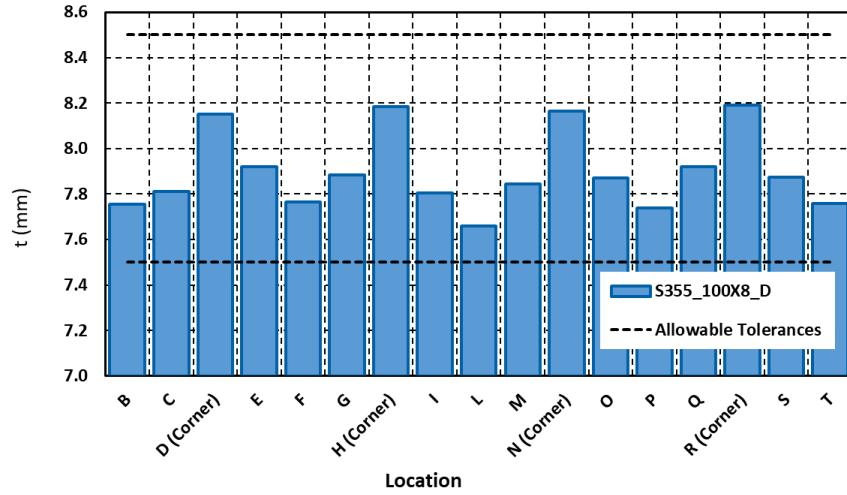


Figure A. 14 Difference between measured and nominal thickness for Specimen S355\_100X8\_D

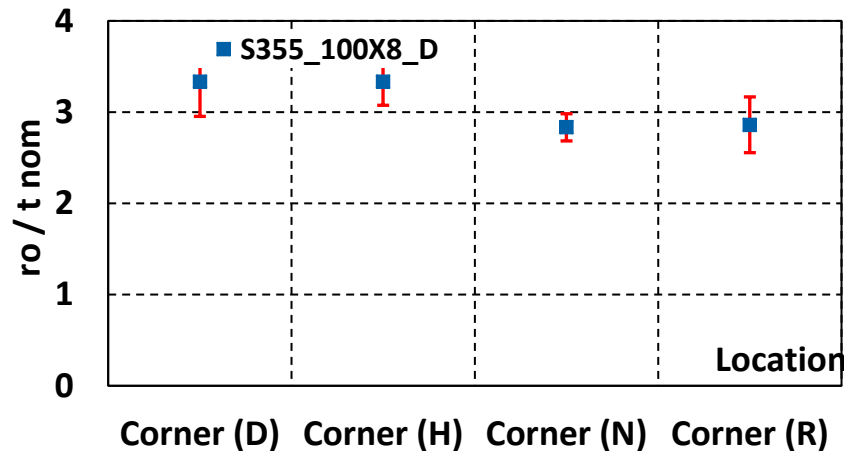


Figure A. 15 Normalized corner radii for specimen S355\_100X8\_D

Table A. 9 Measured thickness, corner radius and width for specimen S355\_200X8\_A

Thickness (mm)			Corner radius (mm)						Avg.	
Location	End A	End B	0		0					
			Location (mm)	R1	R2	R1	R2	R1	R2	
B	7.8	7.4	Corner 1	0	0	0	0	0	0	0.00
C	7.8	7.46	Corner 2	0	0	0	0	0	0	0.00
D (Corner)	8.1	7.79	Corner 3	0	0	0	0	0	0	0.00
E	7.66	7.61	Corner 4	0	0	0	0	0	0	0.00
F	7.54	7.39	Average:	<b>0.00</b>						
G	7.72	7.77	<hr/>							
H (Corner)	8.15	7.78	<b>width</b>							
I	7.7	7.75	Location (mm)	0	0	0	0	0		
L	7.53	7.43	face 1	0	0	0	0	0		0.00
M	7.75	7.82	face 2	0	0	0	0	0		0.00
N (Corner)	8.02	8.04	face 3	0	0	0	0	0		0.00
O	7.6	7.64	face 4	0	0	0	0	0		0.00
P	7.43	7.47	<hr/>							
Q	7.65	7.65								
R (Corner)	7.93	7.88								
S	7.6	7.67								
T	7.66	7.5								
Average	<b>7.70</b>		<hr/>							

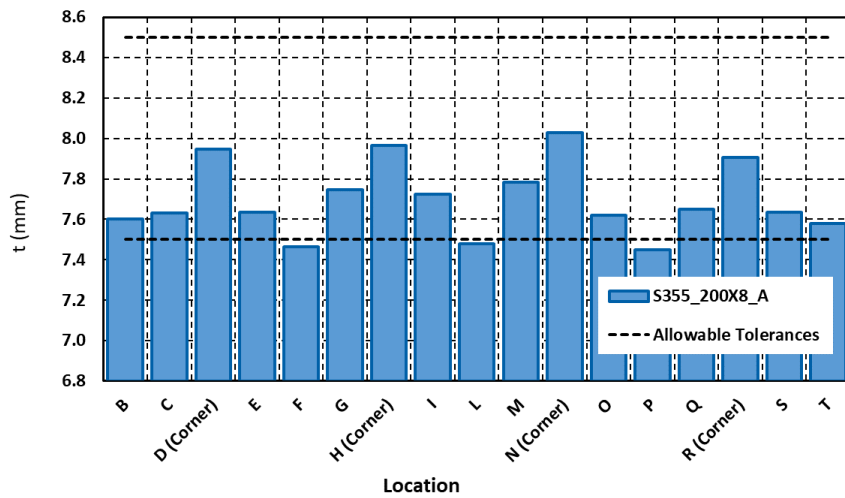


Figure A. 16 Difference between measured and nominal thickness for Specimen S355\_200X8\_A

Table A. 10 Measured thickness, corner radius and width for specimen S355\_200X8\_B

Thickness (mm)			Corner radius (mm)						Avg.	
Location	End A	End B	Location (mm)	0		0		0		
				R1	R2	R1	R2	R1	R2	
B	7.49	7.61	Corner 1	0	0	0	0	0	0	0.00
C	7.59	7.67	Corner 2	0	0	0	0	0	0	0.00
D (Corner)	8.17	8.1	Corner 3	0	0	0	0	0	0	0.00
E	7.63	7.63	Corner 4	0	0	0	0	0	0	0.00
F	7.51	7.54	Average:	<b>0.00</b>						
G	7.6	7.73	<b>width</b>							
H (Corner)	8.08	8.13	Location (mm)	0	0	0	0	0		
I	7.71	7.8	face 1	0	0	0	0	0	0.00	
L	7.49	7.66	face 2	0	0	0	0	0	0.00	
M	7.6	7.79	face 3	0	0	0	0	0	0.00	
N (Corner)	8.02	8.1	face 4	0	0	0	0	0	0.00	
O	7.56	7.73								
P	7.43	7.62								
Q	7.45	7.74								
R (Corner)	8.14	8.17								
S	7.54	7.78								
T	7.36	7.82								
Average	<b>7.74</b>									

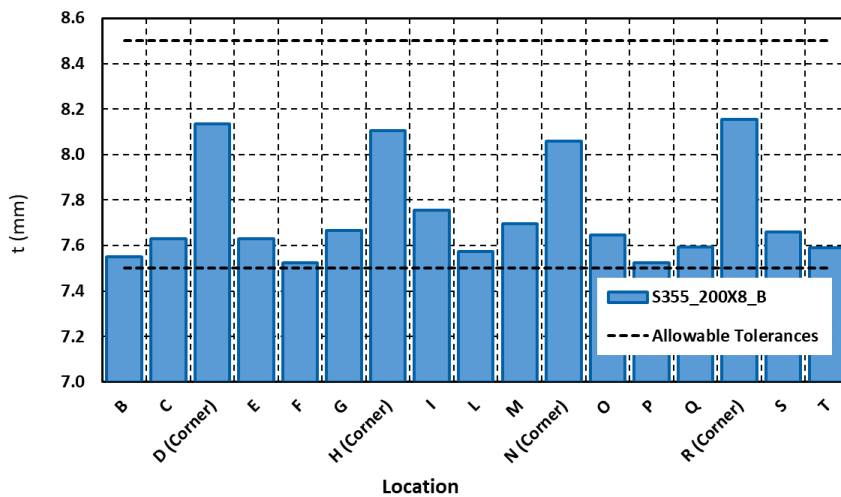


Figure A. 17 Difference between measured and nominal thickness for Specimen S355\_200X8\_B

Figure A. 18 Measured thickness, corner radius and width for specimen S275\_60X40X6\_A

Thickness (mm)			Corner radius (mm)						Average	
Location	End A	End B	Location (mm)	50		550		1050		
B	6.27	6.67	R1	R1	R2	R1	R2	R1	R2	
C	6.3	6.49	Corner 1	10	11	11	10	11	14	11.17
D (Corner)	6.42	6.3	Corner 2	9.5	10.5	9.5	11.5	10	9	10.00
E	6.2	6.25	Corner 3	8.5	9.5	9.5	10	7	9	8.92
F	5.98	6.1	Corner 4	11.5	13	11	12	10	11	11.42
G	6.19	6.28	Average:	<b>10.38</b>						
H (Corner)	6.31	7.03	<b>width</b>							
I	6.08	6.36	Location (mm)	50	300	550	800	1050		
L	5.9	5.91	face 1	40.03	40.11	40.08	40.06	40.59	40.17	
M	6.14	6.02	face 2	60.015	60.12	60.1	60.15	60.13	60.10	
N (Corner)	6.51	6.51	face 3	40.27	40.17	40.11	40.07	40.1	40.14	
O	6.35	6.23	face 4	60.13	60.11	60.28	60.26	60.14	60.18	
P	6.1	6								
Q	6.17	6.29								
R (Corner)	6.26	6.47								
S	6.28	6.32								
T	6.67	6.06								
Average	<b>6.28</b>									

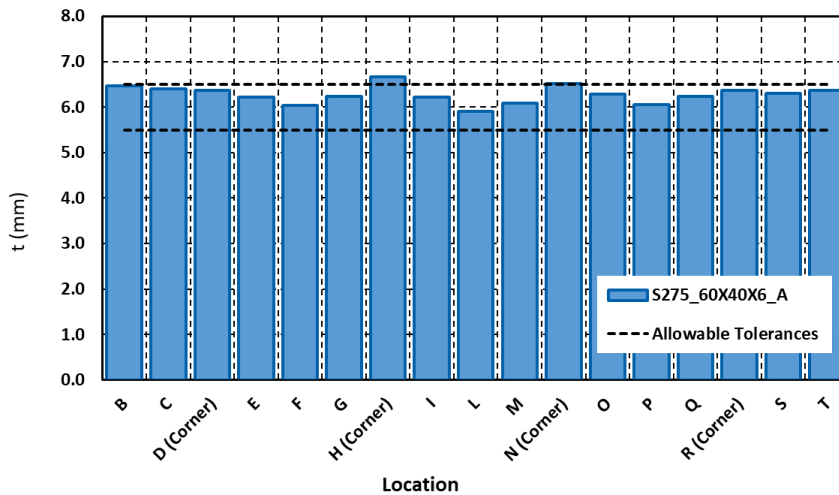


Figure A. 19 Measured thickness, corner radius and width for specimen S275\_60X40X6\_A

Table A. 11 Measured thickness, corner radius and width for specimen S275\_60X40X6\_B

Thickness (mm)			Corner radius (mm)						Average	
Location	End A	End B	Location (mm)	50		250		450		
				R1	R2	R1	R2	R1	R2	
B	6.21	6.62	Corner 1	12	11	11	12	12	14	12.00
C	6.29	6.44	Corner 2	10	9	8	9	10	9	9.17
D (Corner)	6.46	6.25	Corner 3	9	9	10	9	9	10	9.33
E	6.7	6.27	Corner 4	10	12	11	10	11	11	10.83
F	6.02	6.09	Average:	<b>10.33</b>						
G	6.14	6.27	<hr/>							
H (Corner)	6.43	6.85	<b>width</b>							
I	6.13	6.34	Location (mm)	50	0	250	0	450		
L	5.96	5.92	face 1	60.38	0	60.34	0	60.12		36.17
M	6.11	6	face 2	40.14	0	40.32	0	40.13		24.12
N (Corner)	6.53	6.29	face 3	60.13	0	60.85	0	60.11		36.22
O	6.46	6.1	face 4	39.48	0	39.97	0	40.31		23.95
P	6.1	5.98	<hr/>							
Q	6.29	6.3								
R (Corner)	6.29	6.54								
S	6.29	6.3								
T	6.65	6.15								
Average	<b>6.29</b>		<hr/>							

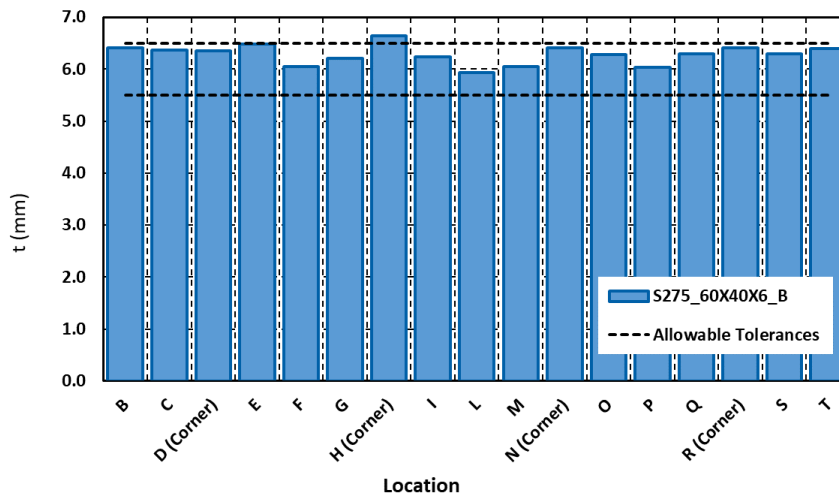


Table A. 12 Difference between measured and nominal thickness for Specimen S275\_60X40X6\_B



Table A. 13 Measured thickness, corner radius and width for specimen S275\_60X40X6\_C

Thickness (mm)			Corner radius (mm)						Avg.	
Location	End A	End B	Location (mm)	50		1175		2300		
				R1	R2	R1	R2	R1	R2	
B	6.35	6.17	Corner 1	9	10	10	11	11	11	10.33
C	6.35	6.27	Corner 2	10	10	9	10	10	11	10.00
D (Corner)	6.37	6.36	Corner 3	9	10	9	11	10	10	9.83
E	6.24	6.51	Corner 4	11	10	11	11	11	12	11.00
F	6.07	5.94	Average:	<b>10.29</b>						
G	6.47	6.2	<hr/>							
H (Corner)	6.55	6.25	<b>width</b>							
I	6.2	6.13	Location (mm)	50	580	1175	1770	2300		
L	5.95	5.88	face 1	60.74	60.1	60.14	60.19	60.29		60.29
M	6.03	6.16	face 2	40.22	40.01	40.37	40.14	40.13		40.17
N (Corner)	6.46	6.58	face 3	60.48	60.12	60.18	60.25	60.14		60.23
O	6.3	6.56	face 4	40.18	41.25	40.4	40.18	40.27		40.46
P	5.94	6.11	<hr/>							
Q	6.34	6.16								
R (Corner)	6.4	6.22								
S	6.2	6.48								
T	6.12	6.48								
Average	<b>6.26</b>									

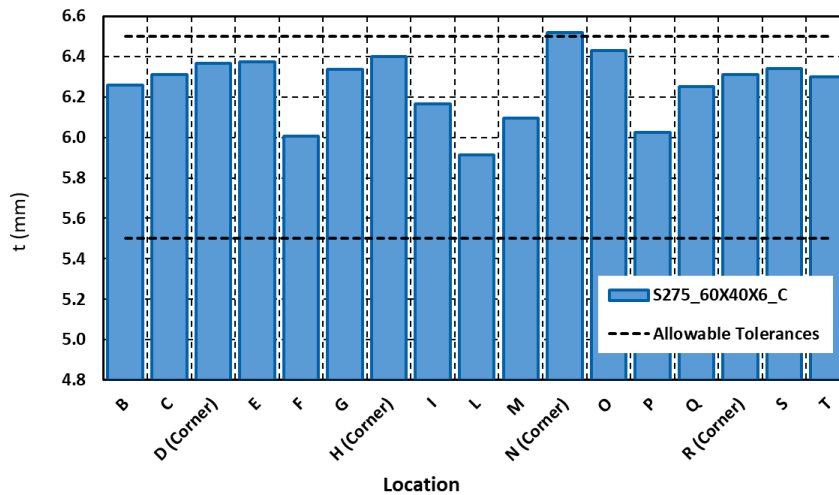


Figure A. 20 Difference between measured and nominal thickness for Specimen S275\_60X40X6\_C

Table A. 14 Measured thickness, corner radius and width for specimen S275\_60X40X6\_D

Thickness (mm)			Corner radius (mm)						Avg.	
Location	End A	End B	Location (mm)	50		875		1700		
				R1	R2	R1	R2	R1	R2	
B	6.48	6.1	Corner 1	9	9	8	9	8	10	8.83
C	6.48	6.29	Corner 2	8	10	9	10	9	10	9.33
D (Corner)	6.2	6.39	Corner 3	10	10	10	11	10	11	10.33
E	6.14	6.34	Corner 4	10	14	11	13	11	14	12.17
F	6.05	5.97	Average:	<b>10.17</b>						
G	6.55	6.46	<hr/>							
H (Corner)	6.57	6.3	<b>width</b>							
I	6.21	6.24	Location (mm)	50	420	875	1330	1700		
L	5.89	5.9	face 1	60.11	60.13	60.08	60.1	60.18	60.12	
M	6.08	6.16	face 2	40.04	40.22	40.33	40.05	40.07	40.14	
N (Corner)	6.33	6.71	face 3	60.17	60.14	60.07	60.14	60.21	60.15	
O	6.49	6.76	face 4	40.08	40.16	40.41	40.32	40.32	40.26	
P	5.96	6.09	<hr/>							
Q	6.42	6.26								
R (Corner)	6.38	6.38								
S	6.35	6.33								
T	6.19	6.33								
Average	<b>6.29</b>		<hr/>							

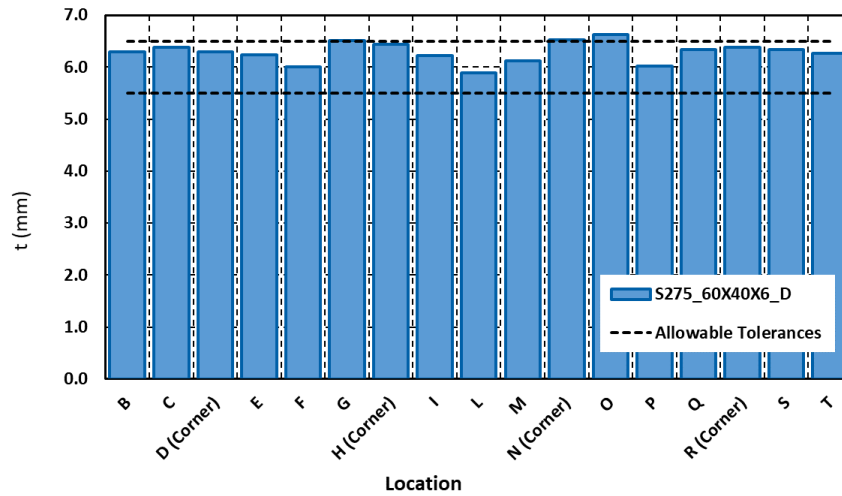


Figure A. 21 Difference between measured and nominal thickness for Specimen S275\_60X40X6\_D

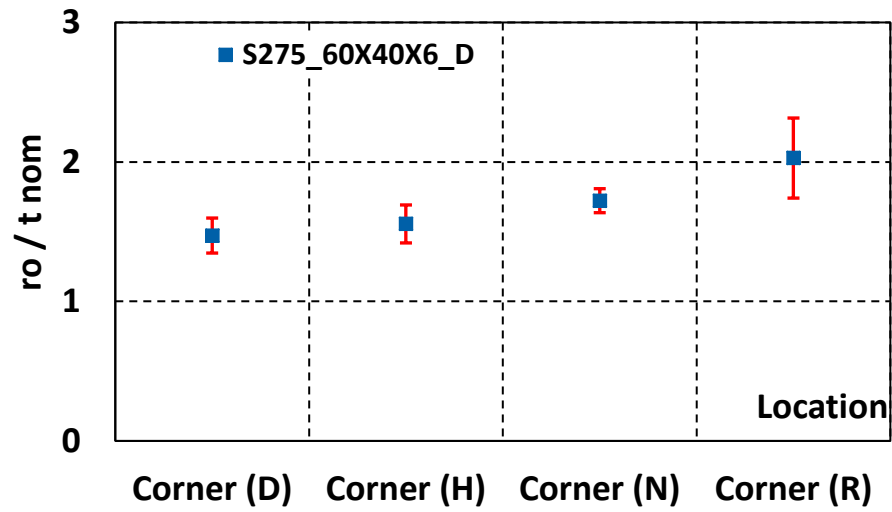


Figure A. 22 Normalized corner radii for specimen S275\_60X40X6\_D

Table A. 15 Measured thickness, corner radius and width for specimen S355\_70X50X6\_A

Thickness (mm)			Corner radius (mm)						Avg.
Location	End A	End B	Location (mm)	50		1000		1950	
B	5.63	5.98	R1	R1	R2	R1	R2	R1	R2
C	5.73	5.98	Corner 1	10	11	11	12	11	11
D (Corner)	5.76	5.69	Corner 2	10	11	10	10	11	11
E	5.68	5.65	Corner 3	11	11	11	11	11	11
F	5.46	5.57	Corner 4	10	10	10	10	9	10
G	5.62	5.89	Average:	<b>10.58</b>					
Thickness (mm)			width						
Location	End A	End B	Location (mm)	50	450	1000	1550	1995	
I	5.65	5.83	face 1	70.14	70.2	70.14	70.13	70.2	70.16
L	5.4	5.4	face 2	50.13	50.18	50.13	50.25	50.14	50.17
M	5.66	5.61	face 3	70.24	70.22	70.23	70.23	70.19	70.22
N (Corner)	5.92	5.79	face 4	50.1	50.14	50.05	50.24	50.05	50.12
O	5.89	5.77							
P	5.55	5.5							
Q	5.61	5.67							
R (Corner)	5.66	5.88							
S	5.76	5.73							
T	5.76	5.8							
Average	<b>5.72</b>								

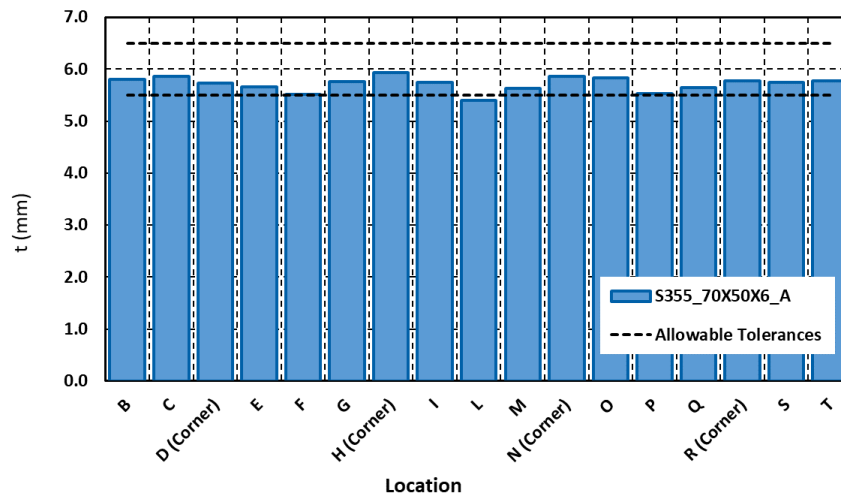


Figure A. 23 Difference between measured and nominal thickness for Specimen S355\_70X50X6\_A

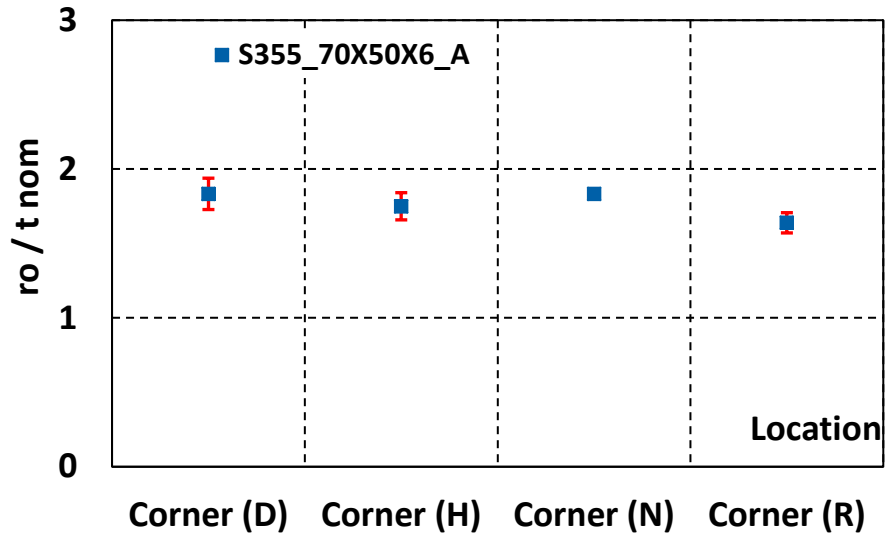


Figure A. 24 Normalized corner radii for specimen S355\_70X50X6\_A

Table A. 16 Measured thickness, corner radius and width for specimen S355\_70X50X6\_B

Thickness (mm)			Corner radius (mm)						Avg.	
Location	End A	End B	Location (mm)	50		650		1300		
				R1	R2	R1	R2	R1	R2	
B	5.73	5.86	Corner 1	12	11	12	11	12	12	11.67
C	5.81	5.86	Corner 2	11	10	12	10	11	11	10.83
D (Corner)	6.04	5.83	Corner 3	11	11	11	11	11	12	11.17
E	5.69	5.73	Corner 4	10	10	10	11	10	11	10.33
F	5.56	5.67	Average:	<b>11.00</b>						
G	5.69	5.87								
H (Corner)	6.03	6.04	<b>width</b>							
I	5.71	5.74	Location (mm)	50	350	650	950	1250		
L	5.47	5.52	face 1	70.17	70.25	70.23	70.2	70.33	70.24	
M	5.66	5.68	face 2	50.19	50.19	50.16	50.3	50.22	50.21	
N (Corner)	6	5.89	face 3	70.34	70.24	70.29	70.25	70.29	70.28	
O	5.93	5.71	face 4	50.18	50.09	50.08	50.22	50.15	50.14	
P	5.62	5.59								
Q	5.7	5.66								
R (Corner)	5.79	5.88								
S	5.62	5.84								
T	5.62	5.75								
Average	<b>5.76</b>									

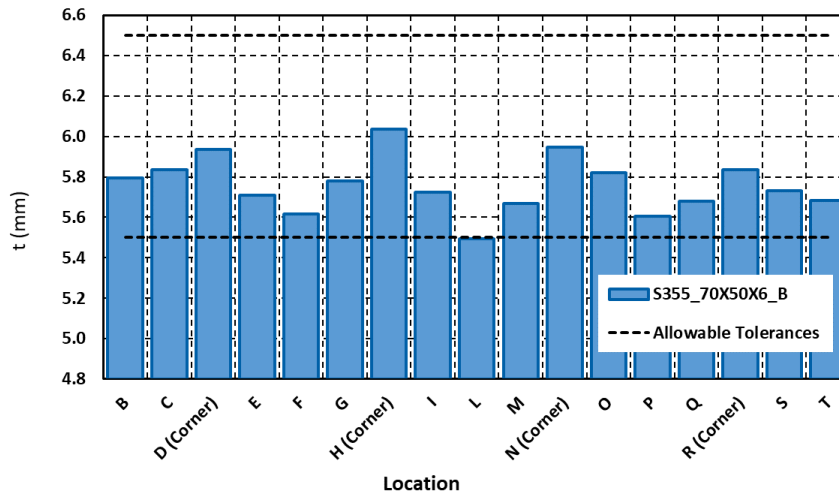


Figure A. 25 Difference between measured and nominal thickness for Specimen S355\_70X50X6\_B

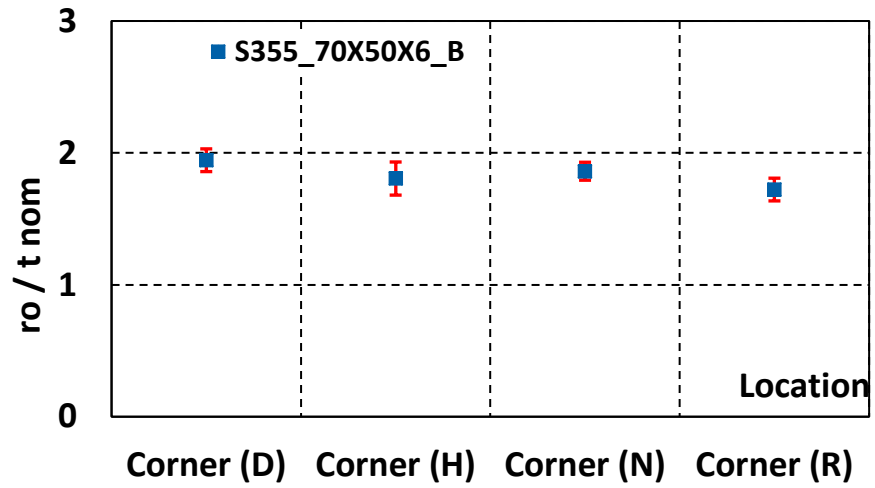


Figure A. 26 Normalized corner radii for specimen S355\_70X50X6\_B

Table A. 17 Measured thickness, corner radius and width for specimen S355\_70X50X6\_C

Thickness (mm)			Corner radius (mm)						Avg.	
Location	End A	End B	Location (mm)	50		1285		2520		
B	5.59	5.68		R1	R2	R1	R2	R1	R2	
C	5.65	5.68	Corner 1	11	12	11	10	11	11	11.00
D (Corner)	5.75	5.63	Corner 2	9	10	10	10	10	10	9.83
E	5.71	5.63	Corner 3	11	11	11	12	11	11	11.17
F	5.46	5.5	Corner 4	10	10	11	10	10	10	10.17
G	5.72	5.79	Average:	<b>10.54</b>						
H (Corner)	5.83	5.8	<b>width</b>							
I	5.66	5.68	Location (mm)	50	620	1285	1950	2520		
L	5.36	5.4	face 1	70.28	70.28	70.24	70.3	70.32	70.28	
M	5.52	5.47	face 2	50.05	50.2	50.03	50.15	50.1	50.11	
N (Corner)	5.75	5.75	face 3	70.19	70.28	70.21	70.21	70.2	70.22	
O	5.87	5.73	face 4	50.14	50.25	50.33	50.21	50.23	50.23	
P	5.51	5.48								
Q	5.58	5.61								
R (Corner)	5.65	5.77								
S	5.65	5.367								
T	5.65	5.64								
Average	<b>5.63</b>									



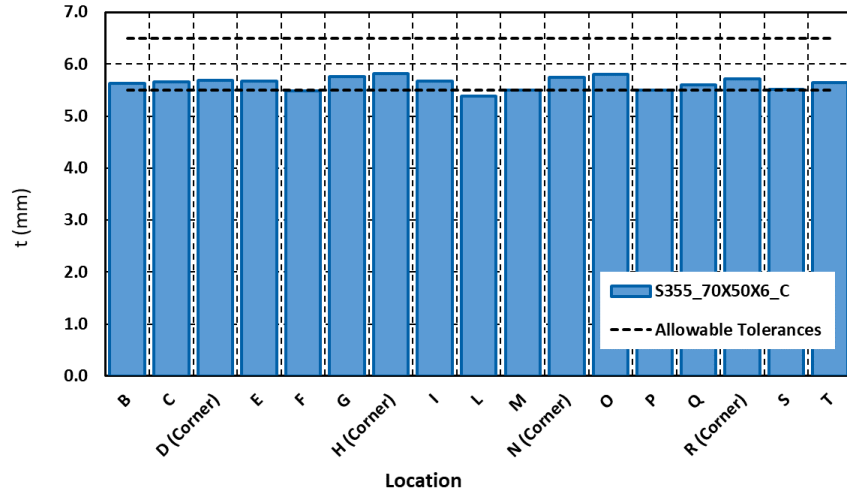


Figure A. 27 Difference between measured and nominal thickness for Specimen S355\_70X50X6\_C

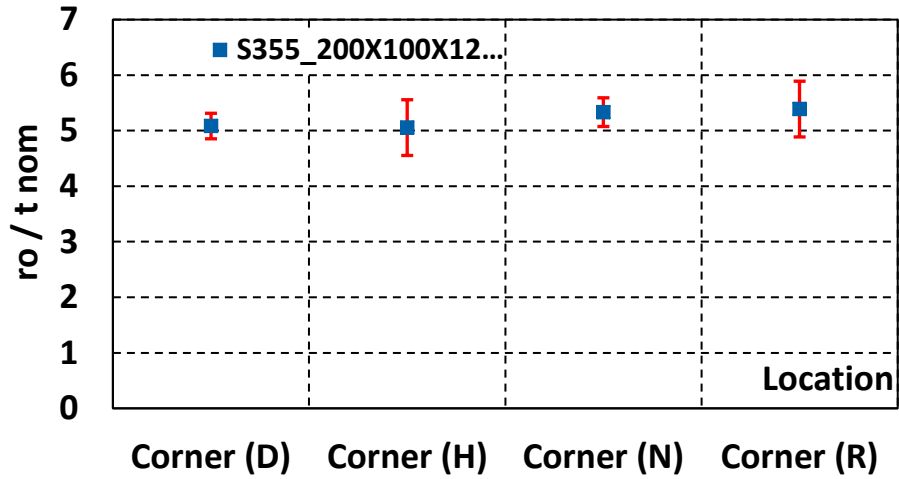


Figure A. 28 Normalized corner radii for specimen S355\_70X50X6\_C

Table A. 18 Measured thickness, corner radius and width for specimen S355\_200X100X12.5\_A

Thickness (mm)			Corner radius (mm)						Avg.	
Location	End A	End B	Location (mm)	?	0	0	0	0		
				R1	R2	R1	R2	R1	R2	
B	12.39	12.32	Corner 1	0	0	0	0	0	0	0.00
C	12.5	12.34	Corner 2	0	0	0	0	0	0	0.00
D (Corner)	12.61	12.5	Corner 3	0	0	0	0	0	0	0.00
E	12.61	12.6	Corner 4	0	0	0	0	0	0	0.00
F	12.29	12.1	Average:	<b>0.00</b>						
G	12.5	12.55								
H (Corner)	12.73	12.57	<b>width</b>							
I	12.28	12.3	Location (mm)	50	300	600	900	1150		
L	12.38	12.2	face 1	100.55	100.51	100.52	100.62	100.1	100.46	
M	12.54	12.2	face 2	200.1	200	200.14	201	201.2	200.49	
N (Corner)	12.67	12.53	face 3	100.75	100.48	100.46	100.47	100.9	100.62	
O	12.68	12.51	face 4	200.18	200.12	200.16	200.08	200	200.11	
P	12.3	12.09								
Q	12.63	12.47								
R (Corner)	12.7	12.5								
S	12.44	12.3								
T	12.6	12								
Average	<b>12.44</b>									

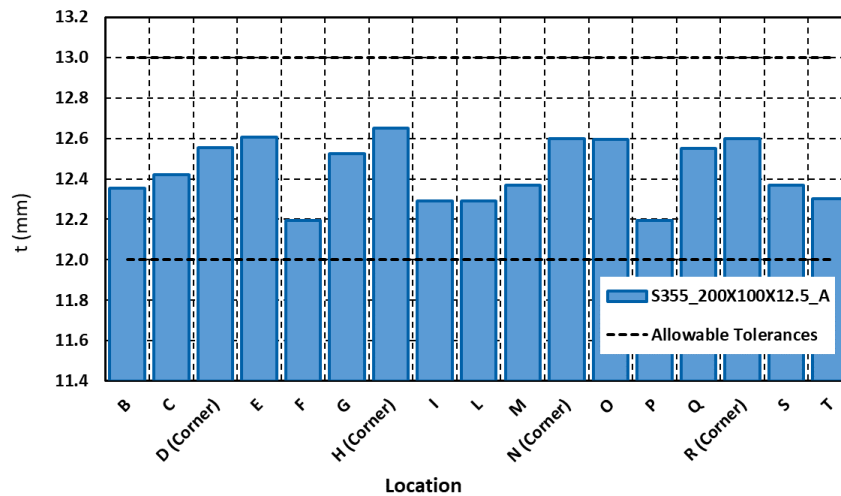


Figure A. 29 Difference between measured and nominal thickness for Specimen S355\_200X100X12.5\_A

Table A. 19 Measured thickness, corner radius and width for specimen S355\_200X100X12.5\_B

Thickness (mm)			Corner radius (mm)						Avg.	
Location	End A	End B	Location (mm)	50		600		1150		
				R1	R2	R1	R2	R1	R2	
B	12.64	12.93	Corner 1	31	29	32	29	32	30	30.50
C	12.53	12.79	Corner 2	27	32	28	33	28	34	30.33
D (Corner)	12.87	12.92	Corner 3	33	31	33	30	34	31	32.00
E	12.43	12.6	Corner 4	29	36	30	35	30	34	32.33
F	12.49	12.36	Average:	<b>31.29</b>						
G	12.51	12.73	<b>width</b>							
H (Corner)	12.64	12.79	Location (mm)	0	0	0	0	0		
I	12.59	12.72	face 1	0	0	0	0	0		0.00
L	12.53	12.65	face 2	0	0	0	0	0		0.00
M	12.72	12.43	face 3	0	0	0	0	0		0.00
N (Corner)	12.67	12.77	face 4	0	0	0	0	0		0.00
O	12.52	12.94								
P	12.34	12.4								
Q	12.61	12.77								
R (Corner)	12.79	12.71								
S	12.62	12.64								
T	12.46	12.5								
Average	<b>12.64</b>									

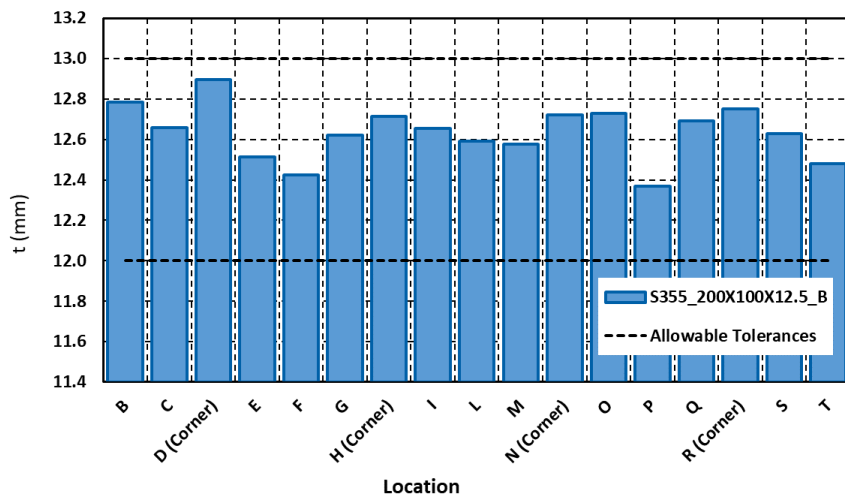


Figure A. 30 Difference between measured and nominal thickness for Specimen S355\_200X100X12.5\_B

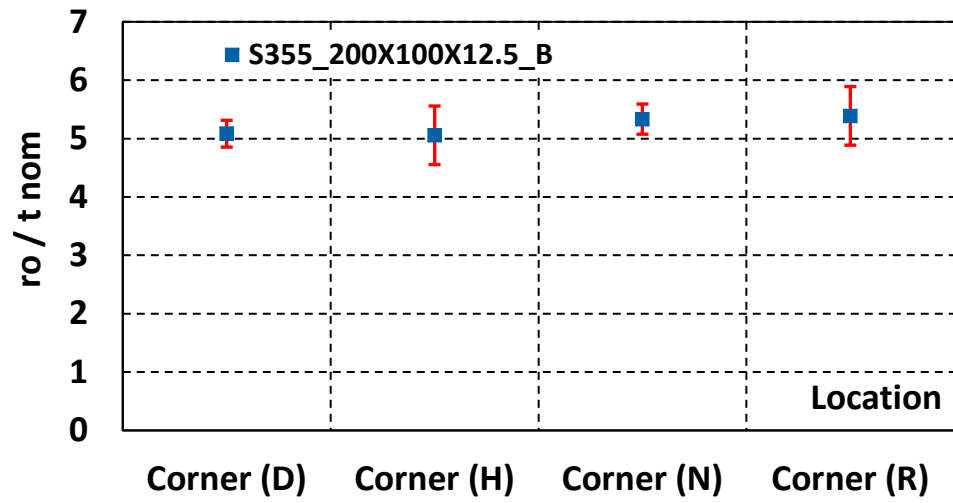


Figure A. 31 Normalized corner radii for specimen S355\_200X100X12.5\_B

Table A. 20 Measured thickness, corner radius and width for specimen S355\_220X140X8\_A

Thickness (mm)			Corner radius (mm)						Avg.	
Location	End A	End B	Location (mm)	0		0		0		
				R1	R2	R1	R2	R1	R2	
B	8	8.42	Corner 1	0	0	0	0	0	0	0.00
C	7.81	7.94	Corner 2	0	0	0	0	0	0	0.00
D (Corner)	8.2	8.32	Corner 3	0	0	0	0	0	0	0.00
E	7.8	8.07	Corner 4	0	0	0	0	0	0	0.00
F	7.66	7.78	Average:	<b>0.00</b>						
G	7.79	7.91	<b>width</b>							
H (Corner)	8.17	8.27	Location (mm)	0	0	0	0	0		
I	7.86	7.95	face 1	0	0	0	0	0		0.00
L	7.67	7.85	face 2	0	0	0	0	0		0.00
M	7.8	7.96	face 3	0	0	0	0	0		0.00
N (Corner)	8.06	8.25	face 4	0	0	0	0	0		0.00
O	7.87	8								
P	7.64	7.75								
Q	7.86	7.88								
R (Corner)	8.24	8.3								
S	7.9	7.94								
T	7.94	8.14								
Average	<b>7.97</b>									

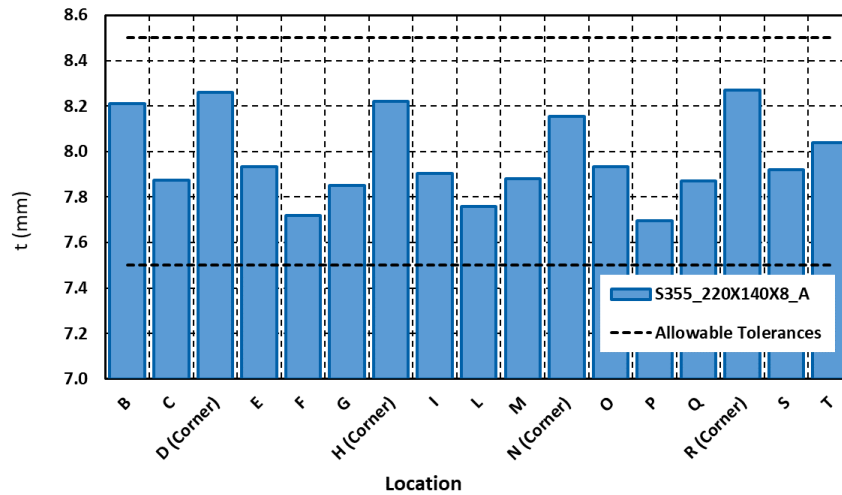


Figure A. 32 Difference between measured and nominal thickness for Specimen S355\_220X140X8\_A

Table A. 21 Measured thickness, corner radius and width for specimen S355\_220X140X8\_B

Thickness (mm)			Corner radius (mm)						Avg	
Location	End A	End B	Location (mm)	0		0		0		
				R1	R2	R1	R2	R1	R2	
B	8.33	8.11	Corner 1	0	0	0	0	0	0	0.00
C	7.95	7.9	Corner 2	0	0	0	0	0	0	0.00
D (Corner)	8.21	8.23	Corner 3	0	0	0	0	0	0	0.00
E	7.93	7.94	Corner 4	0	0	0	0	0	0	0.00
F	7.68	7.72	Average:	<b>0.00</b>						
G	7.94	7.9		<b>width</b>						
H (Corner)	8.22	8.12	Location (mm)	0	0	0	0	0		
I	7.87	7.91	face 1	0	0	0	0	0		0.00
L	7.69	7.79	face 2	0	0	0	0	0		0.00
M	7.84	7.86	face 3	0	0	0	0	0		0.00
N (Corner)	8.22	8.21	face 4	0	0	0	0	0		0.00
O	7.91	8.02								
P	7.66	7.76								
Q	7.93	7.94								
R (Corner)	8.2	8.23								
S	7.83	7.89								
T	8.19	8.18								
Average	<b>7.98</b>									

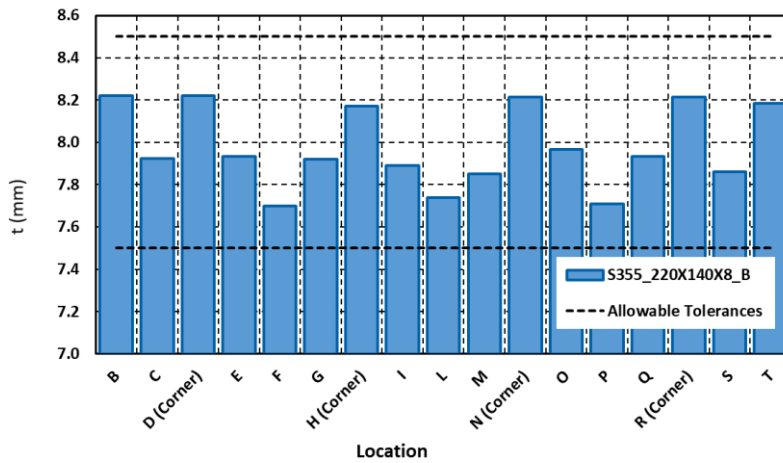


Figure A. 33 Difference between measured and nominal thickness for Specimen S355\_220X140X8\_B

Figure A. 34 Measured thickness, corner radius and width for specimen S355\_200X120X12\_A

Thickness (mm)			Corner radius (mm)						Avg
Location	End A	End B	Location (mm)	0		0		0	
B	12.51	12.46	R1	R2	R1	R2	R1	R2	
C	12.55	12.4	Corner 1	0	0	0	0	0	0.00
D (Corner)	12.58	12.67	Corner 2	0	0	0	0	0	0.00
E	12.75	12.46	Corner 3	0	0	0	0	0	0.00
F	12.3	12.3	Corner 4	0	0	0	0	0	0.00
G	12.61	12.6	Average:	<b>0.00</b>					
H (Corner)	12.83	12.62	<b>width</b>						
I	12.63	12.34	Location (mm)	0	0	0	0	0	
L	12.16	12.27	face 1	0	0	0	0	0	0.00
M	12.32	12.55	face 2	0	0	0	0	0	0.00
N (Corner)	12.66	12.66	face 3	0	0	0	0	0	0.00
O	12.94	12.4	face 4	0	0	0	0	0	0.00
P	12.33	12.28							
Q	12.42	12.66							
R (Corner)	12.71	12.64							
S	12.73	12.62							
T	12.78	12.68							
Average	<b>12.54</b>								

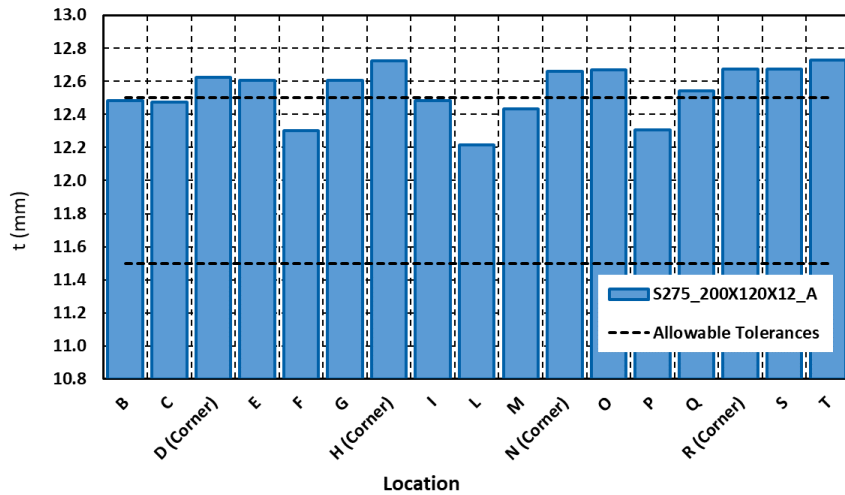


Figure A. 35 Difference between measured and nominal thickness for Specimen S275\_200X120X12\_A

Table A. 22 Measured thickness, corner radius and width for specimen S355\_200X120X12\_B

Thickness (mm)			Corner radius (mm)						Avg.
Location	End A	End B	Location (mm)	Too short		0		0	
				R1	R2	R1	R2	R1	R2
B	12.55	12.45							
C	12.52	12.45	Corner 1	0	0	0	0	0	0.00
D (Corner)	12.68	12.69	Corner 2	0	0	0	0	0	0.00
E	12.46	12.44	Corner 3	0	0	0	0	0	0.00
F	12.3	12.31	Corner 4	0	0	0	0	0	0.00
G	12.51	12.51	Average:	<b>0.00</b>					
H (Corner)	12.57	12.68	<b>width</b>						
I	12.35	12.33	Location (mm)	0	0	0	0	0	
L	12.13	12.23	face 1	0	0	0	0	0	0.00
M	12.53	12.38	face 2	0	0	0	0	0	0.00
N (Corner)	12.62	12.73	face 3	0	0	0	0	0	0.00
O	12.47	12.44	face 4	0	0	0	0	0	0.00
P	12.28	12.43							
Q	12.33	12.32							
R (Corner)	12.59	12.64							
S	12.44	12.28							
T	12.6	12.56							
Average	<b>12.46</b>								

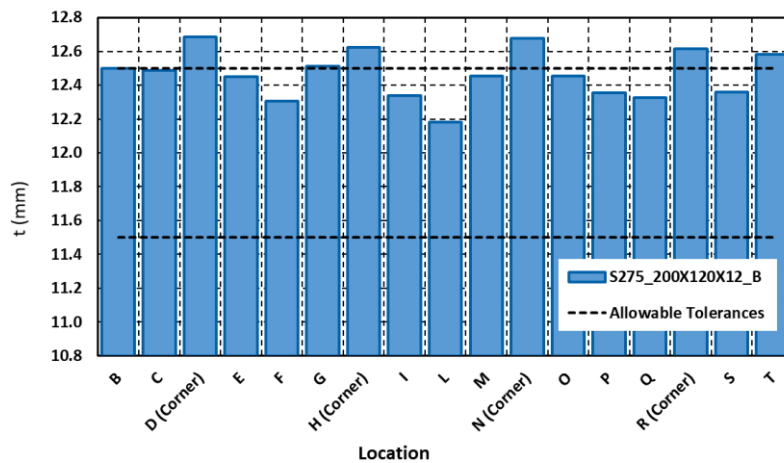


Figure A. 36 Difference between measured and nominal thickness for Specimen S275\_200X120X12\_B



## A.2 Tensile coupon test results

This Appendix presents the complete set of results relative to the cross-section coupons test. the typical positions of the coupon test from the section is shown in Figure A.2 1.

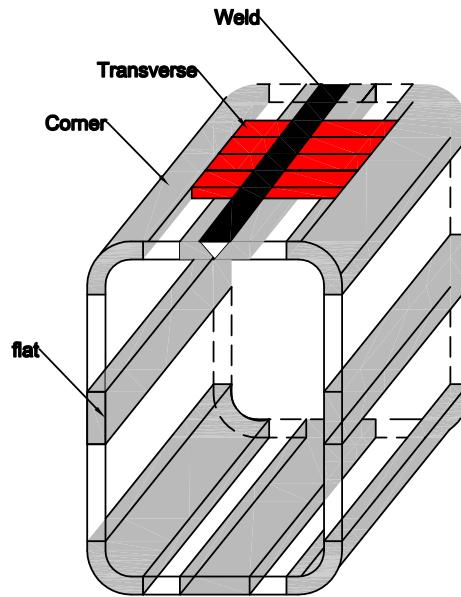
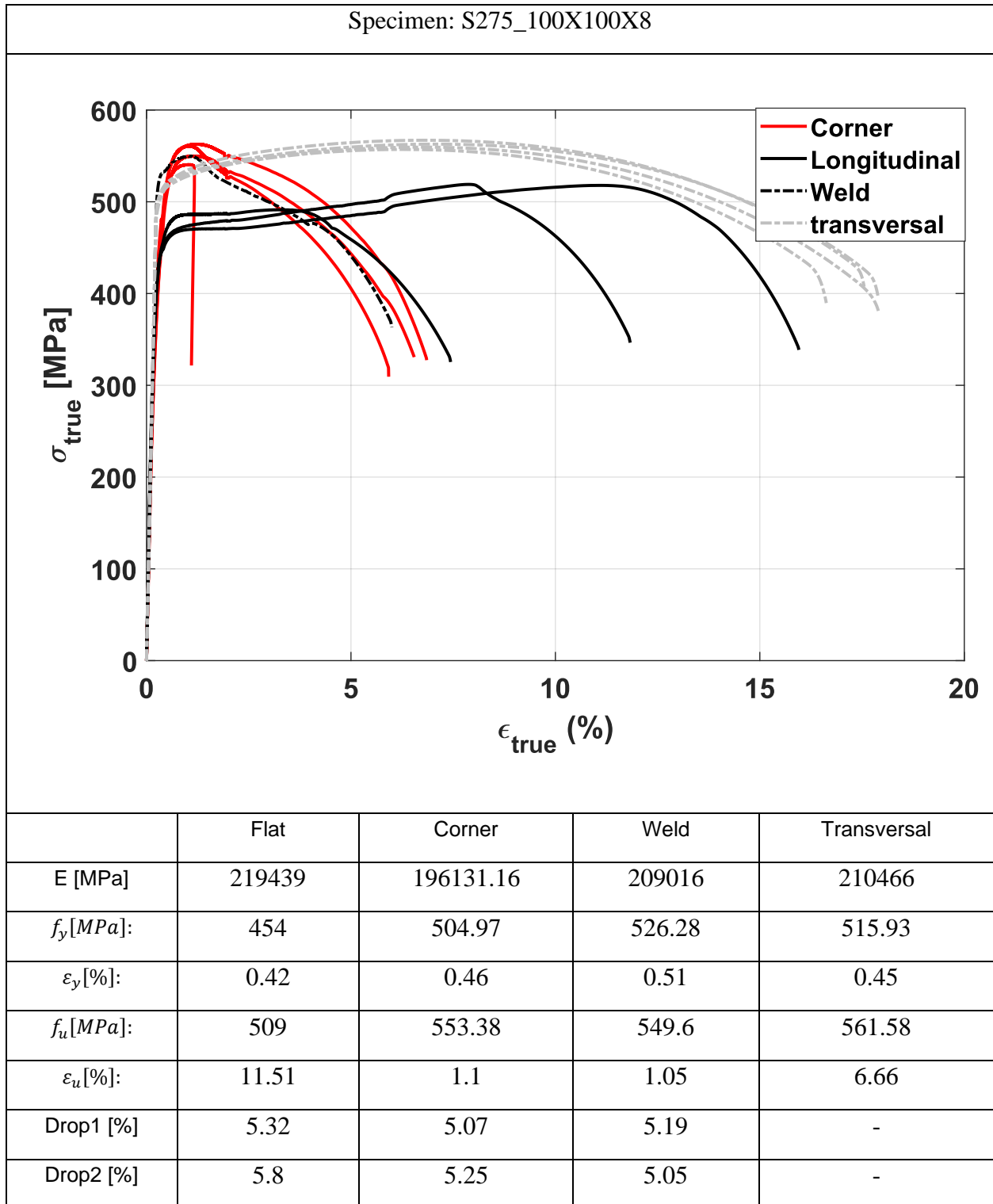


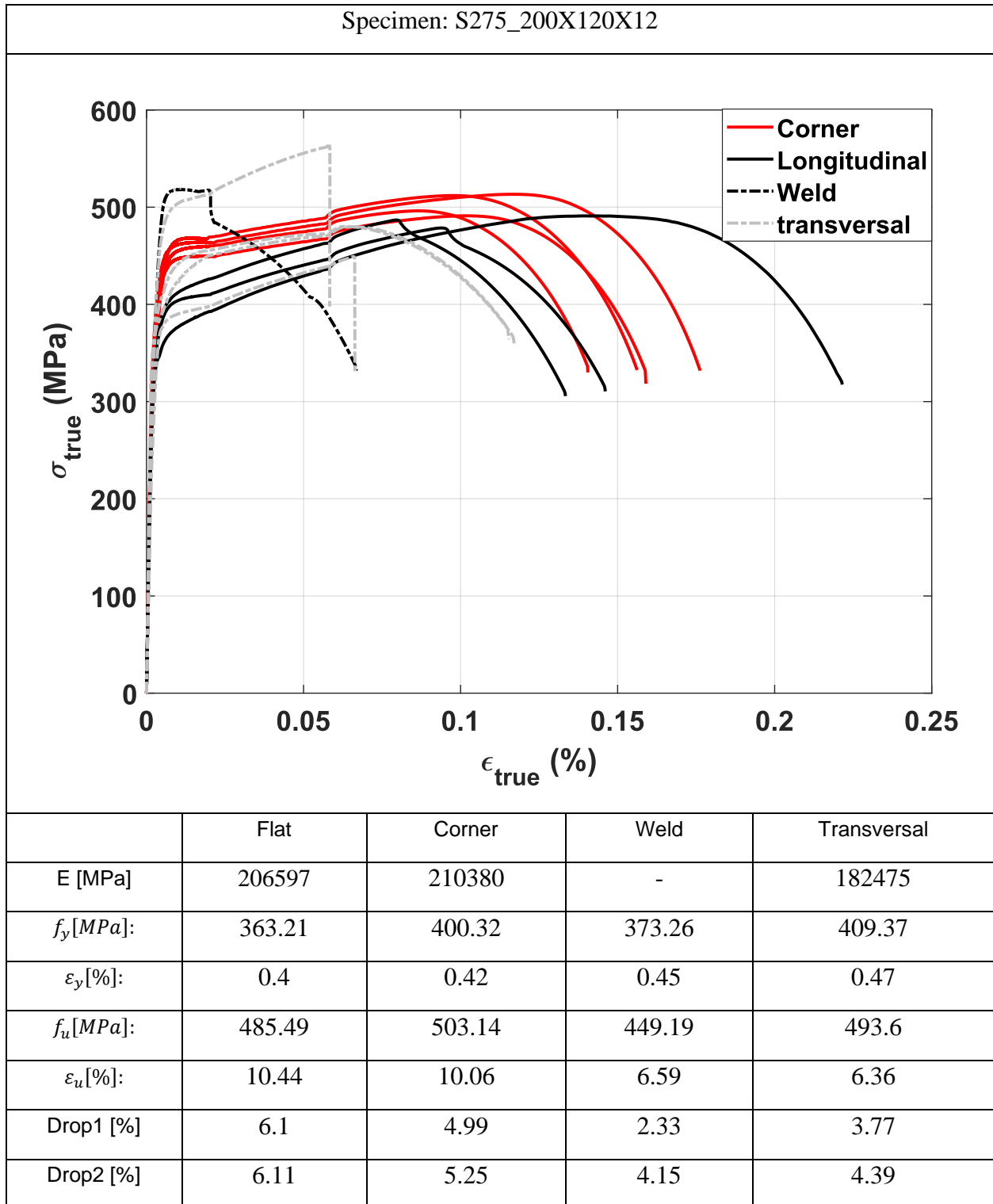
Figure A.2 1 Typical position of the coupons taken from the cross-section

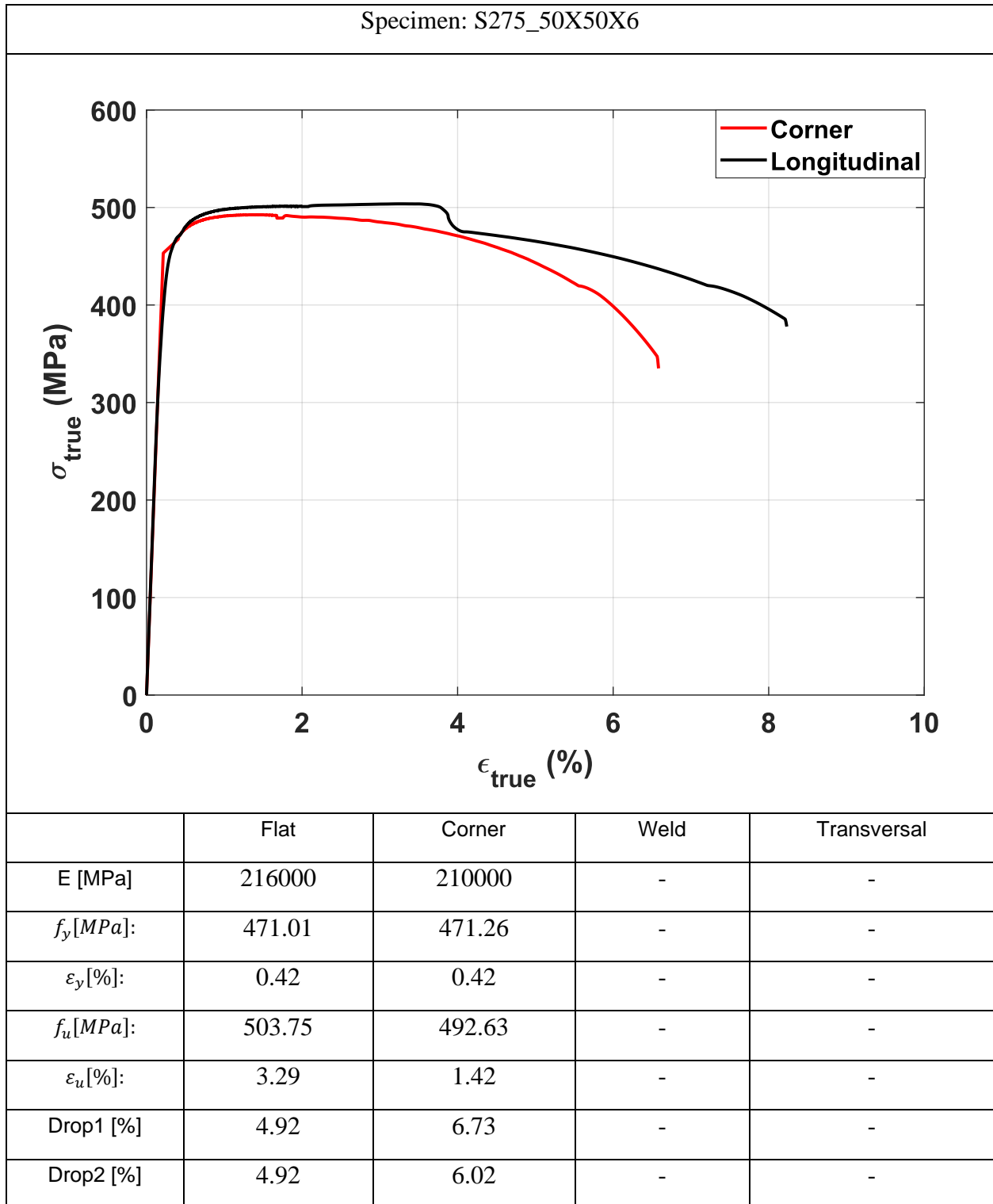
each page provides the following information:

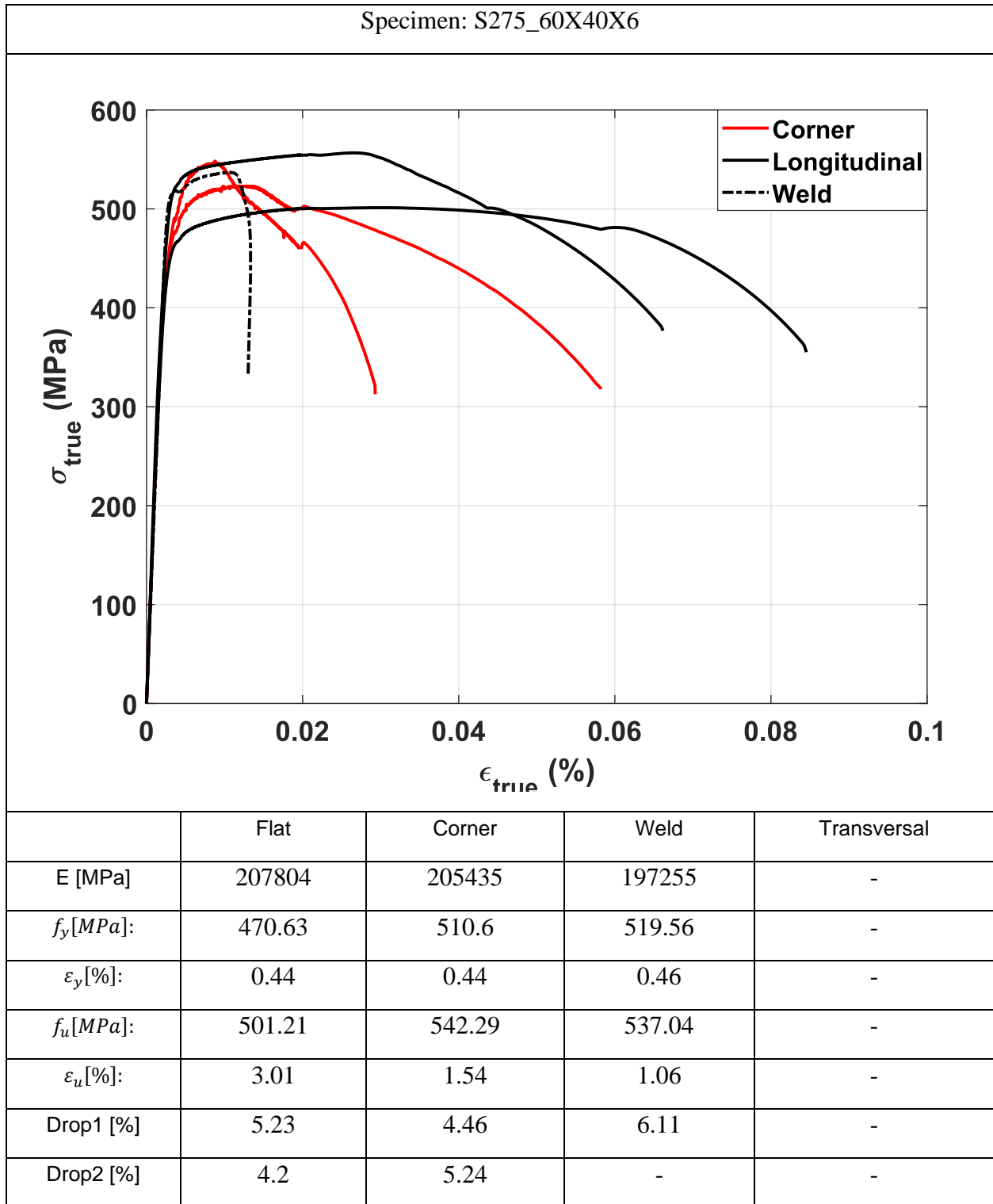
- I) Specimen name
- II) Measured material properties

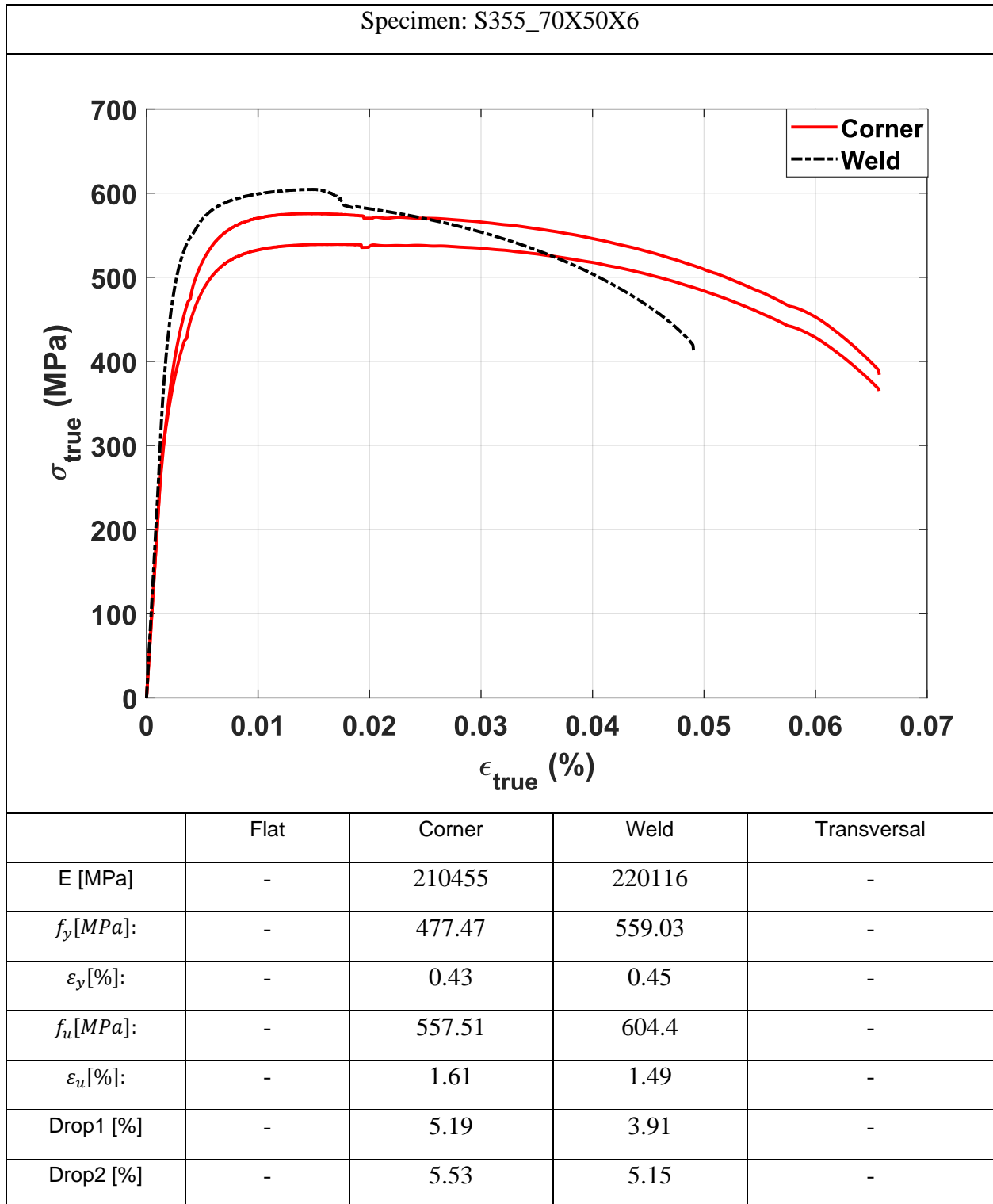
Drop1 and 2 are referring to the stop points in the test, i.e., stress relaxation. The first point is at 0.4% and the second point is at 2% strain.

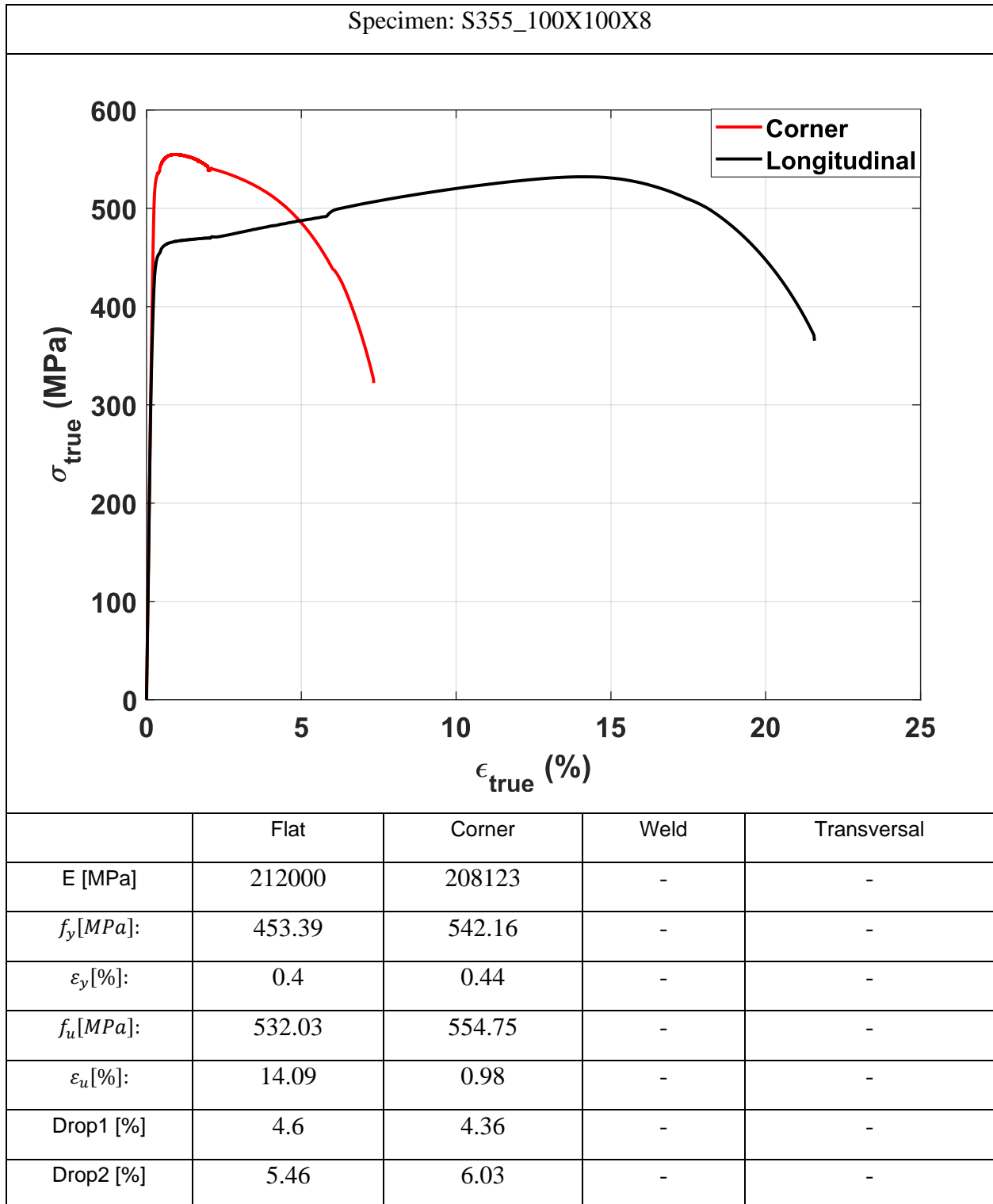


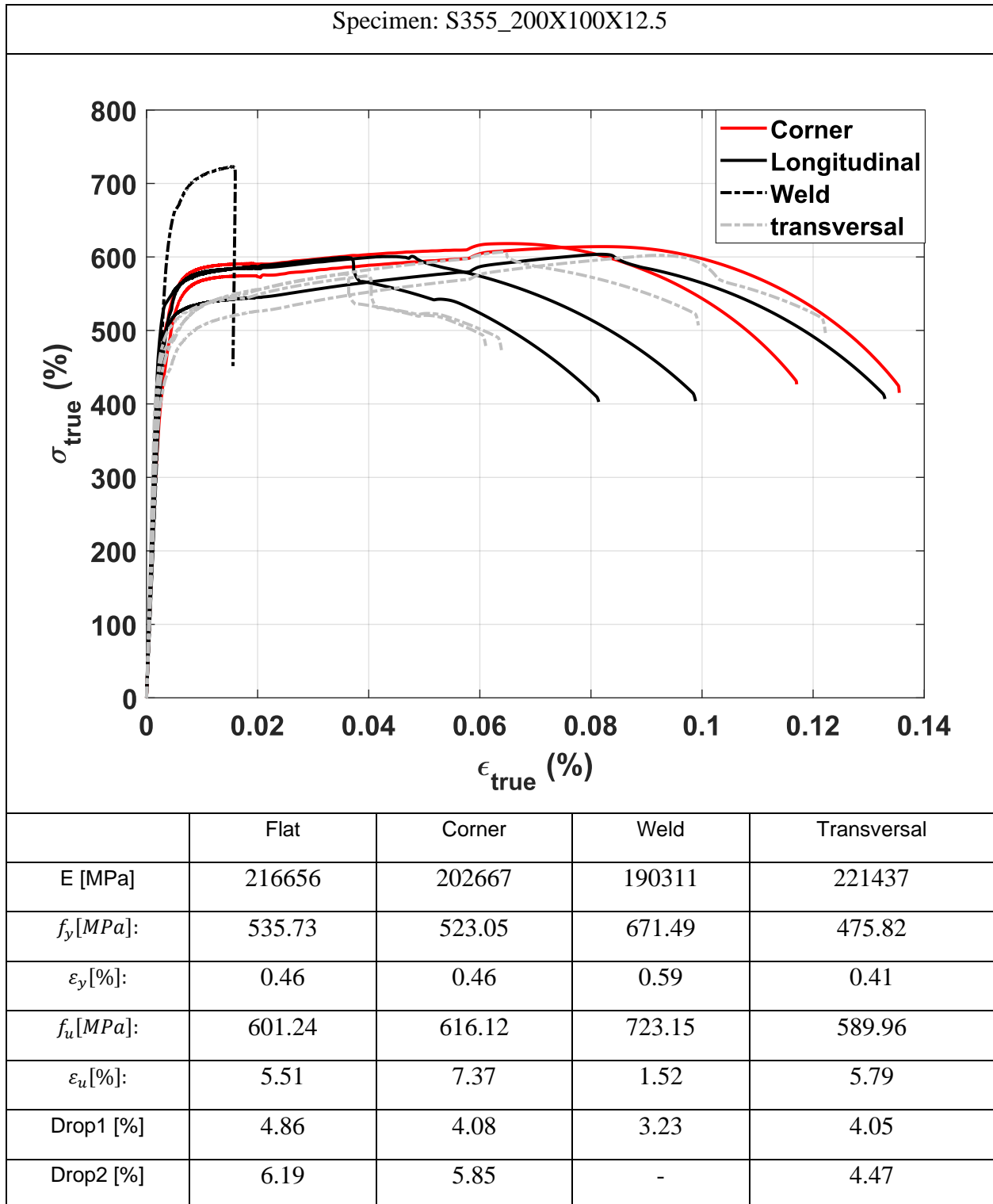






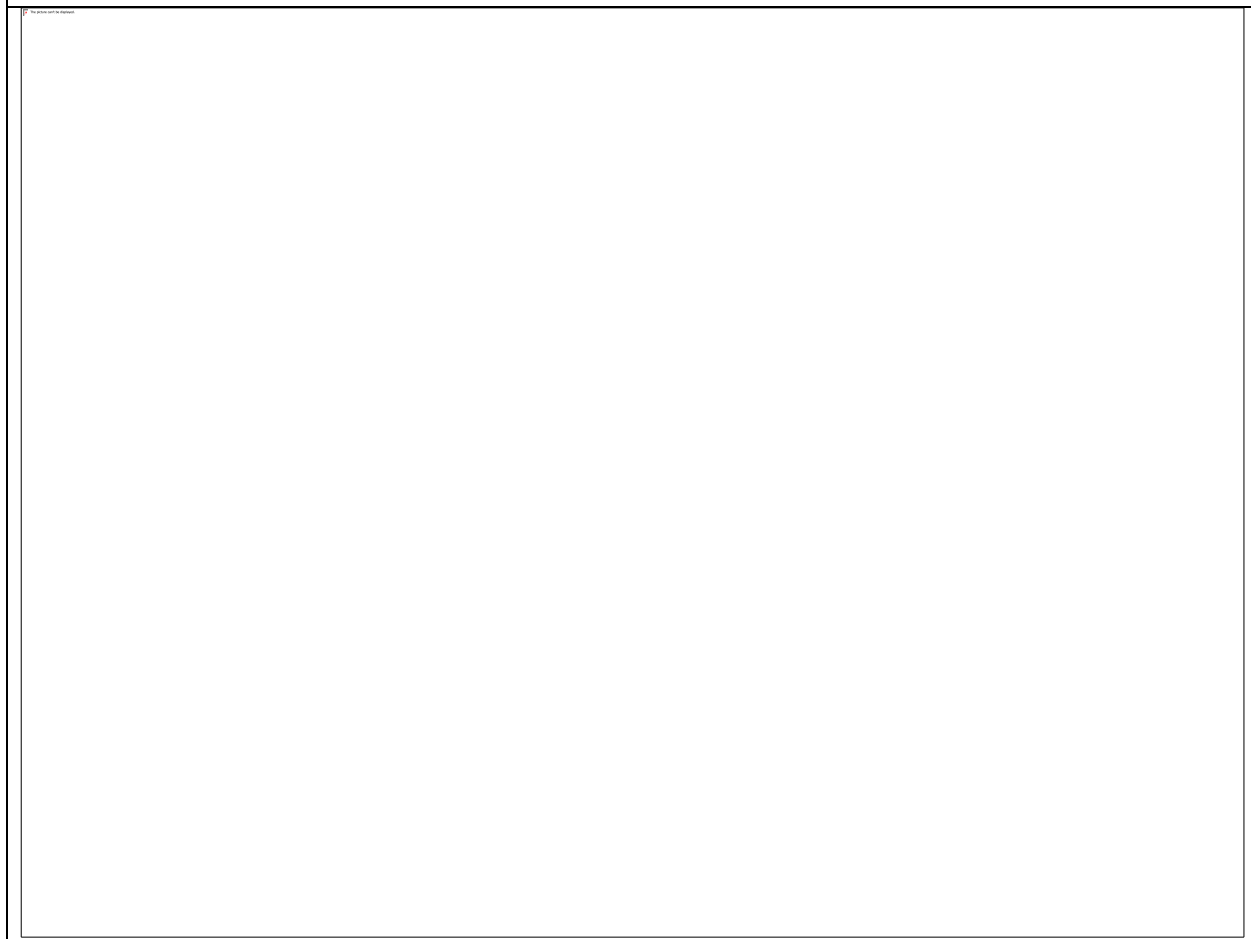








Specimen: S355\_200X200X8



	Flat	Corner	Weld	Transversal
E [MPa]	211152	201113	219132	218682
$f_y$ [MPa]:	463.77	536	525.28	501.66
$\epsilon_y$ [%]:	0.5	0.47	0.51	0.42
$f_u$ [MPa]:	554.91	582.5	621.83	542.77
$\epsilon_u$ [%]:	9.38	1.23	2.36	1.64
Drop1 [%]	6.24	5.37	10.17	4.98
Drop2 [%]	5.5	7.83	4.74	5.15

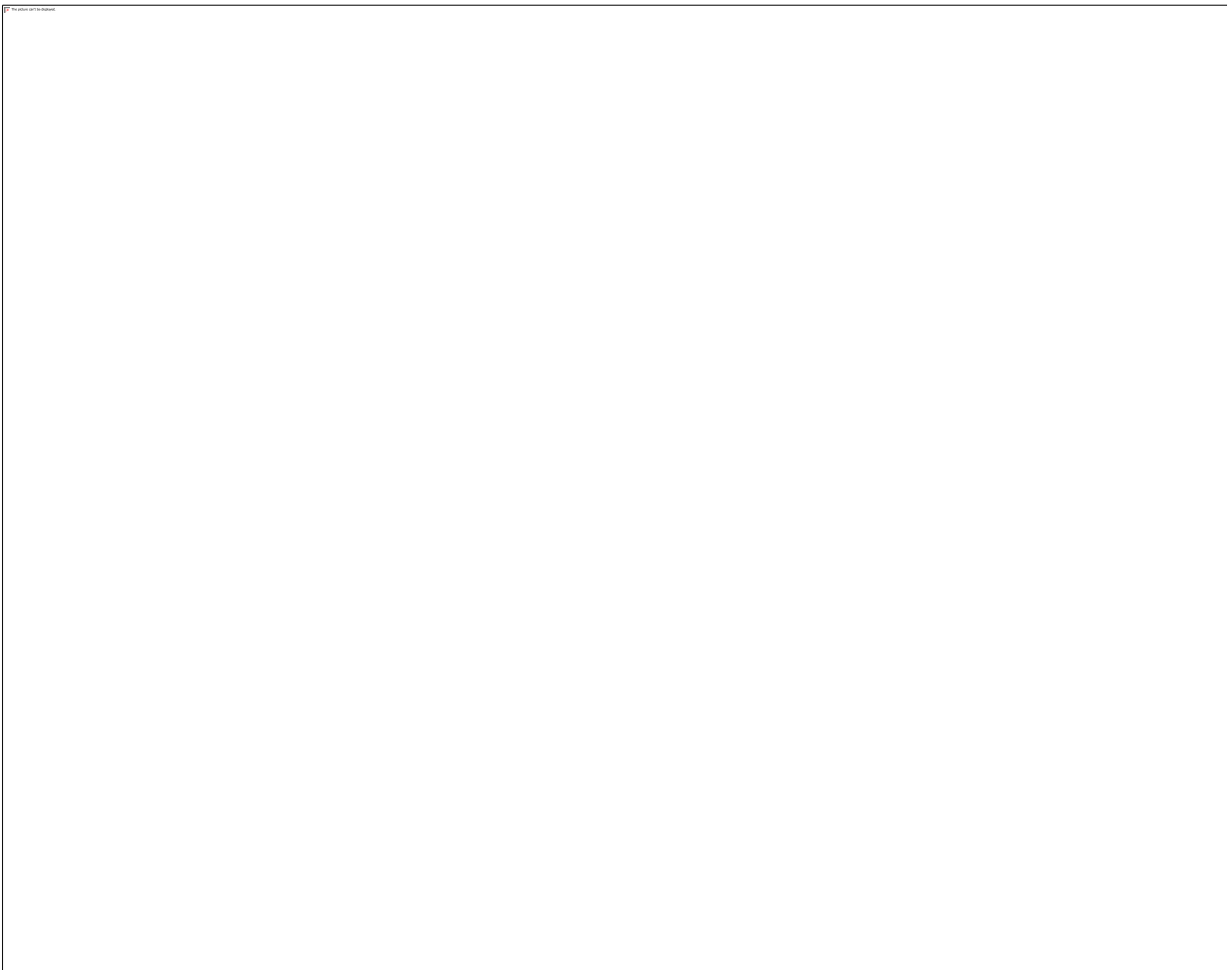
Specimen: S355_220X140X8				
	Flat	Corner	Weld	Transversal
E [MPa]	205404	202017	216352	201234
$f_y$ [MPa]:	445.64	521.95	575.54	485.02
$\varepsilon_y$ [%]:	0.45	0.46	0.41	0.45
$f_u$ [MPa]:	598.09	597.75	621.02	529.36
$\varepsilon_u$ [%]:	13.9	4.39	1.58	1.51
Drop1 [%]	5.44	4.93	4.82	5.13
Drop2 [%]	6.11	5.14	4.6	-

Specimen: S355_50X50X6				
	Flat	Corner	Weld	Transversal
E [MPa]	205287	196559	215321	-
$f_y$ [MPa]:	481.9	524.72	512.27	-
$\varepsilon_y$ [%]:	0.45	0.47	0.4	-
$f_u$ [MPa]:	525.19	565.18	519.39	-
$\varepsilon_u$ [%]:	5.09	1.13	0.84	-
Drop1 [%]	4.57	4.55	3.5	-
Drop2 [%]	5.44	6.33	-	-

Specimen: S275_60X60X6				
	Flat	Corner	Weld	Transversal
E [MPa]	214144	210472	194279	-
$f_y$ [MPa]:	481.28	505.99	577.46	-
$\varepsilon_y$ [%]:	0.44	0.44	0.5	-
$f_u$ [MPa]:	498.1	548.66	586.31	-
$\varepsilon_u$ [%]:	1.8	0.92	0.59	-
Drop1 [%]	4.38	3.72	3.93	-
Drop2 [%]	5.23	4.35	-	-

Specimen: S275_60X60X6				
	Flat	Corner	Weld	Transversal
E [MPa]	214144	210472	194279	-
$f_y$ [MPa]:	481.28	505.99	577.46	-
$\epsilon_y$ [%]:	0.44	0.44	0.5	-
$f_u$ [MPa]:	498.1	548.66	586.31	-
$\epsilon_u$ [%]:	1.8	0.92	0.59	-
Drop1 [%]	4.38	3.72	3.93	-
Drop2 [%]	5.23	4.35	-	-

# **Appendix B Detailed flexural buckling test results and comparison with FE results.**



Comparison of FEM model and experimental results for square sections



Comparison of FEM model and experimental results for rectangular sections

